Constitutive modelling of cyclic sand behaviour for offshore foundations

Liu, H.

DOI
10.4233/uuid:6e3ae33c-e95d-474f-8d6b-d8c0f8aa4788

Publication date
2020

Document Version
Final published version

Citation (APA)
Liu, H. (2020). *Constitutive modelling of cyclic sand behaviour for offshore foundations*. [Dissertation (TU Delft), Delft University of Technology]. https://doi.org/10.4233/uuid:6e3ae33c-e95d-474f-8d6b-d8c0f8aa4788

Constitutive modelling of cyclic sand behaviour for offshore foundations

Constitutive modelling of cyclic sand behaviour for offshore foundations

Dissertation

for the purpose of obtaining the degree of doctor
at Delft University of Technology
by the authority of the Rector Magnificus Prof.dr.ir. T.H.J.J. van der Hagen,
chair of the Board for Doctorates
to be defended publicly on
Thursday 1 October 2020 at 15:00 o'clock

by

柳浧元 **Haoyuan LIU**

Master of Science in Civil Engineering: Geotechnical Engineering,
University of Nottingham, Nottingham, UK,
born in Gansu, China.

This dissertation has been approved by the promotors.

Composition of the doctoral committee:

Rector Magnificus,	chairperson
Prof. dr. M. A. Hicks,	Delft University of Technology, promotor
Dr. F. Pisanò,	Delft University of Technology, promotor
Independent members:	
Prof. dr. G. T. Houlsby,	University of Oxford
Prof. dr. C. di Prisco,	Politecnico di Milano
Prof. dr. C. Jommi,	Delft University of Technology
Prof. dr. K. G. Gavin,	Delft University of Technology
Dr. ir. R. Brinkgreve,	Delft University of Technology

Keywords: sand, cyclic, constitutive model, Finite Element, monopile

Printed by: Ipskamp printing

ISBN 978-94-6384-157-3

An electronic version of this dissertation is available at
http://repository.tudelft.nl/.

献给所有帮助过我的人

dedicated to every one who helped during this journey

Contents

Summary

The wind energy industry has gained a key role in the global fight against greenhouse gas emissions. Although fossil fuels have still the largest share in the global energy mix, the production of wind energy, especially offshore, has rapidly grown since the 1990s. According to the International Energy Association, Europe targets offshore wind to become the main electricity source by 2040. To meet such a goal, significant developments in research and technology are ongoing to reduce/optimise the high costs for materials, manufacturing, transportation, and installation of offshore wind farms. A significant cost item for offshore wind turbines (OWTs) is represented by their supporting structures and foundations, especially as the rush towards bigger OWTs and larger water depths poses a serious threat to cost reduction targets. To make offshore wind competitive in the energy market, reducing investment costs is mandatory. Since OWT foundations mobilise up to around 18% of the total investment in typical offshore wind projects, the importance of reconsidering/improving geotechnical design approaches for offshore foundations is self-apparent.

Monopiles (steel tubular piles of large diameter) are presently the most common foundation type for OWTs, and must be designed to be fully functional over an operational lifetime of 20 $\sim$ 30 years – i.e., under 10^8 to 10^9 loading cycles produced by environmental loads (mostly wind and sea waves). Among a number of relevant design checks, OWT manufacturers recommend that monopiles should not experience a total/permanent lateral rotation (tilt) larger than $0.25 - 0.5^\circ$. However, existing methods for the analysis of pile foundations are not yet well suited to perform reliable design checks in relation to cyclic loading, which can lead to non-optimal, and perhaps erroneous, design choices. In order to alleviate the conservatism normally associated with pile tilt checks, deeper understanding and improved modelling of cyclic soil-monopile interaction is necessary, and therefore of cyclic soil behaviour.

The problem of designing OWT foundations, and particularly of predicting cyclic monopile tilt, has/is promoted/promoting numerous studies worldwide, both experimental and numerical. Among the approaches available in the literature, the Author believes that implicit/step-by-step 3D FE analysis, although computationally demanding, possesses the highest potential to shed light on governing geotechnical mechanisms, and therefore support the improvement of design methods. It should be noted, however, that sound implicit 3D FE predictions may only be achieved when a reliable soil model is adopted in the considered structure/foundation-soil model.

In this work, a fabric-sensitive constitutive model for sand, SANISAND-MS, is developed to support the cyclic analysis of offshore monopiles at a more fundamental level than enabled by traditional, spring-based interaction models. In particular, the constitutive modelling work builds on the theory of bounding surface plasticity,

and focuses on the phenomenological representation of sand fabric effects (and associated load-induced anisotropy). Such effects, especially relevant under cyclic loading conditions, are tracked by the model using the notion of a memory surface. The proposed formulation is validated against a wide set of laboratory test results from the literature, spanning a variety of initial, loading, and drainage conditions. Following a thorough validation of the constitutive equations, SANISAND-MS is finally applied to the 3D FE analysis of a cyclically loaded monopile in dry sand, in order to assess the 'implicit' performance of the constitutive model in a relevant boundary value problem.

In summary, this work boosts confidence about the quality and applicability of SANISAND-MS in the 3D FE modelling of soil-structure interaction problems, particularly with respect to offshore foundations subjected to cyclic loading. The development of the proposed SANISAND-MS 3D FE modelling framework is believed to take a valuable step forward, and will support in the near future the enhancement of monopile design practice.

Samenvatting

De windenergie industry heeft een belangrijke positie verworven in het wereldwijde gevecht tegen de uitstoot van broeikasgassen. Hoewel fossiele brandstoffen nog steeds het grootste aandeel vormen in de wereldwijde energie-mix, is de productie van wind energie, in het bijzonder wind op zee, sinds de jaren ' 90 sterk gegroeid. Volgens het Internationale Energie Agentschap heeft Europa als doel om in 2040 wind op zee de belangrijkste bron voor electriciteit te laten zijn. Om dit doel te bereiken zijn significante ontwikkelingen in onderzoek en technologie gaande om de hoge kosten van materialen, productie, transport en installatie van windparken op zee te reduceren/optimaliseren. Een significante kostenpost voor windturbines op zee wordt gevormd door hun ondersteuningsconstructies en funderingen, waarbij de vlucht naar grotere windturbines en grotere waterdieptes een serieuze bedreiging vormt voor de doelstelling van kostenreductie. Om wind op zee competitief te maken op de energiemarkt is een reductie van investeringskosten noodzakelijk. Omdat de funderingen van offshore windturbines tot 18% van de totale investeringskosten in doorsnee offshore windparken beslaan, is het belang van een herbeschouwing / verbetering van de geotechnische ontwerpbenaderingen voor offshore funderingen evident.

Monopalen (stalen buispalen met grote diameter) zijn op het moment het meest gangbare funderingstype voor offshore windturbines, en moeten worden ontworpen voor een functionele levensduur van 20 - 30 jaar –d.w.z., onder 10^8 tot 10^9 belastingcycli gevormd door omgevingsbelasting (vooral wind en golven). Als onderdeel van een aantal relevante ontwerpeisen bevelen offshore windturbine fabrikanten aan dat monopalen geen rotatie (scheefstand) van meer dan $0.25 - 0.5^\circ$ ondergaan. Echter, bestaande methoden voor het analyseren van paalfunderingen zijn nog niet geschikt genoeg om betrouwbare ontwerpcontroles uit te voeren in relatie tot cyclische belasting, hetgeen kan leiden tot niet-optimale en eventueel foutieve ontwerpkeuzes. Om het conservatisme dat normaalgesproken gepaard gaat met controles op paalscheefstand te verminderen, is een dieper begrip en een verbeterde modellering van cyclische grond-monopaal interactie noodzakelijk, en daarbij van cyclisch grondgedrag.

Het probleem van het ontwerpen van offshore windturbines, en in het bijzonder het voorspellen van cyclische monopaal scheefstand, leidt / heeft aanleiding gegeven tot vele studies, wereldwijd, zowel experimenteel als numeriek. Van de methoden die in de literatuur beschikbaar zijn vindt de Auteur dat impliciete / stap-voorstap 3D eindige-elementenberekeningen, hoewel rekenintensief, het beste potentieel vormen om opheldering te geven op de maatgevende geotechnische mechanismen, en daarom de verbetering van ontwerpmethodes ondersteunen. Het moet echter worden opgemerkt dat correcte impliciete 3D eindige-elementenpredicties

alleen kunnen worden bereikt wanneer een betrouwbaar grondmodel wordt gehanteerd in het beschouwde constuctie/fundering-grond model.

In dit werk is een textuur-sensitief constitutief model voor zand, genaamd SANISANDMS, ontwikkeld om de cyclische berekening van offshore monopalen op een meer fundamenteel niveau te ondersteunen dan wat wordt bereikt middels traditionele interactiemodellen gebaseerd op veren. In het bijzonder bouwt het werk aan constitutieve modellen voort op de theorie van de 'grensvlak plasticiteit' (bounding surface plasticity), en is gericht op de fenomenologische vertegenwoordiging van zand textuur-effecten (en daaraan gerelateerde belastinggestuurde anisotropie). Zulke effecten, die in het bijzonder relevant zijn onder cyclische belastingcondities, worden gevolgd in het model door gebruik te maken van het begrip 'geheugenvlak' (memory surface). De voorgestelde formulering is gevalideerd aan de hand van een brede verzameling van laboratoriumproefresultaten uit de literatuur, welke een reeks van initiële, belasting- en drainagecondities omvat. Na een gedegen validatie van de constitutieve vergelijkingen is het SANISANDMS model uiteindelijk toegepast in een 3D eindige-elementenberekening van een cyclisch belaste monopaal in zand, om daarmee de impliciete prestatie van het constitutieve model in een relevant randvoorwaardeprobleem te beoordelen.

1

Background

1

The global energy demand has been increasing by about 20% per decade due to population growth and lifestyles of higher standard. Even though fossil fuels were still providing more than 85% of global energy at the end of 2017 (NRCan, 2017), they are foreseen to inevitably reduce their market shares due to their negative impact on the environment (e.g., greenhouse gas emissions). In contrast, renewable sources of energy are gaining increasing popularity. To meet the global reduction target for greenhouse gas emission, the European Union proposed an energy transition plan that sets 27% of total energy consumption to be provided by renewable sources by 2030 (Knopf et al., 2015) (with 40% greenhouse gas emissions reduction compared to 1990). In the steadily evolving energy mix, wind power, both from the land and the ocean, has rapidly developed and is now key to achieving international energy goals.

Regarding the harvest of wind energy from the ocean, the offshore wind industry has been considerably growing since 1991, when the first offshore wind farm was installed off the coast of Denmark. To date, Europe dominates worldwide the offshore wind market and the associated power output. In 2019, the offshore wind capacity installed in Europe was 3623 MW, with a total cumulative capacity of about 22 GW (Europe Wind, 2020). Recent figures for annual and cumulative offshore wind capacity in Europe are visualised in Fig. 1.1. As pointed out in the

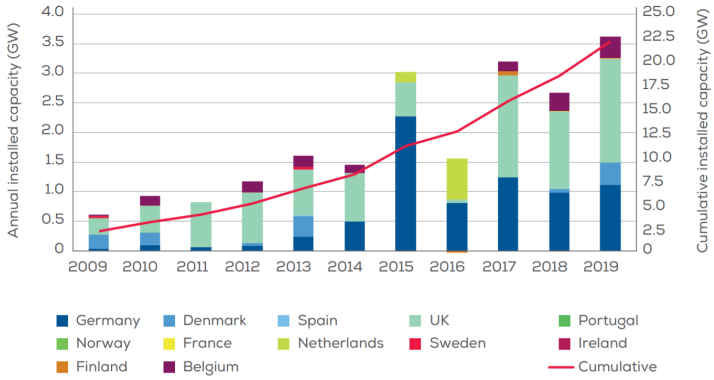

Figure 1.1: Offshore wind capacity in Europe: annual installations by country (left axis) and cumulative capacity (right axis) – reprinted from Europe Wind (2020)

National Energy and Climates Plans (NECPs) and Renewable Energy targets of European countries, the total offshore wind potential is expected to reach 100 GW by 2030 (Europe Wind, 2020). The International Energy Agency (IEA) predicts that, in the longer term, Europe will make a significant step towards meeting the Paris Agreement and becoming carbon-neutral (IEA, 2019). Specifically, the aim is to make offshore wind the main electricity source by 2040, and reach a total installed capacity of 230 to 450 GW by 2050. Offshore wind is, and will continue to be, centre stage in the renewable energy arena.

Even though the offshore wind infrastructure has developed significantly in the recent past, construction and maintenance costs remain relatively high. Globally,

the average levelised cost of onshore wind is around 60 USD/MWh. In comparison, the corresponding costs for offshore wind electricity are 130 USD/MWh (2018) (IREND, 2019), which is more than double for developments on land. To make offshore wind energy competitive in the market, middle/long-term cost reduction targets have been set to achieve $50-90$ USD/MWh by 2030 and $30-70$ USD/MWh by 2050 (see Fig. 1.2). A significant fraction of offshore wind farm costs are asso-

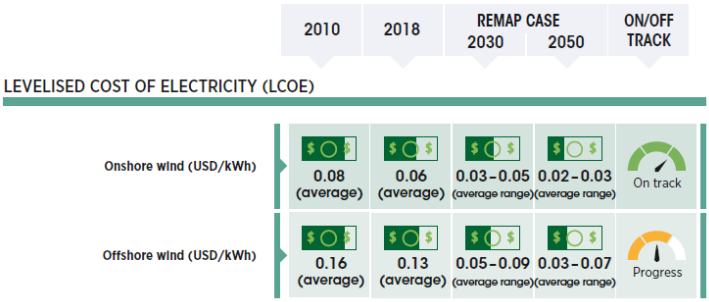

Figure 1.2: Levelised cost of onshore and offshore wind electricity – reprinted from IREND (2019)

ciated with the fabrication and installation of supporting structures and foundation systems. Foundations are known to take up to around 18% of the total investment in typical offshore wind projects (Smart et al., 2016).

Monopile foundations, tubular steel piles driven into the seabed and supporting the overlying wind tower, are the most popular substructure type. At present, about 80% of the offshore wind turbines (OWTs) in Europe are supported by monopiles, followed by jacket and gravity base, see Fig. 1.3. Monopiles are simple to man-

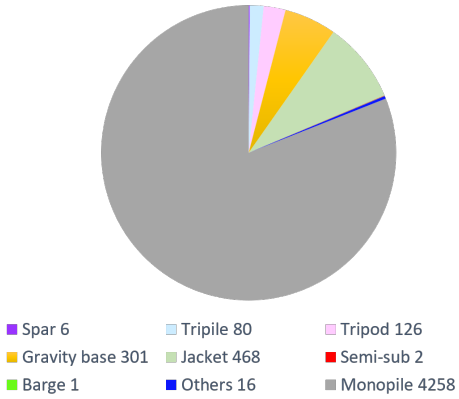

Figure 1.3: Deployment of different OWT substructure/foundation types in Europe – modified after Europe Wind (2020)

ufacture and require limited seabed preparation. Nonetheless, special attention is necessary for their design, which must be such to ensure satisfactory performance

under the significant horizontal/moment loads transmitted by the superstructure. According to the current state of practice, offshore monopiles are normally employed in water depths up to about 30 ∼ 35m, with diameter in the range from 5 to 10 m, and embedment ratio (embedded length over diameter) in the order of 3–6. Due to the depletion of near-shore locations, offshore wind farms have been progressively moved towards deeper waters to exploit more steady and reliable wind power. In recent offshore wind projects, monopiles at larger distance from the shore (from an average distance of 35 km in 2018 to 59 km in 2019) and in deeper waters (~ 50 m) have been considered, along with the installation of bigger and more powerful OWTs (Fig. 1.4) – the average rated capacity of installed turbines increased from 6.8 MW in 2018 to 7.8 MW in 2019 (Europe Wind, 2020).

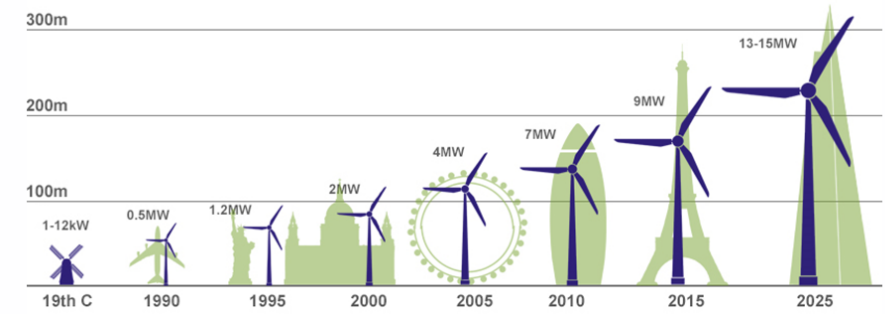

Figure 1.4: Evolution in size and power output of OWTs (from Bloomberg New Energy Finance).

The gradual increase in monopile size and water depth has led to higher foundation costs for materials, manufacture, transportation, and installation (Arany et al., 2015). It is self-apparent that cost optimisation targets cannot be met without reconsidering/improving design criteria and methodologies. At present, offshore monopiles are usually designed based on the use of so-called *p-y* curves, for instance, in the version recommended by the American Petroleum Institute (API) for slender/flexible piles supporting offshore oil and gas platforms (API, 2014; DNV, 2016). The *p-y* method relies on the classical Winkler beam approach, i.e., on representing the pile-soil system as a beam supported by independent non-linear elastic springs (Fig. 1.5a). In this framework, the spring/soil reaction, p, is related at a given depth to the pile lateral displacement y (see a typical example of soil reaction curve in Fig. 1.5b). As previously mentioned, *p-y* formulations were initially conceived for the design of flexible piles with small diameter (approximately 2 m). As monopiles are cylindrical structures of large diameter, the adoption of existing API methods may lead to non-optimal, and perhaps erroneous, design choices. To fill this gap, the PIle Soil Analysis (PISA) project was established in the UK in 2013 to improve design procedures for laterally loaded monopiles using medium-scale field testing and advanced numerical studies (Byrne et al., 2019). The resulting PISA method enhances the traditional *p-y* approach by introducing additional soil reaction components, related to base fixity/shear and shear stresses mobilised along the pile shaft. The PISA approach is applicable to both marine sand (Burd et al.,

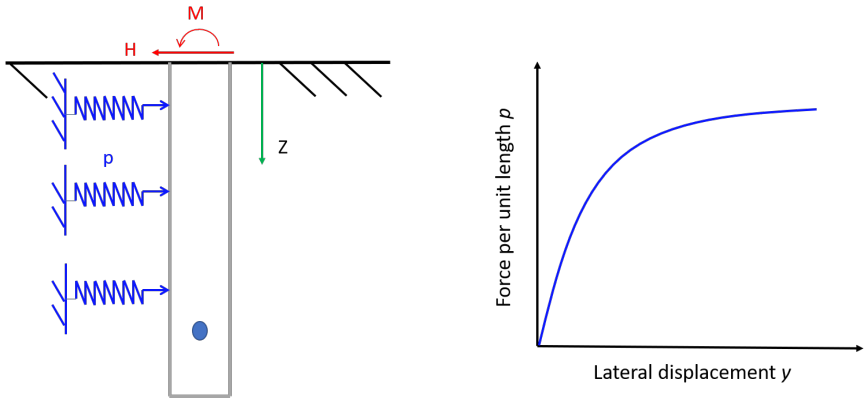

(a) Spring modelling of pile-soil interaction (b) Example of *p-y* soil reaction curve

Figure 1.5: The *p-y* method for the analysis of lateral pile-soil interaction.

2020) and clay till (Byrne et al., 2020), with 3D Finite Element (FE) simulation results used to support the calibration of soil reaction functions. It should be noted, however, that the proposed new method exclusively considers monotonic loading conditions.

Further research on soil-foundation interaction in marine environments is still needed for higher optimisation of OWT support structures and related costs. Offshore monopile design must be such to fulfil requirements regarding foundation capacity, serviceability, and fatigue, in presence of either moderate service loads or exceptional solicitations (Kallehave et al., 2015; Arany et al., 2017). With respect to the limit state design philosophy, the following design checks are considered to be the most relevant (Bhattacharya, 2019; Pisanò et al., 2019):

1. first natural frequency of the turbine-foundation-soil system (f_0) within the so-called 'soft-stiff' range, i.e., $f_{1p} < f_0 < f_{3p}$, where f_{1p} and f_{3p} are the frequencies of rotor revolution and blade-passing, respectively (Bhattacharya, 2019);

2. sufficient resistance to fatigue under prolonged operational loads (FLS, Fatigue Limit State);

3. sufficient capacity under loads of exceptional magnitude (ULS, Ultimate Limit State);

4. full serviceability (limited deformations) under environmental and/or mechanical service loads (SLS, Serviceability Limit State).

The design of OWT monopiles is mostly driven by horizontal/moment loads, and must be carried out in consideration of the following geotechnical factors : (1) highly non-linear soil behaviour, especially under cyclic loading, (2) accumulation of irreversible soil deformations, (3) energy dissipation in the soil, and (4) soil erosion

(scour) around the foundation. Issues related to seismic response are presently receiving increasing attention as new offshore wind farms are being planned/built in seismically active regions, such as the Asia-Pacific area (Kaynia, 2019).

Monopiles for offshore wind turbines must be designed to be fully functional over an operational lifetime of 20 $\sim$ 30 years – i.e., under 10^8 to 10^9 cycles of severe environmental loading induced by wind, sea waves and currents. Lateral displacements and pile head rotation (monopile tilting) may accumulate during such a long operational life. To fulfil relevant SLS requirements, a strict limit of $0.25-0.5^\circ$ on the cumulative pile head rotation (monopile tilt) is normally recommended by turbine manufacturers (DNV, 2016). Such a limit is becoming increasingly design-driving for large monopiles, in that it leads to monopile lengths larger than resulting from ULS capacity checks (Arany et al., 2017).

In order to alleviate the conservatism normally associated with pile rotation SLS checks, deeper understanding/modelling of soil-monopile interaction under cyclic loading is necessary, and therefore of intrinsic cyclic soil behaviour. Relevant experimental work has been recently performed to study cyclic monopile tilting, mostly in sandy soil, for instance through small-scale testing under either normal (LeBlanc et al., 2010; Nicolai and Ibsen, 2014; Nicolai et al., 2017; Albiker et al., 2017; Abadie et al., 2019; Richards et al., 2019) or augmented gravity (Klinkvort, 2013; Rudolph et al., 2014; Nicolai et al., 2017; Truong et al., 2019), or medium-scale testing in the field (Li et al., 2015). As a result, empirical pile tilt relationships have been proposed (Lin and Liao, 1999; LeBlanc et al., 2010; Richards et al., 2019), however with limited possibilities to go beyond the geotechnical/loading conditions considered in the reference dataset. On the other hand, the numerical prediction of cyclic monopile tilt is challenging for at least two reasons (Pisanò et al., 2019): (1) the computational cost is too high when pursued through so-called implicit analysis (Niemunis et al., 2005) – i.e., step-by-step numerical calculation in the time-domain; (2) dearth of soil models able to accurately reproduce the high-cyclic behaviour of soils, i.e. under a number of loading cycles N larger than 10^4 (Wichtmann and Triantafyllidis, 2016). An alternative approach is to combine explicit constitutive models[1] – such as the High-Cyclic Accumulation (HCA) model by Niemunis (2003), or the 'contour diagrams' approach developed at the Norwegian Geotechnical Institute (Andersen et al., 1988) – with 2D/3D FE analysis, so that the monopile response to cyclic loading (for instance, in terms of lateral tilt) can be simulated with lower computational costs. Such an approach is generally referred to as 'explicit' (Achmus et al., 2009; Jostad et al., 2015; Wichtmann et al., 2017; Chong, 2017). Furthermore, analysis approaches based on the 'macro-element' concept have gained substantial popularity (Houlsby et al., 2017; Abadie et al., 2019; Page et al., 2019). The macro-element method directly provides a lumped relationship between force/moment and displacement/rotation components for the whole foundation and the surrounding soils at the interface point with the (OWT) superstructure. Accordingly, macro-elements allow to drastic reduction of the computational burden of time-domain soil-structure simulations, for instance in com-

[1] constitutive models that 'explicitly' relate certain features of cyclic soil behaviour, such as accumulation of strains and pore water pressure, to the number N of loading cycles

parison to fully 3D approaches. However, among all the above methods, implicit 3D FE modelling seems to possess the highest potential to reproduce and explain geotechnical processes around a cyclically loaded monopile.

1.1. Motivation

Thorough understanding of complex soil-structure interaction mechanisms in OWTs is key to improving engineering design methods and optimising fabrication and/or installation costs for OWT support structures. Previous studies have already pointed out how global monopile-soil interaction is closely linked to the high-cyclic behaviour of the surrounding soil under a variety of geotechnical and loading conditions (Cuéllar et al., 2009; Abadie et al., 2019). In this respect, despite their high computational costs, implicit, step-by-step 3D FE analysis is expected to valuably contribute to the understanding of governing geo-mechanisms in OWTs, and to guide the enhancement of foundation design methods in the presence of cyclic loading (Cuéllar et al., 2014).

The soundness of implicit 3D FE analysis largely depends on the accuracy of the constitutive model adopted for the cyclically loaded soil (Pisanò et al., 2019). Reliable 3D FE modelling is expected to provide necessary insight into the behaviour of the pile-soil system, even under conditions not previously monitored in the field or tested in the laboratory (Truong et al., 2019). The selection of a suitable constitutive model is relevant to all the above-mentioned ULS/SLS/FLS design checks (Page et al., 2019). Further, high-fidelity constitutive modelling can potentially help to reduce the scope of specific experimental activities, with additional positive impact on timing and costs. In light of the above considerations, the renewed interest in high-cyclic soil modelling is not only supported by the academic community, but also loudly demanded by the offshore wind industry.

1.2. Objectives

This thesis aims to foster reliable analysis of cyclically loaded foundations, such as monopiles, based on close inspection and modelling of local soil behaviour. The study is limited to the case of sandy soils. A high-cyclic sand constitutive model accounting for fabric effects is developed for use in implicit 3D FE analyses, to help explore the response of monopiles at a scale lower than allowed by spring-based interaction models (e.g., lumped macro-elements or Winkler-type p-y models). The proposed model is believed to make a new tool for the optimisation of cyclically loaded foundations, based on enhanced mathematical representation of cyclic sand behaviour – particularly, of strain accumulation and pore pressure build-up. In more detail, the steps forward taken by this study relate to the following theoretical/numerical developments:

- a new constitutive model is formulated in the framework of bounding surface plasticity with the addition of a so-called 'memory surface'. The model, named SANISAND-MS, is proven able to reproduce high-cyclic strain accumulation in sand specimens under drained loading, over a wide range of initial/boundary

conditions;

- SANISAND-MS is further validated at the sand specimen level against additional laboratory dataset and the concept of 'terminal densities', so as to build an additional trust about the use of the model in 3D soil-foundation interaction problems;
- the modelling capabilities of SANISAND-MS are expanded to include undrained cyclic loading conditions, and particularly the simulation of pore pressure build-up and so-called 'cyclic mobility';
- SANISAND-MS is finally applied to the 3D FE analysis of a laterally loaded monopile. 3D FE results are compared to small-scale test results from the literature, in order to qualitatively assess the performance of the proposed sand model in boundary value problems.

1.3. Outline

The thesis is formed by seven chapters, including this introduction, a review of the state of the art, the main core of the research, and final conclusions and recommendations. All novel findings are covered in Chapters 3 - 6, which are based on four journal papers – see relevant references below. With respect to the relevant publications, Chapters 3-6 have been assembled with an effort to limit certain repetitions (particularly about model formulation details), while preserving the underlying paper-based structure.

Chapter 2 overviews relevant literature concerning cyclic sand behaviour as observed at the scale of laboratory tests. The main factors affecting sand cyclic response are pointed out, and related to existing constitutive modelling strategies. In the latter respect, emphasis is on constitutive theories in the framework of elasto-plasticity, whose suitability has been generally recognised in the past decades by the geotechnical/geomechanical community.

Chapter 3, based on Liu et al. (2019), presents the formulation of a new, memory-enhanced, bounding surface plasticity model for sand (SANISAND-MS). The main novelty of SANISAND-MS lies in its suitability to reproduce high-cyclic ratcheting, i.e., the gradual accumulation of permanent strains under numerous loading cycles. The ratcheting performance of the model, particularly under drained cyclic loading, is validated against experimental data from the literature, including a number of loading cycles up to $10^4 \sim 10^5$. The benefits of the model in the presence of undrained loading conditions are also preliminarily discussed.

Chapter 4, based on Liu and Pisanò (2019), presents further evidence of performance of SANISAND-MS with respect to the numerical prediction of so-called 'terminal densities' under confined cyclic compression (oedometer conditions). Numerical results confirm the ability of the model to naturally reproduce sand high-cyclic response observed in cyclic oedometer tests on dry sand specimens.

Chapter 5, based on Liu et al. (2020a), further expands the reach of SANISAND-MS with respect to undrained cyclic loading conditions, namely to capture cycle-by-cycle trends of pore water pressure build-up and strain accumulation (cyclic

mobility). This is accomplished by adding new model features (enhanced plastic flow rule and memory surface hardening) to the formulation presented in Chapter 3.

Chapter 6, based on Liu et al. (2020b), reports 3D FE results in support of the use of SANISAND-MS in the analysis of cyclic monopile tilt in sand. The aim of the chapter is to numerically investigate relevant soil-pile interaction mechanisms under cyclic loading, with qualitative comparison to small-scale test results from the literature.

Chapter 7 presents relevant conclusions based on previous chapters, as well as recommendations for future research.

2

Literature review

2.1. Introduction

The cyclic behaviour of sand is of great relevance to numerous geotechnical applications, for instance in the fields of earthquake, offshore, and railway engineering. Cyclic loading conditions may be caused by diverse sources, and mobilise features of soil behaviour such as irreversible straining, cyclic hysteresis, and pore pressure build-up. The variety of initial, boundary and drainage conditions that a soil mass may experience under cyclic loading makes the resulting mechanical response very complex to describe comprehensively.

This chapter overviews available experimental evidence regarding the cyclic behaviour of sand, aiming to clarify the fundamental links between soil microstructure and response observed in laboratory tests. The initial experimental review is followed by a summary of existing frameworks for cyclic constitutive modelling, with emphasis on formulations based on elastoplasticity.

2.2. Cyclic behaviour of sand

This section focuses on experimental aspects of cyclic sand behaviour that are immediately relevant to geotechnical problems in offshore (wind) engineering. First, relevant response patterns are introduced, e.g., ratcheting versus shakedown deformation behaviour, or, under undrained conditions, cyclic liquefaction versus cyclic mobility. The role of the main governing factors (loading type, drainage of pore water, and initial soil state) is discussed for each considered class of behaviour. After detailed discussion of response features under drained (Section 2.2.1) and undrained (Section 2.2.2) cyclic loading conditions, insight into micromechanical aspects (fabric effects) is provided in Section 2.2.3.

2.2.1. Drained conditions

Loading repeated over a long period of time can cause significant accumulation of permanent deformations when a given *threshold strain* (Bouckovalas et al., 1984; Chang and Whitman, 1988; Karg et al., 2010) is exceeded (Chong and Santamarina, 2016). Consequently, changes related to soil density, hydraulic conductivity, stiffness and strength become difficult to predict only based on the response to monotonic loading (Park and Santamarina, 2019). Under drained conditions, large deviatoric strains occur under monotonic loading. Upon load reversal, the response of the soil tends to become stiffer, and less permanent strains are produced for the same load increment. Under repeated load reversals, strains accumulate with a decreasing accumulation rate (Tatsuoka and Ishihara, 1974), and asymptotic conditions are approached as the number of loading cycles increases (Tatsuoka and Ishihara, 1974; Bouckovalas et al., 1984; Wan and Guo, 2001b; Wichtmann et al., 2005; Pasten et al., 2014). The progressive decrease in strain accumulation rate is associated with a gradual reduction in hysteretic energy dissipation, which is in turn closely related to a gradual increase in cyclic secant stiffness (Chang and Whitman, 1988; Wichtmann et al., 2005; Narsilio and Santamarina, 2008). In the following, experimental observations about cyclic strain accumulation under drained conditions are summarised, including both deviatoric and volumetric deformation

modes.

Cyclic strain accumulation

Sand samples subjected in the laboratory to cyclic shear loading experience, under drained conditions, deviatoric strain accumulation (Tillemans and Herrmann, 1995; Lekarp and Dawson, 1998). Depending on soil properties and cyclic loading conditions, such accumulation may progress according to different patterns (Alonso-Marroquín, 2004):

1. *Elastic behaviour*. If the applied deviatoric stress amplitude is too small, no cyclic accumulation of irreversible/plastic strain is observed, and the soil can be said to behave (nearly) elastically.

2. *Elastic shakedown*. Plastic deviatoric strain accumulation occurs only during a few initial cycles. As more loading cycles are applied, neither creation/loss of inter-particle contacts nor contact slippage is generated. The steady-state stress-strain behaviour is non-hysteretic, as the deviatoric strain recovers fully in every cycle and asymptotically reaches a stable level (di Prisco and Muir Wood, 2012; Chong and Santamarina, 2016).

3. *Plastic shakedown*. The stress-strain response is hysteretic. The plastic deviatoric strain accumulates progressively within the initial cycles. As more loading cycles are applied, contact slippage and/or particle rearrangement may occur within each cycle. However, a stable stage is achieved in which the accumulated plastic deviatoric strain over each full cycle is nil (Chong and Santamarina, 2016; Park and Santamarina, 2020). This kind of behaviour is often referred to as 'ideal-plastic adaptation' (di Prisco and Muir Wood, 2012) or 'plastic shakedown' (Chong and Santamarina, 2016; Park and Santamarina, 2020).

4. *Ratcheting*. The stress-strain response is hysteretic. Deviatoric straining continuously develops during cycling with a decreasing, though non-vanishing, rate. In other words, ratcheting behaviour is associated wit net deviatoric strain accumulation in each loading cycle.

The response to cyclic loading in terms of volumetric straining is typically characterised by the attainment of a stable, asymptotic density (Narsilio and Santamarina, 2008; Park and Santamarina, 2020). Such stable density (or, equivalently, stable void ratio) has been termed *terminal density* (or *terminal void ratio*) by Narsilio and Santamarina (2008). Soil samples can either contract or dilate to reach the terminal densities. Under monotonic shearing, sand reaches its terminal void ratio at critical state, i.e., when the shear flow of the material develops without further changes in volume. For cyclic loading conditions, the terminal density corresponds with a state in which the accumulated net volumetric strain is equal to zero during a complete stress loop. The terminal density determines the upper limit of the volume change during a predetermined test condition – i.e., the sand density evolves towards its terminal values depending on material properties, cyclic load settings,

and boundary conditions (Lackenby et al., 2007; Narsilio and Santamarina, 2008; Park and Santamarina, 2020). The attainment of a terminal density is transversal to different shear deformation patterns, and may be associated with either ratcheting or shakedown behaviour. A visual representation of drained sand behaviour under triaxial cyclic loading is provided in Fig. 2.1 with reference to shakedown and ratcheting deformation patterns.

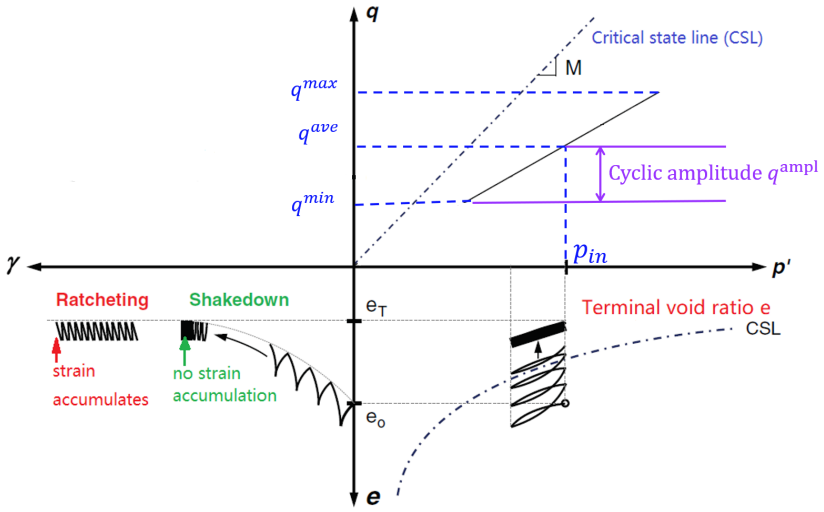

Figure 2.1: Drained sand behaviour under triaxial cyclic loading (modified after Park and Santamarina (2020)).

Factors governing drained cyclic behaviour

As noted in Chapter 1, serviceability checks are often design-driving for wind turbine foundations, i.e., in relation to monopile tilting. As such tilting is closely related to strain accumulation in the soil, this section explains how different geotechnical/loading factors affect the occurrence and evolution of cyclic sand ratcheting. Relevant loading/stress variables are defined in Fig. 2.1, where p_{in} is the initial mean effective stress, q^{ave} the average deviatoric stress, q^{ampl} the cyclic deviatoric stress amplitude, and the average shear stress ratio η^{ave} is calculated as q^{ave}/p_{in}.

Permanent strain may accumulate in sand samples subjected to drained cyclic loading. The accumulation direction in the accumulated strain space (see Fig. 2.2) – defined as the ratio ω between accumulated volumetric ε_{vol}^{acc} and deviatoric strain ε_q^{acc} ($\omega = \varepsilon_{vol}^{acc}/\varepsilon_q^{acc}$) – has been previously studied through laboratory tests (Luong, 1982; Chang and Whitman, 1988; Wichtmann, 2005; Escribano, 2014). All the cyclic tests considered in this review were performed under drained triaxial conditions, and lead to generally conclude that the strain accumulation direction is highly affected by the average stress ratio η^{ave} (see Fig. 2.2), with low influence of the mean effective stress and the initial void ratio. Chang and Whitman (1988) found that

the number of loading cycles N has no effect on the strain accumulation direction for $N \approx 10^3$; however, the high-cyclic test results by Wichtmann (2005) indicate that, with $N = 10^5$, the ratio ω tends to increase slightly with N. Furthermore, Wichtmann (2005) performed drained high-cyclic triaxial tests on the same sand at varying loading frequency, cyclic stress amplitude and static pre-loading, and found only negligible (or unclear) impact of such factors on the direction of strain accumulation.

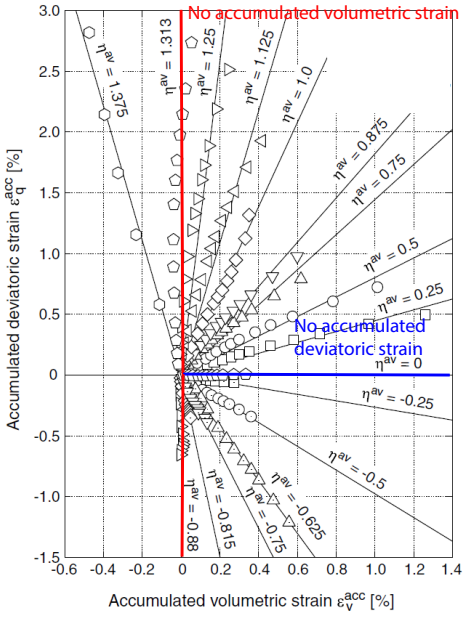

Figure 2.2: Influence of average stress ratio on strain accumulation direction for a quartz sand with sub-angular grains under drained cyclic triaxial loading (modified after Wichtmann (2005)).

The overall magnitude of the accumulated strain ($\varepsilon^{acc} = \sqrt{(\varepsilon_{vol}^{acc})^2/3 + 1.5(\varepsilon_q^{acc})^2}$, with ε_{vol}^{acc} and ε_q^{acc} standing for accumulated volumetric and deviatoric strain, respectively) under drained cyclic loading is strongly affected by loading pattern and sand properties. Strain accumulation progresses with the number of cycles with a decreasing rate. Under otherwise same conditions, the accumulated strain magnitude increases at increasing average stress ratio (Fig. 2.3a) and stress amplitude (Fig. 2.3b).

There is no final consensus on the influence of the average confining pressure p^{ave} (mean effective stress). Experimental results from Wichtmann (2005) hint that p^{ave} affects marginally the magnitude of strain accumulation, at least for a number of loading cycles no larger than 10^4. In Fig. 2.4a, accumulated strains lie within a narrow range for $N < 10^4$. Under more cycles, larger confining pressure results in a lower accumulated strain level. However, the same research group produced later test results regarding a different sand (Wichtmann and Triantafyllidis, 2017), and

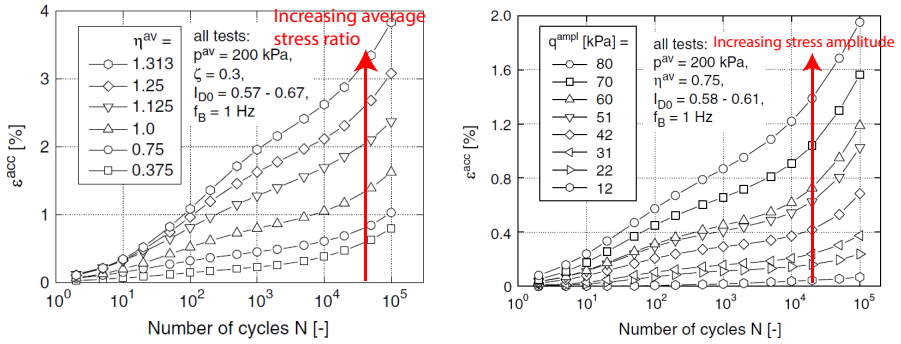

(a) Influence of average stress ratio (b) Influence of cyclic stress amplitude

Figure 2.3: Results from drained high-cyclic triaxial tests on a quartz sand with subangular grains – influence of average and cyclic shear stress on accumulated strain (modified after Wichtmann (2005)).

found a more obvious dependence of strain accumulation on p^{ave}, even for N in the range of 10^{2-3} (see Fig. 2.4b). The same later work suggests that, for a given number of cycles, strain accumulation is positively correlated with the confining pressure.

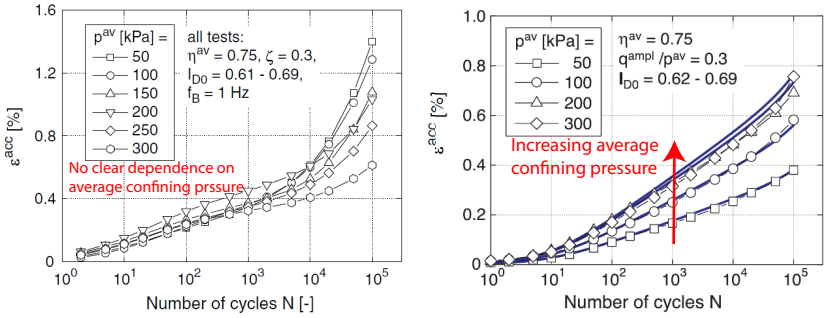

(a) A fine quartz sand (Wichtmann, 2005) (b) Cuxhaven fine sand (Wichtmann and Triantafyllidis, 2017)

Figure 2.4: Drained cyclic triaxial tests results – influence of average confining pressure on accumulated strain (modified after (a) Wichtmann (2005)) and (b) Wichtmann and Triantafyllidis (2017).

Samples with larger initial relative density (or lower void ratio)[1] exhibit lower strain accumulation rate for each loading cycle, and experience a smaller accumulated strain level for given N (see Fig. 2.5). This conclusion is also confirmed by other experimental studies (Silver and Seed, 1971; Wichtmann, 2005; Wichtmann and Triantafyllidis, 2017).

[1]void ratio e is defined as ratio of the volume of voids to volume of solids; relative density D_r is defined as $D_r = (e - e_{min})/(e_{max} - e_{min})$, with $e_{max,min}$ the maximum and minimum void ratio, respectively

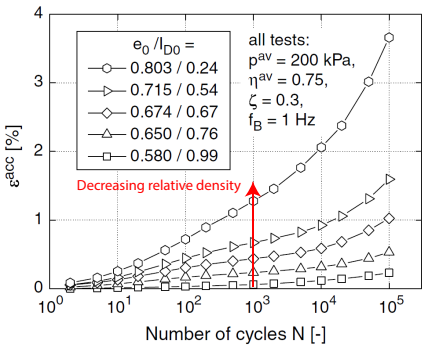

Figure 2.5: Influence of relative density (modified after Wichtmann (2005))

2.2.2. Undrained conditions

Generally, cyclic loading tends to promote sand volumetric contraction. If volume changes are inhibited by hindered pore water drainage, then a build-up in pore pressure is observed, and therefore a decrease in mean effective stress (i.e., in inter-particle contact forces). The undrained cyclic behavior of sand is largely affected by pore pressure build-up (Andersen, 2009), which is accompanied by simultaneous shear stiffness degradation and accumulation of deviatoric strain (Dobry et al., 1985). In this section, general features of undrained sand behaviour are presented in relation to single-amplitude cyclic loading – see Fig. 2.6. Similar definitions as

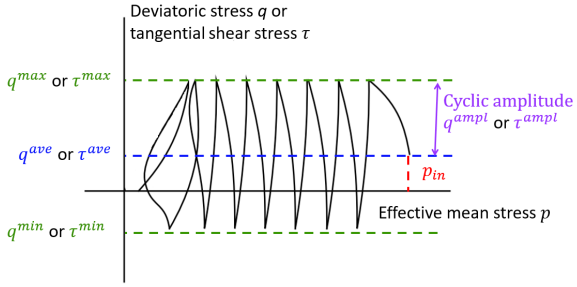

Figure 2.6: Schematic representation of the undrained cyclic testing conditions.

in the previous subsection are adopted herein to discuss undrained triaxial test results: p_{in} is the initial mean effective stress, q^{ave} the average deviatoric stress, q^{ampl} the cyclic deviatoric stress amplitude, and $q^{max,min} = q^{ave} \pm q^{ampl}$. When simple shear (DSS) test results are considered, the tangential shear strain component τ is adopted in lieu of the triaxial deviatoric stress q.

Under undrained cyclic loading, several soil and loading factors influence the occurrence of different deformation/failure modes (Elgamal et al., 2003; Yang and Sze, 2011; Ziotopoulou and Boulanger, 2013): (1) cyclic liquefaction; (2) cyclic mobility; or (3) excessive plastic strain accumulation (failure by loss of serviceability).

In the following subsections, these three failure modes are described in detail for what concerns the (1) pore water pressure build-up and (2) deviatoric strain accumulation. Triggering conditions and governing factors are explicitly pointed out. Relevant explanations are presented with respect to reference experimental data, namely from Wichtmann (2005), Wichtmann and Triantafyllidis (2016)[2] and Sze and Yang (2014).

Cyclic liquefaction

Liquefaction under undrained cyclic shearing occurs when the sand loses its strength and starts to flow as a viscous fluid. In laboratory tests, sand liquefies when the pore water pressure becomes practically as large as the initial mean effective stress, and the sample experiences severe/uncontrollable deformation. In other words, cyclic liquefaction occurs in association with abrupt pore pressure build-up and deviatoric straining. This phenomenon is exemplified in Fig. 2.7, and can only take place in loose sand.

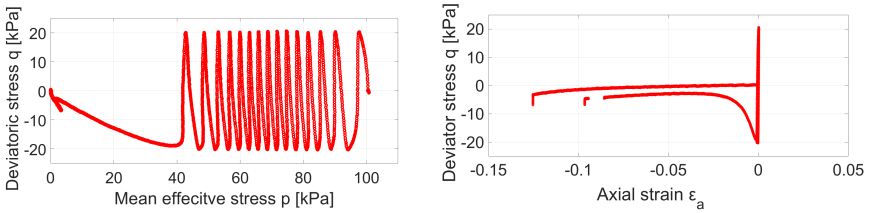

(a) q-p response

(b) q-ε_1 response

Figure 2.7: Cyclic liquefaction under undrained triaxial loading (Wichtmann and Triantafyllidis, 2016). Test conditions: symmetric deviatoric loading, $p_{in} = 100$ kPa, $q^{ampl} = 25$ kPa, relative density $Dr = 25\%$, one drained pre-cycle prior to undrained shearing.

In Fig. 2.7, although the mean effective stress is progressively decreasing under cyclic loading, there is almost no axial strain accumulation until the point where sudden failure is triggered – the mean effective stress decreases drastically from 40 kPa to 0 without further recovery of soil strength, while the axial strain increases rapidly from almost 0 to -0.1. The exact moment in which cyclic liquefaction occurs is difficult to predict, and is normally associated in the field with sudden catastrophic failure.

Cyclic mobility

Medium-dense and dense sands are unlikely to exhibit a liquefaction response of the kind in Fig. 2.7. Instead, so-called 'cyclic mobility' is most usually observed in saturated dilative sand (Fig. 2.8). During cyclic mobility, the effective stress path undergoes a 'butterfly-shaped' evolution along and below the steady-state line (see Fig. 2.8a). Relatedly, transient stages of pore pressure increase and dissipation are observed (due to the alternation of contractive and dilative behavior), and the deviatoric strain accumulates gradually (Ishihara, 1993). Two conditions

[2]online data base: http://www.torsten-wichtmann.de/

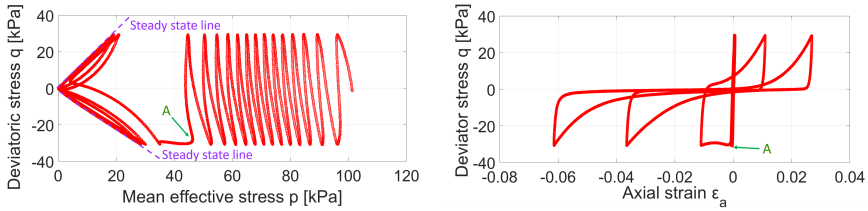

(a) q-p response (b) q-ε_1 response

Figure 2.8: Cyclic mobility under undrained triaxial loading (Wichtmann and Triantafyllidis, 2016). Test conditions: symmetric loading, $p_{in} = 100$ kPa, $q^{ampl} = 30$ kPa, relative density $Dr = 61\%$, one drained pre-cycle prior to undrained shearing.

seem necessary for cyclic mobility to occur, i.e., (1) dilative behaviour, and (2) load reversals between minimum/maximum deviatoric stresses of opposite sign (so-called two-way loading) (Vaid and Chern, 1985).

A specific locus in the stress space, the so-called 'Phase Transformation Line' (PTL), appears to govern the alternation of dilative/contractive response – see $q - p$ illustration in Fig. 2.9. When the stress state lies below the PTL, the soil is

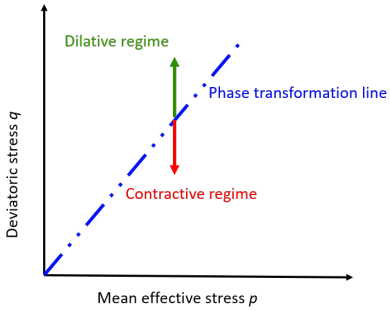

Figure 2.9: Illustration of phase transformation line (PTL) in $q - p$ space.

contractive and positive pore pressure increments occur under shear loading; the opposite takes place (dilative behaviour and pore pressure decrements) when the stress path overcomes the PTL. (Fig. 2.8a). Before approaching the PTL for the first time, purely contractive behaviour is observed, and the pore water pressure builds up with limited deviatoric strain during cycling (see sand states prior to state A in Fig. 2.8). This initial stage is substantially similar to what is observed in loose sand prior to the sudden triggering of liquefaction failure. After crossing the PTL, the mentioned contractive-dilative alternation gives rise to increase-reduction cycles in terms of pore pressure and, therefore, sand stiffness (Ishihara et al., 1975).

Within the cyclic mobility regime, (i) each time the mean effective stress approaches zero (i.e., vanishing shear resistance), finite but significant deviatoric strain develops irreversibly – though without triggering a sudden collapse (Iai et al.,

1992); (ii) the deviatoric strain amplitude gradually increases in each cycle on both positive/negative sides, and leads eventually to test failure due to uncontrollable deformation (Fig. 2.8b).

2

Strain accumulation in the presence of static preshear

When a static preshear is applied so that no change in deviatoric stress sign occurs during undrained cyclic loading (one-way loading), the pore pressure build-up tends to stabilise. Instead of the above-mentioned 'butterfly-shaped' cycles in the $q-p$ plane (Fig. 2.8a), the stress path evolves over 'lens-shaped'[3] loops (Fig. 2.10a). Although there is a clear upper-bound on the pore water pressure regardless of the number of cycles, the deviatoric strain (axial strain in Fig. 2.10b) tends to accumulate cycle by cycle. Under these testing conditions, excessive strain accumulation in one direction leads to sample failure in the form of a 'loss of serviceability'. Yang and Sze (2011) concluded that strain accumulation progresses at an almost constant rate, while Wichtmann and Triantafyllidis (2016) suggested that theh rate decays with the number of cycles. Though no full consensus has yet been achieved, a wide set of experimental observations on both loose and dense sands are nowadays available for theoretical studies and numerical simulation (Ghionna and Porcino, 2006; Yang and Sze, 2011; Wichtmann and Triantafyllidis, 2016).

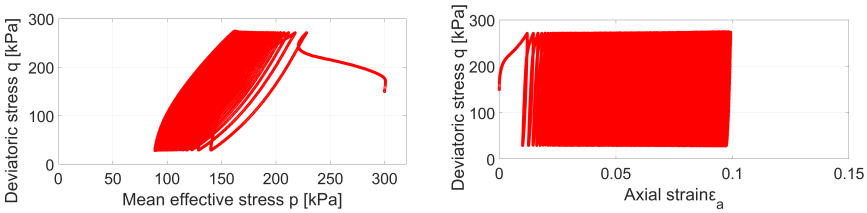

(a) q-p response (b) q-ε_1 response

Figure 2.10: Strain accumulation in the presence of static preshear (Wichtmann and Triantafyllidis, 2016). Triaxial test conditions: $p_{in} = 300$ kPa, $q^{ampl} = 120$ kPa, $q^{ave} = 150$ kPa, relative density $Dr = 64\%$, 1 drained pre-cycle prior to undrained shearing.

Factors governing undrained cyclic behaviour

This subsection overviews the material and loading factors that most affect the undrained cyclic behaviour of sand. Stress-strain response and related failure mode depend on initial void ratio, initial mean effective stress, initial stress ratio (defined as q^{ave}/p_{in}), and cyclic shear stress amplitude. The following three types of cyclic loading are considered herein Randolph and Gourvenec (2011): (a) one-way (with no load reversals); (b) symmetric two-way loading (with load reversals about a nil mean shear/deviatoric stress – $\tau^{ave} = 0$ or $q^{ave} = 0$); (c) non-symmetric two-way loading (with load reversals and $\tau^{ave} \neq 0$ or $q^{ave} \neq 0$). As stated in Section 2.2.2, 'butterfly-shaped' stress paths in the cyclic mobility regime can only occur under

[3]Terminology inspired by Wichtmann and Triantafyllidis (2016).

two-way cyclic loading. For one-way loading, the effective stress path repeatedly passes through a certain lens-shaped loop (Mao, 2000; Wichtmann and Triantafyllidis, 2016), with the deviatoric strain accumulating at a decaying rate. The accumulation direction is governed by the average shear stress level. For example, in undrained one-way cyclic triaxial tests, the axial strain accumulates on the positive side if lens-shaped looping takes place on the compression side (i.e., $q^{min} > 0$) (see Fig. 2.10); for lens-shaped stress loops on the extension side ($q^{max} < 0$) (see Fig. 2.11), negative axial strain accumulates. For symmetric two-way triaxial tests

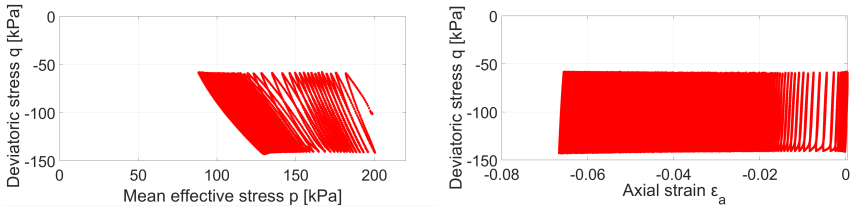

(a) q-p response (b) q-ε_1 response

Figure 2.11: One-way undrained cyclic triaxial test results (Wichtmann and Triantafyllidis, 2016). Test conditions: p_{in} = 200 kPa, q^{ampl} = −100 kPa, q^{ave} = 40 kPa, relative density Dr = 66%, 1 drained pre-cycle prior to undrained shearing.

($q^{ave} = 0$), the strain accumulated on the compression side is larger than that on the extension side in the cyclic mobility state. For non-symmetric two-way cycles, strain accumulation on the compression side prevails if the average stress $q^{ave} > 0$ (see Fig. 2.12a), while negative strain accumulation prevails if $q^{ave} < 0$ (Wichtmann and Triantafyllidis, 2016) (see Fig. 2.12b). Youd and Idriss (2001) indicated that an increase in initial confining pressure increases the resistance to liquefaction (CRR_n, defined as the cyclic stress ratio required to trigger liquefaction after n cycles). Wichtmann and Triantafyllidis (2016) suggested that under constant initial average stress ratio and soil density, the confining pressure has a negligible influence on the liquefaction resistance. Therefore, there seems to be no consensus regarding the influence of the initial confining pressure.

The impact of a static preshear on sand liquefaction resistance has been widely studied (Lee and Seed, 1967; Yoshimi and Oh-oka, 1975; Seed, 1981; Vaid and Chern, 1983; Yang and Sze, 2011; Boulanger and Ziotopoulou, 2013). Both increase (Seed, 1981) and decrease (Yoshimi and Oh-oka, 1975) in liquefaction resistance have been reported to be possible in the presence of a static preshear. The reason for this inconsistency may be often due to the lack of systematic/comprehensive experimental datasets. In most of the aforementioned studies, tests were performed for a narrow density range under relatively small stress levels and low initial static shear levels. To remedy these limitations, Yang and Sze (2011) performed undrained (symmetric and non-symmetric) cyclic triaxial tests on Toyoura sand over a wide range of relative density (from 10% to 70%), and initial effective average pressures p_{in} between 100 and 500 kPa. Initial static stress ratios (defined as $q_s/(2\sigma'_{nc})$, with q_s the initial deviatoric stress; σ'_{nc} the normal consolidation stress

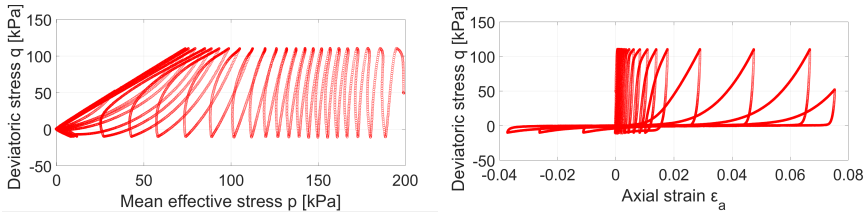

(a) $D_r = 56\%$, $q^{ave} = 50$ kPa, compression strain dominates

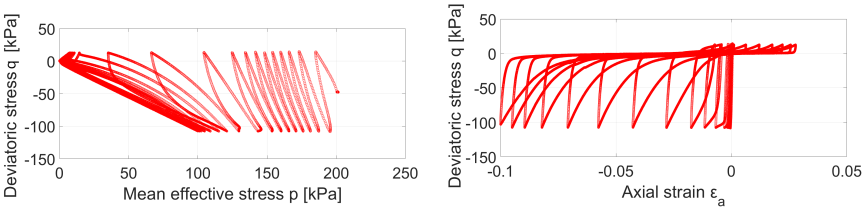

(b) $D_r = 65\%$, $q^{ave} = -50$ kPa, extension strain dominates

Figure 2.12: Non-symmetric two-way undrained cyclic triaxial tests. Test conditions: $p_{in} = 200$ kPa, $q^{ampl} = 60$ kPa, 1 drained pre-cycle applied prior to undrained shearing.

on the $45°$ plane) in the range from 0 to 0.4 were considered. With reference to the examined p_{in} range, the authors concluded that, as illustrated in Fig. 2.13, increasing initial static preshearing enhances the undrained cyclic resistance of dense and medium-dense sand (denser than critical). Conversely, loose samples (looser than critical) show a non-monotonic dependence of the undrained cyclic resistance on the static preshear.

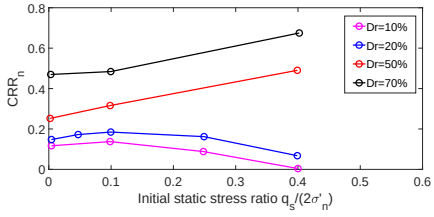

Figure 2.13: Influence of initial static stress ratio on cyclic liquefaction resistance ratio CRR_n (Yang and Sze, 2011). Undrained non-symmetric triaxial test, $\sigma'_{nc} = 300$ kPa.

The effects of the cyclic loading amplitude were studied by Wichtmann and Triantafyllidis (2016) for specimens at the same initial confining pressure, with the same average cyclic stress ratio and relative density. Under two-way loading, soil samples subjected to larger cyclic amplitudes require less loading cycles to reach liquefaction/cyclic mobility – compare Fig. 2.14 to Fig. 2.8). The strain response varies depending on the relative density when two-way loading is applied. For medium-dense and dense sand samples, the magnitude of the developed strain amplitude increases with increasing cyclic stress amplitude, but decreases with in-

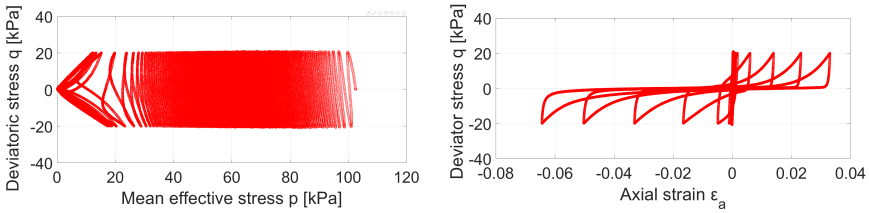

(a) q-p response (b) q-ε_1 response

Figure 2.14: Cyclic mobility in undrained cyclic triaxial test results (Wichtmann and Triantafyllidis, 2016). Test conditions: symmetric loading, $p_{in} = 100$ kPa, $q^{ampl} = 20$ kPa, relative density $Dr = 62\%$, 1 drained pre-cycle prior to undrained shearing.

creasing initial relative density.

In sand samples subjected to one-way loading, larger cyclic amplitude results in a larger stable pore pressure level and faster pore pressure accumulation (Fig. 2.15a). Besides, higher axial strain level is obtained for larger cyclic amplitude for a given number of loading cycles (Fig. 2.15b).

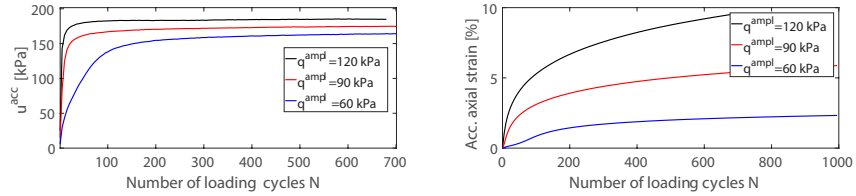

(a) pore water pressure accumulation (b) axial strain accumulation

Figure 2.15: One-way undrained cyclic triaxial tests (Wichtmann and Triantafyllidis, 2016). Test conditions: $p_{in} = 300$ kPa, $q^{ave} = 150$ kPa, relative density $Dr \approx 62\%$, 1 drained pre-cycle applied prior to undrained shearing.

The effect of drained cyclic preloading on the cyclic undrained behaviour has also been investigated (Nemat-Nasser and Tobita, 1982; Wichtmann, 2005). As illustrated in Fig. 2.16, drained cyclic preloading generally contributed to increase the liquefaction resistance. At the same average stress ratio level, higher cyclic stress amplitude and/or a larger number of loading cycles result in higher liquefaction resistance (more loading cycles needed to make the mean effective vanish for the first time). On the other hand, drained preloading cycles do not seem to affect the axial strain accumulation in the cyclic mobility stage – in all the cases considered by Wichtmann (2005), about 6% and -8% axial strain was accumulated on compression and extension sides, respectively, within four cycles during cyclic mobility.

After the experimental evidence presented so far, the next section focuses on its relation with microstructural factors (fabric effects).

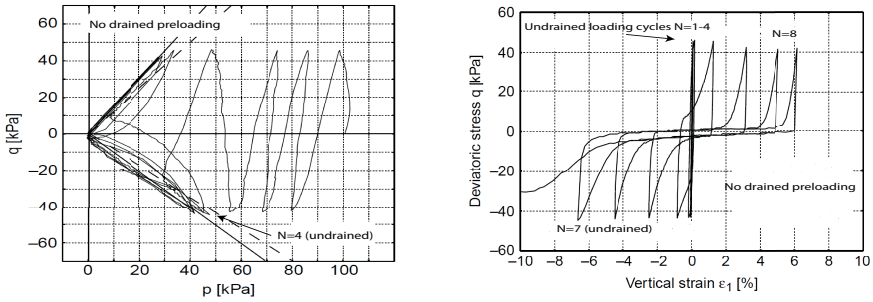

(a) no drained preloaing cycles, $D_r = 63\%$

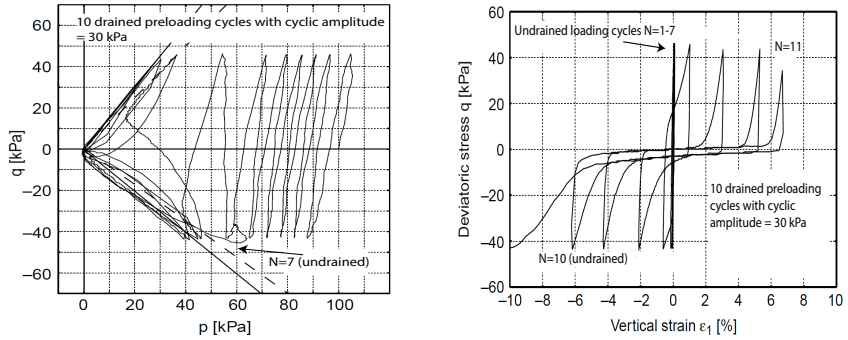

(b) 10 drained preloading cycles with cyclic stress amplitude q^{ampl}=30 kPa, $D_r = 65\%$

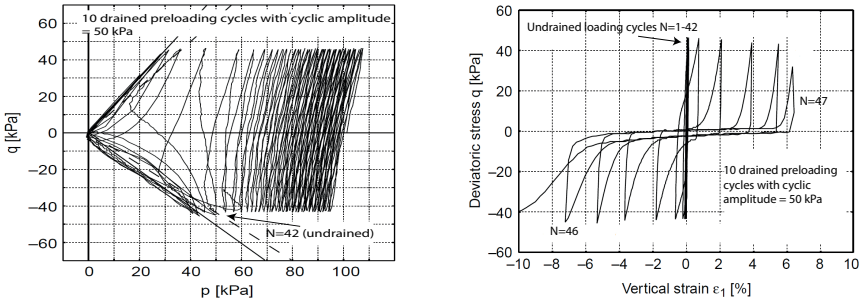

(c) 10 drained preloading cycles with cyclic stress amplitude q^{ampl}=50 kPa, $D_r = 66\%$

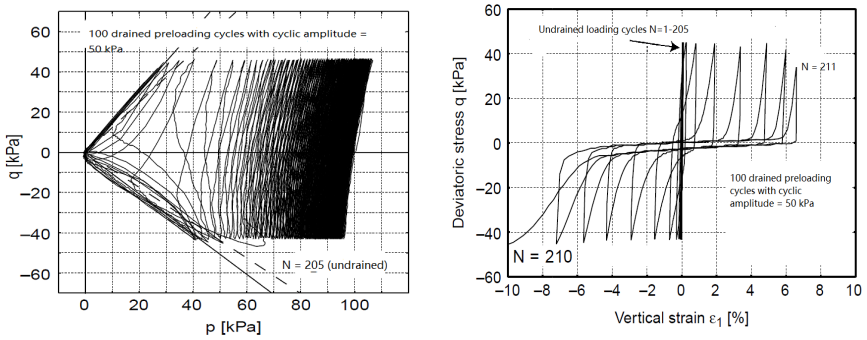

(d) 10 drained preloading cycles with cyclic stress amplitude q^{ampl}=50 kPa, $D_r = 64\%$

Figure 2.16: Impact of drained cyclic preloading on undrained cyclic behaviour (modified after Wichtmann (2005)): initial effective stress p_{in} =100 kPa, undrained cyclic loading amplitude q_{un}^{ampl} = 45 kPa.

2.2.3. Fabric effects

The stress-strain response of sands is deeply affected by their 'fabric' and its evolution under external loading. Sand fabric effects emerge from the complex interplay of particle size and shape, spatial distribution and arrangement of the grains, and contact network (Mitchell et al., 2005). Friction and kinematic constraints at particle contacts contribute to the macroscopic strength (Oda, 1972; Arthur and Menzies, 1972) and stiffness (Zdravkovic and Jardine, 1997; Kuwano and Jardine, 2002) of sand, which exhibit mechanical anisotropy (i.e., dependence on the loading direction) related to microstructural attributes. This has been widely observed in natural deposits, compacted fills and laboratory specimens. The analysis of sand fabric effects in granular materials focuses on the link between micromechnical properties and macroscopic response to external perturbations.

The micromechanical anisotropy of sand fabric is related in sand specimens to both intrinsic and external factors, such as sample preparation, type of (anisotropic) consolidation, and shear loading programme (Oda et al., 1985). For presentation purposes, fabric effects, and related sand anisotropy, are often distinguished as either 'inherent' or 'induced' (Casagrande and Carrillo, 1944; Oda, 1972). Inherent fabric concerns the microstructure of sand prior to loading (Oda, 1972). In contrast, induced fabric relates to the evolution experienced under the action of external loads. The main contributors to what is called inherent fabric are: (1) the direction of the major particle axis with respect to the bedding plane (i.e., the plane perpendicular to gravity), (2) the orientation of interparticle contact normals with respect to gravity, and (3) the preferential orientation of void spaces (Oda, 1972; Li and Dafalias, 2002; Tong et al., 2014). Among these three factors, (1) shows the strongest stability and slow evolution under shear loading up to critical state, while (2) and (3) may change abruptly form the very onset of loading (Oda, 1972; Jafarzadeh et al., 2008; Fonseca, 2011). In other words, inherent fabric is altered by loading and contributes to the evolution of load-induced anisotropy.

Laboratory testing studies

Specimens made by preparing the same sand at the same density, but through different methods, feature different inherent anisotropy (Nemat-Nasser and Tobita, 1982) and, therefore, different mechanical behaviour (Miura and Toki, 1982; Porcino et al., 2004; Sze and Yang, 2014; Wichtmann, 2016). In fact, micromechanical arguments suggest that different sampling methods produce significant differences in inherent sand fabric.

Sample pluviation usually leads to elongated soil grains lying with their major axis perpendicular to gravity. Preparation through tamping results in a slightly preferred orientation perpendicular to the horizontal plane, which tends to disappear under shear loading (Mitchell et al., 2005). Grain contact normals are to a large extent oriented along the vertical direction for samples prepared by moist tamping, while it is much less obvious to draw a similar conclusion for air-pluviated samples. Similarly to pluviated samples, specimens prepared using the tamping method exhibit an initial fabric in which the particles' major axes are more aligned along the horizontal plane. For samples prepared via dry deposition, the major axis of sand

particles is mainly oriented along the horizontal direction, which turns out to be a rather stable fabric configuration. Typical sand fabric arrangements as resulting after dry deposition and moist tamping are illustrated in Fig. 2.17.

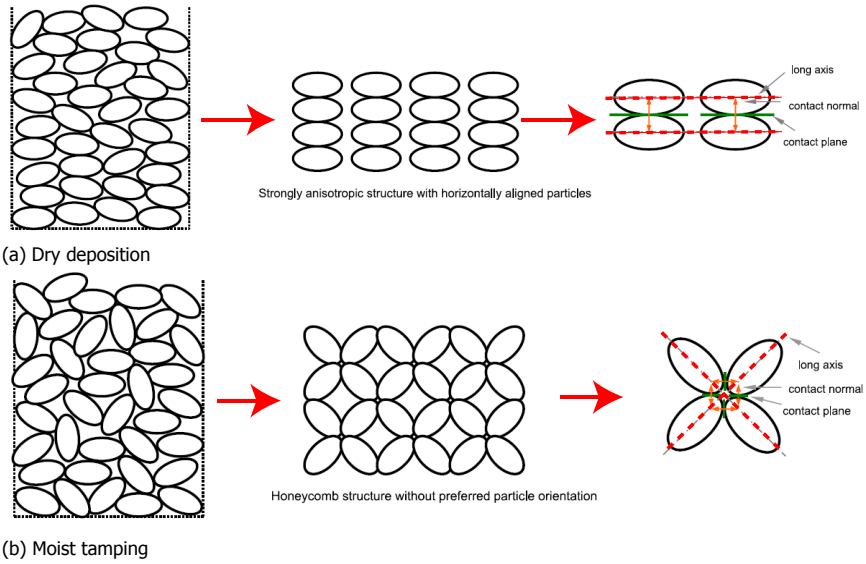

Figure 2.17: Types of sand fabric generated by different sampling methods (modified after Sze and Yang (2014).)

Wan and Guo (2001a) sought quantitative links to explain how observed fabric effects depend on fabric orientation and degree of anisotropy, concluding that:

1. the bedding plane of samples prepared via water sedimentation and dry deposition is perpendicular to the direction of particle falling and tamping, respectively. Therefore, parallel bedding planes (i.e., most contact normals aligned with the vertical direction) are generally produced for both methods. If the bedding plane turns out to be vertical and parallel to the direction of the maximum principal stress, then samples tend to be weak in the vertical direction and more likely to experience volume changes. Conversely, a horizontal bedding plane with most contact normals oriented along the vertical direction is associated with high strength and stiffness;

2. a high degree of anisotropy contributes to larger strength in the axial direction and more dilative soil behavior. Thus, samples prepared using moist tamping are stronger in the vertical direction than samples prepared via dry deposition under otherwise same conditions;

3. particle shape is another influential factor. For instance, samples with elongated grains tend to exhibit a behaviour that is inherently more anisotropic (Wang and Mok, 2008).

Regarding cyclic loading conditions, Wichtmann et al. (2020) performed drained high-cyclic ($N = 10^5$) triaxial tests on clean Karlsruhe fine sand samples prepared using different sampling methods. Similar strain accumulation patterns (see Section 2.2.1) were observed regardless of the sampling method – including similar strain accumulation rates, and negligible influence on the strain accumulation direction. In more detail, dry and water pluviation methods resulted in similar accumulated strain magnitude, both being much larger than that measured for samples prepared via dry loose deposition followed by compaction. Sand relative density was found to affect the 'intensity' of fabric effects. At low densities, moist tamping sampling led to larger cumulative residual strain compared to experimental results after air pluviation sampling. However, opposite conclusions were drawn for samples of increasing relative density.

Under undrained cyclic loading, fabric anisotropy impacts the occurrence of the aforementioned failure modes (Sze and Yang, 2014), and generally the resistance to cyclic liquefaction. This observation is corroborated by extensive experimental studies (Ladd, 1974; Mitchell and Carpenter, 1976; Mulilis et al., 1977; Tatsuoka et al., 1986; Yamashita and Toki, 1993). Under otherwise same conditions, the number of loading cycles required to trigger liquefaction is much larger for specimens prepared via moist tamping than observed for those prepared using dry deposition (Sze and Yang, 2014) (see Fig. 2.18).

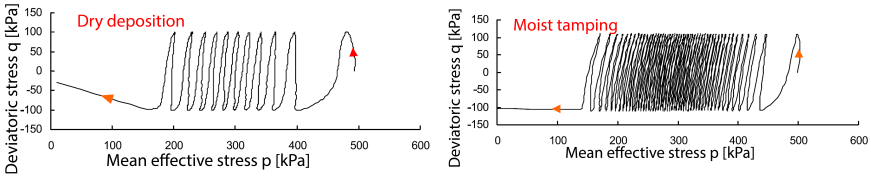

(a) Dry deposition (b) Moist tamping

Figure 2.18: Undrained cyclic behaviour of sand with no static pre-shear (Dr=20%, $\sigma_{nc} = 500$ kPa (modified after Sze and Yang (2014)).

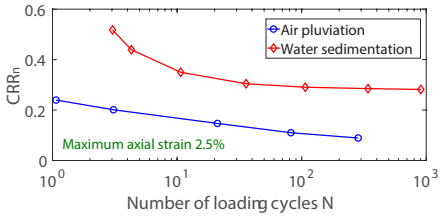

Figure 2.19: Effect of the sample preparation method on sand liquefaction resistance (Ghionna and Porcino, 2006)

The comparison of different sample preparation methods, including moist tamping and air pluviation – with the latter followed or not by sample compaction, sug-

gests that: (1) samples prepared by moist tamping exhibit higher liquefaction resistance in comparison to the case of water pluviation; (2) air pluviation produces the sand samples with the lowest resistance to liquefaction among the considered sampling approaches (Mulilis et al., 1977; Ibrahim and Kagawa, 1991); (3) uncompacted samples prepared using air pluviation present the lowest CRR_n; (4) sand samples prepared by water sedimentation possess liquefaction resistance CRR_n higher than samples prepared by air pluviation – see Fig. 2.19 (Ghionna and Porcino, 2006).

Numerical Discrete Element studies

In addition to the general description of fabric effects in laboratory tests, more quantitative insight into sand fabric and its evolution can be gained using numerical simulations based on the Discrete Element Method (DEM) (Cundall, 1971; Cundall and Strack, 1979). Resorting to DEM analysis make it possible to reproduce the formation/evolution of inhomogeneous contact networks in granular materials. The contact network carries most of the loading owing to 'force chains' developing through soil particles (Majmudar and Behringer, 2005; Muir Wood, 2007). The orientation of force chains are mostly aligned with the major principal stress, and are sensitive to the rotation of principal stress directions (Muir Wood, 2007). Further, the DEM analysis of particle contacts is not limited to the identification of contact normals, but also includes detailed quantification of the total number of contacts and of the so-called 'coordination number' (average number of contacts per particle).

O'Sullivan et al. (2008) used a 3D DEM model to study the micromechanics of sand drained cyclic response by applying 50 strain-controlled loading cycles on specimens of uniform spheres. Based on the simulation results, it was possible to conclude that: (1) a higher coordination number can be related to a stiffer sand response; (2) as previously concluded by Majmudar and Behringer (2005), the applied load is not uniformly borne by sand particles, but carried by force chains oriented along the direction of the major principal stress; (3) simulated cyclic stresses are more closely related to the strong fabric tensor (a fabric tensor determined by the contacts that carry the largest contact forces) rather than the global fabric tensor (a fabric tensor determined by all contacts); (4) at the maximum cyclic strain level, the coordination number increases slightly with subsequent loading cycles; (5) compared to the global fabric tensor, the strong fabric tensor varies less during cyclic loading.

Yimsiri and Soga (2010) performed 3D DEM analyses on non-uniform particle assemblies with different initial distribution of contact normals, and concluded that sand becomes stiffer, stronger, and more dilative upon shearing along the direction of most contact normals. Under drained conditions, fabric anisotropy changes rapidly as soil behaviour transits from the contractive to the dilative regime. The opposite occurs under undrained conditions, i.e., soil fabric changes develop most rapidly in the transition from dilative to contractive behaviour. Furthermore, during undrained dilative phases, the reduction in shear resistance is more related to the redistribution of contact forces rather than particle reorganisation – which is limited by the constraint of constant volume deformation.

Hu et al. (2010) studied the evolution of sand fabric under drained cyclic loading using 2D DEM. The analysis of DEM results led to conclude that anisotropic consolidation enhances sand inherent anisotropy, whereas isotropic consolidation reduces it. The authors quantified sand fabric (more specific, the overall orientation of the contact normals) using a fabric tensor defined as in Oda (1982); Oda et al. (1985); Rothenburg and Bathurst (1989). Thorough analysis of principal fabric tensor values indicated that samples with a large deviatoric fabric component tend to accumulate more permanent axial strain.

Kuhn et al. (2015) considered four different aspects of fabric anisotropy (particle bodies, particle surface, the contact normals and the void space) and proposed 13 measures (i.e. 13 quantitative representations of sand fabric) to study the link between particle arrangement and macroscopic sand behaviour. Their conclusions confirmed that contact orientation largely impacts the mechanical response of sand in terms of strength and stiffness. Soil stresses can be related to the most heavily loaded contacts, while the average contact orientation is likely to be linked to the incremental bulk stiffness.

Quantifying fabric effects

As remarked by O'Sullivan (2011), there is a need to translate micromechanical fabric information (i.e., individual components of contact normals, orientation of particles and voids, etc.) into phenomenological ingredients, so as to support the constitutive macroscale modelling of sand behaviour for engineering applications. Despite numerous attempts (i.e., O'Sullivan et al. (2008); Hu et al. (2010); Kuhn et al. (2015), etc), there is still no unique approach to the mathematical representation of sand fabric (Zhang et al., 2020). However, there are a few options that have grown most popular in relation to constitutive modelling developments.

Oda (1982) suggested that sand fabric at the microscale can be represented via continuum second order fabric tensors. This suggestion has been adopted in many later works, for instance, to interpret DEM simulation results (Li and Dafalias, 2002; O'Sullivan et al., 2008; Yimsiri and Soga, 2010; Hu et al., 2010; Wang and Xie, 2013; Kuhn et al., 2015), or formulate fabric-sensitive constitutive models (Papadimitriou and Bouckovalas, 2002; Dafalias and Manzari, 2004; Zhao and Guo, 2013; Zhang et al., 2020). Other attempts to incorporate fabric effects into constitutive theories for sand includes the adoption of additional surface loci, as proposed, e.g., by Nemat-Nasser and Tobita (1982); Jafarzadeh et al. (2008); Corti (2016).

2.3. Constitutive modelling approaches

Constitutive models are usually adopted to describe mechanical relationships between stresses and strain in continuum media, with the possibility of including multiphysical effects – e.g., hydraulic, thermal or chemical (Wu et al., 2004; Khalili and Selvadurai, 2004; Cleall et al., 2007; Chen et al., 2016). In the context of geoengineering, the need for high-fidelity soil models is particularly felt, for instance when modelling the complex effects of cyclic loading is of the essence. Relevant areas of applications include, but are not limited to, earthquake, offshore, and transportation geotechnics, where soil-structure interaction problems are typically

dominated by cyclic loading conditions.

The numerical prediction of cyclic soil deformations over a number N of loading cycles can be tackled in at least two ways, known in the literature as 'explicit' and 'implicit' approaches (Niemunis et al., 2005):

- the explicit method links 'explicitly' accumulated strains to the number of loading cycles N, so that relevant strain components in the soil are only calculated/accumulated at the end of each loading cycle;

- the implicit method relies on conventional constitutive modelling, aiming to describe the soil response through a sequence of stress-strain increments over each loading cycle. The overall response over the considered cyclic loading history results from the time integration of all stress-strain increments.

Explicit models are most usually based on extensive laboratory testing. Accordingly, strong simplifications are necessary, as testing possibilities are inevitably limited with respect to the many features of cyclic behaviour. Some explicit models are set to describe only one relevant aspect of cyclic strain accumulation (e.g., volumetric or deviatoric component, total strain magnitude or direction), while governing factors such as number of cycles, confining stress or void ratio are empirically incorporated through *ad hoc* tuning functions (Lentz and Baladi, 1981; Sawicki and Swidzinski, 1989; Sweere, 1992). More sophisticated explicit formulations have also been proposed to reproduce the cyclic evolution of the whole strain tensor, i.e., in magnitude and direction (Marr and Chrisitian, 1981; Bouckovalas et al., 1984; Kaggwa et al., 1991; Suiker and de Borst, 2003; Niemunis et al., 2005; Achmus et al., 2009; François et al., 2010). Owing to their low computational costs, explicit formulations have been widely applied to the 3D FE analysis of soil-structure interaction problems, by reducing real cyclic loading histories to sequences of N-driven monotonic steps (Niemunis et al., 2005; Achmus et al., 2009; Wichtmann et al., 2010b; Pasten et al., 2014; Jostad et al., 2015; Triantafyllidis et al., 2016; Chong and Pasten, 2018; Staubach and Wichtmann, 2020).

Implicit models relate to the conventional simulation of soil behaviour through a 'causal' sequence of stress/strain increments, to be integrated step-by-step in time domain analyses. A number of challenges in this area, specifically about the case of sandy soils, are self-apparent:

- cyclic strains/displacements develop under the influence of numerous factors (e.g., sand fabric and loading history) that cannot be fully described by only using customary state variables and properties, such as stresses, strains and relative density;

- numerical approximation errors are inevitably produced during the time integration of stress/strain increments in each loading cycle. This fact can cause the accumulation of significant errors when simulations span a large number of cycles. Such inconvenience can only be mitigated by adopting time integration algorithms of appropriate accuracy;

– the need for accurate time integration over numerous loading cycles implies high computational costs of 3D FE analyses based on implicit soil modelling. The case of offshore foundations, e.g., monopiles for offshore wind turbines, is particularly meaningful in that they can experience up to $10^7 \sim 10^8$ cycles during their operational life. At present, attempts to analyse the effects of long-lasting loading histories through fully implicit, time-domain simulations may still prove unsuccessful.

The above considerations seem to pose serious restrictions to the use of implicit cyclic modelling in design-oriented calculations. However, research on the implicit constitutive modelling of soils has received ever growing attention since the 1970s (Van Eekelen and Potts, 1978; Zienkiewicz et al., 1999). Such attention is justified by the superior ability of implicit modelling to explain, through FE computations, the mechanics of relevant soil-structure interaction problems, as well as highlight governing geotechnical factors. Such ability relies on the possibility to link local soil behaviour to the global performance of the considered soil-structure system, at a level of detail that may hardly be achieved through explicit modelling. Furthermore, implicit soil models do represent an indispensable resource for the analysis of geosystems under relatively short cyclic loading events, such as earthquakes or environmental storms. At any rate, implicit models should be always regarded as a precious tool to gain insight into the problem under examination, and inspire the conception of simplified/faster engineering approaches – for instance, based on explicit modelling.

In the past decades, numerous (implicit) constitutive models have been developed according to different constitutive approaches, most commonly the theory of elastoplasticity. In what follows, the standard theory of small-strain, rate-independent elastoplasticity is summarised and further specified for the relevant cases of multi-surface and bounding surface plasticity modelling (Prévost, 1982). While far from exhaustive, the following summary aims to point out some conceptual aspects that are especially relevant to the remainder of this work. The reader interested in further theoretical and computational aspects regarding (different types of) soil plasticity is referred to Muir Wood (2003); Houlsby and Puzrin (2006); di Prisco and Muir Wood (2012); Puzrin (2012); Mašín et al. (2019); Borja (2013).

2.3.1. Standard elastoplasticity

A fundamental assumption of small-strain elastoplasticity is the additive decomposition of the strain increment tensor ($d\boldsymbol{\varepsilon}$) into elastic/recoverable ($d\boldsymbol{\varepsilon}^e$) and plastic/irrecoverable ($d\boldsymbol{\varepsilon}^p$) components:

$$d\boldsymbol{\varepsilon} = d\boldsymbol{\varepsilon}^e + d\boldsymbol{\varepsilon}^p \tag{2.1}$$

In standard plasticity, the determination of the total strain increment, and its individual components, requires the formulation of four main ingredients (Muir Wood, 2003).

First, a relationship is needed between stresses and recoverable strains. Such

a relationship is termed 'elastic' if the stress tensor can be expressed as a single-valued function of the elastic strain tensor:

$$\boldsymbol{\sigma} = f\left(\boldsymbol{\varepsilon}^e\right) \tag{2.2}$$

which can be then differentiated to obtain the following incremental form:

$$d\boldsymbol{\sigma} = \boldsymbol{D} : d\boldsymbol{\varepsilon}^e \tag{2.3}$$

where the elastic (fourth-order) stiffness tensor $\boldsymbol{D}$ is obtained as $\partial f / \partial \boldsymbol{\varepsilon}^e$. Direct formulation of an incremental elastic relationship in the form Equation (2.3) leads to so-called 'hypoelastic' laws. Although widely used in soil modelling, hypoelastic formulations have been known for a long time to not guarantee energy conservation under arbitrary cyclic loading, as clearly pointed out by Zytynski et al. (1978) and, more recently, by Einav and Puzrin (2004b). A sound alternative, consistent with the First Law of Thermodynamics, is to develop 'hyperelastic' models starting from the definition of an energy potential function, from which stresses (or strains) and stiffness (or compliance) moduli can be obtained through differentiation (Houlsby and Puzrin, 2006). A recent overview, and critical assessment, of existing hyperelastic formulations for soils is provided by Amorosi et al. (2020). The need for non-linear, non-isotropic (hyper)elastic models stands out clearly if accurate representation of real small-strain behaviour is to be pursued Houlsby et al. (2005). Some conceptual difficulties, not further discussed herein, arise with the inclusion of pycnotropy (i.e., dependence on the current void ratio) (Roesler, 1979; Hardin and Blandford, 1989; Presti et al., 1993), which inevitably gives rise to coupled elastic and plastic deformations (Maier and Hueckel, 1979; Collins and Houlsby, 1997).

In addition to the elastic relationship, the following three ingredients are necessary to obtain the incremental plastic strain tensor – or, equivalently, magnitude and direction of the plastic strain increment:

1. *Yield criterion*. The yield criterion defines the boundary of elastic behavior, and therefore the transition from elastic to elastoplastic behaviour. Such a boundary is usually expressed in the form of a yield surface, i.e., a geometrical locus in the stress space defined by the nullity of a yield function f. In the case of perfectly elastoplastic media (non-hardening), a fixed yield limit is defined as a function of the current stress state:

$$f(\boldsymbol{\sigma}) = 0 \tag{2.4}$$

   If the stress state lies within the yield surface, the mechanical response is purely elastic.

2. *Plastic flow rule*. A plastic flow rule is necessary to determine the direction of the plastic strain increment. Two main approaches are possible: (i) direct prescription of a direction tensor ($\boldsymbol{R}$) (Prévost, 1985; Dafalias, 1986); (ii) direction of plastic flow set along the gradient of a plastic potential function g. A plastic flow rule is termed 'associated' or 'non-associated' depending on whether the direction of the plastic strain increment coincides or not with the

current normal to the yield function, i.e., $f = g$ or $f \neq g$, respectively. To reproduce available experimental evidence, it is most typical for geomaterials to adopt a non-associated flow rule (Nova et al., 2010), and obtain incremental plastic strains as:

$$d\boldsymbol{\varepsilon}^p = < L > \frac{\partial g}{\partial \boldsymbol{\sigma}} \tag{2.5}$$

where $< L >$ is the so-called plastic multiplier, and <> the Macaulay brackets operator. L is a non-negative scalar quantity that defines the amplitude of the plastic strain increment, and can be determined as shown in the following.

3. *Hardening rule*. A wide class of realistic material behaviours can be reproduced through the idealisation of a hardening (or softening) material. Accordingly, the yield limit is history-dependent, a feature commonly embodied by evolving hardening variables. In the simplest case of a single/scalar hardening variable, the yield locus reads as:

$$f(\boldsymbol{\sigma}, \kappa) = 0 \tag{2.6}$$

with no loss of generality with respect to the case of multiple hardening variables (scalar, vectorial, or tensorial). It is customary to model microstructural/irreversible changes in the material (e.g., fabric effects) by linking the increments of all hardening variables (e.g., $d\kappa$) to (the norm of) the plastic strain increment ($d\boldsymbol{\varepsilon}^p$):

$$d\kappa = h||d\boldsymbol{\varepsilon}^p|| \tag{2.7}$$

where h is scalar, positive (negative) coefficient when linear hardening (softening) is considered. Hardening laws in the form of Equation (2.7) give rise to so-called 'strain hardening' models – 'work hardening' formulations are also possible, in which $d\kappa$ is linked to the plastic work (Ziegler and Wehrli, 1987; Houlsby and Puzrin, 2000). The evolution of the chosen hardening variables determines gradual transformation of the yield locus $f(\boldsymbol{\sigma}, \kappa) = 0$ in the stress space, most usually in the form of a homothetic expansion/contraction ('isotropic hardening'), a rigid translation/rotation ('kinematic hardening'), or a combination of both mechanisms ('mixed isotropic-kinematic hardening').

When plastic behaviour is triggered by the fulfilment of the yielding condition ($f = 0$), the material response in the current step increment can be either newly elastic ('elastic unloading', when $\frac{\partial f}{\partial \boldsymbol{\sigma}} : d\boldsymbol{\sigma} < 0$) or elastoplastic[4] ('plastic loading', when $\frac{\partial f}{\partial \boldsymbol{\sigma}} : d\boldsymbol{\sigma} > 0$) (hence the terms of 'bilinear' or 'lumped' incremental nonlinearity). In the latter case, it is postulated that plastic strains develop in a way that continues to fulfil the yielding condition, i.e. the stress state may change but must remain on the (evolving) yield surface. Therefore, not only $f = 0$, but also the following 'consistency condition' must apply:

$$df = 0 \Rightarrow \frac{\partial f}{\partial \boldsymbol{\sigma}} : d\boldsymbol{\sigma} + \frac{\partial f}{\partial \kappa} d\kappa = 0 \tag{2.8}$$

[4]The boundary case of 'neutral loading' is also possible, in which the stress state moves along the tangent to the yield locus, i.e. $\frac{\partial f}{\partial \boldsymbol{\sigma}} : d\boldsymbol{\sigma} = 0$

The combination of Equations (2.1), (2.3), (2.8) and (2.5) leads to find a general relationship between stress increment and total strain increment:

$$d\boldsymbol{\sigma} = \left[\boldsymbol{D} - \frac{\left(\boldsymbol{D} : \frac{\partial g}{\partial \boldsymbol{\sigma}}\right) \otimes \left(\frac{\partial f^T}{\partial \boldsymbol{\sigma}} : \boldsymbol{D}\right)}{\frac{\partial f^T}{\partial \boldsymbol{\sigma}} : \boldsymbol{D} : \frac{\partial g}{\partial \boldsymbol{\sigma}} + H}\right] d\boldsymbol{\varepsilon} = \boldsymbol{D}^{ep} d\boldsymbol{\varepsilon} \qquad \text{with} \qquad H = -\frac{\partial f}{\partial \kappa} \frac{\partial \kappa^T}{\partial \boldsymbol{\varepsilon}^p} : \frac{\partial g}{\partial \boldsymbol{\sigma}} \tag{2.9}$$

where $\boldsymbol{D}^{ep}$ is the elastoplastic stiffness tensor, and H the so-called hardening modulus. It is worth noting that the $\frac{\partial \kappa}{\partial \boldsymbol{\varepsilon}^p}$ term in Equation (2.3.1) can be readily obtained from the hardening law Equation (2.7).

The above approach can enable successful modelling of numerous aspects of soil behaviour. However, formulating plasticity models through direct specification of the above-mentioned ingredients does not always guarantee compliance with basic thermodynamic principles. In the presence of dissipative processes, the Second Law of Thermodynamics requires the local rate of a 'properly defined' dissipation to be non-negative. For an elastoplastic continuum undergoing isothermal deformation, the basic energy equation reads as (Collins, 2005):

$$\delta W \equiv \boldsymbol{\sigma} : d\boldsymbol{\varepsilon} = d\Psi + \delta\Phi \tag{2.10}$$

for each representative volume element (RVE), where δW the increment in applied work; Ψ the free energy function; and $\delta\Phi$ the increment in dissipation (i.e., unrecoverable fraction of the applied work) – such that $\delta\Phi \geq 0$. In particular, whenever possible to express the free energy Ψ as the sum of elastic (Ψ^e) and plastic (Ψ^p) components (Collins and Houlsby, 1997), Equation (2.10) can be further specialised as follows:

$$\delta W^p \equiv \boldsymbol{\sigma} : d\boldsymbol{\varepsilon}^p = d\Psi^p + \delta\Phi \tag{2.11}$$

in which the increments in plastic work (δW^p) and plastic free energy ($d\Psi^p$) are explicitly put in a relationship with the (non-negative) dissipation Φ. It should be noted that plasticity models formulated in the above standard way would normally allow the evaluation of $\delta W^p \equiv \boldsymbol{\sigma} : d\boldsymbol{\varepsilon}^p$ under any loading programme, but not the individual increments in plastic free energy and mechanical dissipation (Collins and Houlsby, 1997) – which are not distinguished in the constitutive formulation. As a consequence, compliance with thermodynamic principles may not be guaranteed.

Over the past decades, an alternative approach, named 'hyperplasticty', has been developed and systematised for the formulation of thermodynamically consistent plasticity models – see the monograph on the subject by Puzrin and Houlsby (2001). In essence, the hyperplastic approach relies on the use of two distinct scalar functions to describe energy potential and (non-negative) mechanical dissipation rate, from which all the (incremental) constitutive equations can be elegantly derived by differentiation. Accordingly, it is possible to re-obtain a wide class of plasticity models already formulated within the standard approach, but with the proven advantage of *a priori* fulfilling both First and Second Laws of Thermodynamics. At the same time, it is possible to prove how well-established 'starting' concepts in

standard plasticity, such as yielding or non-associated plastic flow, emerge spontaneously as a consequence of very reasonable hypotheses on the modelling of dissipation. It should be noted, however, that elastoplastic models formulated outside the hyperplastic framework do not necessarily violate thermodynamic requirements – though a general methodology to prove whether that is the case is still missing. More recently, renewed interest has been devoted to the *a posteriori* check of thermodynamic consistency, e.g., in the work of Jeremic and co-workers related to the numerical analysis of seismic soil-structure interaction problems (Yang et al., 2018, 2019, 2020).

Apart from the thermodynamic framing, the need to simulate cyclic loading effects has pushed significant developments of constitutive modelling theories. The theory of standard elastoplasticity has been refined over the years to improve the simulation of soil stiffness during subsequent stress reversals, hysteretic energy dissipation (damping), and cyclic pore pressure build-up under undrained conditions. Particularly, but not exhaustively, the fundamentals of multi-surface (Mróz, 1967; Iwan, 1967; Prévost, 1985) and bounding surface (Dafalias and Popov, 1975; Krieg, 1975) elastoplasticity are summarised in the following and linked to the remainder of this dissertation.

Multi-surface elastoplasticity

The basic assumption of Mróz's multi-surface (elasto)plasticity is to regard the total strain increment as the sum of elastic and plastic components, with the latter resulting from multiple plastic sub-mechanisms (Mróz, 1967):

$$d\boldsymbol{\varepsilon} = d\boldsymbol{\varepsilon}^{e} + \sum_{n=1}^{N} d\boldsymbol{\varepsilon}^{p(n)} \tag{2.12}$$

Each plastic component $d\boldsymbol{\varepsilon}^{p(n)}$ is associated with individual yield surfaces $(f_1, f_2, ..., f_n)$ that govern the fulfillment of distinct yield limits, and give rise to a discrete field of plastic moduli (Yu, 2007). For simplicity, each yield surface is independently related to a single plastic strain sub-component, without coupling among different yielding/plastification mechanisms. A straightforward multi-mechanism generalisation of Equation (2.5) reads as (Houlsby and Puzrin, 2006):

$$d\boldsymbol{\varepsilon}^{p(n)} =< L^{(n)} > \frac{\partial g^{(n)}}{\partial \boldsymbol{\sigma}} \tag{2.13}$$

where each n^{th} flow rule only applies to the corresponding n^{th} sub-mechanism whenever active (i.e., when $f^{(n)} = 0$), while $< L^{(n)} >= 0$ in relation to all other surfaces.

During stages of elastoplastic loading, the current stress point moves in the stress space and determines an evolution of each active yield locus – through rigid translations/rotations in the common case of kinematic hardening modelling. This modelling process is exemplified in Fig. 2.20, where the multi-surface simulation of a loading-unloading-reloading response is illustrated next to the evolution of circular

yield loci in the deviatoric stress plane (Prévost, 1985). First, the stress point moves from the origin along the direction of positive $d\sigma_1$ until reaching the inner/smaller yield locus, while all other surfaces retain their initial position. A first linear stress-strain branch results during this first loading phase – see $\sigma - \varepsilon$ response in Fig. 2.20a. Afterwards, if the stress point continues to move upwards, the yield surface follows it by translating in the deviatoric plane, until touching the next/larger surface – the first sub-component of plastic strain develops during this second stage. As the stress state progresses along the same direction, the first and the second surfaces translate together by remaining in contact at the same point, until they both reach the third surface. The piece-wise linear stress-strain response in Fig. 2.20b is the obvious outcome of the described process, at least when simple linear hardening rules are adopted for each plastic mechanism. Upon unloading, the evolution of the stress state is reversed, and the elastic response is recovered while approaching new contact with the closest/smallest yield surface. The unloading response results from considerations similar to those applied during first loading, and is illustrated in Fig. 2.20c. The same process, and surface translation mechanisms, can be iterated as many times as desired, leading to cyclic stress-strain loops causing hysteretic (i.e., rate-independent) material damping. More complex hardening rules and model loci can be introduced to improve the simulation of experimental cyclic data within the same multi-surface framework.

Based on the work of Mróz (1967), several multi-surface models have been developed for sandy soils subjected to cyclic loading, such as the kinematic hardening model proposed by Prévost (1985). Later on, the same idea of Prévost (1985) was further refined by Elgamal et al. (2003), and then by Yang and Elgamal (2008) and Khosravifar et al. (2018), to more accurately simulate stiffness degradation and cyclic mobility under undrained cyclic loading. Di Benedetto et al. (2014) introduced the 'loading memory surface' concept into the multi-surface framework to predict the cyclic response. Unfortunately, the simulation of drained (high-)cyclic behaviour was not addressed in these studies. The (conditional) ability of multi-surface plasticity to reproduce different cyclic soil responses – in the form of elastic shakedown, plastic adaptation, or ratcheting – has been theoretically investigated by di Prisco and Mortara (2013).

Bounding surface elastoplasticity

Bounding surface plasticity, independently proposed by Dafalias and Popov (1975) and Krieg (1975), entails the adoption of two loci in the constitutive formulation – hence the alternative name of 'two-surface plasticity': (1) an inner loading/yield surface ($f = 0$) enclosing the pure elastic domain, and (2) an outer bounding/limit surface ($f^B = 0$) including all the admissible stress states compatible with the material strength (see Fig. 2.21). The main building stone of bounding surface plasticity is assuming that material hardening is determined by the distance between the current stress state on the yield surface and a suitable projection of it onto the outer bounding surface (i.e., the distance a in Fig. 2.21). Following its initial conception in the field of metal plasticity, bounding surface modelling has been widely applied to geomaterials. Its mathematical foundation is exhaustively covered in Dafalias (1986).

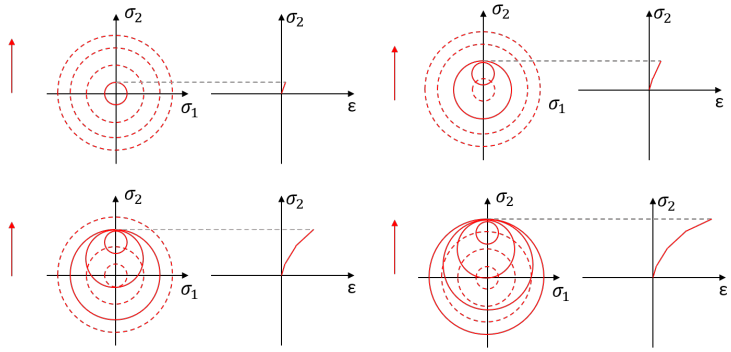

(a) loading phase

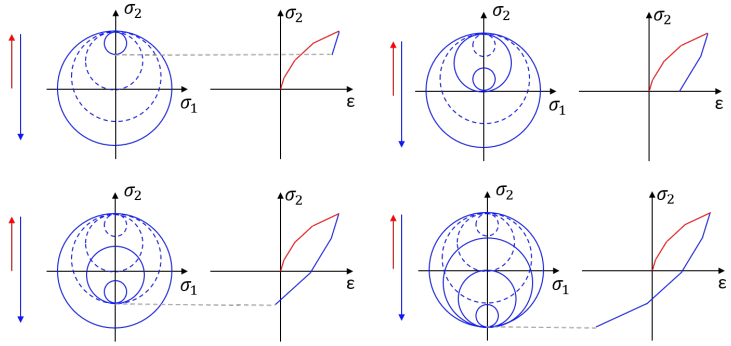

(b) unloading phase

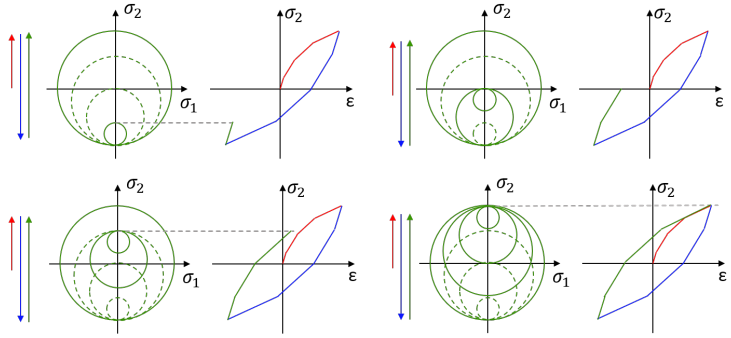

(c) reloading phase

Figure 2.20: Soil cyclic response as simulated through multi-surface elastoplasticity

Bardet (1986) enriched bounding surface plasticity with critical state theory ingredients for sand, although the resulting model would still require different sets of parameters to model the behaviour of a given sand at different relative densities. This drawback was later overcome by introducing in sand constitutive modelling the notion of 'state parameter', reappraised by Been and Jefferies (1985) after Wroth

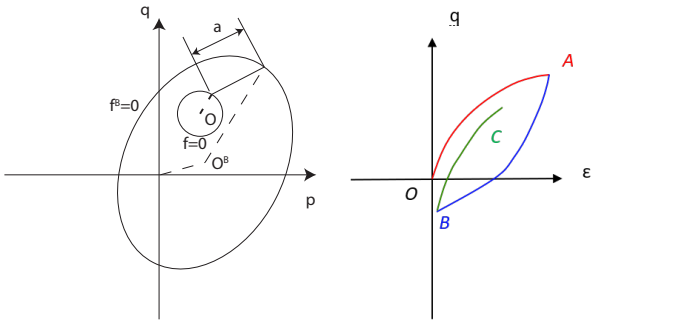

(a) Relevant model loci

(b) stress-strain response to loading-unloading-reloading

Figure 2.21: soil cyclic response as simulated through bounding surface elastoplasticity

and Bassett (1965). The incorporation of the state parameter concept into bounding surface plasticity with kinematic hardening gave birth to the family of SANISAND models, the main ancestor of the constitutive modelling work presented herein.

In the late 1990s, the first SANISAND model was proposed by Manzari and Dafalias (1997). The name *SANISAND* is the acronym for 'Simple ANIsotropic SAND' model, and first appeared in Taiebat and Dafalias (2008). Existing SANISAND models are built on critical state soil mechanics, and mainly focus on the bounding surface plasticity 'implicit' simulation of sand cyclic behavior. The use of the state parameter as defined by Been and Jefferies (1985) has been embraced since the work of Manzari and Dafalias (1997), following the previous proposal of Muir Wood and Belkheir (1994). Later members of the SANISAND family were introduced over the years to remedy specific limitations of the original formulation. Papadimitriou et al. (2001) introduced a scalar, fabric-related ingredient into the plastic modulus, in order to capture the drastic decrease in shear stiffness caused by dilative plastic volume changes under undrained cyclic loading. The same goal was more comprehensively tackled by Dafalias and Manzari (2004), who adopted as a 'dilatancy-tuning' internal variable the inherent fabric tensor. Taiebat and Dafalias (2008) added a cap-hardening mechanism to enable plastic straining even for stress paths at constant deviatoric stress ratio. More recently, Dafalias and Taiebat (2016) proposed an incrementally non-linear (hypoplastic) formulation with zero elastic range (SANISAND-Z), while Papadimitriou et al. (2019) and Petalas et al. (2020) incorporated the Anisotropic Critical State Theory (ACST) emerged from the work of Li and Dafalias (2011). The model proposed by Petalas et al. (2020), SANISAND-FN, enhances the previous formulation by Petalas et al. (2019) (SANISAND-F), and takes a step forward in the simulation of fabric effects in the the presence of principal stress axes rotation. Lastly, Barrero et al. (2020) embedded a new state variable (the so-called 'strain liquefaction factor') into SANISAND's hardening law and dilatancy rule, and succeeded in the simulation of undrained cyclic mobility under symmetric simple shear loading.

In addition to SANISAND models, other bounding surface formulations for sand

are available in the literature and worth citing (Gajo and Muir Wood, 1999a,b; Loukidis and Salgado, 2009; Boulanger and Ziotopoulou, 2013; Pisanò and Jeremić, 2014; Gao and Zhao, 2015; Zhang et al., 2020). In most of the aforementioned bounding surface models, the effects of fabric are introduced via either scalar or tensorial variables, mostly for the simulation of cyclic liquefaction. In contrast, the bounding surface model proposed by Corti et al. (2016) adopted an additional locus named the 'memory surface' to phenomenologically capture sand fabric effects. This model (particularly, the featured combination of bounding surface plasticity and memory surface) appeared immediately very promising, and led the Author to attempt a memory surface enhancement of the SANISAND model by Dafalias and Manzari (2004). The outcomes of this endeavour are described in detail in the following chapters.

Multi-surface vs bounding surface elastoplasticity

In an early study on the subject, Prévost (1982) compared the main merits and shortcomings of multi-surface and bounding surface plasticity modelling. A paraphrase of Prévost's arguments may read as follows:

- multi-surface plasticity theory is appreciated for its flexibility in adapting to diverse experimental evidence, although "*it suffers from inherent storage inconveniences*" (in relation to the the presence of multiple yield loci and associated hardening variables). The approximation of a measured non-linear response through distinct linear hardening branches is notably in favour of straightforward model calibration;

- bounding surface plasticity (named 'two-surface plasticity' in the original publication) is a competitive option in that it requires, originally, only two model loci and a set of scalar functions to continuously describe material hardening. Therefore, "storage inconveniences" are largely resolved, although selected translation/expansion rules may ultimately lack the generality needed to cope with very diverse features of behaviour.

Prévost concluded that "*which theory should be preferred is obviously a trade-off decision*" as both approaches suffer from inherent limitations.

Almost 40 years later, the argument regarding storage inconveniences seems outdated in light of present computer power, while the flexibility offered by a series of distinct yielding mechanisms is still a notable advantage of the multi-surface approach. Interestingly, it has also been shown over the years how to reformulate multi-surface plasticity (and its generalisation with an infinite number of yield surfaces) within the hyperplastic framework, which guarantees compliance with thermodynamic principles (Houlsby and Puzrin, 2006) – see discussion above. Relevant to this dissertation is also the recent extension of multi-surface hyperplasticity to include the modelling of material ratcheting under numerous loading cycles (Houlsby et al., 2017). However, definitive energy potential and dissipation functions suitable to capture the complex cyclic behaviour of sand (as presented in Section 2.2) do not seem to be available yet.

As for bounding surface plasticity, most fundamental aspects and limitations – in addition to the analysis in Prévost (1982) – were discussed by Dafalias (1986), and later by Houlsby and Puzrin (2006) in a general comparison among different plasticity theories. From a theoretical standpoint, it has not been possible yet to re-frame bounding surface plasticity within some form of hyperplasticity – as a consequence, thermodynamic consistency can only be analysed on a case-by-case basis, with all the intrinsic difficulties about distinguishing plastic free energy and dissipation in Equation (2.11). Another more practical shortcoming concerns the phenomenon of so-called 'overshooting', already acknowledged by Dafalias (1986), and recently tackled in more detail, e.g., by Mojtaba and Taiebat (2014) and Dafalias and Taiebat (2016). Overshooting occurs in most bounding surface models in the presence of unloading-reloading cycles of small amplitude within general/irregular loading histories. Overshooting results in unrealistically stiff behaviour upon reloading, due to the changes in size/location of the loading surface in response to stress reversals. This issue, particularly relevant to seismic loading conditions, has been already given plausible solutions, but will not be further explored in this work due to the specific loading conditions considered in the following.

A more substantial limitation of bounding surface plasticity is the tendency to exaggerate material ratcheting under prolonged cyclic shear loading, especially in the presence of a level of shear preloading (biased cyclic loading). This drawback, already noted by Houlsby and Puzrin (2006) and Corti et al. (2016), is a serious threat to the analysis of soil-structure interaction problems, especially those in which accurate prediction of cyclic displacement is of the essence. Noting that this is the case for OWT monopiles tilting under lateral cyclic loading, the urgency of a bounding surface formulation with ratcheting control is self-apparent for applications in offshore wind geotechnics. Indeed, this line of work is pursued in the following research starting from Dafalias' SANISAND family of models, which has gained over the years large popularity for the solution of cyclic/dynamic problems in sandy soils.

2.4. Concluding remarks

The cyclic behaviour of sand exhibits a great deal of complexity in relation to a number of governing factors, including features of the loading programme, density state, pore water drainage, and, importantly, state and evolution of the microstructure (sand fabric). In this chapter, salient experimental evidence at the scale of a laboratory sample has been overviewed, with reference to both drained and undrained cyclic loading conditions. As for the former, major attention has been devoted to high-cyclic ratcheting behaviour, particularly to the impact of several geotechnical factors on the magnitude and direction of cyclic strain accumulation. Regarding undrained cyclic loading, relevant failure modes have been presented, including cyclic liquefaction, cyclic mobility, and loss of serviceability due to excessive strain accumulation. The key soil/loading factors that affect the occurrence of such modes have been pointed out. Overall, the complexity of fabric effects in the cyclic response of sand has been described, with focus on lessons learned from laboratory tests and numerical DEM studies.

The second part of the chapter has been dedicated to constitutive modelling

strategies. After introducing the distinction between explicit and implicit cyclic modelling, existing elastoplastic approaches in the latter area have have been overviewed. Quoting Houlsby and Puzrin (2006), *"the constitutive relations are simply approximations to the behaviour of real materials; none of which will behave exactly according to the idealizations employed. Thus constitutive relations are never 'true' for a real material; they can only provide solutions that approximate what happens in reality to a certain degree of precision. Of course, in certain branches of mechanics (notably the elasticity of metals within a limited stress range), the precision of the constitutive model is so good that, for all practical purposes, it can be treated as a 'true' model. [...] Whoever uses the models should understand this and must try to assess its implications for the problem in hand"*. While the main merits and drawbacks of different plasticity theories have been briefly discussed, no attempt has been made to 'rank' the considered modelling approaches – not even in relation to their cyclic performance. The main conclusion of the chapter is the selection of 'memory-enhanced' bounding surface plasticity as a framework for the modelling of (high-)cyclic sand behaviour, and for the analysis of cyclic soil-structure interaction problems. The open question regarding the (general) thermodynamic consistency of SANISAND models will not find new answers in the remainder of this work, but is put forward as an issue to which the geomechanical community should devote further research in the near future.

3

SANISAND-MS: Model Formulation and High-cyclic Performance

Parts of this chapter have been published in Géotechnique (Liu et al., 2019).

3.1. Introduction

Predicting the cyclic response of sands is relevant to numerous geotechnical applications, for instance in the fields of earthquake, offshore and railway engineering. Such a response emerges from complex micro-mechanical processes that give rise to a highly non-linear hydro-mechanical behaviour at the macro-scale, featuring irreversible deformation, hysteresis, pore pressure build-up, etc. (di Prisco and Muir Wood, 2012). The engineering analysis of these phenomena proves even more challenging for long-lasting cyclic loading events ('high-cyclic' loading), such as those experienced by soils and foundations under operating offshore structures (e.g. offshore drilling rigs, pipelines, wind turbines) (Andersen, 2009, 2015; Randolph and Gourvenec, 2011). A typical example is given at present by monopile foundations for offshore wind turbines, whose design must assure full functionality of the structure during its whole operational life – 10^8-10^9 loading cycles with alternating sequences of small-amplitude vibrations and severe storm loading (LeBlanc et al., 2010; Abadie, 2015; Truong et al., 2019; Richards et al., 2019).

Despite the current ferment around offshore wind geotechnics (Pisanò and Gavin, 2017), frustrating uncertainties still affect the engineering analyses performed to assess the capacity, serviceability and fatigue resistance of wind turbine foundations. In this context, a major role is played by the phenomenon of 'sand ratcheting': this term denotes the gradual accumulation of plastic strains under many loading cycles, as opposed to the occurrence of 'shakedown' (long-term response with no plastic strain accumulation) (Houlsby et al., 2017). While micromechanical studies aim to describe the occurrence and modes of sand ratcheting at the granular level (Alonso-Marroquin and Herrmann, 2004; McNamara et al., 2008; O'Sullivan and Cui, 2009; Calvetti and di Prisco, 2010), usable engineering methods are currently being devised for predictions at the soil-foundation-structure scale. Both 'implicit' and 'explicit' numerical methods in this area have pros and cons (see Chapter 2).

The present chapter tackles the modelling of sand ratcheting within the phenomenological framework of bounding surface plasticity. For this purpose, the critical state SANISAND04 model by Dafalias and Manzari (2004) is enriched with a third locus – termed 'memory surface' – to reproduce fabric effects relevant to cyclic ratcheting. The suitability of the memory surface approach has been recently shown by Corti (2016) and Corti et al. (2016) in combination with the bounding surface model by Gajo and Muir Wood (1999b,a). The resulting model has been successfully applied to the cyclic analysis of certain offshore soil-structure interaction problems, involving e.g. mudmat foundations (Corti et al., 2017) and plate anchors (Chow et al., 2015). In this work, the SANISAND conceptual platform has been preferred also in light of the several open-source implementations already available (Mazzoni et al., 2007; Gudehus et al., 2008; Ghofrani and Arduino, 2018).

With the main focus on drained loading conditions, the model described in the following improves the achievements of Corti et al. (2016) in several respects: (i) general multiaxial formulation, with pressure-sensitive hardening rules suitable to accommodate the different backbone model (SANISAND04) under monotonic and cyclic loading; (ii) improved analytical "workability" achieved through a formulation based on the "true" stress tensor, and the use of a memory locus with circular

deviatoric section; (iii) modified plastic flow rule to refine the simulation of volume changes under cyclic loading conditions. Importantly, the ratcheting performance of the model has been tested up to 10^4 loading cycles, and validated against a wider set of literature results, including high-cyclic triaxial (both standard and non-standard) and simple shear tests..

The ultimate goal of the chapter is to help bridge implicit and explicit approaches through the proposed plasticity model. Its 'implicit' use will enable more accurate time-domain simulations of cyclic/dynamic soil-structure interaction under relatively short-lasting loading (e.g. storms, earthquakes, etc.) (Corciulo et al., 2017; Kementzetzidis et al., 2019). As more experimental data become available and further calibration exercises are carried out, it will also contribute to explicit high-cyclic procedures by supporting the prediction of strain accumulation trends with a lower demand on laboratory test results.

3.2. Towards a high-cyclic SANISAND model

While massive efforts have been devoted to modelling the undrained cyclic behaviour of sands, the cyclic performance under drained loading conditions has received far less attention. A few works tackled this issue by enhancing the bounding surface framework with fabric-related modelling concepts, such as Khalili et al. (2005); Kan et al. (2013); Gao and Zhao (2015); outside traditional bounding surface plasticity, the contributions by Wan and Guo (2001b); Di Benedetto et al. (2014); Liu et al. (2014); Tasiopoulou and Gerolymos (2016) are also worth citing. However, none of the mentioned works focused explicitly on drained strain accumulation under a large number of loading cycles.

The cyclic sand model proposed in this study builds upon two main pillars, namely the SANISAND04 model by Dafalias and Manzari (2004) and the addition of a memory locus accounting for fabric effects during cyclic loading (Corti, 2016; Corti et al., 2016). Since its first introduction in 1997 (Manzari and Dafalias, 1997), the family of SANISAND models has expanded with new members improving certain limitations of the original formulation, regarding e.g. dilatancy and fabric effects, hysteretic small-strain behaviour, response to radial stress paths, incremental nonlinearity (Papadimitriou et al., 2001; Papadimitriou and Bouckovalas, 2002; Dafalias and Manzari, 2004; Taiebat and Dafalias, 2008; Loukidis and Salgado, 2009; Pisanò and Jeremić, 2014; Dafalias and Taiebat, 2016). In particular, the SANISAND04 formulation includes a fabric-related tensor improving the phenomenological simulation of post-dilation fabric changes upon load reversals, with a beneficial impact on the prediction of pore pressure build-up during undrained cyclic loading.

Unfortunately, the set of modelling ingradients as assembled in SANISAND04 cannot quantitatively reproduce high-cyclic ratcheting, nor its dependence on relevant loading parameters (especially stress obliquity, symmetry and amplitude of the loading programme). In SANISAND04, (i) the use of the (phenomenological) fabric tensor $\boldsymbol{z}$ is only suitable to capture the effects of initial inherent anisotropy, as explained in detail by Li and Dafalias (2011); (ii) fabric evolution is solely activated for denser-than-critical conditions, after the stress path crosses the phase transformation line. This latter strategy has proven not sufficient to capture fabric

effects occurring during (drained) cyclic loading, for instance related to the evolving distributions of voids and particle contacts (Oda et al., 1985; O'Sullivan et al., 2008; Zhao and Guo, 2013). A significant impact of these facts on numerical simulations is that the SANISAND04 model produces only slight soil stiffening under drained (high-)cyclic shear loading, resulting in exaggerated strain accumulation. While acknowledging the benefits of improved fabric tensor formulations (Papadimitriou and Bouckovalas, 2002), a different path based on the memory surface concept will be followed in the remainder of this work.

The plasticity modelling of ratcheting phenomena has received a few valuable contributions (di Prisco and Mortara, 2013), originally regarding metals and alloys. These contributions have been reviewed by Houlsby et al. (2017), and generalised into a hyper-plastic multi-surface framework for the macro-element analysis of offshore monopiles.

This chapter proposes an alternative approach based on bounding surface plasticity and the use of an additional memory surface to keep track of fabric changes relevant to the ratcheting response. The concept of memory surface (or history surface) was first proposed by Stallebrass and Taylor (1997) for overconsolidated clays, and then applied to sands within different modelling frameworks by Jafarzadeh et al. (2008); Maleki et al. (2009); Di Benedetto et al. (2014). Herein, the latest version by Corti et al. (2016) and Corti (2016) is adopted and enhanced within the SANISAND family. Accordingly, the regions of the stress-space that have already experienced cyclic loading are represented by an evolving memory locus, within which cyclic strain accumulation occurs at a lower rate than under virgin loading conditions.

3.3. Model formulation

This section presents the main analytical features of the proposed model, with the focus on embedding the memory surface concept into the SANISAND04 backbone formulation. The model belongs to the well-known SANISAND model family and is named as SANISAND-MS ('MS' for memory surface). Similarly to SANISAND04, the new model is based on a bounding surface, kinematic hardening formulation to capture cyclic, rate-independent behaviour. The model links to the well-established Critical State theory through the notion of 'state parameter' (Been and Jefferies, 1985), which enables the behaviour of a given sand to be captured over the loose-to-dense range with a single set of parameters. Overall, the new model uses three relevant loci – yield, bounding and memory surface (Figure 3.1). All constitutive equations are presented by first summarising the features inherited from Dafalias and Manzari (2004), and then focusing on the latest memory surface developments.

Notation Tensor quantities are denoted by bold-face characters in a direct notation. The symbols :, tr and ⟨⟩ stand for tensor inner product, trace operator and Macauley brackets, respectively.

Stresses are meant as 'effective' throughout this work. $\boldsymbol{\sigma}$ and $\boldsymbol{\varepsilon}$ denote effective stress and strain tensor. Usual decompositions into deviatoric and isotropic components are used throughout, namely $\boldsymbol{\sigma} = \boldsymbol{s} + p\boldsymbol{I}$ ($\boldsymbol{s}$ – deviatoric stress tensor,

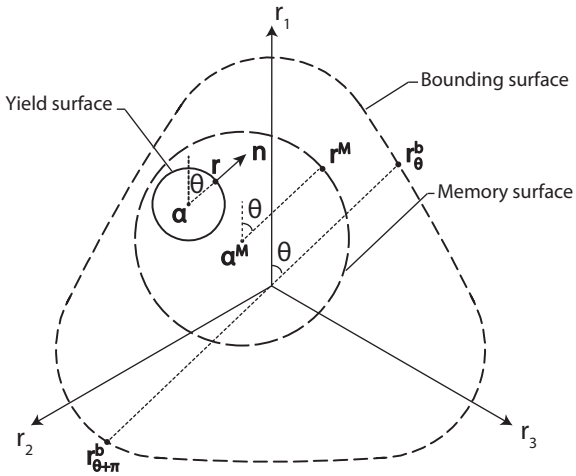

Figure 3.1: Relevant loci/tensors in the normalised π plane.

$p = (\mathrm{tr}\boldsymbol{\sigma})/3$ – isotropic mean stress) and $\boldsymbol{\varepsilon} = \boldsymbol{e} + (\varepsilon_{vol}/3)\boldsymbol{I}$ ($\boldsymbol{e}$ – deviatoric strain tensor, $\varepsilon_{vol} = \mathrm{tr}\boldsymbol{\varepsilon}$ – volumetric strain). $\boldsymbol{I}$ is the second-order identity tensor, the deviatoric stress ratio $\boldsymbol{r} = \boldsymbol{s}/p$ is also widely employed in the formulation. The superscripts e and p are used with the meaning of 'elastic' and 'plastic'.

3.3.1. Model features from SANISAND04

For the sake of brevity, a multi-axial formulation is directly provided, while conceptual discussions in a simpler triaxial environment may be found in Dafalias and Manzari (2004). For the same reason, model details shared with SANISAND04 are only briefly recalled, whereas Table 3.1 provides a synopsis of all equations and material parameters (Dafalias and Manzari, 2004). For smoother incorporation of the memory surface, the formulation of SANISAND-MS has been first developed using the deviatoric stress ratio r as main variable (see equations in Table 3.1, applicable to Chapters 3 and 4). A slightly different formulation is adopted later in Chapter 5, in which the use of the back-stress ratio alpha (in lieu of **r**) is reappraised as done in SANISAND04 (Dafalias and Manzari, 2004). Generally, non-triaxial loading paths may lead the yield locus partially outside the bounding surface and, in some rare cases, let the latter be overcome by the stress point during elastic loading stages – with an artificial softening response resulting as a mere consequence of the formulation. Though this artificial softening response is not observed in the simulations presented in Chapters 3 and 4, model formulations employing back stress ratio $\boldsymbol{\alpha}$ are presented in Appendix B, compared with model equations employing stress ratio $\boldsymbol{\alpha}$. In Chapters 5 and 6, back stress-ratio based model formulations are employed instead.

Similarly to most SANISAND formulations, the proposed model relies on the assumption that plastic stains only occur upon variations in stress ratio $\boldsymbol{r}$, so that all plastic loci and hardening mechanisms can be effectively described in the nor-

malised π plane (Figure 3.1). Importantly, the overall formulation remains based on 'true' stress ratio variables, while Gajo and Muir Wood (1999a,b) and Corti et al. (2016) used stress normalised with respect to the current state parameter.

Elastic relationship Sand behaviour is assumed to be (hypo)elastic inside the yield locus, with a constant Poisson ratio ν and pressure-dependent shear modulus defined as per Li and Dafalias (2000):

$$G = G_0 p_{atm}[(2.97 - e)^2/(1 + e)]\sqrt{p/p_{atm}} \tag{3.1}$$

in which p_{atm} is the reference atmospheric pressure, G_0 a dimensionless shear stiffness parameter, and e the current void ratio.

The use of a hypoelastic law is customary in previous versions of SANISAND, and is retained also in this work which is mainly concerned with further development of SANISAND04 (Dafalias and Manzari, 2004). Such a choice is typically motivated by its simplicity and substantial agreement with available experimental data (Houlsby et al., 2005), but is not impeccable in one relevant respect. As already observed in Chapter 2, the use of a hypoelastic relationship may result in a non-conservative response under certain loading paths, for instance in situations similar to that illustrated by Zytynski et al. (1978). A definitive solution to this issue would be the adoption of a "hyperelastic" formulation, providing the small-strain stress-strain relationship, and particularly the (stress-dependent) elastic moduli, after differentiation of a scalar energy function. A number of valuable contributions have been made in this area, some of which quite recently (Houlsby et al., 2005; Gajo and Bigoni, 2008; Houlsby et al., 2019; Amorosi et al., 2020). In light of the theoretical analysis by Zytynski et al. (1978), the issue of elastic energy conservation appears generally less concerning for most of the cyclic stress paths considered later on in this chapter. However, the implications for the analysis of boundary value problems may be more serious, and can only be assessed by comparatively inspecting the performance of models using a hypoelastic or hyperelastic formulation (Einav and Puzrin, 2004a). Although out of the scope of this dissertation, future work will have to be devoted to this important matter.

Yield locus An open conical yield locus $f = 0$ is used, whose axis rotation and (constant) small opening are governed by the evolution of the back-stress ratio $\boldsymbol{\alpha}$ and the parameter m:

$$f = \sqrt{(\boldsymbol{s} - p\boldsymbol{\alpha}) : (\boldsymbol{s} - p\boldsymbol{\alpha})} - \sqrt{2/3}mp = 0 \tag{3.2}$$

Critical state locus A unique critical state locus is assumed and defined in the multidimensional $e - \boldsymbol{\sigma}$ space. Its projection on the $e - p$ plane, i.e. the critical state line, reads as (the subscript c stands for 'critical'):

$$e_c = e_0 - \lambda_c (p_c/p_{atm})^{\xi} \tag{3.3}$$

and requires the identification of three material parameters – e_0, λ_c and ξ (Li and Wang, 1998). The aforementioned state parameter $\Psi(e, p) = e - e_c$ quantifies the

distance between current and critical void ratios (Been and Jefferies, 1985; Muir Wood and Belkheir, 1994), which is key to modelling sand behaviour at varying relative density.

The projection of the critical state locus on the normalised π plane can be conveniently expressed as a deviatoric tensor $\boldsymbol{r}_\theta^c$:

$$\boldsymbol{r}_\theta^c = \sqrt{2/3}\, g(\theta) M \boldsymbol{n} \tag{3.4}$$

providing the critical state stress ratio associated with the current stress ratio $\boldsymbol{r}$ through the unit tensor, normal to the yield locus (Figure 3.1):

$$\boldsymbol{n} = (\boldsymbol{r} - \boldsymbol{\alpha})/\sqrt{2/3} m \tag{3.5}$$

The function g describes the Argyris-type shape of the critical locus depending on the 'relative' Lode angle θ[1] (see Table 3.1 and Dafalias and Manzari (2004)). The parameter M appears in its traditional meaning of critical stress ratio under triaxial compression (directly related to the constant-volume friction angle).

It should also be recalled that the assumption of an unique critical state locus is still a matter of scientific debate, and is certainly not the only option available – nonetheless, several theoretical studies may be cited in its support (Li and Dafalias, 2011; Zhao and Guo, 2013; Gao and Zhao, 2015). An evolving version of the locus (Eq. (3.3)) could be adopted in the future upon conclusive consensus on the subject – for instance, according to the path followed by Papadimitriou et al. (2005).

Plastic flow rule Plastic strain increments – deviatoric and volumetric – are obtained as:

$$d\boldsymbol{e}^p = \langle L \rangle \boldsymbol{R}' \qquad d\varepsilon_{vol}^p = \langle L \rangle D \tag{3.6}$$

where $\boldsymbol{R}'$ and D are the tensor of deviatoric plastic flow direction (Dafalias and Manzari, 2004) and the dilatancy coefficient, respectively. The plastic multiplier L (or loading index) results from the enforcement of plastic consistency and can be expressed in the following form:

$$L = \frac{1}{K_p} \frac{\partial f}{\partial \boldsymbol{\sigma}} : d\boldsymbol{\sigma} \tag{3.7}$$

with K_p commonly referred to as plastic modulus.

Kinematic hardening and bounding surface The back-stress ratio $\boldsymbol{\alpha}$ (axis of the yield locus) is assumed to evolve according to the following hardening law:

$$d\boldsymbol{\alpha} = \frac{2}{3} \langle L \rangle h(\boldsymbol{r}_\theta^b - \boldsymbol{r}) \quad \Rightarrow \quad K_p = \frac{2}{3} p h (\boldsymbol{r}_\theta^b - \boldsymbol{r}) : \boldsymbol{n} \tag{3.8}$$

which in turn implies the expression of K_p reported by Dafalias and Manzari (2004). According to Eq. (3.8), the centre of the yield locus translates in the π plane along

[1] $\cos 3\theta = \sqrt{6} tr \boldsymbol{n}^3$ (Manzari and Dafalias, 1997)

Table 3.1: Model synopsis: constitutive equations and material parameters.

	Constitutive equations	**Material parameters**
Elastic moduli	$G = G_0 p_{atm}[(2.97-e)^2/(1+e)](p/p_{atm})^{1/2}$ $K = 2(1+\nu)G/[3(1-2\nu)]$	G_0 dimensionless shear modulus ν Poisson's ratio
Critical state line	$e_c = e_0 - \lambda_c (p_c/p_{atm})^{\xi}$	e_0 reference critical void ratio λ_c, ξ critical state line shape parameters
Yield function	$f = \sqrt{(\boldsymbol{s}-p\boldsymbol{\alpha}):(\boldsymbol{s}-p\boldsymbol{\alpha})} - \sqrt{2/3}pm$	m yield locus opening parameter
Memory function	$f^M = \sqrt{(\boldsymbol{s}-p\boldsymbol{\alpha}^M):(\boldsymbol{s}-p\boldsymbol{\alpha}^M)} - \sqrt{2/3}pm^M$	
Deviatoric plastic flow	$d\boldsymbol{e}^p = \langle L\rangle \boldsymbol{R}'$ $\boldsymbol{R}' = B\boldsymbol{n} - C[\boldsymbol{n}^2 - (1/3)\boldsymbol{I}]$ $\boldsymbol{n} = (\boldsymbol{r}-\boldsymbol{\alpha})/\sqrt{2/3}m$ $B = 1 + 3(1-c)/(2c)g(\theta)\cos 3\theta$ $C = 3\sqrt{3/2}(1-c)g(\theta)/c$ $g(\theta) = 2c/[(1+c)-(1-c)\cos 3\theta]$	
Volumetric plastic flow	$d\varepsilon^p_{vol} = \langle L\rangle D$ $D = [A_0 \exp(\beta\langle \tilde{b}^M_d\rangle/b_{ref})](\boldsymbol{r}^d_\theta - \boldsymbol{r}):\boldsymbol{n}$ $\boldsymbol{r}^d_\theta = \sqrt{2/3}g(\theta)M\exp(n^d\Psi)\boldsymbol{n}$ $\tilde{b}^M_d = (\tilde{\boldsymbol{r}}^d_\theta - \tilde{\boldsymbol{r}}^M):\boldsymbol{n}$ $b_{ref} = (\boldsymbol{r}^b_\theta - \boldsymbol{r}^b_{\theta+\pi}):\boldsymbol{n}$ $\boldsymbol{r}^b_{\theta+\pi} = \sqrt{2/3}g(\theta+\pi)M\exp(-n^b\Psi)(-\boldsymbol{n})$	A_0 'intrinsic' dilatancy parameter β dilatancy memory parameter n^d void ratio dependence parameter
Yield surface evolution	$d\boldsymbol{\alpha} = (2/3)\langle L\rangle h(\boldsymbol{r}^b_\theta - \boldsymbol{r})$ $\boldsymbol{r}^b_\theta = \sqrt{2/3}g(\theta)M\exp(-n^b\Psi)]\boldsymbol{n}$ $h = \frac{b_0}{(\boldsymbol{r}-\boldsymbol{r}_{in}):\boldsymbol{n}}\exp\left[\mu_0\left(\frac{p}{p_{atm}}\right)^{0.5}\left(\frac{b^M}{b_{ref}}\right)^2\right]$ $b_0 = G_0 h_0(1-c_h e)/\sqrt{(p/p_{atm})}$ $b^M = (\boldsymbol{r}^M - \boldsymbol{r}):\boldsymbol{n}$	M critical stress ratio (triaxial compression) n^b void ratio dependence parameter c compression-to-extension strength ratio μ_0 ratcheting parameter h_0, c_h hardening parameters
Memory surface evolution	$dm^M = \sqrt{3/2}d\boldsymbol{\alpha}^M:\boldsymbol{n} - (m^M/\zeta)f_{shr}\langle -d\varepsilon^p_{vol}\rangle$ $d\boldsymbol{\alpha}^M = (2/3)\langle L^M\rangle h^M(\boldsymbol{r}^b_\theta - \boldsymbol{r}^M)$ $h^M = \frac{1}{2}\left[\frac{b_0}{(\boldsymbol{r}^M-\boldsymbol{r}_{in}):\boldsymbol{n}} + \sqrt{\frac{3}{2}}\frac{m^M f_{shr}\langle -D\rangle}{\zeta(\boldsymbol{r}^b_\theta - \boldsymbol{r}^M):\boldsymbol{n}}\right]$	ζ memory surface shrinkage parameter

the $\boldsymbol{r}^b_\theta - \boldsymbol{r}$ direction, with its magnitude governed by the hardening factor h. $\boldsymbol{r}^b_\theta$ represents the projection of the current stress ratio onto the so-called bounding surface:

$$\boldsymbol{r}^b_\theta = \sqrt{2/3}g(\theta)M\exp(-n^b\Psi)\boldsymbol{n} \tag{3.9}$$

The size of the bounding surface is modulated by the state parameter Ψ and the corresponding material constant n^b. At the critical state, $\Psi = 0$ and the bounding surface coincides with the critical locus. It is worth noting that, for better compatibility with memory surface developments, the present formulation reappraises projection rules based on the stress ratio $\boldsymbol{r}$ rather than the back-stress ratio $\boldsymbol{\alpha}$ – compare e.g. Dafalias (1986) to Manzari and Dafalias (1997).

3.3.2. Additional memory surface for ratcheting control

Novel developments related to the memory surface concept are detailed in this subsection, with direct impact on the factors h and D in Eqs. (3.8) and (3.6).

Meaning and definition

Figure 3.1 illustrates, in the normalised π plane, the three main loci involved in the model formulation:

– *yield surface*, distinguishes stress states associated with either negligible or significant plastic straining;

– *memory surface*, distinguishes stress states associated with either vanishing or severe changes in granular fabric;

– *bounding surface*, separates admissible/pre-failure and ultimate stress states;

Although the above transitions may not be as sharp in nature, the above idealisation provides conceptual input to phenomenological constitutive modelling.

The memory locus is adopted to track the global (re)orientation of particle contacts, and in turn the degree of loading-induced anisotropy. Accordingly, it will be possible to describe weak fabric changes induced by moderate high-cyclic loads, possibly 'overwritten' by more severe loading afterwards – henceforth termed 'virgin loading' (Nemat-Nasser, 2000; Jafarzadeh et al., 2008).

From an analytical standpoint, the memory locus $f^M = 0$ is represented by an additional conical surface:

$$f^M = \sqrt{(\boldsymbol{s} - p\boldsymbol{\alpha}^M) : (\boldsymbol{s} - p\boldsymbol{\alpha}^M)} - \sqrt{2/3} m^M p = 0 \tag{3.10}$$

endowed with its own (memory) back-stress ratio and opening variable $\boldsymbol{\alpha}^M$ and m^M. As shown in the following, the choice of a conical memory locus with circular deviatoric section results in simpler projection rules and evolution laws (no lengthy algebra from the differentiation of the third stress invariant). Nevertheless, keeping the typical Argyris-shape for the outer bounding surface (Eq. (3.9)) preserves a dependence of both stiffness and strength on the Lode angle θ.

It is postulated that, during plastic straining, (i) the stress point on the yield surface can never lie outside the memory surface, (ii) the memory surface can only be larger than the elastic domain, or at most coincident. These requisites are compatible with the following reformulation of the hardening coefficient h in K_p:

$$h = \frac{b_0}{(\boldsymbol{r} - \boldsymbol{r}_{in}) : \boldsymbol{n}} \exp\left[\mu_0 \left(\frac{p}{p_{atm}}\right)^{n=0.5} \left(\frac{b^M}{b_{ref}}\right)^{w=2}\right] \tag{3.11}$$

in which

$$\begin{aligned} b^M &= (\boldsymbol{r}^M - \boldsymbol{r}) : \boldsymbol{n} \\ b_{ref} &= (\boldsymbol{r}^b_\theta - \boldsymbol{r}^b_{\theta+\pi}) : \boldsymbol{n} \end{aligned} \tag{3.12}$$

and $\boldsymbol{r}^b_{\theta+\pi}$ is the opposite projection onto the bounding surface, along the direction $-\boldsymbol{n}$ with relative Lode angle $\theta + \pi$ (Eq. (3.9), Figure 3.1 – therefore, $b_{ref} > 0$ always). The SANISAND04 definition of the hardening factor b_0 is recalled in Table 3.1. The above definitions include the image stress point $\boldsymbol{r}^M$ on the memory surface, which is obtained as the projection of $\boldsymbol{r}$ on the memory surface along the direction of $\boldsymbol{n}$ (Eq. (3.5)):

$$\boldsymbol{r}^M = \boldsymbol{\alpha}^M + \sqrt{2/3} m^M \boldsymbol{n} \tag{3.13}$$

The left factor in Eq. (3.11) coincides with the h coefficient in Dafalias and Manzari (2004) (with b_0 model parameter and $\boldsymbol{r}_{in}$ load-reversal tensor[2]), whilst the right factor introduces the memory surface concept into SANISAND04 with the additional material parameter μ_0 (Corti et al., 2016, 2017). In essence, h receives additional influence from the yield-to-memory surface distance b^M: as a consequence, higher K_p and soil stiffness result at increasing distance b^M (see evolution laws later on), but a virgin SANISAND04 response is recovered when the yield and the memory loci are tangent at the current stress point $\boldsymbol{\sigma} \equiv \boldsymbol{\sigma}^M$ ($\rightarrow b^M = 0$).

The two material parameters, n and w, have been pre-set in Eq. (3.11) for easier model calibration. In particular, extensive comparisons to experimental data (see next sections) confirmed the need for a pressure-dependent memory surface term (Corti et al., 2017), along with a quadratic dependence on the distance b^M. Additional experimental evidence may support in the future more flexibility about n and w, as well as other fundamental dependences (for instance on the void ratio e).

The following subsections introduce the evolution laws for the size and position of the memory surface, as well its effect on sand dilatancy.

Memory surface size

The expansion of the memory surface (isotropic hardening) aims to capture phenomenologically the experimental link between gradual change in fabric and sand stiffening.[3] This evidence is translated into an increasing size m^M of the memory surface and a larger distance between $\boldsymbol{r}$ and $\boldsymbol{r}^M$ in Eqs. (3.11)–(3.12). As clarified in the following, variations in size and position of the memory surface cannot be independent, but it is convenient to address the former aspect prior to the latter. For this purpose, the evolution of m^M is established on a geometrical basis starting from a situation of incipient virgin loading – memory surface coincident or tangent to the yield locus (Figure 3.2).

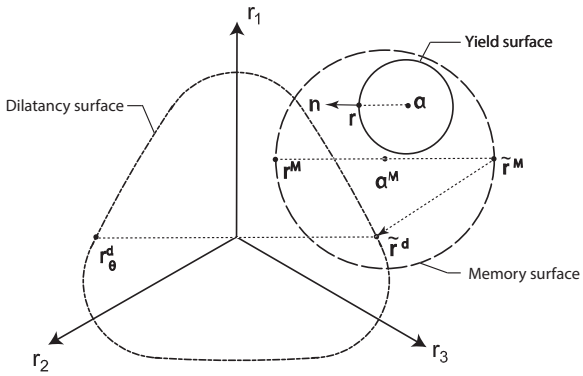

Figure 3.2: Memory surface expansion during virgin loading.

[2] $\boldsymbol{r}_{in}$ is the value of $\boldsymbol{r}$ at the onset of load reversal. It is updated to current $\boldsymbol{r}$ each time the condition $(\boldsymbol{r} - \boldsymbol{r}_{in}) : \boldsymbol{n} < 0$ is fulfilled.

[3] The effects of a varying void ratio are already accounted for as inheritance from SANISAND04.

Specifically, plastic loading starting from $\boldsymbol{\sigma} \equiv \boldsymbol{\sigma}^M$ is assumed to produce a uniform expansion of the memory surface around the pivot stress point $\boldsymbol{r}_A^M$, diametrically opposite to $\boldsymbol{r}^M$ and this is kept fixed throughout the process. From an analytical standpoint, this coincides with enforcing the incremental nullity of the memory function f^M at the fixed stress point A (i.e. $d\boldsymbol{\sigma}_A^M = 0$):

$$df^M\left(\boldsymbol{\sigma}_A^M\right) = \frac{\partial f^M}{\partial \boldsymbol{\sigma}_A^M} : d\boldsymbol{\sigma}_A^M + \frac{\partial f^M}{\partial \boldsymbol{\alpha}^M} : d\boldsymbol{\alpha}^M + \frac{\partial f^M}{\partial m^M} dm^M = 0 \tag{3.14}$$

Trivial manipulations (see Appendix A) lead to the following relationship:

$$dm^M = \sqrt{\frac{3}{2}} d\boldsymbol{\alpha}^M : \boldsymbol{n} \tag{3.15}$$

which is significantly simpler than that obtained by Corti (2016) for a memory surface with non-circular π-section. It is further assumed by analogy that Eq. (3.15) determines the relationship between expansion (dm^M) and translation ($d\boldsymbol{\alpha}^M$) of the memory locus under any loading conditions, not only virgin.

While $dm^M > 0$ (expansion) underlies 'fabric reinforcement' and sand stiffening within the expanded memory locus, an opposite effect is usually induced by dilative deformation stages and increase in void ratio (Nemat-Nasser and Tobita, 1982). Such a 'damage' to the fabric configuration results in lower sand stiffness. Here, the suggestion by Corti (2016) is followed, and an additional contraction term is cast into Eq. (3.15) to let the memory surface shrink only during dilation (negative $d\varepsilon_{vol}$):

$$dm^M = \sqrt{\frac{3}{2}} d\boldsymbol{\alpha}^M : \boldsymbol{n} - \frac{m^M}{\zeta} f_{shr} \left\langle -d\varepsilon_{vol}^p \right\rangle \tag{3.16}$$

in which the contraction term on the right is proportional to the current locus size m^M and plastic volumetric strain increment $d\varepsilon_{vol}^p$, with a purely geometrical factor f_{shr} described with more detail in the Appendix A. The contraction rate during dilation is governed by the material parameter ζ, assumed for simplicity not to depend on any stress/state variables (e.g. p, e, etc.).

Memory surface translation

In analogy with the translation rule for the yield locus, the centre of the memory surface is assumed to translate along the direction of $\boldsymbol{r}_\theta^b - \boldsymbol{r}^M$ (Figure 3.1):

$$d\boldsymbol{\alpha}^M = \frac{2}{3} \left\langle L^M \right\rangle h^M (\boldsymbol{r}_\theta^b - \boldsymbol{r}^M) \tag{3.17}$$

The hardening law (3.17) shares the same structure with Eq. (3.8), and requires a method to derive the 'memory-counterparts' of the plastic multiplier and the hardening coefficient, namely L^M and h^M. The same approach used for the isotropic memory hardening is re-adopted: the translation rule for $\boldsymbol{\alpha}^M$ is rigorously specified

for virgin loading and then extended to any other conditions. Accordingly, analytical derivations and material parameters are substantially reduced in a way proven successful by the the results in the following.

It is assumed that during virgin loading ($\boldsymbol{\sigma} \equiv \boldsymbol{\sigma}^M$) the same magnitude of the incremental plastic strain can be derived by using the yield or memory loci indifferently. The equalities below follow directly (see relevant derivations in the Appendix A):

$$L^M = L$$

$$h^M = \frac{1}{2}\left[\frac{b_0}{(\boldsymbol{r}^M - \boldsymbol{r}_{in}) : \boldsymbol{n}} + \sqrt{\frac{3}{2}\frac{m^M f_{shr}\langle -D\rangle}{\zeta(\boldsymbol{r}_\theta^b - \boldsymbol{r}^M) : \boldsymbol{n}}}\right] \tag{3.18}$$

and are then extended by analogy to non-virgin loading.

Memory surface: effect on the sand dilation

As a phenomenological recorder of fabric effects, the memory surface is also exploited to enhance the dilatancy factor D in Eq. (3.6), in a new way different from SANISAND04. The goal is to use the memory surface to obtain increased dilatancy (or pore pressure build-up in undrained conditions) upon load reversals following dilative deformation (Dafalias and Manzari, 2004). For this purpose, the memory surface is handled in combination with the same dilatancy locus defined by Dafalias and Manzari (2004), responsible for the transition from contractive to dilative response:

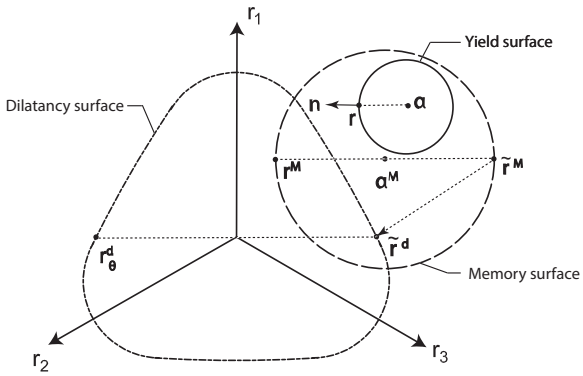

Figure 3.3: Geometrical definitions for the enhancement of the dilatancy coefficient.

$$\boldsymbol{r}_\theta^d = \sqrt{2/3}g(\theta)M\exp(n^d\Psi)\boldsymbol{n} \tag{3.19}$$

where the positive parameter n^d governs its evolution towards critical state ($\Psi = 0$). For the sake of clarity, Figure 3.3 displays certain geometrical quantities associated with the relative position of the memory and dilatancy surfaces. The distance $\tilde{b}_d^M$ is first defined as:

$$\tilde{b}_d^M = (\tilde{\boldsymbol{r}}^d - \tilde{\boldsymbol{r}}^M) : \boldsymbol{n} \tag{3.20}$$

with $\tilde{\boldsymbol{r}}^M$ and $\tilde{\boldsymbol{r}}^d$ projections of $\boldsymbol{r}$ on the memory and dilatancy surfaces along the $-\boldsymbol{n}$ direction. When $\tilde{b}_d^M > 0$ the post-dilation contractancy produced by D in Eq. (3.6) is enhanced as follows:

$$D = \left[A_0 \exp\left(\beta \langle \tilde{b}_d^M \rangle / b_{ref}\right)\right] (\boldsymbol{r}_\theta^d - \boldsymbol{r}) : \boldsymbol{n} \tag{3.21}$$

where A_0 and β are two material parameters. In Eq. (3.21) the exponential term is deactivated by $\tilde{b}_d^M < 0$, that is when the image stress ratio $\tilde{\boldsymbol{r}}^M$ lies outside the dilatancy surface (i.e. after dilative deformation prior to load reversal). Conversely, additional contractancy arises in the opposite case $\tilde{b}_d^M > 0$ with $\tilde{\boldsymbol{r}}^M$ lying inside the memory surface. Compared to SANISAND04, the dilatancy coefficient accounts for fabric effects through the same memory locus employed to enhance the plastic modulus coefficient in Eq. (3.11).

3.4. Calibration of constitutive parameters

The new model requires the calibration of sixteen constitutive parameters, only one more than SANISAND04. Two subsets of parameters may be distinguished: the first includes material parameters already present in the original SANISAND04 formulation – namely, from G_0 to n^d in Table 3.2; the remaining parameters govern directly the (high-)cyclic performance under both drained and undrained loading. The calibration of material parameters is discussed hereafter with reference to the monotonic and cyclic laboratory tests performed by Wichtmann (2005) on a quartz sand – $D_{50} = 0.55$ mm, $D_{10} = 0.29$ mm, $C_u = D_{60}/D_{10} = 1.8$ (non-uniformity index), $e_{max} = 0.874$, $e_{min} = 0.577$. Numerical simulations are executed with yield and memory surfaces set to be initially coincident.

Table 3.2: Model parameters for the quartz sand tested by Wichtmann (2005)

Elasticity		Critical state					Yield
G_0	ν	M	c	λ_c	e_0	ξ	m
110	0.05	1.27	0.712	0.049	0.845	0.27	0.01
Plastic modulus		Dilatancy			Memory surface		
h_0	c_h	n^b	A_0	n^d	μ_0	ζ	β
5.95	1.01	2.0	1.06	1.17	260	0.0005	1

The calibration of the first subset against monotonic tests is based on the procedure detailed in Dafalias and Manzari (2004). The shear modulus G_0 can be derived from the small-strain branch of experimental stress-strain curves, or alternatively from well-established empirical relationships (e.g. Hardin and Black (1966)). A Poisson's ratio equal to 0.05 was assumed following the suggestion of Dafalias and Manzari (2004) for an open-wedge yield surface. The opening of yield surface $m = 0.01$ is also consistent with the SANISAND04 model. The parameters governing the shape of critical state line in the $e - \ln p$ plane (e_0, λ_c and ξ) and the critical state shear strength (M and c) have been identified by fitting both strength and volumetric strain trends at ultimate conditions for different void ratios and stress

levels, as illustrated in Figure 3.4 by means of deviatoric stress – axial strain ($q-\varepsilon_a$) and volumetric strain – axial strain ($\varepsilon_{vol}-\varepsilon_a$) plots. More details about the calibration of the remaining plastic modulus (h_0, c_h and n_b) and dilatancy (A_0 and n_d) parameters are available in Dafalias and Manzari (2004) and Taiebat and Dafalias (2008). Due to the limited availability of monotonic tests for the considered quartz sand, these parameters have been determined by fitting the available stress – strain ($q-\varepsilon_a$) and volumetric strain – axial strain ($\varepsilon_{vol}-\varepsilon_a$) trends as shown in Figure 3.4. All calibrated soil parameters are reported in Table 3.2.

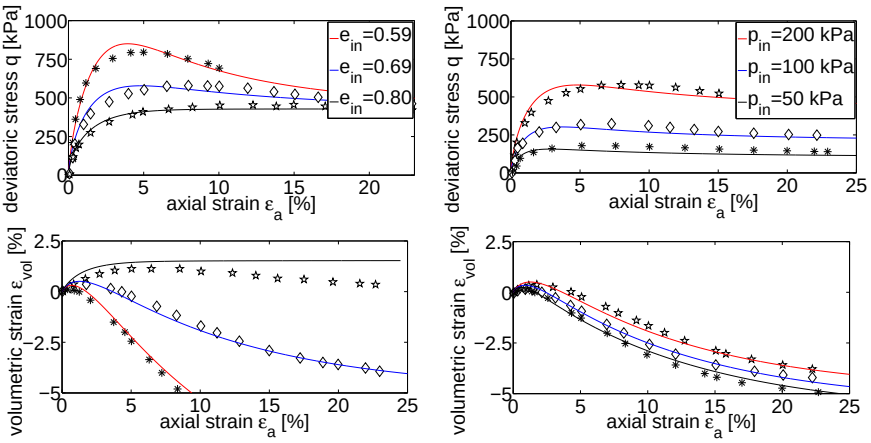

(a) constant p_{in} = 200 kPa, varying e_{in} (b) constant e_{in} = 0.69, varying p_{in}

Figure 3.4: Calibration of model parameters against the monotonic drained triaxial test results by Wichtmann (2005) – experimental data denoted by markers.

The new parameters linked to the proposed memory surface (μ_0, ζ and β) can be identified by best-fitting cyclic test results, possibly from both drained and undrained triaxial cyclic tests. Here, only the drained triaxial cyclic tests documented in Wichtmann (2005) are exploited for calibration purposes, while their impact on the undrained response is qualitatively discussed. In particular, Wichtmann's experiments concern one-way asymmetric cyclic loading performed in two stages (Figure 3.5): after the initial isotropic consolidation up to $p = p_{in}$, p-constant shearing is first performed to reach the target average stress ratio $\eta^{ave} = q^{ave}/p_{in}$; then, cyclic axial loading at constant radial stress is applied to obtain cyclic variations in deviatoric stress q about the average value q^{ave}, i.e. $q = q^{ave} \pm q^{ampl}$ (Figure 3.5b). High-cyclic sand parameters are tuned to match the evolution during regular cycles of the accumulated total strain norm ε^{acc} defined as:

$$\varepsilon^{acc} = \sqrt{\left(\varepsilon_a^{acc}\right)^2 + 2\left(\varepsilon_r^{acc}\right)^2} = \sqrt{\frac{1}{3}\left(\varepsilon_{vol}^{acc}\right)^2 + \frac{3}{2}\left(\varepsilon_q^{acc}\right)^2} \tag{3.22}$$

where ε_a^{acc}, ε_r^{acc}, ε_q^{acc} and ε_{vol}^{acc} stand for axial, radial, deviatoric and volumetric accumulated strain, respectively.

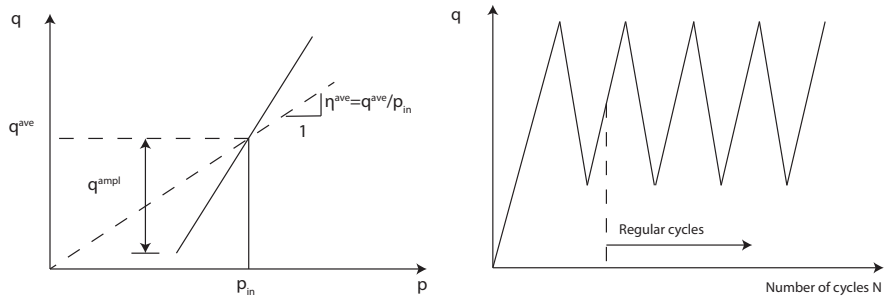

(a) stress path

(b) 'sawtooth' cyclic loading sequence

Figure 3.5: Stress paths and shear loading sequence in the tests considered for simulation (Wichtmann, 2005).

As illustrated in Figure 3.6, the ratcheting response of the soil under drained loading is governed by the μ_0 parameter in Eq. (3.11). Figure 3.6a proves the superior capability of the memory surface formulation to reproduce the transition from ratcheting to shakedown. The gradual sand stiffening occurs in combination with reduced plastic dissipation, as denoted by the decreasing area enclosed by subsequent stress-strain loops. The sensitivity of ε^{acc} to μ_0 is visualised in Figure 3.6b and exploited to reproduce the experimental data from Wichtmann (2005). μ_0 is in this case set to 260 by fitting the trend of ε^{acc} against the number of loading cycles.

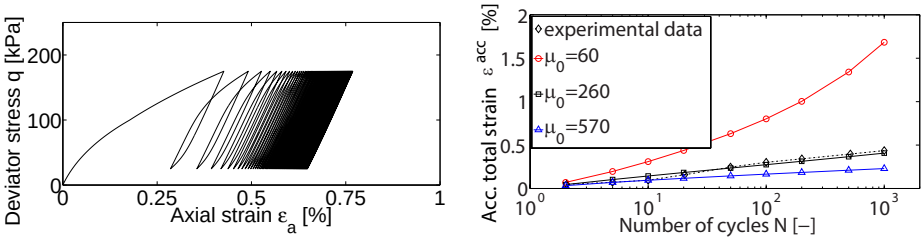

(a) Deviatoric stress- axial strain response predicted by the new model with $\mu_0 = 100$

(b) Influence of μ_0 on the accumulated total strain norm

Figure 3.6: Influence of μ_0 (Eq. (3.11)) on sand response. The comparison to the experimental data by Wichtmann (2005) refers to the following test/simulation settings: e_{in} = 0.702, q^{ampl} = 60 kPa, p_{in} = 200 kPa, η^{ave} = 0.75.

Dilative deformations tend to 'damage' the granular fabric and thus erase 'sand memory'. This granular process is phenomenologically reproduced by the shrinkage of the memory surface, at a rate governed by the parameter ζ in Eq. (3.16). However, the effect of ζ – only relevant to stress paths beyond the dilative threshold, Eq. (3.19) – is most apparent under undrained conditions: larger ζ values reduce the contraction rate of the memory surface and postpone the build-up of positive

pore pressure in the post-dilation unloading regime (Figure 3.7a). Under drained high-cyclic loading, increasing ζ still promotes the aforementioned memory surface contraction, and affects soil ratcheting in the dilative regime. For the quartz sand tested by Wichtmann (2005), a drained high-cyclic triaxial test with a stress path crossing the phase transformation line is selected for the calibration of the memory surface shrinkage parameter ζ. The influence of ζ on the accumulation of the total strain ε^{acc} in Eq. (3.22) is presented in Figure 3.7b. $\zeta = 0.0005$ has been selected to reproduce the results of high-cyclic drained tests mobilising sand dilation, – see Figure 3.7b.

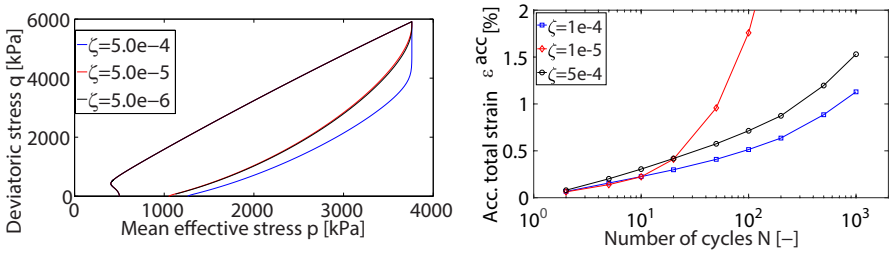

(a) Post-dilation undrained unloading response

(b) Drained high-cyclic strain accumulation

Figure 3.7: Influence of ζ (Eq. (3.16)) on sand response. Simulation settings: (a) p_{in}=500 kPa, e_{in} = 0.6, load reversal at ε_a = 0.07; (b) p_{in} = 200 kPa, η^{ave}=1.125, e_{in} = 0.68, q^{ampl} = 60 kPa.

The last parameter β appears in the new definition of the dilatancy coefficient D in Eq. (3.21), and mainly controls the post-dilation reduction of the mean effective stress in undrained tests. Larger β values allow for larger reductions in effective mean stress, possibly up to full liquefaction (Figure 3.8a). Since the considered set of drained test results does not support the calibration of β, $\beta = 1$ has been set judiciously with negligible influence on the strain accumulation predicted during drained cyclic tests (see Figure 3.8b). Although beyond the scope of this work on drained strain accumulation, the marked influence of β on the undrained response is briefly illustrated in Appendix A.

3.5. Model predictions of high-cyclic behaviour

This section overviews the predictive capability of the model against drained high-cyclic test results from the literature. The parameter set in Table 3.2 is used to simulate sand ratcheting under different cyclic loading conditions, namely triaxial and simple shear. All model results have been obtained via single-element FE simulations performed on the OpenSees simulation platform (Mazzoni et al., 2007). The new model with ratcheting control has been implemented starting from the existing open-source implementation of SANISAND04 developed at the University of Washington (Ghofrani and Arduino, 2018).

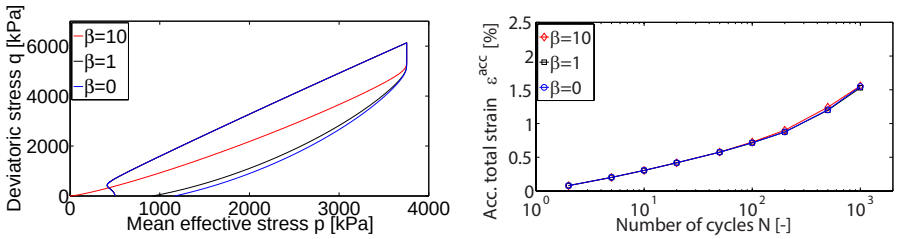

(a) Post-dilation undrained unloading response (b) Drained high-cyclic strain accumulation

Figure 3.8: Influence of β (Eq. (3.21)) on sand response. Simulation settings: (a) the quartz sand, p_{in}=500 kPa, e_{in} = 0.6, load reversal at ε_a = 0.07; (b) the quartz sand, p_{in}=200 kPa, η^{ave}=1.125, e_{in} = 0.68, q^{ampl} = 60 kPa.

3

3.5.1. Cyclic triaxial tests

This section considers triaxial test results from Wichtmann (2005), not previously used for parameter calibration. The experimental data concern the same quartz sand and both standard and non-standard triaxial loading.

Standard triaxial loading

The model is first validated against standard triaxial tests of the kind sketched in Figure 3.5, i.e. with constant radial stress during axial cyclic loading. The drained ratcheting response is predicted at varying p_{in}, e_{in}, η^{ave} and q^{ampl}. Importantly, a large number of cycles $N = 10^4$ is considered, and a very satisfactory agreement with experimental data is obtained in most cases.

Influence of initial confining pressure p_{in} The experimental data by Wichtmann (2005) show a quite low influence of p_{in} on the $\varepsilon^{acc} - N$ curves, especially for $N < 10^4$ (Figure 3.9a). This is clearly in contrast with what the new model predicts if no pressure-dependence is incorporated in the hardening coefficient h (Eq. (3.11)), i.e. if the exponent n of the p/p_{atm} factor is set to zero (Figure 3.9b). Conversely, the intrinsic pressure-dependence of SANISAND models can be counterbalanced through a pressure factor $(p/p_{atm})^n$ in h. To avoid a burst in the number of free parameters, a default exponent $n = 1/2$ is adopted, also in agreement with the pressure-dependence typically found for sand stiffness. The comparison between Figures 3.9a and 3.9c proves the quantitative suitability of Eq. (3.11).

Influence of initial void ratio e_{in} The experimental evidence from Wichtmann (2005) confirms the intuitive expectation of higher strain accumulation at increasing e_{in} (looser sand specimens). Figure 3.10 illustrates the potential of the new model to capture void ratio effects, though with slight overestimation of ε^{acc} for very dense and very loose specimens. It is worth recalling, however, that the parameters in Table 3.2 have been calibrated in an effort to capture relevant response features with a single set of parameters.

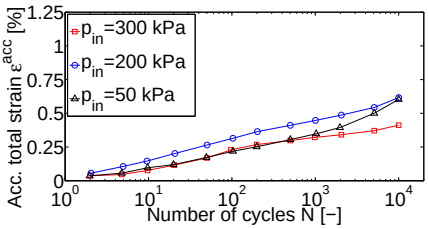

(a) Experimental data (Wichtmann, 2005)

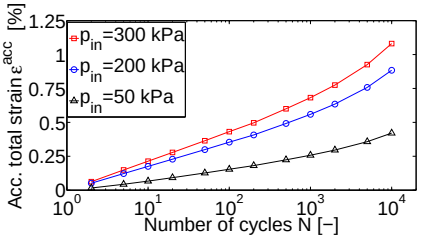

(b) Model simulations: $n = 0$

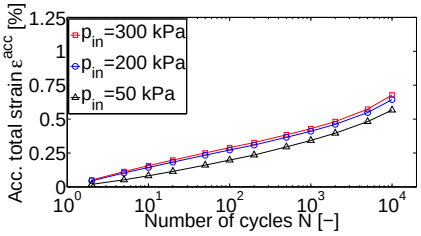

(c) Model simulations: $n = 1/2$

Figure 3.9: Influence of the initial mean pressure p_{in} on cyclic strain accumulation. Test/simulation settings: e_{in}=0.684, η^{ave}=0.75, stress amplitude ratio $\varsigma^{ampl} = q^{ampl}/p_{in}$=0.3.

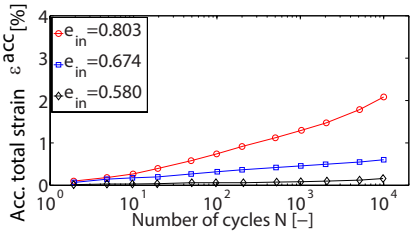

(a) Experimental data (Wichtmann, 2005)

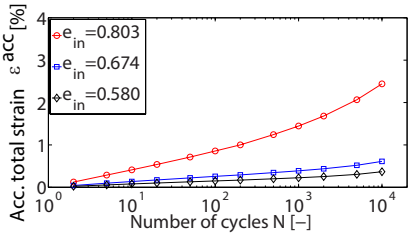

(b) Model simulations

Figure 3.10: Influence of the initial void ratio e_{in} on cyclic strain accumulation. Test/simulation settings: p_{in}= 200 kPa, η^{ave}= 0.75, q^{ampl}= 60 kPa.

Influence of cyclic stress amplitude q^{ampl} The experimental and numerical results in Figure 3.11 agree on the higher strain accumulation produced by increasing cyclic stress amplitude q^{ampl}. In particular, satisfactory model predictions are shown for medium-dense sand specimens associated with $e_{in} = 0.702$.

Influence of average stress ratio η^{ave} The dependence of sand ratcheting on the average stress obliquity about which stress cycles occur is extremely relevant to practical applications. Indeed, soil elements under/around a foundation experience cyclic loading starting from different stress obliquities, implying different distance from the value related to shear failure.

Figure 3.12 presents another set of experimental-numerical comparisons at

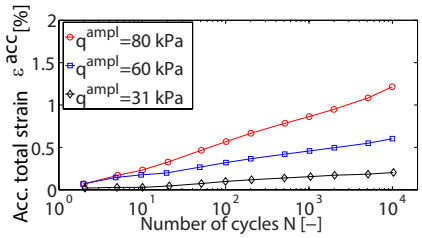

(a) Experimental data (Wichtmann, 2005)

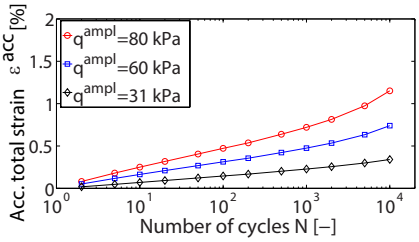

(b) Model simulations

Figure 3.11: Influence of the cyclic stress amplitude q^{ampl} on cyclic strain accumulation. Test/simulation settings: p_{in}= 200 kPa, η^{ave}= 0.75, e_{in}= 0.702.

varying average stress ratio η^{ave}. The model can reproduce the experimental increase in strain accumulation rate for larger η^{ave} values, although less accurately as $\eta^{ave} > 1$. Specifically, the simulation with $\eta^{ave} = 1.125$ overestimates ε^{acc} significantly when $N > 1000$: high-cyclic loading at large η^{ave} jeopardises the effectiveness of the memory surface concept, as the model tends again towards the SANISAND04 limit. While near-failure high-cyclic loading seems not too relevant to operational conditions in the field, some concerns could also be raised about the reliability of test measurements performed under such conditions, possibly due to strain localisation phenomena (Escribano et al., 2018).

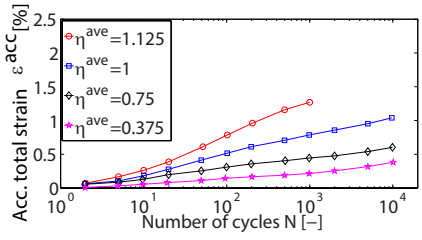

(a) Experimental data (Wichtmann, 2005)

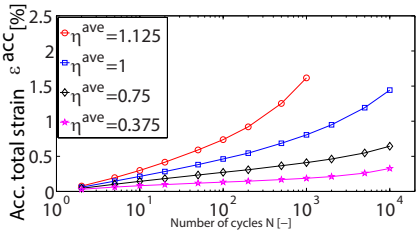

(b) Model simulations

Figure 3.12: Influence of the average stress ratio η^{ave} on cyclic strain accumulation. Test/simulation settings: p_{in}= 200 kPa, e_{in}= 0.684, q^{ampl}= 60 kPa.

Non-standard triaxial loading

Alternative triaxial loading conditions can be generated by varying both axial and radial stresses during the test. As discussed by Wichtmann (2005), this can produce 'polarised' stress-strain cyclic paths, which seem to enhance the tendency to strain accumulation. Unlike most modelling exercises, the model performance is here assessed also in relation to polarised triaxial loading. For this purpose, the following polarisation angle α_{PQ} and amplitude are first defined in the $Q - P$ plane (Figure

3.13) for direct comparison with Wichtmann's data:

$$\tan \alpha_{PQ} = \frac{Q^{ampl}}{P^{ampl}}$$
$$S^{ampl} = \sqrt{(P^{ampl})^2 + (Q^{ampl})^2} \tag{3.23}$$

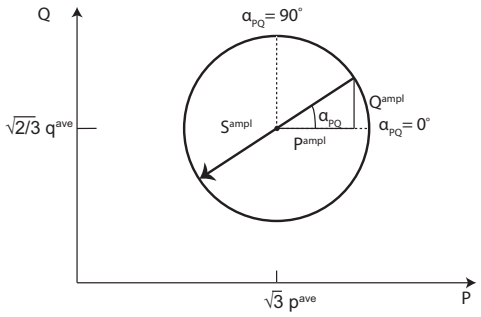

Figure 3.13: Non-standard triaxial stress paths in the $Q-P$ plane as defined by Wichtmann (2005).

where $Q = \sqrt{2/3}q$ and $P = \sqrt{3}p$ are isomorphic transformations of the stress invariants p and q, and the superscript ^{ampl} denotes cyclic variations about the initial values $p^{ave} \equiv p_{in}$ and q^{ave}.

The model response to non-standard triaxial loading is compared to Wichtmann et al.'s experimental data in Figure 3.14 at varying polarisation angle α_{PQ}, and Figure 3.15 at varying loading amplitude S^{ampl}. The results in Figure 3.14 span polarisation angles in the range from $0°$ to $90°$, and show very satisfactory $\varepsilon^{acc} - N$ trends in most cases. The only exception is the case $\alpha_{PQ} = 10°$, in which the model underpredicts the corresponding strain accumulation. This singular outcome is directly caused by the analytical expression (3.2) of the yield locus, conical and open-ended: in fact, triaxial stress paths at $\alpha_{PQ} = 10°$ happen to be mostly oriented along the uncapped zone of the elastic domain, resulting in underestimated plastic strains.

The effect of the cyclic stress amplitude S^{ampl} at a finite polarisation angle ($\alpha_{PQ} = 75°$) can be observed in Figure 3.15. Strain accumulation is accelerated by increasing S^{ampl}, as testified by simulation results in good agreement with all laboratory data.

Compliance with $\varepsilon_{vol}^{acc}/\varepsilon_q^{acc}$ ratio

While experimental and numerical results were compared above in terms of strain norm ε^{acc} (Eq. (3.22)), it is also interesting to inspect the accumulation of volumetric (ε_{vol}^{acc}) and deviatoric (ε_q^{acc}) strains individually – as exemplified in Figure 3.16. Based on experimental observations, Wichtmann (2005) concluded that the $\varepsilon_{vol}^{acc}/\varepsilon_q^{acc}$ ratio mainly depends on the average stress ratio η^{ave} held during

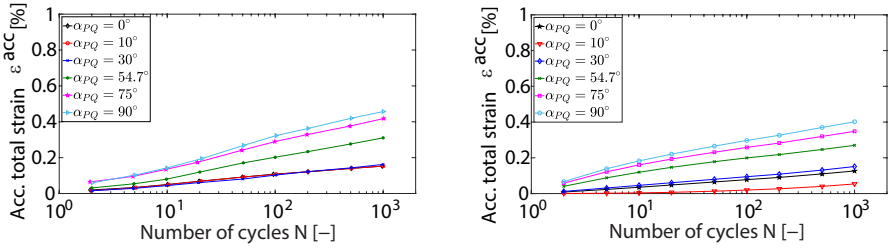

(a) Experimental data (Wichtmann, 2005) (b) Model simulations

Figure 3.14: Influence of the polarisation angle α_{PQ} on cyclic strain accumulation. Test/simulation settings: p_{in}= 200 kPa, e_{in}= 0.69, η^{ave}= 0.5, stress amplitude in the $Q-P$ plane S^{ampl}= 60 kPa.

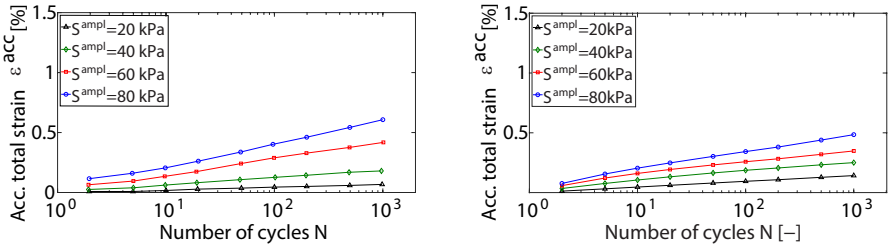

(a) Experimental data (Wichtmann, 2005) (b) Model simulations

Figure 3.15: Influence of the stress amplitude S^{ampl} in the $Q-P$ plane on cyclic strain accumulation. Test/simulation settings: p_{in}= 200 kPa, e_{in}= 0.69, η^{ave}= 0.5, α_{PQ} = 75°.

cyclic loading. Other factors like void ratio, confining pressure and stress amplitude seemed to play limited roles. The new model is found to reproduce such a ratio correctly in the medium/high strain range, although with an overall underestimation of ε_{vol}^{acc} (Figure 3.16 – note that the experimental and predicted trend lines become parallel for $\varepsilon_{q}^{acc} > 0.4$).

It is believed that these inaccuracies relate mostly to the assumed modelling of sand dilatancy, and future efforts will be spent to remedy this shortcoming. However, it is also worth reflecting here on the link between Wichtmann's results and other related published results. In particular, Narsilio and Santamarina (2008) postulated on an experimental basis the existence of a so-called 'terminal density', that is a state of constant void ratio and steady fabric – including critical state as a particular instance. Every sand appears to attain a specific terminal density depending on the initial, boundary and loading conditions (Narsilio and Santamarina, 2008; Chong and Santamarina, 2016), with a direct influence on the observed accumulation of all strain components (for a detailed investigation and simulation on this topic refer to Chapter 4). However, the experimental trend in Figure 3.16 from Wichtmann (2005) does not seem to evolve towards such a terminal state. Further studies about such a discrepancy and, more widely, about the existence and the

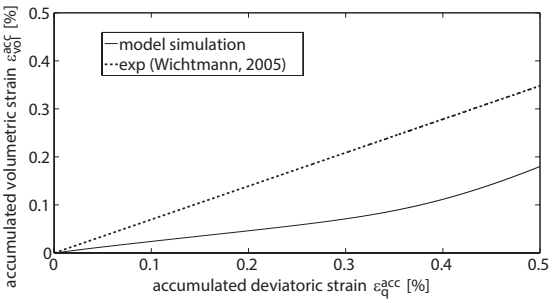

Figure 3.16: High-cyclic evolution of deviatoric and volumetric strain under drained triaxial loading. Test/simulation settings: p_{in}= 200 kPa, e_{in} = 0.7, η^{ave}= 0.75, q^{ampl} = 60 kPa, $N = 10^4$.

properties of terminal density loci will positively affect future modelling efforts on the high-cyclic response of soils.

3.5.2. Cyclic simple shear tests

Simple shear tests are also well-established in the geo-experimental practice, and allow the soil response to loading paths implying rotation of the principal stress axes to be explored. Simple shear loading closely represents conditions relevant to many soil sliding problems, e.g. in the triggering of landslides or in the mobilisation of the shaft capacity of piles.

The experimental work of Wichtmann (2005) also included high-cyclic simple shear tests on the same quartz sand previously tested in the triaxial apparatus – the validity of the same sand parameters in Table 3.2 can be thus assumed. Two types of cyclic simple shear tests were performed: (i) cyclic shear loading applied along a single direction; (ii) so-called cyclic multidimensional simple shear (CMDSS) tests, in which the direction of shear loading is shifted by $90°$ in the horizontal plane after, in this case, $N = 1000$ cycles. As all tests were performed by controlling the shear strain amplitude, the experimental results were visualised in terms of residual (volumetric) strain accumulation, the residual strain ε_{res}^{acc} in strain-controlled simple shear tests coincides with the permanent vertical strain:

$$\varepsilon_{res}^{acc} = \varepsilon_v^{acc} \tag{3.24}$$

where ε_v^{acc} stands for the accumulated vertical strain.

Experimental and numerical curves corresponding with cyclic shear strain amplitude $\gamma^{ampl} = 5.8{\times}10^{-3}$ are compared in Figure 3.17, where the dashed lines denote the shift in shear loading direction at $N = 1000$ – relevant to CMDSS tests. Despite unavoidable stress/strain inhomogeneities in simple shear experiments (Dounias and Potts, 1993), reasonably similar residual strain accumulations are displayed in Figures 3.17a–3.17b. The model is also able to capture the temporary increase in accumulation rate produced by the sudden change in shear loading direction.

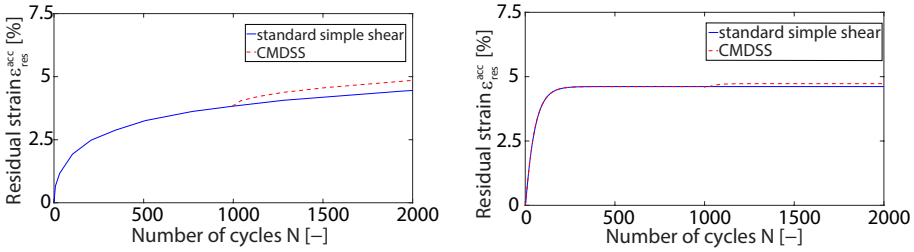

(a) Experimental results (b) Simulation results

Figure 3.17: Cyclic simple shear tests (single loading direction and CMDSS) – comparison between experimental results and model predictions. Test/simulation settings: σ_a= 24 kPa (initial vertical stress), e_{in}= 0.69, $\gamma^{ampl} = 5.8 \times 10^{-3}$.

3.5.3. Impact on undrained cyclic response

Table 3.3: Toyoura sand parameters shared by SANISAND04 and the new model – after tests by Ishihara et al. (1975)

Elasticity		Critical state				
G_0	ν	M	c	λ_c	e_0	ξ
120	0.05	1.25	0.712	0.019	0.934	0.7
Yield	Plastic modulus			Dilatancy		
m	h_0	c_h	n^b	A_0	n^d	
0.01	7.05	0.968	1.1	0.704	3.5	

While the main body of the chapter focused on the modelling and simulation of drained cyclic strain accumulation, some space is given here to preliminarily compare the proposed model and the parent SANISAND04 formulation in terms of undrained cyclic performance. For this purpose, the experimental results from Ishihara et al. (1975) are taken as a reference after Dafalias and Manzari (2004) – in particular, an undrained cyclic triaxial test performed on a Toyoura sand specimen at constant cell pressure $p_{in} = 294$ kPa, initial void ratio $e_{in} = 0.808$ and amplitude of applied deviatoric stress $q_{ampl} = 114.2$ kPa. The SANISAND04 parameters shared by the proposed model are reported in Table 3.3 as identified by Dafalias and Manzari (2004).

The comparison between experimental data and SANISAND04 simulation is reported in Figure 3.18a. The SANISAND04 model captures the cyclic decrease in effective mean stress, in a way positively affected by the enhanced post-dilation contractancy achieved through the fabric-tensor formulation. However, the model does not accurately predict the pore pressure build-up during each cycle and, in turn, the number of cycles required to reach the phase transformation line (PTL). Conversely, Figure 3.18b shows the improved performance of the proposed model, based on the memory surface concept combined with the new dilatancy coefficient defined in Eq. (3.21). The proposed model accounts for the gradual stiffening

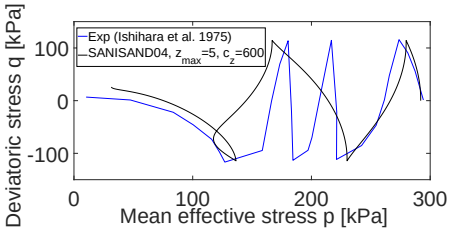

(a) Comparison between experimental result (Ishihara et al., 1975) and SANISAND04 simulation result (Dafalias and Manzari, 2004).

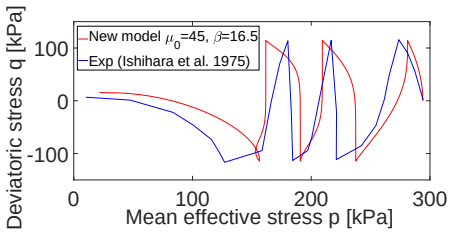

(b) Comparison between experimental result (Ishihara et al., 1975) and new model simulation result ($\mu_0 = 45$, $\zeta = 0.00001$, $\beta = 16.5$).

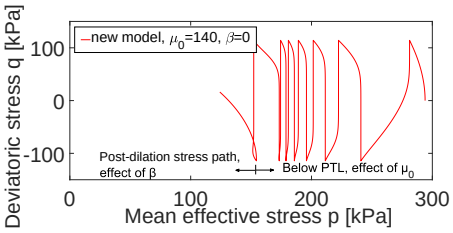

(c) Influence of μ_0 and β on the undrained performance of the new model ($\mu_0 = 140$, $\zeta = 0.00001$, $\beta = 0$).

Figure 3.18: Undrained cyclic behavior of Toyoura sand. Test/simulation settings: $p_{in} = 294$ kPa, $e_{in} = 0.808$, $q^{ampl} = 114.2$ kPa.

over consecutive cycles and predicts better the number of loading cycles to phase transformation. Comforting predictions are also obtained in terms of pore pressure vaules beyond phase transformation, along with the nearly nil effective mean stress reached upon unloading. Overall, the new memory-surface-based flow rule seems a promising alternative to the approach followed by Dafalias and Manzari (2004).

As highlighted in Figure 3.18c in comparison to Figure 3.18b, the proposed model offers higher flexibility in reproducing the undrained cyclic behaviour, depending on the set of cyclic parameters μ_0, ζ and β selected. In general, the initial pore pressure build-up prior to phase transformation can be controlled through the parameter μ_0; the post-dilation stress path is mainly governed by the parameter β, which affects indirectly the shrinkage of the memory surface – the larger β, the smaller the minimum effective stress reached upon post-dilation unloading.

3.6. Conclusions

The critical state, bounding surface SANISAND04 model has been endowed with an additional locus in the stress space (memory surface) to improve the simulation of high-cyclic sand ratcheting under a variety of initial, boundary and loading conditions. The constitutive equations, directly presented in a multi-axial framework, were implemented in the finite element code OpenSees, based on an existing open-source implementation of SANISAND04. Compared to previous formulations, the proposed model has proven more accurate in reproducing sand ratcheting under

various drained loading conditions, as well as potentially more flexible in terms of pore pressure build-up under undrained loading. Extensive validation against experimental results was performed with regard to triaxial (standard and non-standard) and simple shear drainded cyclic tests.

It is anticipated that deeper insight and more reliable empirical correlations may be obtained for a range of sandy materials. This will support the use of ratcheting models, both implicit and explicit, to compensate for the usual lack of specific data about strain accumulation trends.

4

SANISAND-MS: Oedometer Simulation of Terminal Densities

Parts of this chapter have been published in Géotechnique Letters (Liu and Pisanò, 2019).

4.1. Introduction

This chapter concerns the SANISAND-MS simulation of high-cyclic sand behavior under "zero lateral strain" (oedometer conditions). Cyclic oedometer-like loading is relevant to multiple soil-foundation interaction problems in offshore geotechnics – for instance regarding 'push-pull' mechanisms under multi-legged structures (Bienen et al., 2018; Pisanò et al., 2019), or vibratory pile driving (Galavi et al., 2017).

The SANISAND-MS model developed in Chapter 3 has proven capable of reproducing both quantitatively and quantitatively experimental data from drained high-cyclic tests. This chapter takes a step forward about the application of SANISAND-MS to high-cyclic problems. An opportunity for building further trust about the model has been recently offered by Chong and Santamarina (2016) and Park and Santamarina (2019), who published novel data concerning dry sand compaction in high-cyclic oedometer tests. This chapter aims to bring new evidence about the capabilities of SANISAND-MS, with emphasis on the prediction of 'terminal densities' (Narsilio and Santamarina, 2008) and associated stiffness evolution.

4.2. Modelling of cyclic oedometer tests – part I

Though cyclic oedometer test results are more rare in the literature, a recent instance is reported by Chong and Santamarina (2016) for three different sands (Ottawa F110 and Ottawa 50/70). The following simulations concern oedometer tests on Ottawa 50/70 specimens ($D_{10} = 0.26$ mm, $D_{50} = 0.33$ mm, $C_u = 1.43$, $e_{max} = 0.87$, $e_{min} = 0.55$) prepared at two different void ratios, $e_{in} = 0.765$ and $e_{in} = 0.645$. From a constitutive modelling standpoint, oedometer loading constrains the translation of the yield and memory surfaces in the deviatoric stress ratio plane, with the cylindrical symmetry imposing their evolution along the (projected) principal axis associated with the vertical stress component (Figure 4.1).

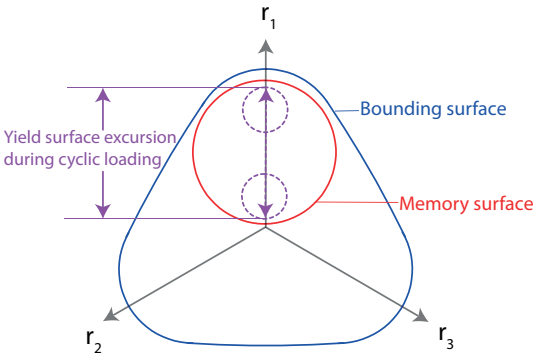

Figure 4.1: Translation of the yield and memory surface under oedometer loading.

Both loose and dense specimens were subjected to stages of monotonic-cyclic-monotonic loading, at either low or high vertical static stress (Figure 4.2a): (i) *low*

static load – monotonic compression up to 100 kPa → cyclic vertical loading in the range 200–100 kPa (100 cycles) → monotonic re-compression up to 1.4 MPa; (ii) *high static load*: monotonic compression up to 1 MPa → cyclic vertical loading in the range 1.1–1 MPa (100 cycles) → monotonic re-compression up to 1.4 MPa. The calibration of all SANISAND-MS parameters has been carried out as follows: first, the thirteen SANISAND04 parameters (from G_0 to n^d) have been identified based on drained monotonic triaxial tests on Ottawa sand from the literature (Lin et al., 2015); then, the oedometer high-cyclic response has been simulated by either (i) keeping the same (μ_0, ζ, β) set in Table 3.2 (Figure 4.2b), or adjusting the three parameters for best-fit purposes (Figure 4.2c). Experimental and numerical results are compared in Figure 4.2 in terms of void ratio vs vertical stress curves, for consistency with the original plots in Chong and Santamarina (2016).

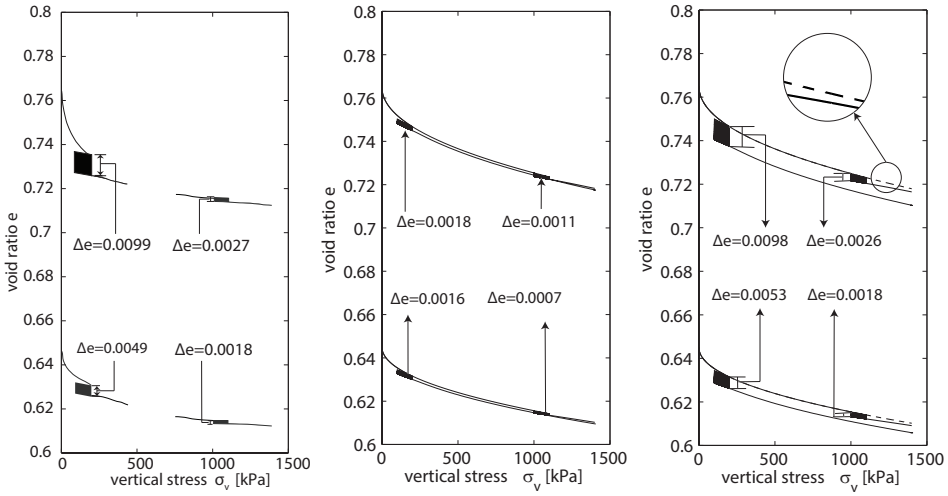

(a) Experimental data (Chong and Santamarina, 2016) (b) Model simulations – μ_0 and ζ from Table 3.2 (c) Model simulations – all parameters from Table 4.1

Figure 4.2: Cyclic oedometer tests – comparison between experimental results and model predictions.

Table 4.1: Model parameters for the Ottawa 50/70 sand tested by Chong and Santamarina (2016)

Elasticity		Critical state					Yield
G_0	ν	M	c	λ_c	e_0	ξ	m
90	0.05	1.28	0.8	0.012	0.898	0.7	0.01
Plastic modulus		Dilatancy		Memory surface			
h_0	c_h	n^b	A_0	n^d	μ_0	ζ	β
5.25	1.01	1.2	0.4	1.35	44	0.005	1

The void ratio vs vertical effective stress results in Figure 4.2 show that most experimental-numerical mismatch is produced during monotonic loading stages,

which a model with an open conical yield surface is not suited to reproduce accurately. As for cyclic compaction, the parameters calibrated from Wichtmann's tests tend to underpredict the reduction in void ratio. In contrast, satisfactory numerical results are displayed in Figure 4.2c after re-calibrating μ_0 and ζ as well (Table 4.1, same β). Two steps have been followed to re-calibrate μ_0 and ζ: (1) the loose specimen is selected to calibrate μ_0 parameter under the loading condition that cyclic vertical loading in the range 200–100 kPa, since under this condition the parameters ζ and β have no impact on the cyclic behaviour; (2) the dense sample under the same cyclic loading conditions is selected to calibrate ζ with the μ_0 determined in step (1). Other simulations have been conducted with the same parameters. Expectedly, the model captures two relevant aspects:

- at a given initial vertical stress, the looser sand compacts more than the dense sand; for a given initial void ratio, a higher initial compression level results in lower cyclic compaction;
- after cyclic loading, the void ratio evolves during re-compression towards the initial virgin compression line (Figure 4.2c).

It could also be shown that fully realistic values of the horizontal-to-vertical stress ratio are obtained, owing to the rotational mechanism of the narrow yield surface (and regardless of the low Poisson's ratio selected – Table 4.1). The predictions of the monotonic oedometer response could be improved by introducing a capped yield surface as proposed by Taiebat and Dafalias (2008).

4.3. Modelling of cyclic oedometer tests – part II

Following Chong and Santamarina (2016), Park and Santamarina (2019) further investigated the response of dry sand in high-cyclic oedometer tests. Vertical stress-strain loops and variations in void ratio were obtained for each test, along with bender element measurements of the shear wave velocity. Park and Santamarina's work revolves around the concept of 'terminal density', the asymptotic (terminal) void ratio (density) eventually approached by cyclically-loaded sands. In reflection of the initial fabric, sands evolve towards terminal densities depending mechanical properties, loading and boundary conditions (Lackenby et al., 2007; Narsilio and Santamarina, 2008). Before giving details of model simulation results, it is worth recalling the following features of Park and Santamarina's experimental programme – see Table 4.2:

- tests performed on Ottawa 20/30 sand with $D_{50} = 0.72$ mm, $e_{max} = 0.742$, $e_{min} = 0.502$, $G_s = 2.65$;
- four-stage loading sequence: (i) static compression up to σ_0, (ii) cyclic loading of amplitude $\Delta\sigma$ between σ_0 and $\sigma_0 + \Delta\sigma$, (iii) static compression to the maximum vertical stress $\sigma_{max} > \sigma_0 + \Delta\sigma$, (iv) unloading;
- 33 tests in total (including repetitions), with 11 different combinations of initial/loading conditions and number of cycles $N = 10^4$.

In Park and Santamarina (2019) and throughout this chapter, e_0 denotes the initial, 'pre-cyclic' void ratio at the beginning of cyclic loading.

Table 4.2: Test conditions in Park and Santamarina (2019) – D_{r0}: initial relative density, e_0: initial void ratio, σ_0: pre-cyclic vertical stress, $\Delta\sigma$: cyclic stress amplitude, $\Delta\sigma/\sigma_0$: cyclic stress amplitude ratio.

Test #	$D_{r0}[\%]$	e_0 [−]	$\sigma_0[kPa]$	$\Delta\sigma[kPa]$	$\Delta\sigma/\sigma_0$ [−]
1	30	0.6700	67	100	1.5
2	40	0.6460	174	138	0.8
3	40	0.6460	105	138	1.3
4	40	0.6460	105	276	2.7
5	40	0.6460	105	414	4
6	50	0.6220	67	100	1.5
7	70	0.5740	174	138	0.8
8	70	0.5740	105	138	1.3
9	70	0.5740	67	100	1.5
10	70	0.5740	105	276	2.7
11	70	0.5740	105	414	4

4.3.1. Parameter calibration for Ottawa 20/30 sand

Herein, all model parameters were identified following the procedure in Chapter 3. Table 4.3 reports the parameter set for Ottawa 20/30 sand, calibrated against different data sources. The calibration of critical-state-related parameters relies on

Table 4.3: Model parameters for the Ottawa 20/30 sand tested by Chong and Santamarina (2016)

Elasticity		Critical state					Yield
G_0	ν	M	c	λ_c	e_0	ξ	m
160	0.05	1.12	0.75	0.025	0.732	0.6	0.01
Plastic modulus		Dilatancy			Memory surface		
h_0	c_h	n^b	A_0	n^d	μ_0	ζ	β
4.8	1.2	2.68	0.71	1.2	200	0.005	0.5

the test results from Santamarina and Cho (2001) ('simple critical state tests'). The reference critical void ratio e_0 has been estimated as slightly smaller than e_{max} ($e_0 = 0.732$), while λ_c and ξ were obtained by fitting Eq. (3.3) to the critical state data from drained and undrained triaxial tests (Fig. 4.3). The test results from Lin et al. (2015) (in total, three drained monotonic triaxial tests) allowed the finial identification of the remaining monotonic parameters[1]. Model simulation and

[1]the three drained monotonic triaxial tests were performed under the same initial void ratio but different initial confining pressure. Herein, only these few triaxial data could be used for calibration purposes, and deemed sufficient owing to the (unusually) comprehensive critical state data. However, it is generally recommended to calibrate the model against monotonic test results for varying relative density and p_{in}, if available.

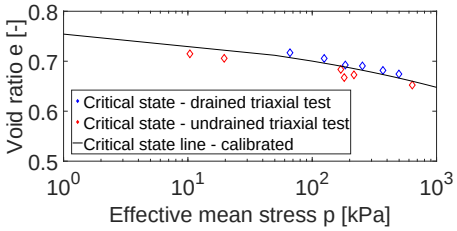

Figure 4.3: Calibration of model parameters for critcial state line against experimental results from Santamarina and Cho (2001).

experimental results are compared Fig. 4.4.

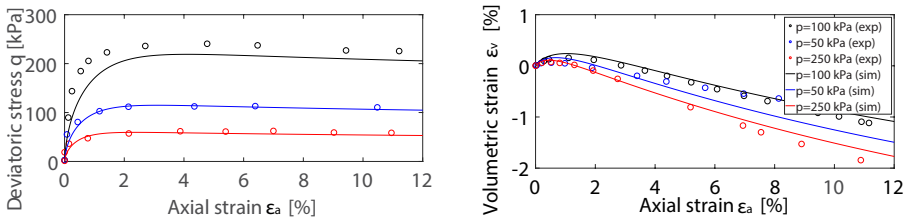

(a) $q - p$ response (b) $q - \varepsilon_a$ response

Figure 4.4: Calibration of monotonic model parameters against drained triaxial tests results from Lin et al. (2015). $e_{in} = 0.65$.

Only two tests out of Park and Santamarina's dataset have been employed to calibrate memory-related parameters – μ_0, ζ and β – in two steps:

1. high-cyclic loading ($N = 10^4$, $\sigma_0 = 105$ kPa, $\Delta\sigma = 138$ kPa) on a loose sample ($e_0 = 0.631$) has been first considered to identify μ_0 far from dilatancy effects (i.e. with negligible influence of ζ and β). Setting $\mu_0 = 200$ allowed simulation of the same cyclic reduction in void ratio e as measured experimentally – see Figures 4.5a-4.5c;

2. with the same μ_0, the (ζ, β) pair has been calibrated by fitting the response of a denser sample ($e_0 = 0.534$) to the same loading programme – see Figures 4.5d-4.5f.

An iterative procedure has been followed to transit from an assumed initial void ratio e_{in} to the target pre-cyclic value e_0 – in order to eliminate possible inaccuracies emerging from monotonic oedometer loading. This procedure enabled the pre-cyclic initialisation of all hardening variables, and to final identification of μ_0-ζ-β values in good agreement with those calibrated in Liu et al. (2019) for the quartz sand tested by Wichtmann (2005). Figures 4.5c and 4.5f give insight into the stress mechanism underlying the simulated responses. $q - p$ stress paths indicate that, after the monotonic stage, the stress ratio q/p evolves in response to

cyclic compression, which induces variations in mean radial stress compliant with compatibility requirements (no lateral strain). This process approaches a steady state along with the memory surface size m^M (Eq. (3.16)), and determines the final terminal density.

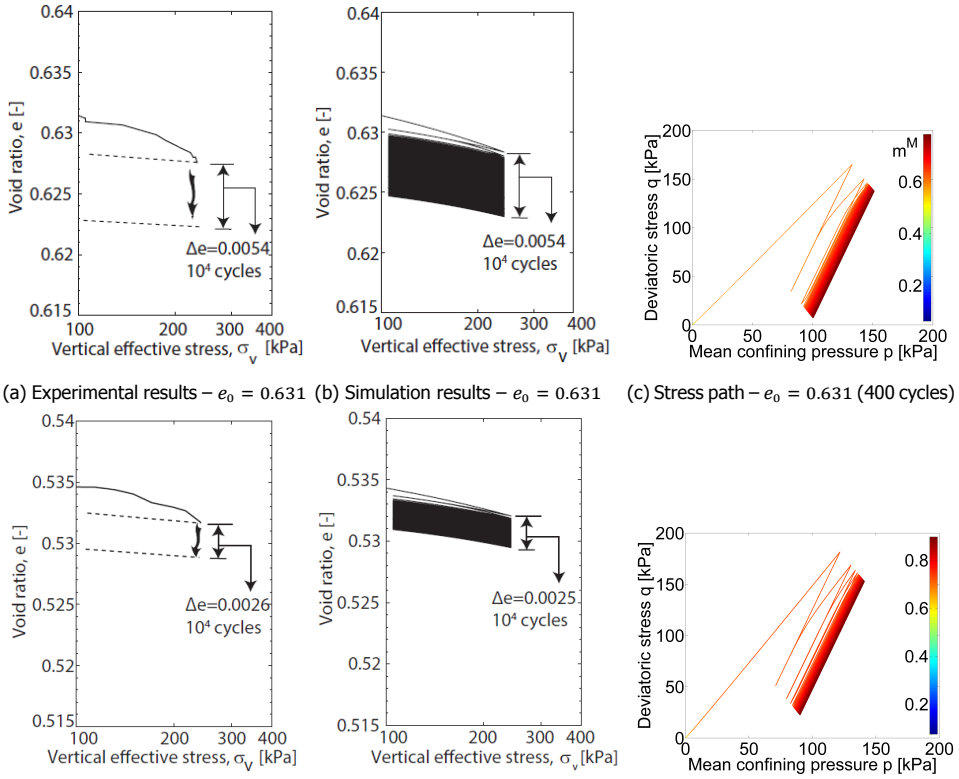

(a) Experimental results – $e_0 = 0.631$ (b) Simulation results – $e_0 = 0.631$ (c) Stress path – $e_0 = 0.631$ (400 cycles)

(d) Experimental results – $e_0 = 0.534$ (e) Simulation results – $e_0 = 0.534$ (f) Stress path – $e_0 = 0.534$ (400 cycles)

Figure 4.5: Comparison between Park and Santamarina's data and model simulations in terms of cyclic compaction for a loose and a dense sand sample. Oedometer test conditions: $\sigma_0 = 105$ kPa, $\Delta\sigma = 138$ kPa, $N = 10^4$.

4.3.2. Empirical compaction trends

Terminal density (terminal void ratio) can be assessed based on the following empirical relationship by Park and Santamarina (2019):

$$e_i = e_T + (e_1 - e_T)\left[1 + \left(\frac{i-1}{N^*}\right)^m\right]^{-1} \tag{4.1}$$

For oedometer high-cyclic conditions, Eq. (4.1) estimates the void ratio e_i at the i^{th} cycle as a function of:

(i) the terminal void ratio e_T ($e_i \to e_T$ as $i \to \infty$);

(ii) the characteristic number of cycles N^*, related to the number of cycles $1+N^*$ needed for half of the total compaction $(e_1 - e_T)/2$ to occur;

(iii) the empirical exponent m in the order of $m = 0.45 \pm 0.05$ (Park and Santamarina, 2019).

Park and Santamarina (2019) fitted experimental compaction trends by identifying N^* in Eq. (4.1), so as to predict e_T if reached with $N > 10^4$. For comparison, the same has been done for simulated compaction trend, as shown in Figure 4.6 with respect to the same tests in Figure 4.5.

Numerical cyclic responses (grey lines) are plotted along with the associated upper/lower bounding curves obtained through Eq. (4.1) (red lines), as well as with the curves identified by Park and Santamarina (2019) as experimental bounds (black lines). The asymptotic evolution of m^M towards terminal density is confirmed by the same plots. Further parametric studies (not reported for brevity) also confirmed the robustness of the model in terms of input-output relationship: small variations/uncertainties in high-cyclic parameters (mainly μ_0 and β) result in only slightly different terminal densities.

Table 4.4: Estimated terminal density e_T and characteristic number of cycles N^* based on Park and Santamarina's experimental results and model simulations in Figure 4.5.

	bound	$D_{i=0}$	m	N^*	e_T
Exp	upper	44%	0.4	350	0.6213
		86%		200	0.5288
	lower	44%		200	0.6209
		86%		200	0.5284
Sim	upper	44%	0.45	794	0.6227
		86%		631	0.5303
	lower	44%		1291	0.6208
		86%		1111	0.5287

Despite some differences in terms of identified (N^*, m) pairs, experiment-based and simulation-based bounding curves provide consistent estimates of the terminal void ratio e_T – see Figure 4.6 and Table 4.4. SANISAND-MS can thus predict high-cyclic compaction reliably, and in turn e_T through Eq. (4.1) for $N \to \infty$.

4.3.3. Model prediction of terminal densities

The model performance resulting from the parameters in Table 4.3 is now evaluated against the whole set of Park and Santamarina's test results. Simulations were performed for the eleven cases in Table 4.2, spanning different relative densities ($30\% < D_r < 70\%$) and cyclic stress amplitude ratios ($0.8 < \Delta\sigma/\sigma_0 < 4$). In all cases the lower bounds of the numerical $e - N$ compaction curves were identified by setting $m = 0.45$ in Eq. (4.1) and searching suitable N^* values. The obtained bounding curves were then used to infer e_T for $N \to \infty$ and compare to experimental results.

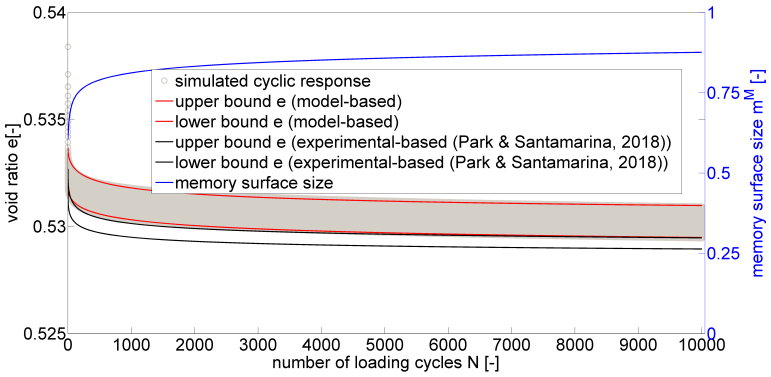

(a) Pre-cyclic void ratio $e_0 = 0.631$

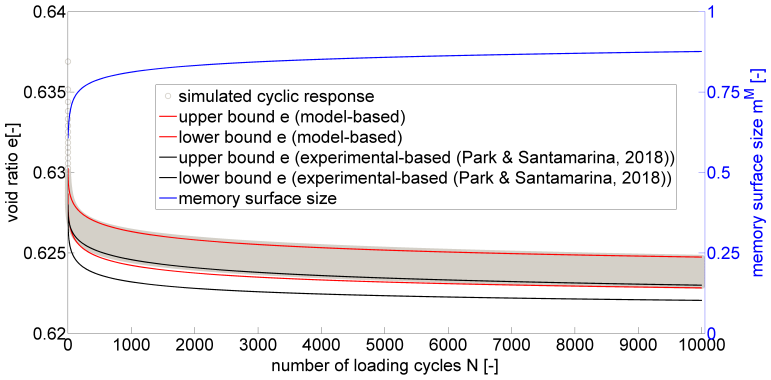

(b) Pre-cyclic void ratio $e_0 = 0.534$

Figure 4.6: Void ratio evolution over $N = 10^4$ loading cycles for loose and dense sand samples (Park and Santamarina, 2019) – pre-cyclic vertical stress $\sigma_0 = 105$ kPa, cyclic stress amplitude $\Delta\sigma = 138$ kPa.

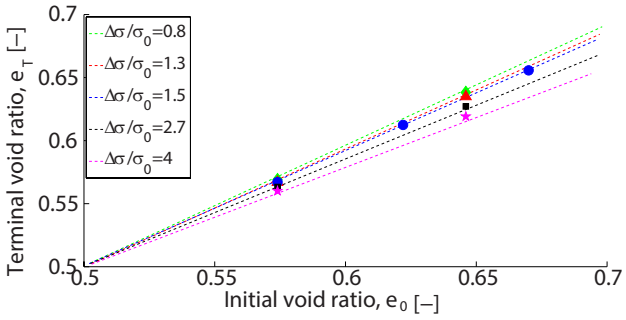

Figure 4.7: Relation between terminal and initial void ratios for different cyclic stress ratios – dash lines: interpolation of Park and Santamarina's data; markers: model simulations; same colours assigned to related dash lines and markers.

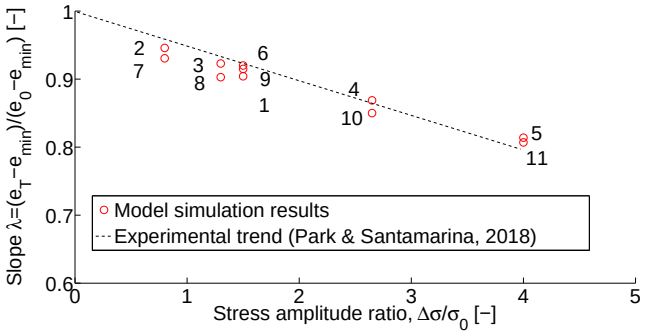

Figure 4.8: Dimensionless volume contraction $D.V.C$ against cyclic stress amplitude ratio $\Delta\sigma/\sigma_0$. Numbering of simulation points refers to test numbers in Table 4.2.

In Figure 4.7 experimental and numerical findings are compared in terms of the relation between terminal (e_T) and initial void (e_0) ratios at varying $\Delta\sigma/\sigma_0$. Simulation results confirm experimental evidence: (i) at given e_0, e_T tends to decrease for higher $\Delta\sigma/\sigma_0$; (ii) lowest initial e_0 values lead to lowest e_T at given $\Delta\sigma/\sigma_0$. Although sands evolve towards different fabric configurations depending on properties and loading, the memory of the initial state will not be erased (López-Querol and Coop, 2012; Park and Santamarina, 2019). Park and Santamarina (2019) also post-processed their data in terms of dimensionless volume contraction $D.V.C.$[2]:

$$D.V.C. = \frac{e_T - e_{min}}{e_0 - e_{min}} \tag{4.2}$$

which is found to depend linearly on $\Delta\sigma/\sigma_0$. The same empirical trend emerges also from the model predictions in Figure 4.8.

Additionally, Park and Santamarina (2019) inspected experimental compaction trends in terms of maximum/terminal variations in relative density (ΔD_T):

$$\Delta D_T = \frac{e_0 - e_T}{e_{max} - e_{min}} \tag{4.3}$$

and recognised a dependence on the cyclic stress amplitude ratio of the following kind ($D_{i=0}$ represents in Eq. (4.4) the pre-cyclic relative density):

$$\Delta D_T = \frac{(\Delta\sigma/\sigma_0)(1 - D_{i=0})^n}{B} \tag{4.4}$$

with $B \approx 20 \sim 25$ and $n = 0.7$ estimated parameters for Ottawa 20/30 sand. Model predictions of ΔD_T for all eleven scenarios (Table 4.2) are compared to experimental trends in Figure 4.9. The memory-enhanced model predicts with reasonable accuracy the non-linear $\Delta D_T - D_{i=0}$ relationship for the all considered cyclic stress ratios.

[2]Indicated as λ in Park and Santamarina (2019).

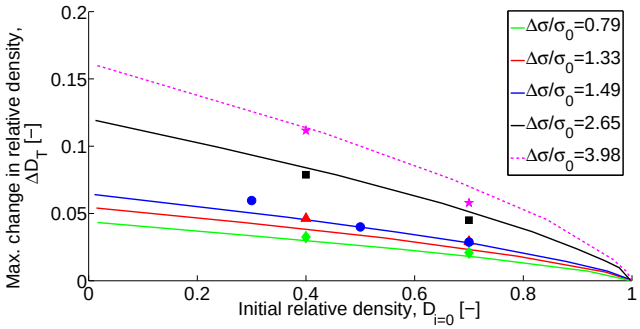

Figure 4.9: Maximum changes in relative density ΔD_T against initial/pre-cyclic values $D_{i=0}$ – dash lines: interpolation of Park and Santamarina's data; markers: model simulations; same colours assigned to related dash lines and markers.

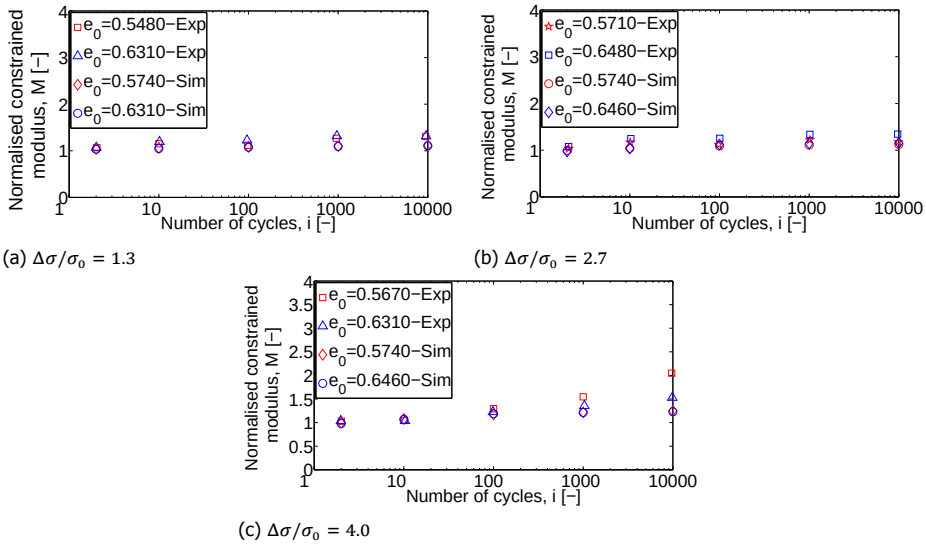

(a) $\Delta\sigma/\sigma_0 = 1.3$ (b) $\Delta\sigma/\sigma_0 = 2.7$

(c) $\Delta\sigma/\sigma_0 = 4.0$

Figure 4.10: Dependence of the normalised constrained modulus M on the number of cycles N. Considered stress stress amplitude ratios: (a) $\Delta\sigma/\sigma_0 = 1.3$; (b) $\Delta\sigma/\sigma_0 = 2.7$; (c) $\Delta\sigma/\sigma_0 = 4.0$.

4.3.4. Evolution of constrained modulus

Park and Santamarina (2019) found an empirical correlation between the shear wave velocity V_s and the 1D constrained modulus M^{oed}:

$$M_i^{oed} = \frac{\Delta\sigma}{\Delta\varepsilon_i^{pp}} \tag{4.5}$$

In Eq. (4.5) $\Delta\varepsilon_i^{pp}$ denotes the peak-to-peak amplitude of the i^{th} vertical strain loop.

In Figure 4.10 experimental and numerical results are compared in terms of constrained modulus normalised with respect to its first cycle value, i.e. $M_i =$

M_i^{oed}/M_1^{oed} – plots relate to both dense and loose samples subjected to $\Delta\sigma/\sigma_0$ equal to 1.3 (Figure 4.10a), 2.7 (Figure 4.10b) and 4 (Figure 4.10c). Both experiments and simulations confirm the expected increase in M^{oed} due to high-cyclic densification.

4.4. Concluding remarks

The results from recent experimental and modelling works have been compared in terms of high-cyclic sand response under 1D oedometer compression. The adopted SANISAND-MS model, based on memory-enhanced bounding surface plasticity, has proven able to predict cyclic oedometer compaction over a wide range of initial/boundary conditions. Terminal void densities have been well captured in all cases, with sound dependencies on the factors taken into account.

This chapter has gathered new evidence regarding the suitability of combining memory and bounding surface frameworks for high-cyclic geotechnical problems. Building trust about such modelling tools helps the transition towards constitutive models used in support of expensive experimental programmes when empirical cyclic strain accumulation laws are demanded.

5

SANISAND-MS: Improvement of Undrained Cyclic Performance

The contents of this chapter have been published in the JGGE (Liu et al., 2020a).

5.1. Introduction

In the past decades, a plethora of constitutive models – from very simple to highly sophisticated – have been proposed to reproduce the undrained cyclic behaviour of soils. The case of sandy soils attracted particular attention after catastrophic geotechnical failures during seismic events (Ishihara, 1993). Special mention in this context goes to the SANISAND04 model proposed by Dafalias and Manzari (2004), built on Manzari and Dafalias (1997) and ancestor of several later formulations (Zhang and Wang, 2012; Boulanger and Ziotopoulou, 2013; Dafalias and Taiebat, 2016; Petalas et al., 2019). Among these models, the PM4Sand model (Boulanger and Ziotopoulou, 2013; Ziotopoulou and Boulanger, 2016) possesses remarkable capabilities to reproduce undrained cyclic behaviour, including the simulation of pore pressure build-up, liquefaction triggering and, in medium-dense/dense sands, 'cyclic mobility' (Elgamal et al., 2003) – in turn associated with transient regains in shear resistance, and gradual shear strain accumulation at vanishing confinement. Cyclic mobility is relevant to the serviceability of earth structures and foundations under prolonged cyclic loading (Ziotopoulou and Boulanger, 2016), as well as to seismic site response (Roten et al., 2013).

In Chapter 3 and Liu et al. (2019), the SANISAND-MS model has been introduced to better account for fabric-related effects and their impact on cyclic ratcheting behaviour (Houlsby et al., 2017). The model can predict variations in soil stiffness and strain accumulation under thousands of drained loading cycles (high-cyclic loading). The same modelling features also allow better simulation of the undrained hydro-mechanical response, especially in terms of extent and timing of cyclic pore pressure accumulation (Liu et al., 2018). It has been noted, however, that further improvements are needed to unify the simulation of undrained cyclic behaviour over a wide range of initial sand densities and loading conditions.

This chapter takes further the achievements presented in Chapter 3, with reference to undrained cyclic loading. Besides the ability of capturing liquefaction triggering, the emphasis of what follows lies on the following aspects: (i) cyclic pore pressure build-up, including its cycle-by-cycle timing in the pre-liquefaction stage; (ii) stress-strain response in the post-liquefaction phase (cyclic mobility behaviour); and (iii) influence of previous loading history on the undrained cyclic response. These objectives are accomplished without compromising the previous achievements of the original model presented in Chapter 3 - 4. The performance of the upgraded SANISAND-MS formulation is inspected in detail, and thoroughly validated against the experimental datasets from Wichtmann (2005) and Wichtmann and Triantafyllidis (2016) – including undrained cyclic triaxial tests on both isotropically and anisotropically consolidated sand specimens. The present research is largely motivated by current offshore wind developments, where the need for advanced analysis of cyclic soil-foundation interaction is particularly felt.

5.2. Upgraded SANISAND-MS formulation

The upgraded SANISAND-MS formulation builds on most of the constitutive equations provided in Chapter 3. In contrast to the equation set given in Chapter 3, the

model formulation is based here on the use of the back stress variable, with minor influence on model implementation and calibration – see discussion in Section 3.3.1 and Appendix B. For brevity, Table Table 5.1 reports the whole set of (previous and new) constitutive equations, while the following focuses on defining and discussing new model features. New relationships for memory surface evolution, plastic flow rules and hardening laws are presented in this section. The new model ingredients do not affect the capabilities of the previous formulation, but do influence the calibration of certain cyclic parameters. Calibration and role of newly defined parameters are discussed in what follows. Ideally, four extra-tests would be needed for their calibration, including stress-controlled undrained cyclic triaxial tests at different relative densities and cyclic stress ratios. Nevertheless, the upgraded model can be reduced to a 'lighter' version whenever convenient.

The implications of the mentioned improvements are elucidated by comparing previous and updated SANISAND-MS simulations of triaxial test results from Wichtmann and Triantafyllidis (2016). The reference cyclic undrained tests were performed on Karlsruhe fine sand ($D_{50} = 0.14mm$, $C_u = D_{60}/D_{10} = 1.5$, $e_{max} = 1.054$, $e_{min} = 0.677$). Simulations of the previous SANISAND-MS model are related to the soil parameters given in Table 5.2 from Liu et al. (2018).

Memory surface and its evolution

The memory surface (f^M) tracks stress states already experienced by the sand during its (cyclic) loading history. It accounts for fabric changes and load-induced anisotropy via the evolution of its size (m^M) and back-stress ratio ($\boldsymbol{\alpha}^M$) (Corti et al., 2016; Liu and Pisanò, 2019). The expansion of the memory surface (i.e., increase in m^M) corresponds to the experimental observation of sand becoming stiffer as fabric is reinforced by cycling within the 'non-virgin' domain. On the other hand, the occurrence of dilation causes loss of sand stiffness (Nemat-Nasser and Tobita, 1982), which can be reproduced by the model through a decrease in m^M. This experimental evidence led to postulate a parallel shrinking mechanism for the memory surface, so that the change in memory surface size (dm^M) is decomposed into two terms: a memory surface expansion term dm_+^M and a memory surface contraction term dm_-^M :

$$dm^M = dm_+^M + dm_-^M \tag{5.1}$$

Enforcing plastic consistency under virgin loading in the contractive regime allows the derivation of the (positive) expansion rate dm_+^M:

$$dm_+^M = \sqrt{3/2} d\boldsymbol{\alpha}^M : \boldsymbol{n} \tag{5.2}$$

As discussed in Chapter 3, variations in size and location of the memory surface are inter-related. $d\boldsymbol{\alpha}^M$ describes the translation of the memory surface centre, assumed to take place along the direction of $\boldsymbol{\alpha}^b - \boldsymbol{r}_\alpha^M$:

$$d\boldsymbol{\alpha}^M = 2/3\langle L \rangle h^M (\boldsymbol{\alpha}^b - \boldsymbol{r}_\alpha^M) \tag{5.3}$$

in which $\boldsymbol{\alpha}^b$ is the bounding back-stress ratio and $\boldsymbol{r}_\alpha^M = \boldsymbol{\alpha}^M + \sqrt{2/3}(m^M - m)\boldsymbol{n}$. h^M, as stated in Chapter 3, is the counterpart of the hardening coefficient defined with respect to the memory surface — its updated expression is specified later on.

Table 5.1: Upgraded SANISAND-MS constitutive equations.

	Constitutive equations	**Material parameters**
Elasticity	$G = G_0 p_{atm}(2.97 - e)^2/(1+e)\sqrt{p/p_{atm}}$ $K = 2(1+\nu)G/[3(1-2\nu)]$	G_0 dimensionless shear modulus ν Poisson ratio
Critical state line	$e_c = e_0 - \lambda_c(p_c/p_{atm})^{\xi}$	e_0 reference critical void ratio λ_c, ξ CSL shape parameters
Yield surface	$f = \sqrt{(\boldsymbol{s} - p\boldsymbol{\alpha}) : (\boldsymbol{s} - p\boldsymbol{\alpha})} - \sqrt{2/3}pm$	m yield locus opening parameter
Memory surface	$f^M = \sqrt{(\boldsymbol{s} - p\boldsymbol{\alpha}^M) : (\boldsymbol{s} - p\boldsymbol{\alpha}^M)} - \sqrt{2/3}pm^M$	
Plastic hardening	$d\boldsymbol{\alpha} = (2/3)\langle L\rangle h(\boldsymbol{\alpha}^b - \boldsymbol{\alpha})$ $\boldsymbol{\alpha}^b = \sqrt{2/3}\left[g(\theta)M\exp(-n^b\Psi) - m\right]\boldsymbol{n}$ $g(\theta) = 2c/[(1+c) - (1-c)\cos 3\theta]$ $L = (1/K_p)\partial f/\partial\boldsymbol{\sigma} : d\boldsymbol{\sigma}$ $K_p = (2/3)ph(\boldsymbol{\alpha}^b - \boldsymbol{\alpha}) : \boldsymbol{n}$ $\boldsymbol{n} = (\boldsymbol{r} - \boldsymbol{\alpha})/\sqrt{2/3}m$ $\Psi = e - e_c$ $h = \dfrac{b_0}{(\boldsymbol{\alpha} - \boldsymbol{\alpha}_{in}) : \boldsymbol{n}}\exp\left[\mu_0\left(\dfrac{p}{p_{atm}}\right)^{0.5}\left(\dfrac{b^M}{b_{ref}}\right)^{w_1}\dfrac{1}{\eta^{w_2}}\right]$ $b_0 = G_0 h_0(1 - c_h e)/\sqrt{p/p_{atm}}$ $b^M = (\boldsymbol{r}_\alpha^M - \boldsymbol{\alpha}) : \boldsymbol{n}$ $b_{ref} = (\boldsymbol{\alpha}^b - \tilde{\boldsymbol{\alpha}}^b) : \boldsymbol{n}$ $\tilde{\boldsymbol{\alpha}}^b = -\sqrt{2/3}[g(\theta+\pi)M\exp(-n^b\Psi) - m]\boldsymbol{n}$ $\boldsymbol{r}_\alpha^M = \boldsymbol{\alpha}^M + \sqrt{2/3}(m^M - m)\boldsymbol{n}$	n^b bounding surface evolution parameter M critical stress ratio c extension-to-compression strength ratio μ_0, w_1 memory-hardening parameters w_2 cyclic stress ratio parameter h_0, c_h hardening parameters
Memory surface evolution	$dm^M = dm_+^M + dm_-^M$ $dm_+^M = \sqrt{3/2}d\boldsymbol{\alpha}^M : \boldsymbol{n}$ $dm_-^M = -(m^M/\zeta)f_{shr}\langle b_r^b\rangle m_+^M\langle -d\varepsilon_{vol}^p\rangle$ $F = \ln[1 + \lvert m_-^M\rvert/(\lvert m_-^M\rvert + \lvert m_+^M\rvert)^{0.5}]$ $b_r^b = (\boldsymbol{\alpha}^b - \boldsymbol{\alpha}) : \boldsymbol{n}$ $d\boldsymbol{\alpha}^M = (2/3)\langle L^M\rangle h^M(\boldsymbol{\alpha}^b - \boldsymbol{r}_\alpha^M)$ $h^M = \dfrac{1}{2}\left[\dfrac{b_0}{(\boldsymbol{r}_\alpha^M - \boldsymbol{\alpha}_{in}) : \boldsymbol{n}} + \sqrt{\dfrac{3}{2}}\dfrac{m^M m_+^M\langle b_r^b\rangle f_{shr}\langle -D\rangle}{\zeta(\boldsymbol{\alpha}^b - \boldsymbol{r}_\alpha^M) : \boldsymbol{n}}\right]$	ζ memory surface shrinkage parameter
Deviatoric plastic flow	$d\boldsymbol{e}^p = \langle L\rangle\boldsymbol{R}' = \langle L\rangle\{B\boldsymbol{n} - C\left[\boldsymbol{n}^2 - (1/3)\boldsymbol{I}\right]\}$ $B = 1 + 3(1-c)/(2c)\mathrm{g}(\theta)\cos 3\theta$ $C = 3\sqrt{3/2}(1-c)/cg(\theta)$	
Volumetric plastic flow	$d\varepsilon_{vol}^p = \langle L\rangle D$ $d = (\boldsymbol{\alpha}^d - \boldsymbol{\alpha}) : \boldsymbol{n}$ $D = A_d d$ $A_d = A_0$ (for $d \geq 0$ and $\tilde{b}_d^M \leq 0$) $A_d = A_0\exp\left[\beta_1 F\left(\dfrac{p}{p_{max}}\right)^{0.5}\right]g^k(\theta)$ (for $d \geq 0$ and $\tilde{b}_d^M > 0$) $A_d = A_0\exp\left[\beta_2 F\left(1 - \left(\dfrac{p}{p_{max}}\right)^{0.5}\right)\dfrac{d}{\lvert\lvert\boldsymbol{\alpha}^c\rvert\rvert}\right]\dfrac{1}{g(\theta)}$ (for $d < 0$) $\boldsymbol{\alpha}^c = \sqrt{2/3}(g(\theta)M - m)\boldsymbol{n}$ $\boldsymbol{\alpha}^d = \sqrt{2/3}\left[g(\theta)M\exp(n^d\Psi) - m\right]\boldsymbol{n}$ $\tilde{b}_d^M = (\tilde{\boldsymbol{\alpha}}^d - \tilde{\boldsymbol{r}}_\alpha^M) : \boldsymbol{n}$ $\tilde{\boldsymbol{\alpha}}^d = -\sqrt{2/3}\left[g(\theta+\pi)M\exp(n^d\Psi) - m\right]\boldsymbol{n}$	A_0 'intrinsic' dilatancy parameter β_1 dilatancy parameter k dilatancy parameter β_2 dilatancy parameter n^d dilatancy surface evolution parameter

Table 5.2: Parameters of original SANISAND-MS model in Chapter 3 for the Karlsruhe fine sand tested by Wichtmann and Triantafyllidis (2016)

Elasticity		**Critical state**					**Yield**
G_0	ν	M	c	λ_c	e_0	ξ	m
95	0.05	1.35	0.81	0.055	1.035	0.36	0.01
Plastic modulus			**Dilatancy**		**Memory surface**		
h_0	c_h	n^b	A_0	n^d	μ_0	ζ	β
7.6	0.97	1.2	0.74	1.79	82	0.0005	4

As a new feature, the shrinkage rate of the memory surface dm_-^M is further linked to the induced cumulative expansion of the memory surface size $m_+^M = \int dm_+^M$ over the whole loading history experienced from a known initial state. The introduction of the term m_+^M, monotonically increasing under shearing and consequent plastic straining, ensures rapid degradation of the memory surface at large strain levels. Therefore, virgin loading conditions are quickly reinstated upon load increment reversal after severe dilation (due to inhibited memory surface effects). This feature is consistent with the observations of Yimsiri and Soga (2010) and Ziotopoulou and Boulanger (2016), who noted that sand behaviour at large strain levels is mainly governed by the current relative density:

$$dm_-^M = -\frac{m^M}{\zeta} f_{shr} \langle b_r^b \rangle m_+^M \left\langle -d\varepsilon_{vol}^p \right\rangle \tag{5.4}$$

where ζ is a parameter governing the shrinking rate of the memory surface, see Appendix A for details about the geometrical factor f_{shr}.

The term $< b_r^b >$ in Eq. (5.4) is also introduced to properly handle strain-softening stages: during strain softening, $(\boldsymbol{\alpha}^b - \boldsymbol{\alpha}) : \boldsymbol{n} < 0$, which may result in $b_r^b = (\boldsymbol{\alpha}^b - \boldsymbol{r}_\alpha^M) : \boldsymbol{n} < 0$ and contemporary shrinkage of both bounding and memory surfaces may occur. As a consequence, $dm_+^M < 0$ and m_+^M may decrease, which would be in contrast with the assumption of non-decreasing m_+^M.

The following expression of the memory surface hardening coefficient h^M in Eqs. (5.2)–5.3 results from derivations similar to those in Chapter 3 (see Table 3.1) and Appendix A:

$$h^M = \frac{1}{2}\left(\tilde{h} + \hat{h}\right) = \frac{1}{2}\left[\frac{b_0}{(\boldsymbol{r}_\alpha^M - \boldsymbol{\alpha}_{in}) : \boldsymbol{n}} + \sqrt{\frac{3}{2}} \frac{m^M m_+^M f_{shr} \langle b_r^b \rangle \langle -D \rangle}{\zeta (\boldsymbol{\alpha}^b - \boldsymbol{r}_\alpha^M) : \boldsymbol{n}}\right] \tag{5.5}$$

where b_0 is the hardening factor given by Dafalias and Manzari (2004) (Table 5.1), and $\boldsymbol{\alpha}_{in}$ the back-stress ratio at stress increment reversal. Closer inspection of Eq. (5.5) leads to recognise the chance of a vanishing denominator in $\hat{h}$ (e.g., if either $\boldsymbol{\alpha}^b = \boldsymbol{r}_\alpha^M$ or $\boldsymbol{n} \propto (\boldsymbol{\alpha}^b - \boldsymbol{r}_\alpha^M)$), which may abruptly accelerate the evolution of $\boldsymbol{\alpha}^M$ and temporarily leave the yield locus outside the (shrinking) memory surface. The effects of such occurrence, rare but possible, may be mitigated in the numerical implementation of the model, for instance by inhibiting shrinkage of the memory surface when becoming tangent to the yield surface.

Overall, the above upgraded laws for memory surface evolution allow fabric effects to be erased at large strain levels, in agreement with available experimental evidence (Yimsiri and Soga, 2010; Ziotopoulou and Boulanger, 2016).

Dilatancy

The model as presented in Chapter 3 can already predict liquefaction triggering (according to Seed and Lee (1966), the first occurrence of $p' \approx 0$), and provides for medium-dense/dense sands reasonable stress path shapes in the post-dilation phase ('butterfly-shaped' $q-p$ response). However, accurate simulation of peculiar stress-strain loops during cyclic mobility is beyond the possibilities of that model. Amending this short-coming requires introducing changes to the formulation governing sand dilatancy. Indeed, as discussed by Elgamal et al. (2003) and Boulanger and Ziotopoulou (2013), the modelling of cyclic mobility is intimately related to the description of sand dilatancy. Within the SANISAND framework, the dilatancy coefficient D in the plastic flow rule is generally expressed as (Table 5.1):

$$D = A_d d \tag{5.6}$$

where

$$d = (\boldsymbol{\alpha}^d - \boldsymbol{\alpha}) : \boldsymbol{n} \tag{5.7}$$

and $\boldsymbol{\alpha}^d$ represents the image back-stress ratio on the dilatancy surface. In Chapter 3, the term A_d was already set to depend on the sign of plastic volume changes (i.e., contraction or dilation) before the previous load increment reversal through the term $\langle \tilde{b}_d^M \rangle = \left\langle (\tilde{\boldsymbol{\alpha}}^d - \tilde{\boldsymbol{r}}_\alpha^M) : \boldsymbol{n} \right\rangle$. Such a dependence was introduced to capture the increase in pressure build-up upon post-dilation load increment reversals — a phenomenon that Dafalias and Manzari (2004) reproduced through the concept of fabric tensor. Compared to the original definition in Chapter 3, the definition of A_d is here enhanced with some new features, mainly instrumental to the simulation of undrained cyclic mobility:

- in the case of (plastic) contraction ($d \geq 0$) following previous contraction ($\tilde{b}_d^M \leq 0$):

$$A_d = A_0 \tag{5.8}$$

- in the case of (plastic) contraction ($d \geq 0$) following previous dilation ($\tilde{b}_d^M > 0$)

$$A_d = A_0 \exp\left[\beta_1 F \left(\frac{p}{p_{max}}\right)^{0.5}\right] g^k(\theta) \tag{5.9}$$

- in the case of dilation ($d < 0$)

$$A_d = A_0 \exp\left[\beta_2 F \left(1 - \left(\frac{p}{p_{max}}\right)^{0.5}\right) \frac{d}{||\boldsymbol{\alpha}^c||}\right] \frac{1}{g(\theta)} \tag{5.10}$$

In the above relationships, A_0 is the 'intrinsic' dilatancy parameter already present in Dafalias and Manzari (2004). $||\boldsymbol{\alpha}^c||$ in Eq. (5.10) is the Euclidean norm of $\boldsymbol{\alpha}^c$ (see Table 5.1) introduced for normalisation purposes, which represents the distance between the origin of the deviatoric stress ratio plane and the image back-stress ratio on the critical surface f^c. The new dilatancy features in Eqs. (5.9)-5.10 are phenomenologically associated with the following mechanical factors:

- **Fabric history**
  F is a non-decreasing scalar variable related to the previous history of fabric evolution:

$$F = \ln\left[1 + \frac{|m_-^M|}{(|m_+^M| + |m_-^M|)^{0.5}}\right] = \ln\left[1 + \frac{\int |dm_-^M|}{(\int |dm_+^M| + \int |dm_-^M|)^{0.5}}\right] \quad (5.11)$$

  F plays a similar role as the 'damage index' in Boulanger and Ziotopoulou (2013), that is to progressively degrade A_d at increasing number of cycles. This feature helps reproducing progressive shear strain accumulation, for instance in undrained DSS tests with imposed symmetric shear loading (Arulmoli et al., 1992; Andersen, 2009). The effect of this modelling ingredient can be appreciated by comparing model simulations in Fig. 5.1a and Fig. 5.1b, performed with the previous and upgraded SANISAND-MS, respectively. It should also be noted that, as F is a non-decreasing variable, it will permanently have an influence also on the post-cyclic response, possibly featuring different drainage conditions. Post-cyclic drained behaviour, for instance, would be more (less) contractive (dilative) than without the use of F in the flow rule. There is hardly any experimental evidence available to either support or falsify such occurrence, so that caution is recommended when applying the model to problems with very variable drainage conditions and/or distinct stages of consolidation.

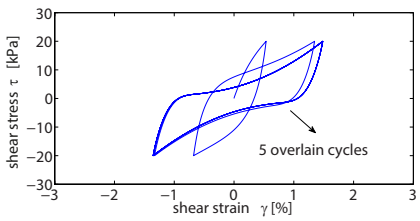

(a) formulation in Chapter 3

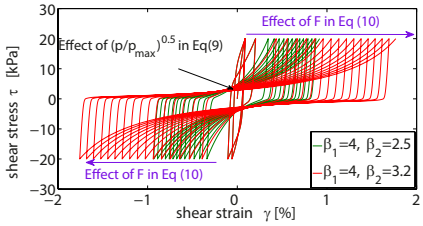

(b) upgraded formulation

Figure 5.1: Cyclic DSS simulations via SANISAND-MS. Simulation conditions: $e_{in} = 0.812$ (initial void ratio), $\sigma_v = 100$ kPa (effective vertical stress), $\tau_{ampl} = \pm 20$ kPa (cyclic shear stress amplitude); cyclic parameters in the upgraded model: $\mu_0 = 65$, $\zeta = 0.0003$, $w_1 = 2.5$, $w_2 = 1.5$, $k = 2$.

- **Sensitivity to stress state and path**
  Dependence on the (relative) Lode angle function ($g(\theta)$) and the term $d/||\boldsymbol{\alpha}^c||$ were suggested by experimental results as a way to modulate the response,

and particularly strain accumulation, with respect to different cyclic stress paths (e.g., triaxial or simple shear). Typical simulation results of previous and upgraded SANISAND-MS models are shown in Figs. 5.2a and 5.2b, respectively. The pressure term $(p/p_{max})^{0.5}$ (p_{max} is the highest effective mean pressure ever experienced) reflects the greater proneness to shear straining observed at very low effective stress levels, progressively reducing at increasing p – see Fig. 5.1b and Fig. 5.2b.

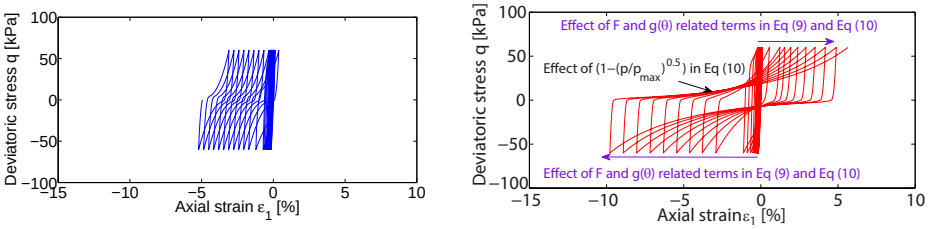

(a) formulation in Chapter 3

(b) upgraded formulation

Figure 5.2: Cyclic triaxial simulations on isotropically consolidated sand via SANISAND-MS. Simulation settings: $e_{in} = 0.825$, $p_{in} = 200$ kPa, $q_{ampl} = 60$ kPa. Cyclic parameters in the upgraded model: $\mu_0 = 65$, $\zeta = 0.0003$, $w_1 = 2.5$, $w_2 = 1.5$, $\beta_1 = 4.0$, $\beta_2 = 3.2$, $k = 2$.

Dilatancy features in the upgraded model can be tuned to experimental data through the material parameters β_1 and β_2 in Eqs. (5.9) and 5.10. These parameters govern cyclic shear straining in the dilative regime – cyclic volume changes before any dilation mostly depend on the parameter A_0 and the memory-hardening parameter μ_0 in Table 5.1. Sound calibration of β_1 requires data from undrained cyclic triaxial tests in which initial liquefaction is triggered. As exemplified in Fig. 5.3, the parameter β_1 influences the undrained triaxial stress-strain response in terms of ultimate normalised accumulated pore pressure (throughout this work, pore water pressure generation is tracked at the end of each full cycle when $q = q_{ave}$). Larger β_1 results in higher u^{acc}/p_{in} ratios (i.e., smaller residual effective stress). For the considered Karlsruhe fine sand $\beta_1 = 4$ was selected, with β_2 negligibly affecting the final u^{acc} level.

At a given β_1, increasing β_2 results in larger accumulation of cyclic shear strain in undrained cyclic DSS tests (see Fig. 5.1b). Unfortunately, in the lack of undrained cyclic DSS tests performed on the same Karlsruhe sand, β_2 had to be identified, together with k in Eq. (5.9), by a trial-and-error procedure. In the case of triaxial loading, increasing β_2 determines larger cyclic axial strain (see Fig. 5.4b), whereas the parameter k in Eq. (5.9) governs the influence of the stress path through the relative Lode angle θ. Fig. 5.4b shows that, for a cyclic triaxial test, higher k results in positive/compressive cyclic axial strains larger than on the negative/extension side. The comparison to Wichtmann and Triantafyllidis (2016)'s triaxial test results (Fig. 5.4a) led to identify the parameter pair $\beta_2 = 3.2$ and $k = 2$. Some attention should be paid to the following two remarks about formulation and limitations of the new flow rule::

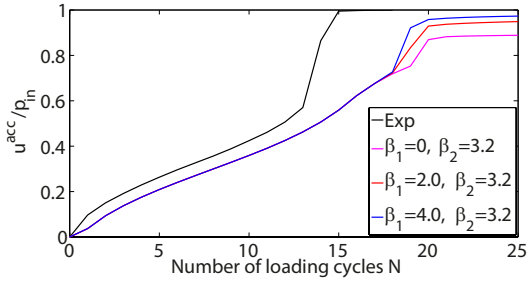

Figure 5.3: Calibration of β_1. Test/simulation settings and cyclic parameters are as in Fig. 5.2b. Test data from Wichtmann & Triantafyllidis (2016).

1. The piece-wise definition of A_d implies discontinuity in the dilatancy coefficient D when the material transits from contractive to dilative behaviour (i.e., when the yield locus crosses the dilatancy surface) – even in the presence of continuous variations in stress ratio $\boldsymbol{r}$ (thus, in loading direction $\boldsymbol{n}$). Consequently, continuity of volumetric plastic strain increments may not be guaranteed, similarly to Boulanger and Ziotopoulou (2013) and Khosravifar et al. (2018);

2. In contrast with the (inconclusive) findings of some experimental studies, the model predicts less obvious strain saturation during cyclic mobility – compare to Fig. 5.4a, where only limited strain increments are observed in the last few loading cycles. While other modelling assumptions are certainly possible (Barrero et al., 2020), the latter point will receive further attention when broader consensus about underlying physical mechanisms is reached (Wang and Wei, 2016; Wang et al., 2016).

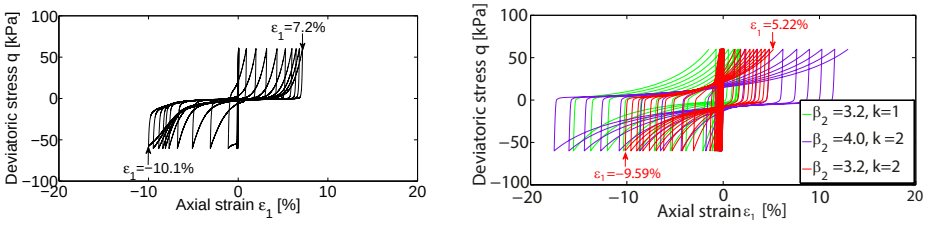

(a) triaxial test (Wichtmann and Triantafyllidis, 2016) (b) upgraded SANISAND-MS simulations

Figure 5.4: Calibration of β_2 and k. Test/simulation settings: $e_{in} = 0.8$, $p_{in} = 200$ kPa, $q_{ampl} = 60$ kPa. Cyclic parameters in the upgraded model: $\mu_0 = 65$, $\zeta = 0.0003$, $w_1 = 2.5$, $w_2 = 1.5$, $\beta_1 = 4.0$. Number of loading cycles after initial liquefaction $N = 10$.

Hardening coefficient

In its initial version, SANISAND-MS had limited capability to quantitatively reproduce complex relationships between cyclic pore pressure accumulation and relevant load-

ing factors. Fig. 5.5 compares the performance of previous SANISAND-MS (blue lines, formulation in Chapter 3, i.e., as in Liu et al. (2019)) in reproducing Wichtmann and Triantafyllidis (2016)'s triaxial data (blacks lines) regarding undrained pre-liquefaction behaviour under cyclic symmetric loading at varying cyclic amplitude ratios ($\eta_{ampl} = q_{ampl}/p_{in}$, with q_{ampl} the cyclic shear amplitude and p_{in} the initial mean effective stress). The previous SANISAND-MS predicts more limited variation in the number of loading cycles N_{ini} to trigger initial liquefaction ($u^{acc}/p_{in} \approx 1$ for the first time).

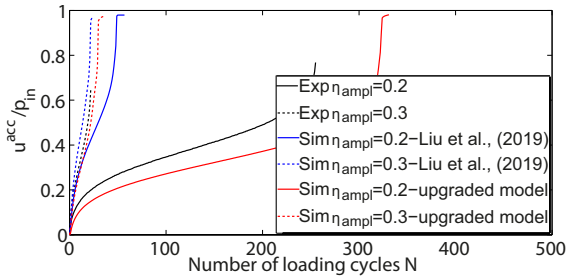

Figure 5.5: Performance of previous and upgraded SANISAND-MS (model parameters in Table 5.2 and Table 5.3, respectively) on pore pressure accumulation in isotropically consolidated sand under varying stress amplitude ratios η_{ampl}. Test/simulation settings: performed with an initial drained loading cycle, $p_{in} = 300$ kPa, $e_{in} = 0.846$ when $\eta_{ampl} = 0.2$; $e_{in} = 0.816$ when $\eta_{ampl} = 0.3$. Experimental data from Wichtmann & Triantafyllidis (2016).

The comprehensive database of Wichtmann and Triantafyllidis (2016) supports the idea that more cycles are required to trigger liquefaction (higher N_{ini}) at low η_{ampl}. It could thus be attempted to link the increase in N_{ini} to higher values of the hardening coefficient h through explicit dependence on η_{ampl}. However, as η_{ampl} cannot be a priori defined in general boundary value problems, the current stress ratio η instead of η_{ampl} is adopted in the upgraded definition of the hardening coefficient h:

$$h = \frac{b_0}{(\boldsymbol{\alpha} - \boldsymbol{\alpha}_{in}) : \boldsymbol{n}} \exp\left[\mu_0 \left(\frac{p}{p_{atm}}\right)^{0.5} \left(\frac{b^M}{b_{ref}}\right)^{w_1} \frac{1}{\eta^{w_2}}\right] \tag{5.12}$$

where $\eta = q/p = \sqrt{3J_2}/p$. b^M represents the distance between the current back-stress ratio $\boldsymbol{\alpha}$ and its image point $\boldsymbol{r}_\alpha^M$ on the memory surface, while b_{ref} is a reference normalisation factor (Table 5.1). The term $1/\eta^{w_2}$ (with w_2 new model parameter), explicitly accounts for the deviatoric span of the loading path – for more robust numerical implementation, m (radius of the yield surface in the stress ratio π plane) is set as η's lower bound.

Input to the calibration of the w_2 parameter can be obtained from the experimental relationship between N_{ini} and η_{ampl} in triaxial tests on isotropically consolidated sand. As mentioned above, increase in N_{ini} is linked to higher values of the hardening coefficient h, which is in turn inversely related to η_{ampl} (i.e.,

$N_{ini} \propto h \propto [\exp(\text{factor} \cdot 1/\eta_{ampl}^{w_2})]$. Such observation prompted the investigation of the relationship between $\ln(N_{ini})$ and $1/\eta_{ampl}^{w_2}$). It was concluded that for fixed η_{ampl}, dense sands (i.e., with D_{r0} larger than critical) experience more loading cycles before liquefaction. In summary, the experimental relationship between $\ln(N_{ini})/D_{r0}$ and $1/(\eta_{ampl}^{w_2})$ emerging from a set of tests is proposed as a tool to calibrate w_2 – see Fig. 5.6. This requires at least four stress-controlled undrained triaxial tests on isotropically consolidated specimens, at varying η_{ampl} and D_{r0}, until cyclic liquefaction is triggered. However, since in Eq. (5.12) the current stress ratio η is adopted instead of directly using η_{ampl}, the calibrated w_2 may need further adjustment together with w_1 and μ_0 (for which calibration procedures are given in the following section). Should available data be insufficient, $w_2 = 0$ is suggested as an initial value, and followed with a sensitivity study to determine its relevance and possibly motivate the gathering of the data for its calibration.

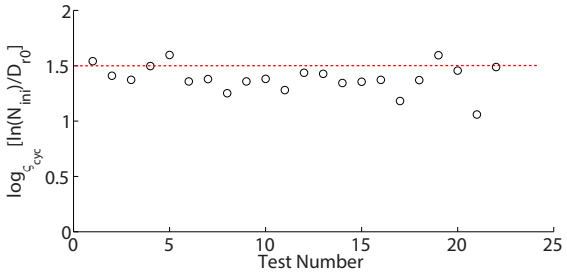

Figure 5.6: Calibration of w_2 based on the results of undrained cyclic triaxial tests on isotropically consolidated sand from Wichtmann & Triantafyllidis (2016).

The other exponent w_1 in Eq. (5.12) was pre-set to 2 in Chapters 3 and 4 for simplicity. Herein, w_1 is re-activated as a free model parameter for more flexibility. Its value, together with μ_0's, was calibrated mostly by trial-and-error, starting from the default setting $w_1 = 2$. The same test data-set used for calibrating w_2 can also support the identification of w_1 when looking at pore pressure accumulation trends, e.g., in terms of u^{acc}/p_{in} versus number of loading cycles. Fig. 5.7 shows that good agreement for the examined Karlsruhe sand is achieved for $\mu_0 = 65$ and $w_1 = 2.5$.

Fig. 5.5 also shows the performance of upgraded SANISAND-MS (red lines). As discussed in the following section, the upgraded model appears better suited to capture the dependence of N_{ini} (number of cycles to liquefaction) on the cyclic stress amplitude at different relative densities.

5.3. Prediction of undrained cyclic response

This section demonstrates the predictive capabilities of the model with respect to upgraded undrained cyclic loading. Using the set of calibrated parameters in Table 5.4, the model performance is assessed against additional triaxial test results on Karlsruhe fine sand (Wichtmann and Triantafyllidis, 2016), not previously used

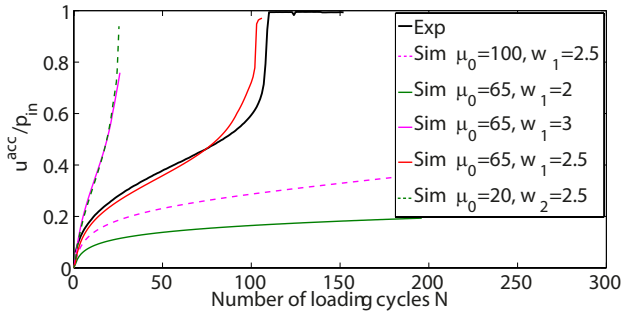

Figure 5.7: Calibration of w_1 and μ_0. Test/simulation settings: performed with an initial drained loading cycle, $e_{in} = 0.808$, $p_{in} = 300$ kPa, $\eta_{ampl} = 0.25$. Cyclic parameters in the upgraded model: $\beta_1 = 4.0$, $\beta_2 = 3.2$, $w_2 = 1.5$, $k = 2$, $\zeta = 0.0003$.

for calibration.

5

5.3.1. Response of isotropically consolidated sand

Cyclic pore pressure accumulation

Cyclic build-up of pore pressure may cause stiffness and strength losses (cyclic liquefaction), for instance during seismic events. Many empirical models have been developed (Dobry et al., 1985; Idriss and Boulanger, 2006; Ivšić, 2006; Chiaradonna et al., 2018) to simplify the prediction of such build-up by directly relating the pore pressure ratio (u^{acc}/p_{in}) to the ratio between current number of cycles (N) and total number of cycles to liquefaction (N_{ini}). It seems interesting to verify how pore pressure predictions from SANISAND-MS (both previous and upgraded versions) compare to empirical models, such as that recently proposed by Chiaradonna et al. (2018). In Fig. 5.8, SANISAND-MS and empirical model predictions are compared to experimental data from Wichtmann and Triantafyllidis (2016), concerning triaxial tests performed at varying cyclic stress amplitude ratio. Although both plasticity and empirical models reproduce well the experimental data, it is worth noting that the simulation of pore pressure accumulation trends is usually easier when pursued in terms of normalised number of cycles N/N_{ini}. It is shown hereafter that reproducing the absolute N_{ini} value poses a more serious challenge for constitutive modelling.

Table 5.3: Upgraded SANISAND-MS parameters for the Karlsruhe fine sand tested by Wichtmann & Triantafyllidis (2016)

Elasticity		**Critical state**					**Yield**	**Plastic modulus**		
G_0	ν	M	c	λ_c	e_0	ξ	m	h_0	c_h	n^b
95	0.05	1.35	0.81	0.055	1.035	0.36	0.01	7.6	0.97	1.2
Dilatancy					**Memory surface**					
A_0	n^d	β_1	β_2	k	μ_0	ζ	w_1	w_2		
0.74	1.79	4.0	3.2	2	65	0.0003	2.5	1.5		

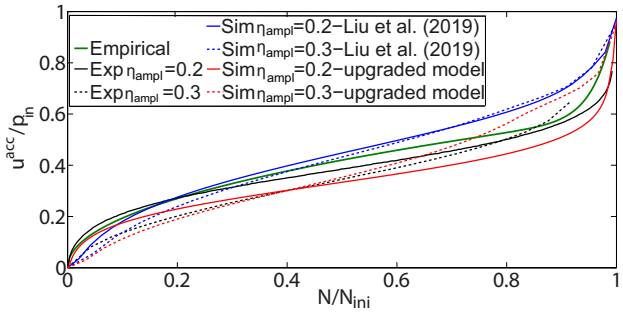

Figure 5.8: Pore pressure accumulation curves. Same test/simulation settings as in Fig. 5.5. Comparison among experimental data (Wichtmann & Triantafyllidis, 2016), empirical fit (Chiaradonna et al., 2018) and SANISAND-MS simulations.

Influence of initial effective mean pressure Experimental test results from Wichtmann and Triantafyllidis (2016) (Fig. 5.9) show that it is not straightforward to interpret the influence of the initial consolidation pressure p_{in} in tests featuring constant cyclic stress amplitude ratio ($\eta_{ampl} = q_{ampl}/p_{in}$). Axial strain accumulation in the cyclic mobility stage does not show obvious dependence on p_{in} either. Simulation results obtained with the upgraded SANISAND-MS formulation support similar conclusions (Fig. 5.9b). For instance, the considered cases with $\eta_{ampl} = 0.25$ and p_{in} =100, 200, 300 kPa are associated in experiments with N_{ini} values equal to 100, 77 and 110, respectively – i.e., with no monotonic dependence of N_{ini} on p_{in} (and arguably with an influence of specimen preparation). Overall, the proposed SANISAND-MS formulation shows good ability to predict the impact of p_{in} both in terms of pore pressure build-up and strain accumulation, with the upgraded formulation performing better than its previous version.

Influence of cyclic amplitude ratio The reference experimental data show that higher values of the cyclic amplitude stress ratio ($\eta_{ampl} = q_{ampl}/p_{in}$) result in faster triggering of liquefaction (i.e., lower N_{ini}) – see Fig. 5.10a and Fig. 5.10e. Both SANISAND-MS versions prove sensitive to this effect (see Fig. 5.10b and Fig. 5.10e). However, while the formulation in Chapter 3 largely underestimates N_{ini} for $\eta_{ampl} = 0.2$ and 0.25, the upgraded model predicts accurate N_{ini} values in all considered cases. This confirms the effectiveness of the new hardening modulus definition in Eq. (5.12). Further, the upgraded formulation captures well the axial strain accumulation, both on the positive and negative sides (compare Fig. 5.10c and Fig. 5.10d).

Influence of initial relative density Wichtmann and Triantafyllidis (2016)'s data also confirm the expectation that, under given conditions, the effective mean pressure vanishes faster at lower initial relative density (see stress paths in Fig. 5.11a and Fig. 5.11e). Both SANISAND-MS versions succeed also in this respect (Fig. 5.11b and Fig. 5.11e). Nonetheless, the new formulation improves quan-

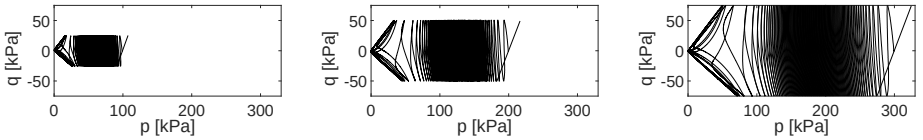

(a) Experimental results: q-p response with, p_{in}=100, 200, 300 kPa (from left to right)

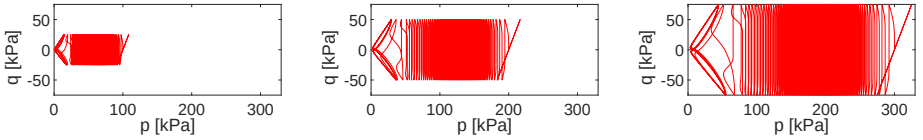

(b) Upgraded SANISAND-MS results: q-p response with, p_{in}=100, 200, 300 kPa (from left to right)

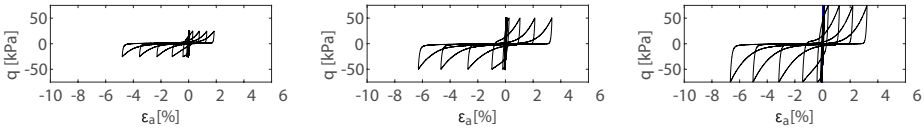

(c) Experimental results: q-ε_a response with, p_{in}=100, 200, 300 kPa (from left to right)

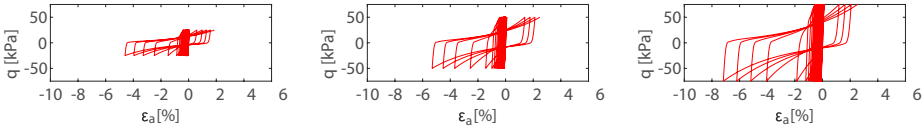

(d) Upgraded SANISAND-MS results: q-ε_a response for p_{in}=100, 200, 300 kPa (from left to right)

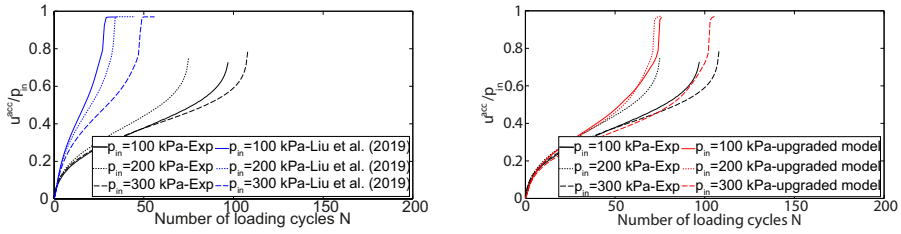

(e) SANISAND-MS vs experimental results: pore pressure accumulation predictions from formulation in Chapter 3 (left) and upgraded model (right)

Figure 5.9: Influence of initial effective mean pressure on pore pressure accumulation in isotropically consolidated sand. Test/simulation settings: performed with an initial drained loading cycle, p_{in} = 100 kPa (e_{in} = 0.798), 200 kPa (e_{in} = 0.813) and 300 kPa (e_{in} = 0.808), η_{ampl} = 0.25. Comparison between experimental data (Wichtmann & Triantafyllidis, 2016) and SANISAND-MS simulations.

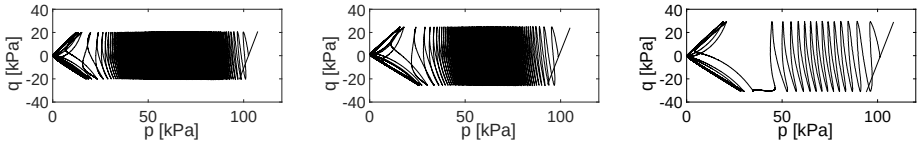

(a) Experimental results: q-p response for η^{ampl}=0.2, 0.25, 0.3 (from left to right)

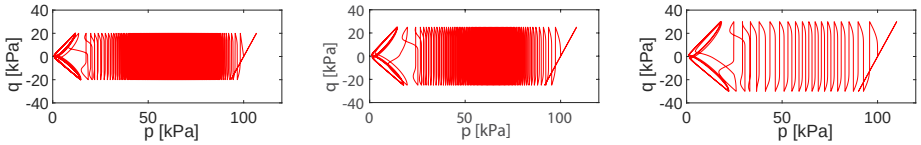

(b) Upgraded SANISAND-MS results: q-p response for η^{ampl}=0.2, 0.25, 0.3 (from left to right)

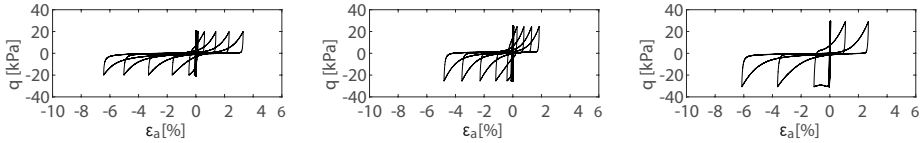

(c) Experimental results: q-ε_a response for η^{ampl}=0.2, 0.25, 0.3 (from left to right)

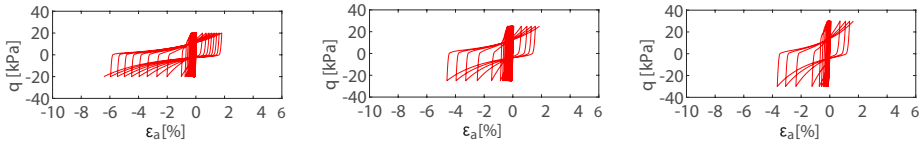

(d) Upgraded SANISAND-MS results: q-ε_a response for η^{ampl}=0.2, 0.25, 0.3 (from left to right)

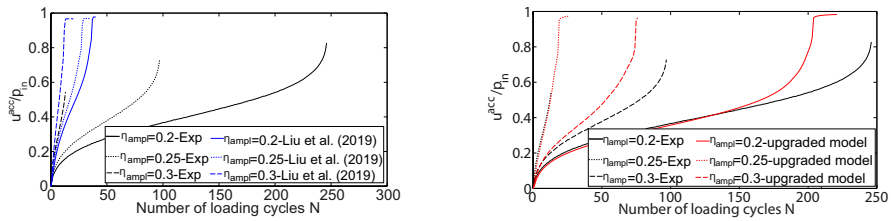

(e) SANISAND-MS vs experimental results: pore pressure accumulation predictions formulation from Chapter 3 (left) and upgraded model (right)

Figure 5.10: Influence of cyclic amplitude ratio η_{ampl} on undrained cyclic behaviour of isotropically consolidated sand. Test/simulation settings: performed with an initial drained loading cycle, e_{in} = 0.821, 0.798, 0.825 for η_{ampl} = 0.2, 0.25 and 0.3, respectively; p_{in} = 100 kPa. Comparison between experimental data (Wichtmann & Triantafyllidis, 2016) and SANISAND-MS simulations.

titative pore pressure predictions owing to the new material parameter w_2, which scales cyclic amplitude effects with respect to the void ratio (see Eq. (5.12) and Fig. 5.7) – compare experimental data and upgraded model predictions in Figs. 5.11a to 5.11b). The new model, however, seems to reproduce the influence on strain accumulation of the initial relative density (Figs. 5.11c to 5.11d) less accurately than of other input factors (Figs. 5.9 - 5.10).

5.3.2. Response of anisotropically consolidated sand

SANISAND-MS was further challenged to reproduce the undrained response of anisotropically consolidated sand specimens. Useful insight in this respect can be obtained from the comparison in Fig. 5.12 between effective stress paths from experimental results (Wichtmann and Triantafyllidis, 2016) and SANISAND-MS simulations. In particular, cases with cyclic stress amplitude ratio ($\eta_{ampl} = q_{ampl}/p_{in}$) smaller or larger than the initial average stress ratio ($\eta_{ave} = q_{ave}/p_{in}$) were considered in both experiments and simulations – Figs. 5.12a, 5.12b. Fig. 5.12 suggests that, when $\eta_{ampl} < \eta_{ave}$ (i.e., with no compression-to-extension reversals in terms of current cyclic stress ratio, Fig. 5.12a), effective stress paths evolve towards steady loops after a few loading cycles – with no liquefaction triggering ($u^{acc}/p_{in} < 1$). This occurrence corresponds with the attainment of a pore pressure plateau in $u^{acc}/p_{in} - N$ plots (Fig. 5.12c). Further, the characteristic butterfly shape of the steady stress path is well captured for $\eta_{ampl} > \eta_{ave}$ (see Fig. 5.12b). When compared to laboratory data, SANISAND-MS simulations reproduce quite well such experimental evidence, including reasonable timing of effective mean pressure reduction against the number of cycles (Fig. 5.12c), especially for $\eta_{ampl} > \eta_{ave}$.

Table 5.4: Upgraded SANISAND-MS parameters for the quartz sand tested by Wichtmann (2005)

Elasticity		**Critical state**					**Yield**	**Plastic modulus**		
G_0	ν	M	c	λ_c	e_0	ξ	m	h_0	c_h	n^b
110	0.05	1.27	0.712	0.049	0.845	0.27	0.01	5.95	1.01	2
Dilatancy					**Memory surface**					
A_0	n^d	β_1	β_2	k	μ_0	ζ	w_1	w_2		
1.06	1.17	1.9	2.1	1	260	0.0001	2	0		

5.3.3. Influence of drained cyclic pre-loading

It is well-known that previous loading history affects the hydro-mechanical response of sands to undrained cyclic loading, including their susceptibility to liquefaction. In this section the impact of drained cyclic pre-loading on subsequent undrained pore pressure build-up is explored. To this end, results from a different experimental database were considered. Fig. 5.13 shows SANISAND-MS simulation results for the quartz sand tested by Wichtmann (2005) ($D_{50} = 0.55$ mm, $D_{10} = 0.29$ mm, $C_u = D_{60}/D_{10} = 1.8$, $e_{max} = 0.874$, $e_{min} = 0.577$), corresponding with $p_{in} = 100$ kPa, $e_{in} = 0.684$, undrained cyclic stress amplitude $q_{ampl}^{pre} = 45$ kPa. The model parameters calibrated for this second sand are reported in Table 5.4. Monotonic parameters and μ_0 (i.e., from G_0 to μ_0 in Table 5.4) coincide with those calibrated

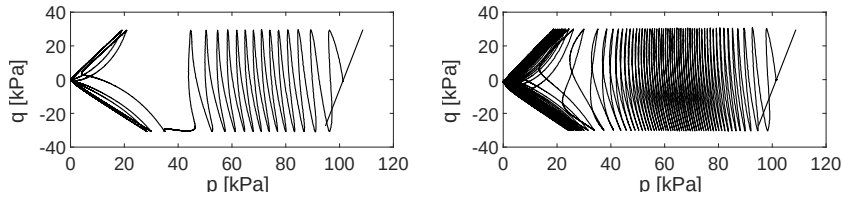

(a) Experimental results: q-p response for e_{in} =0.825 (left) and e_{in} =0.759 (right)

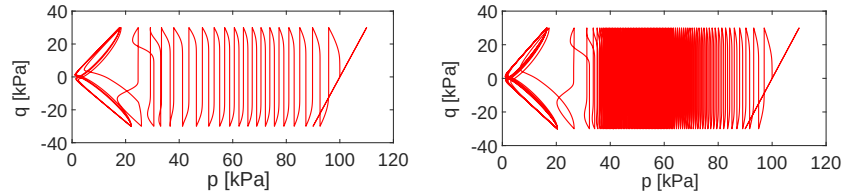

(b) Upgraded SANISAND-MS results: q-p response for e_{in} =0.825 (left) and e_{in} =0.759 (right)

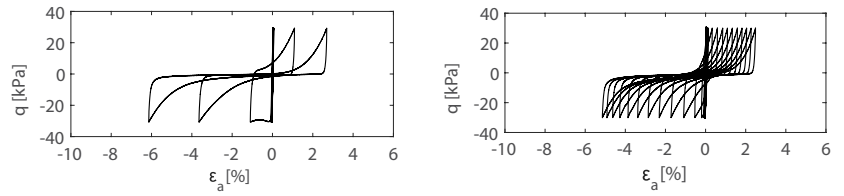

(c) Experimental results: q-ε_a response for e_{in} =0.825 (left) and e_{in} =0.759 (right)

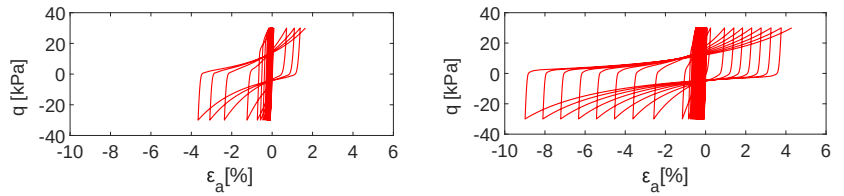

(d) Upgraded SANISAND-MS results: q-ε_a response for e_{in} =0.825 (left) and e_{in} =0.759 (right)

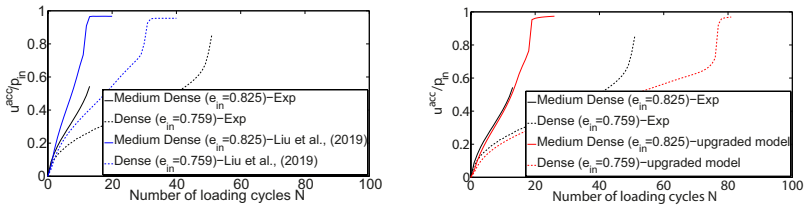

(e) SANISAND-MS vs experimental results: pore pressure accumulation predictions from formulation in Chapter 3 (left) and upgraded model (right)

Figure 5.11: Influence of initial relative density on pore pressure accumulation in isotropically consolidated sand. Test/simulation settings: performed with an initial drained loading cycle, medium-dense sand ($e_{in} = 0.825$) and dense sand ($e_{in} = 0.759$), $p_{in} = 100$ kPa, $\eta_{ampl} = 0.3$. Comparison between experimental data (Wichtmann & Triantafyllidis, 2016) and SANISAND-MS simulations.

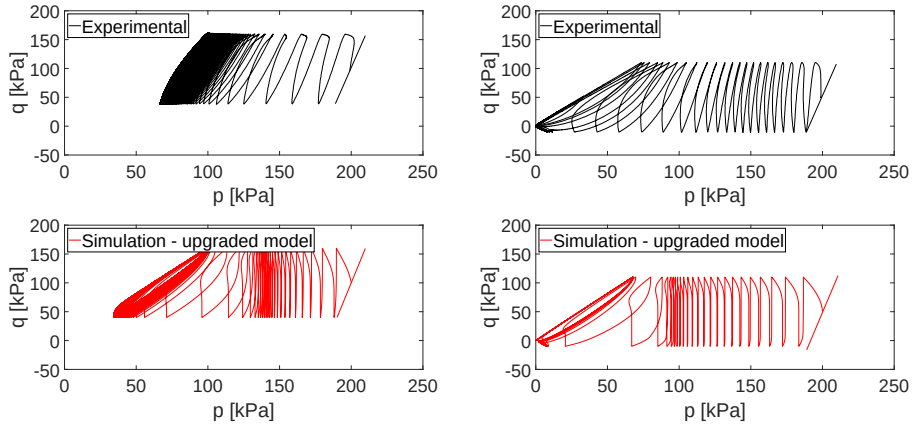

(a) $\eta_{ampl} = 0.3 < \eta_{ave} = 0.5$, $e_{in} = 0.838$ (b) $\eta_{ampl} = 0.3 > \eta_{ave} = 0.25$, $e_{in} = 0.843$

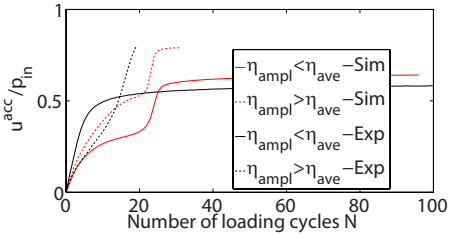

(c) pore pressure generation

Figure 5.12: Relative effect of cyclic stress amplitude ratio η_{ampl} and initial average stress ratio η_{ave} on the undrained effective stress path in anisotropically consolidated sand. Test/simulation settings: performed with an initial drained loading cycle, p_{in} = 200 kPa, q_{ampl} = 60 kPa. Experimental data from (Wichtmann and Triantafyllidis, 2016)).

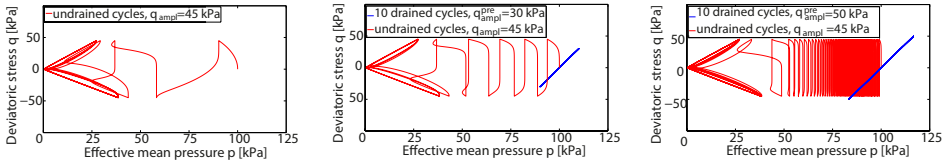

(a) without drained pre-cycles (b) 10 pre-cycles, $q^{pre}_{ampl} = 30kPa$ (c) 10 pre-cycles, $q^{pre}_{ampl} = 50kPa$

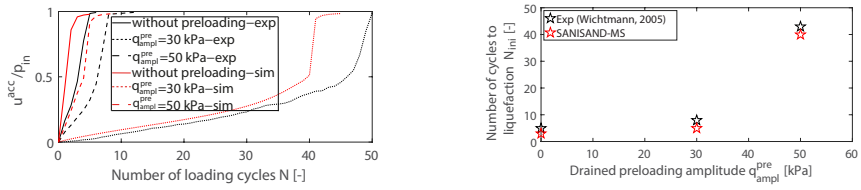

(d) pore pressure build-up curve (e) Dependence of N_{ini} on q^{pre}_{ampl}

Figure 5.13: Effect of drained cyclic pre-loading on the undrained cyclic triaxial response of the quartz sand (Wichtmann, 2005) – isotropically consolidated sand. Test/simulation settings: e_{in} = 0.678, p_{in} = 100 kPa, cyclic stress amplitude during undrained loading: q_{ampl} = 45 kPa.

by Liu et al. (2018) and presented in Chapter 3, while the aforementioned default values $w_1 = 2$ and $w_2 = 0$ were assumed; β_1, β_2, k and ζ were calibrated against the deviatoric stress-axial strain response from only one stress-controlled triaxial test at constant cyclic amplitude.

Upgraded SANISAND-MS simulations were carried out for three different cases: (1) without drained pre-loading cycles; (2) with 10 drained pre-cycles of amplitude $q_{ampl}^{pre} = 30$ kPa, followed by undrained cyclic loading; (3) with 10 drained pre-cycles of amplitude $q_{ampl}^{pre} = 50$ kPa, followed by undrained cyclic loading. It is generally observed that drained cyclic pre-loading under the phase-transformation line tends to delay the onset of liquefaction (i.e., to increase N_{ini}, see $q - p$ stress paths in Figs. 5.13a–5.13c).

Simulation results in Fig. 5.13d (red lines) are in very good agreement with experimental measurements (black lines) in terms of pore water pressure accumulation, and support the suitability of the adopted memory surface framework. In essence, applying drained cyclic pre-loading contributes to the "reinforcement" of sand fabric. This aspect is phenomenologically tracked by the model through the corresponding evolution of the memory surface size/location, and thus exploited to re-tune soil stiffness and dilatancy. The evolution of the memory surface prior to the undrained cycles is given in Figure 5.14 – higher drained pre-loading amplitude (in compressive regime) results in larger m^M. The larger m^M, the higher the resistance to liquefaction, i.e., the larger N_{ini} (compare Figure 5.13b with Figure 5.13c). As highlighted in Fig. 5.13e, accurate simulation of effective stress paths enables the dependence of N_{ini} on the amplitude of drained pre-cycles to be reliably predicted. It is finally worth noting that the parent SANISAND04 model (Dafalias and Manzari, 2004) would be practically insensitive to drained cyclic pre-loading, except for the effect of a slightly different void ratio at the beginning of undrained cycling.

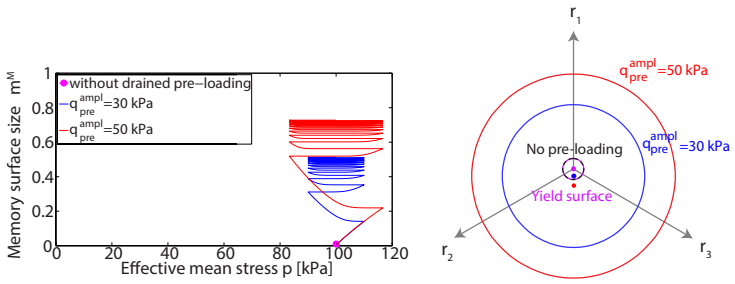

(a) Evolution of the memory surface size

(b) location and size of memory surface

Figure 5.14: Memory surface before the undrained shearing for test conditions: (1) without pre-loading applied (black circle); (2) 10 drained preloading with q_{pre}^{ampl} = 30kPa (blue circle) and (3) 10 drained pre-loading with q_{pre}^{ampl} = 50kPa (red circle). The yield surface is presented using dashed purple circle.

5.4. Concluding remarks

The SANISAND-MS formulation introduced in Chapter 3, has been improved to reproduce essential features of the hydro-mechanical response of sands to undrained cyclic loading. The previous mathematical formulation has been upgraded by: (i) modifying memory surface evolution laws to better reflect fabric effects at larger strains; (ii) enhancing the description of sand dilatancy through new terms accounting for fabric evolution history, and stress state/path; (iii) incorporating a deviatoric stress ratio term into the hardening modulus. A few aspects of the proposed constitutive model will require further research in the near future, for instance to: (a) avoid discontinuities in the dilatancy formulation; (b) more flexibly model deviatoric strain accumulation during cyclic mobility, e.g., by allowing for strain saturation limits if observed in experimental data; (c) investigate the evolution of fabric history effects through varying drainage conditions.

The above modifications have produced substantial improvement in the simulation of pore pressure build-up and cyclic mobility. After parameter calibration, the model has been thoroughly validated against published results of undrained cyclic triaxial tests. Further qualitative insight into the effect of different loading conditions (e.g., under simple shear loading) has also been provided.

6

SANISAND-MS: 3D FE Modelling of Cyclic Monopile Tilt

The contents of this chapter have been submitted for publication (Liu et al., 2020b).

6.1. Introduction

It has been noted in Chapter 1 that most offshore wind turbines (OWTs) are to date founded on monopiles, tubular steel piles of large diameter ($\sim 5-10$ m) and low embedment ratio (embedded length/diameter, $\sim 3-6$). Due to very high material and installation costs, optimisation of foundation design is crucial for cost-effective offshore wind developments. In this respect, it has been also underlined how a concern for designers is to avoid excessive accumulation of monopile rotation/deflection (tilt) under repeated loading. Specifically, OWT manufacturers prescribe that permanent OWT-monopile tilt should not exceed $\sim 0.5°$ over the whole operational life, also including imperfect verticality after installation (Arany et al., 2015). Relevant small-scale experimental work has been devoted in the past decade to the study of monopile tilt under high-cyclic lateral loading, mostly for the case of sandy soils under drained conditions (i.e., disregarding pore pressure effects) – see for instance LeBlanc et al. (2010); Klinkvort and Hededal (2013); Rudolph et al. (2014); Nicolai and Ibsen (2014); Li et al. (2015); Albiker et al. (2017); Abadie et al. (2019); Truong et al. (2019); Richards et al. (2019). As for numerical modelling research, it is worth recalling here the approaches for tilt analysis that have been most frequently considered – see also Chapter 2:

- methods based on '0D' modelling of soil-monopile interaction. In this approach, distributed/continuum geotechnical mechanisms are lumped into a single macro-element formulated in terms of only a few pairs (six at most) of generalised static (forces/moments) and kinematic (displacement/rotations) variables (Houlsby et al., 2017; Abadie et al., 2019). Non-linear monopile macro-elements have also been used to account for soil-foundation interaction effects in the dynamic analysis of OWTs (Page et al., 2019);
- methods based on well-known '1D' $p-y$ modelling, in which the monopile is idealised as an Winkler beam interacting with compliant soil springs of given one-dimensional behaviour (Bhattacharya, 2019). The recent PISA project has rivisited the application of *p-y* modelling to the case of short/stiff piles, although cyclic loading conditions have not been addressed yet within the proposed framework (Byrne et al., 2019);
- methods based on 'explicit' 3D soil-foundation modelling, in which empirical strain accumulation laws are integrated over the soil domain to calculate monopile deformations against the number of loading cycles (Achmus et al., 2009; Jostad et al., 2015; Wichtmann et al., 2017; Chong, 2017). While relevant field equations are usually solved after finite element (FE) discretisation of the 3D domain, good computational efficiency is achieved by avoiding step-by-step simulation of cyclic soil response ('implicit modelling', in the terminology used by Niemunis et al. (2005)).

To date, the above numerical approaches have proven computationally more convenient than implicit 3D simulations – so far only rarely applied to monopile tilt problems (Barari et al., 2017). Nonetheless, implicit 3D FE modelling appears to possess high potential to explain/predict governing geo-mechanisms (Pisanò et al.,

2019), and is being increasingly adopted to study the cyclic/dynamic performance of OWT-monopile-soil systems (Cuéllar et al., 2014; Kementzetzidis et al., 2018, 2019, 2020). The soundness of implicit 3D FE calculations is largely influenced by the following two aspects: (i) accumulation of numerical errors under prolonged high-cyclic loading (Niemunis et al., 2005); (ii) constitutive modelling of cyclic soil behaviour.

This chapter focuses on applying, for the very first time, the SANISAND-MS model developed so far to the 3D FE analysis of cyclic monopile tilt in sand. The main goal is gain general insight into the predictive potential of the constitutive model in relation to cyclic soil-structure interaction problems. For this purpose, qualitative comparison to small-scale pile test results from the literature is presented, though with no attempt to pursue a complete calibration-validation-prediction exercise – future work on this subject will be carried in the near future. As this preliminary study is exclusively concerned with monopiles in dry sand, the first SANISAND-MS version described in Chapter 3 (model formulation based on the back stress variable, see Appendix B) is adopted. This choice will not alter general conclusions about the suitability of the modelling platform for soil-structure interaction problems not involving hydro-mechanical effects (drained conditions).

6.2. SANISAND-MS modelling of multi-amplitude cyclic tests on sand

The calibration and validation of SANISAND-MS has been conducted in previous chapters with exclusive reference to single-amplitude cyclic loading – as most usually done in geotechnical research and practice. However, soils under offshore foundations are normally subjected to highly irregular, non-stationary cyclic loads, whose impact on the interpretation and modelling of cyclic soil behaviour is still an open research question (Andersen, 2015; Zografou et al., 2019). Before exploring 3D FE monopile tilt predictions, this section adds evidence about the performance of SANISAND-MS under multi-amplitude cyclic loading. In particular, compliance with so-called 'Miner's rule' is verified to boost more general confidence about strain accumulation predictions.

Miner's rule is an empirical postulate originally conceived to describe cyclic fatigue mechanisms in metals (Miner et al., 1945; Wilkins, 1956), whose validity was later extended to cyclic straining in soils (Kaggwa et al., 1991; Wichtmann et al., 2010a). The essence of Miner's rule in relation to sand's cyclic behaviour can be summarised by the following two statements:

1. accumulation of irreversible plastic strains is only possible when the current cyclic load amplitude is the highest ever experienced by the material;
2. given a cyclic loading history formed by segments (or packages) of different amplitude, the specific sequence of such packages has only minor influence on the plastic strains finally accumulated (residual strains).

In order to validate SANISAND-MS from a Miner's rule standpoint, the results of multi-amplitude, high-cyclic triaxial tests reported by Wichtmann et al. (2010a) have

been numerically simulated. Laboratory tests were performed on dry, medium-coarse quartz sand (sand properties see Chapter 3), whose SANISAND-MS model parameters have been already identified in Chapter 3 with respect to single-amplitude cyclic loading (see Table 3.2). However, μ_0 has been reduced from 260 to 200 for better simulation of longer loading histories ($N = 10^5$ instead of $N = 10^4$).

All experimental/numerical results reported herein correspond with the following triaxial test settings: $p_{in} = 200$ kPa (mean stress at the beginning of, and during, cyclic loading), $q^{ave} = 150$ kPa (average deviatoric stress during cyclic loading), and initial, pre-cyclic relative density set to $Dr = 59\%$ ($e_{in} = 0.698$, initial void ratio) in numerical simulations to represent the experimental range of $58\% - 63\%$. Cyclic packages of four different deviatoric stress amplitude ($q^{ampl} = 20, 40, 60, 80$ kPa) have been applied according to the following load sequences (Fig. 6.1):

a) 20 kPa → 40 kPa → 60 kPa → 80 kPa;

b) 20 kPa → 60 kPa → 40 kPa → 80 kPa;

c) 60 kPa → 20 kPa → 40 kPa → 80 kPa;

d) 80 kPa → 60 kPa → 40 kPa → 20 kPa.

For each sequence, the accumulated total strain ε^{acc} has been recorded at the end of each cycle when $q = q^{ave}$, without accounting for the very first cycle (see Eq. (3.22))

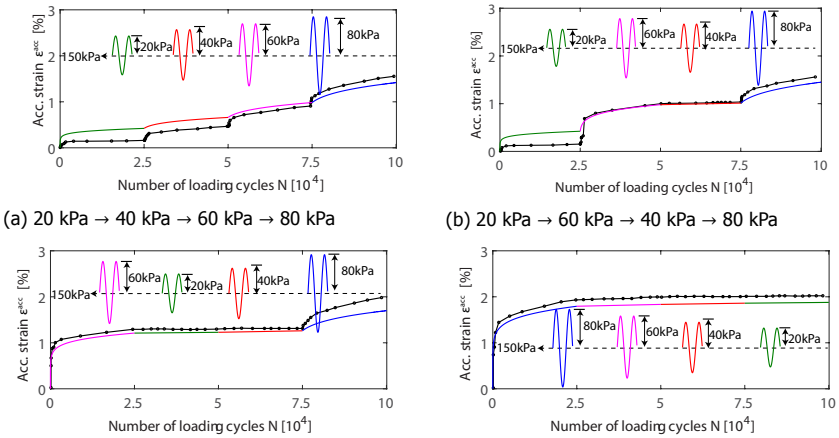

(a) 20 kPa → 40 kPa → 60 kPa → 80 kPa

(b) 20 kPa → 60 kPa → 40 kPa → 80 kPa

(c) 60 kPa → 20 kPa → 40 kPa → 80 kPa

(d) 80 kPa → 60 kPa → 40 kPa → 20 kPa

Figure 6.1: Strain accumulation patterns under different cyclic load sequences. Triaxial test settings: $q^{ave} = 150$ kPa, $p_{in} = 200$ kPa, $e_{in} = 0.698$ ($D_r = 59\%$). Comparison between experimental data from Wichtmann et al. (2010a) (dotted black lines) and SANISAND-MS results (solid lines in colour).

Fig. 6.1 shows generally good agreement between experimental and SANISAND-MS results over the 10^5 cycles considered in the testing programme (4 packages comprising 25000 cycles each). In particular, Fig. 6.1a displays gradual monotonic

increase in ε^{acc} with the number of cycles N, at a rate depending on the current cyclic load amplitude. In Fig. 6.1b obvious strain accumulation occurs during the second package ($q^{ampl} = 60$ kPa), at a rate faster than observed during the first segment of lower amplitude ($q^{ampl} = 20$ kPa); the lower cyclic load in the third stage leads to practically no ratcheting, finally re-activated by the highest load amplitude in the fourth package. Strain accumulation patterns fully consistent with Miner's rule/statement 1 can also be observed for the third (Fig. 6.1c) and fourth (Fig. 6.1d) load sequences. The last case in Fig. 6.1d corroborates the idea of cyclic strain accumulation being dominated by highest load amplitudes as experienced by the soil for the first time.

At the same time, the results in Fig. 6.1 are also open to a reflection on the validity of Miner's rule/statement 2. While individual $\varepsilon^{acc} - N$ trends are specific to the considered load sequence, the residual strain $\varepsilon^{acc}\left(N = 10^5\right)$ lies in all cases in a narrow range, namely $1.7 \sim 2.0\%$. It may thus be concluded that the specific arrangement of cyclic packages has only a weak impact on $\varepsilon^{acc}\left(N = 10^5\right)$, i.e., only a few, high-amplitude packages affect ratcheting in the longest term. On this ground, the results in Fig. 6.1 would seem to confirm the validity of Miner's rule/statement 2. However, note also the seeming tendency of the largest accumulated strain level to occur when the loading package of largest amplitude is applied first –the accumulated strain in Fig. 6.1c and 6.1d is around 2.0% after 10^5 cycles, larger than 1.7% in Fig. 6.1a and 6.1b. Such a difference, confirmed both by experimental and numerical results, may be exacerbated by a larger number of loading cycles, in a way that could lead to question the validity of Miner's rule.

The successful 'Miner's rule performance' of SANISAND-MS (particularly about statement 1) is mainly enabled by the memory surface hardening mechanism described in Chapter 3. As the load sequence transits from higher to lower cyclic amplitude, the relatively large size of the memory surface results in significant distance between the memory surface and yield back-stresses, high soil stiffness through Eqs. (3.8)–(3.11), and therefore limited or negligible strain accumulation. Conversely, an increase in load amplitude implies at its onset 'virgin loading' conditions (yield locus tangent to the memory surface at the current stress point), which gives rise to lower cyclic stiffness and visible ratcheting (until larger memory-to-yield-surface distance is eventually re-established by prolonged repeated loading). Fig. 6.1 adds confidence about applying SANISAND-MS to soil-structure interaction problems involving irregular cyclic loading, with soil parameters calibrated against data from common single-amplitude tests.

6.3. 3D FE modelling of monopiles under lateral cyclic loading

Adequate modelling of soil ratcheting is considered key to numerically reproducing geotechnical mechanisms underlying monopile tilting under lateral cyclic loading (Abadie et al., 2019). For this purpose, sand constitutive modelling based on SANISAND-MS has been combined with 3D FE modelling capabilities offered by the OpenSees FE platform (McKenna, 2011). This section covers relevant information

regarding setup and verification of the 3D FE sand-monopile model. Additional general details in this respect can be found in Corciulo et al. (2017) and Taborda et al. (2019).

6.3.1. Soil and monopile

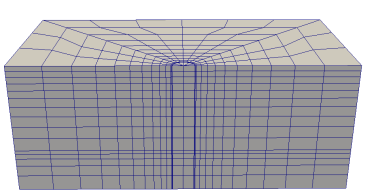

(a) 2300 elements

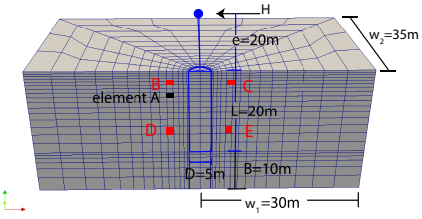

(b) 4100 elements – mesh finally selected

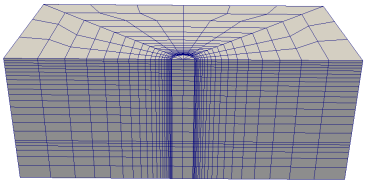

(c) 5400 elements

Figure 6.2: FE model domain and mesh sensitivity study.

Fig. 6.2b illustrates the soil-monopile model set up for the parametric studies discussed in the following. The 3D FE model features:

- elastic tubular monopile,initially 'wished-in-place'. Diameter, embedded length and wall thickness of the pile equal to $D = 5$ m, $L = 20$ m, and $t = 10$ cm, respectively, and are representative of average full-scale monopiles;
- soil domain size characterised by $[W_1, W_2, L + B] = [30\text{m}, 35\text{m}, 30\text{m}]$ (Fig. 6.2b). As the following discussion concerns mono-directional lateral loading, only half domain was modelled/discretised for computational convenience;
- lateral loading applied with eccentricity $e_{ecc} = 20$ m above the soil surface. The load application point was connected to the 3D pile head at the mudline through an elastic Timoshenko beam.

Both soil and embedded monopile were discretised using 8-node, one-phase SSP brick elements, whose stabilised, single-point formulation has proven effective against

shear/volumetric locking issues in the FE analysis of elasto-plastic media (McGann et al., 2015). Non-linear static simulations of cyclic pile loading were performed using implicit, backward Euler integration, with the iterative solution of each step based on the Krylov–Newton algorithm described by Scott and Fenves (2003). SANISAND-MS constitutive equations were integrated at each stress point by means of the explicit 4th-order Runge-Kutta method with sub-stepping and automatic error control (Sloan et al., 2001). Soil boundary conditions were set to obtain a fully fixed bottom surface, free upper surface, and no horizontal displacement along the direction perpendicular to the lateral surface.

All FE results were obtained using the reference SANISAND-MS parameters in Table 3.2, calibrated in Chapter 3 for the quartz sand most often tested by Wichtmann and co-workers under high-cyclic loading conditions (Wichtmann, 2005; Wichtmann et al., 2010a). Typical values of Young's modulus ($E_{steel} = 221$GPa) and Poisson's ratio ($\nu_{steel} = 0.3$) were set for the elastic steel monopile.

Following the simplified approach by Griffiths (1985), the pile-sand interface was modelled by introducing around the pile a thin layer of soil bricks with different mechanical properties. Accordingly, 'degraded' interface properties were selected to reproduce possible effects of pile installation, though without attempting to model interface gapping during cyclic loading (Day and Potts, 1994; Cerfontaine et al., 2015). The interface layer in the final model is as thick as $\backsim 2\%$ of the monopile diameter, and characterised by perfectly elasto-plastic behaviour (Drucker-Prager model). The following interface material properties were selected: Young's modulus $E_{int} = 257$ MPa, Poisson's ratio $\nu_{int} = 0.3$, cohesion $c_{int} = 0$ kPa, friction angle $\phi_{int} = 23.5°$ (triaxial compression), dilatancy angle $\psi_{int} = 0°$.

6.3.2. Numerical simulation programme

Although non-stationary and multi-directional in reality (LeBlanc et al., 2010; Rudolph et al., 2014; Richards et al., 2019), only mono-directional lateral loading applied in single-amplitude cycles was considered for simplicity. Numerical parametric studies were performed according to the simulation programme in Table 6.1, encompassing two values of initial relative density in the sand domain, $D_r = 30\%$ and 70%. Such values were selected as representative of generally loose and dense sand, though without trying to match specific soil conditions in the reference small-scale experiments (see next section). In all cases, the total number of cycles was limited to $N = 100$, which made less concerning the aforementioned issue of numerical error accumulation.

The simulation programme in Table 6.1 has been conceived to study in a 3D FE environment the influence of different load settings on cyclic monopile tilt. In particular, minimum/maximum lateral load values (H in Fig. 6.2b) were set up to modify the amplitude and form of cyclic loading according to the following dimensionless groups defined by LeBlanc et al. (2010):

$$\zeta_b = \frac{H_{max}}{H_{ref}} = \frac{M_{max}}{M_{ref}} \qquad \zeta_c = \frac{H_{min}}{H_{max}} = \frac{M_{min}}{M_{max}} \tag{6.1}$$

where H_{max} (M_{max}) and H_{min} (M_{min}) (as illustrated in Fig. 6.5) stand for maximum

Table 6.1: Numerical simulation programme.

Test label	D_r	ζ_b	ζ_c	Test label	D_r	ζ_b	ζ_c
L1	30%	0.8	0	D1	70%	0.8	0
L2	30%	0.5	0	D2	70%	0.5	0
L3	30%	0.3	0	D3	70%	0.3	0
L4	30%	0.5	0.8	D4	70%	0.5	0.8
L5	30%	0.5	0.5	D5	70%	0.5	0.4
L6	30%	0.5	0.3	D6	70%	0.5	0.2
L7	30%	0.5	-0.3	D7	70%	0.5	-0.2
L8	30%	0.5	-0.5	D8	70%	0.5	-0.5
L9	30%	0.5	-0.7	D9	70%	0.5	-0.8

and minimum horizontal load (moment) at mud line, respectively. H_{ref} (M_{ref}) is the reference horizontal force (moment) that causes a given reference displacement (or rotation) at the soil surface. Based on typical serviceability arguments, H_{ref} (M_{ref}) has been associated with a rotation of the pile equal to $\theta_{ref} = 0.5°$, and quantified through 3D FE calculations to be 5600 kN and 4400 kN for $D_r = 70\%$ and $D_r = 30\%$, respectively. Both one-way loading ($\zeta_c \geq 0$, positive H_{max} and H_{ref}) and (biased) two-way loading ($-1 < \zeta_c < 0$, positive H_{max} and negative H_{min}) have been considered in the simulations, with cyclic loading applied in the form of sinusoidal load histories.

6.3.3. Sensitivity of FE results to space discretisation

After following tested guidelines for sizing the soil domain (Fig. 6.2b, cf. to Corciulo et al. (2017)), the sensitivity of FE results to space discretisation was investigated. To this end, results from the three different FE meshes in Fig. 6.2 were compared for the L6 case in Table 6.1 – total SSP element number equal to 2300, 4100 and 5400 in Figs. 6.2a, 6.2b, 6.2c, respectively. Fig. 6.3 illustrates simulated pile responses at varying number of elements, namely in terms of force-displacement behaviour (Fig. 6.3a, pile displacement recorded at soil surface) and accumulated pile displacement against the number of loading cycles (Fig. 6.3b). Finer FE discretisation results in higher displacement accumulation at the soil surface. However, since a converging trend was observed upon mesh refinement, the intermediate mesh in Fig. 6.2b (4100 elements) was finally selected as a trade-off between accuracy and efficiency.

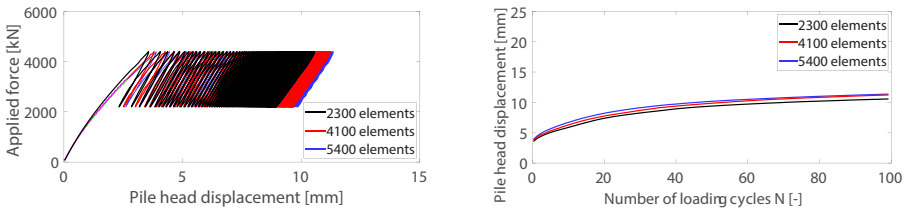

(a) Lateral force vs pile head displacement at soil surface (b) Pile head displacement vs number of loading cycles

Figure 6.3: Monopile response to lateral cyclic loading loading predicted through SANISAND-MS ($D_r = 30\%$). Influence of FE discretization.

6.4. Cyclic monopile tilt simulations

There is wide evidence in recent experimental literature that cyclic monopile tilt in dry sand is mostly affected by (i) soil type/behaviour, (ii) pile geometry/properties, and (iii) lateral loading conditions – including amplitude and asymmetry of load cycles, spatial orientation, eccentricity with respect to soil surface (Houlsby, 2016). In this section, general features of 3D FE results (Table 6.1) are inspected by qualitative comparison to 1g small-scale test results from the literature. As already stated above, the following 3D FE results are no attempt to reproduce the response of a specific pile-sand system, but rather to verify general compliance with established experimental knowledge. Special consideration is given to the data reported by LeBlanc et al. (2010) and Richards et al. (2019):

- LeBlanc et al. (2010): Yellow Leighton Buzzard 14/25 sand ($D_{50} = 0.81$ mm, $D_{10} = 0.56$ mm, maximum (dry) unit weight $\gamma_{max} = 17.64$ kN/m^3, minimum (dry) unit weight $\gamma_{min} = 14.43$ kN/m^3, coefficient of uniformity $C_u = D_{60}/D_{10} = 1.55$, critical friction angle $\phi_{cr} = 34.3°$), embedded pile length $L = 360$ mm, diameter $D = 80$ mm ($D/L = 0.22$), wall thickness $t = 2$ mm ($t/D = 0.025$), load eccentricity $e_{ecc} = 430$ mm ($e_{ecc}/L = 1.19$).
- Richards et al. (2019): Yellow Leighton Buzzard sand ($D_{50} = 0.8$ mm, $D_{10} = 0.63$ mm, maximum (dry) unit weight $\gamma_{max} = 17.58$ kN/m^3, minimum (dry) unit weight $\gamma_{min} = 14.65$ kN/m^3, coefficient of uniformity $C_u = D_{60}/D_{10} = 1.35$, critical friction angle $\phi_{cr} = 34.3°$), embedded pile length $L = 320$ mm, diameter $D = 80$ mm ($D/L = 0.25$), wall thickness $t = 5$ mm ($t/D = 0.0625$), load eccentricity $e_{ecc} = 800$ mm ($e_{ecc}/L = 2.5$).

As different soil/pile/loading settings were considered in numerical simulations and reference experiments, emphasis is on verifying that SANISAND-MS can reproduce general features of cyclic soil-monopile interaction in loose and dense sand. In what follows, the term 'pile head' refers to pile response at the level of soil surface.

6.4.1. Cyclic tilt accumulation

Typical cyclic responses recorded at the pile head are plotted in Fig. 6.4 for the example cases D2 and L2 in Table 6.1. Figs. 6.4a and 6.4c clearly show that the pile head displacement induced by the first monotonic loading (i.e., up to point P in the figures) is significantly larger than the displacement generated within each of the subsequent loading cycles. Displacement accumulation can be observed to progress under cyclic loading at a gradually decreasing rate. This kind of ratcheting behaviour at the pile scale appears fully related to the cyclic ratcheting of sand samples tested in the laboratory (Wichtmann, 2005; Liu et al., 2019). Alternative visualisation of pile head ratcheting is provided in Figs. 6.4b and 6.4d in terms of accumulated displacement/rotation against the number of cycles N. Under the same load settings and drained conditions, the relative density has a quantitative impact on soil-pile deformation, though not on qualitative features of behaviour. Fig. 6.4 is overall encouraging about the performance of SANISAND-MS when compared with typical pile behaviour emerging from experimental studies (Houlsby, 2016).

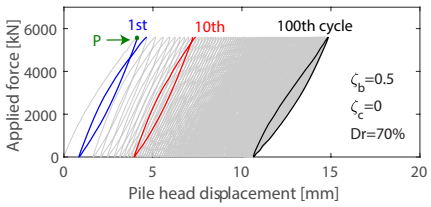

(a) Lateral force vs pile head displacement (D_r = 70%)

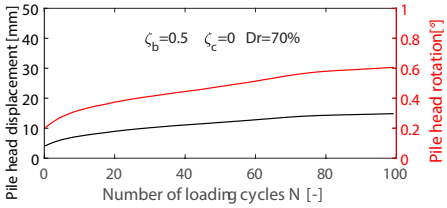

(b) Pile head displacement/rotation vs number of cycles (D_r = 70%)

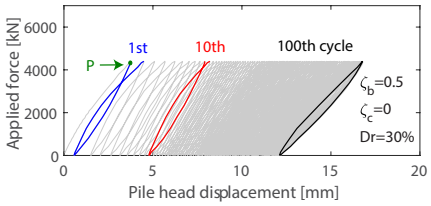

(c) Lateral force vs pile head displacement (D_r = 30%)

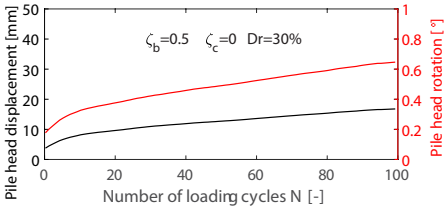

(d) Pile head displacement/rotation vs number of cycles (D_r = 30%)

Figure 6.4: Cyclic pile head response associated with the use of SANISAND-MS in 3D FE simulations – example cases D2 and L2 in Table 6.1.

6

For a clearer interpretation of cyclic lateral behaviour, it is common to present pile rotation outputs after normalisation with respect to a reference rotation θ_s. Numerical results regarding monopile tilt accumulation are provided in the following in the normalised form $\Delta\theta/\theta_s$, where $\Delta\theta = \theta_N - \theta_0$ is the difference between rotation accumulated after N cycles (θ_N) and rotation at the end of monotonic loading (θ_0) (see Fig. 6.5), and θ_s is assumed to coincide with θ_0.

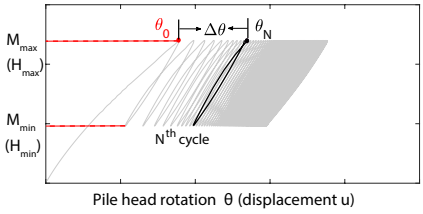

Figure 6.5: Definition of relevant pile rotation values.

Lin and Liao (1999) suggested that normalised pile head rotation, $\Delta\theta/\theta_s$, accumulates linearly with $\ln(N)$, in a way found to gradually diverge from experimental data at large N. Conversely, LeBlanc et al. (2010) proposed to use a bi-logarithmic relationship in the form $\log(\Delta\theta/\theta_s) \propto \log(N)$. In light of experimental results, for instance from LeBlanc et al. (2010) and Truong et al. (2019), the latter approach seems preferable for short/stiff monopiles.

Pseudo-colour plots of D_r evolution in the soil are displayed in Fig. 6.6 for the same tests $L2$ (D_r = 30%) and $D2$ (D_r = 70%). In particular, D_r distributions

after 10 and 100 cycles are illustrated at longitudinal/vertical (along pile diameter parallel to loading direction) and transverse/horizontal ($2.5m$ below soil surface) cross-sections.

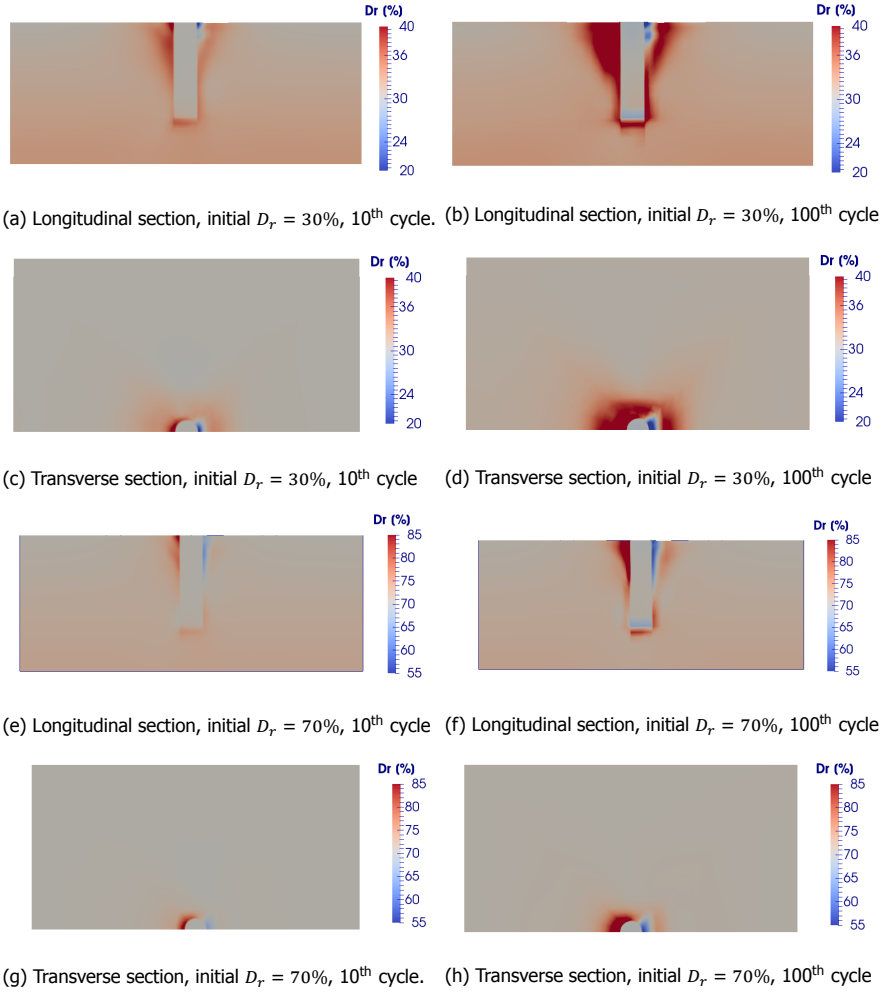

(a) Longitudinal section, initial $D_r = 30\%$, 10th cycle. (b) Longitudinal section, initial $D_r = 30\%$, 100th cycle

(c) Transverse section, initial $D_r = 30\%$, 10th cycle (d) Transverse section, initial $D_r = 30\%$, 100th cycle

(e) Longitudinal section, initial $D_r = 70\%$, 10th cycle (f) Longitudinal section, initial $D_r = 70\%$, 100th cycle

(g) Transverse section, initial $D_r = 70\%$, 10th cycle. (h) Transverse section, initial $D_r = 70\%$, 100th cycle

Figure 6.6: Distribution of sand relative density (D_r) after 10 and 100 loading cycles – example cases L2 (a-d) and D2 (e-h) in Table 6.1.

D_r pseudo-colour plots in Fig. 6.6 confirm available evidence about cyclic densification from the literature (Cuéllar et al., 2009). It is generally observed that D_r variations are more pronounced in loose sand than in dense sand. As the selected FE results concern pure one-way loading ($\zeta_b = 0.5, \zeta_c = 0$), asymmetric sand densification is predicted on the opposite sides of the pile, most severely in the shallowest soil. Unsurprisingly, transverse cross-sections show asymmetric distributions along horizontal radii of different orientation. Occurrence of some sand loosening is also

visible along the upper shaft on the back-side with respect to the loading direction (Fig. 6.2b), due to compression relief and, in dense sand, shear-induced dilation.

Implicit 3D FE analyses return a wealth of information regarding the local response of the soil while the pile is cyclically loaded. Illustrative examples are provided hereafter with reference to the same cases $L2$ ($D_r = 30\%$) and $D2$ ($D_r = 70\%$) discussed so far. Figs. 6.7 - 6.10 display the cyclic response of the soil at four specific locations, spanning shallow (elements B and C in Fig. 6.2b) and deeper depths (elements D and E) on two opposite sides of the symmetry plane with respect to the pile at the centre. The first monotonic branch is excluded from the soil response plots, while focus is on the cyclic results following the first occurrence of $H = H_{ave}$ ($= (H_{Max} + H_{min})/2$) at the monopile head.

The cyclic evolution of volumetric (ε_{vol}) and deviatoric (ε_{dev}) strain invariants is illustrated in Fig. 6.7 for the four elements B, C, D, and E. The shallowest elements (element B and C are placed about 1.8 m below the soil surface) seem to be more prone to strain accumulation, both volumetric and deviatoric, than elements D and E located at about 15 m depths. For a given depth, there is an asymmetry in response promoted by the applied load bias H_{ave}, so that elements B and D (on the side of compressed by H_{ave}) tend to experience weaker deviatoric straining than elements C and E on the opposite side of the pile. As expected, strain accumulation is substantially affected by the initial relative density, with more pronounced volume changes (especially at shallow locations) observed in the case of looser sand ($D_r = 30\%$). In contrast, D_r has limited influence on the 'cyclic flow rule', i.e., on the ratio between accumulated volumetric and deviatoric strains.

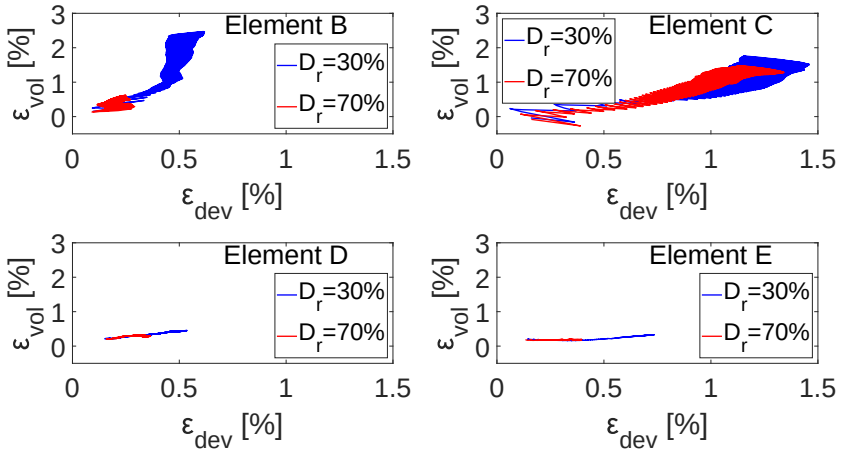

Figure 6.7: Cyclic evolution of volumetric and deviatoric strains at elements B - E in Fig. 6.2b.

The evolution of the effective mean stress p in elements B - E against the volumetric strain ε_{vol} is illustrated in Fig. 6.8. It is interesting to note a substantial cyclic reduction in p for the case $D_r = 30\%$, especially at the shallowest soil locations. Conversely, the case with denser sand ($D_r = 70\%$) shows different p-trends on the

two sides of the pile, probably due to different triggering and evolution of dilative deformations. The soil response at element C is characterised by p approaching zero for both $D_r = 30\%$ and 70%, in a way that would be more normally expected under undrained conditions (it is worth recalling that only dry sand is considered in this chapter). Variations in p are much lower at deeper soil locations, which leads to confirm the general belief that variations in lateral pile stiffness are more strongly affected by the sand mass closer to the free surface.

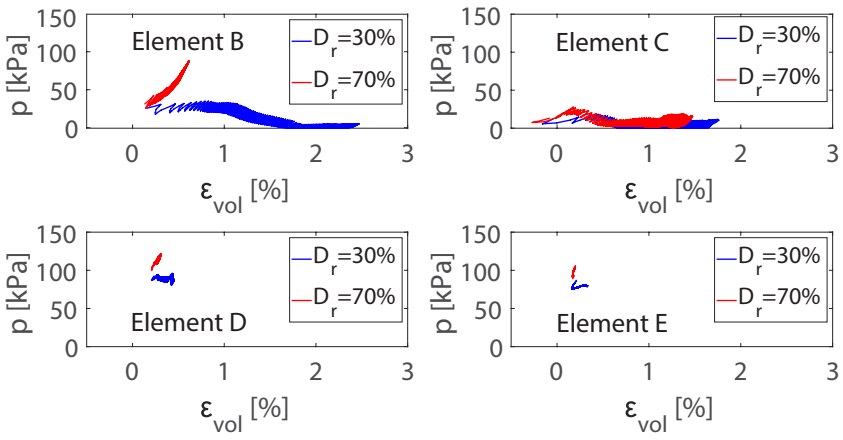

Figure 6.8: Cyclic p - ε_{vol} response at elements B - E in Fig. 6.2b.

Additional information is provided by the soil $q - p$[1] stress paths in Fig. 6.9. Deeper soil elements (D and E) experience a drastic reduction in deviatoric loading, even though the corresponding changes in p are relatively small. Reversals in the sign of q are only observed for elements B and C, which therefore are subjected to both compressive and extensive type of loading. The vanishing of p already shown in Fig. 6.8 is complemented in Fig. 6.9 by the 'butterfly' shape of the stress paths at elements B (for the loose sand case) and C (for both L2 and D2 simulations). Such a behaviour resembles the undrained cyclic mobility response widely discussed in Chapter 5. A plausible explanation of such occurrence lies in the action of 'spontaneous' volumetric constraints due to current boundary/loading conditions, which may in turn pose a limit on cyclic volume changes even with no pore fluid – in a way similar to the experimental results shown by Tsuha et al. (2012) for piles under cyclic axial loading. This conjecture is confirmed by Fig. 6.10, where the evolution of the volumetric strain at element C is plotted against the number of loading cycles N. Indeed, Fig. 6.10 shows negligible cyclic compaction after about 20 cycles both in loose and dense sand, and therefore confirms the establishment of nearly 'isochoric' conditions – hence, the peculiar undrained-like shape of the reference stress path in Fig. 6.9.

[1]Under general multiaxial conditions, the deviatoric stress q is defined as $\sqrt{3J_2}\cos 3\theta$, with $\cos 3\theta = (3\sqrt{3}J_3)/(2J_2^{1.5})$. J_2 and J_3 are the second and the third stress invariant, respectively

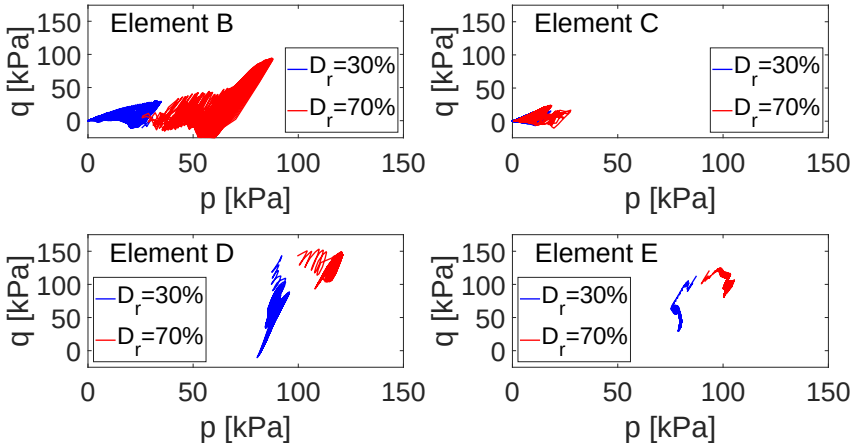

Figure 6.9: Cyclic stress paths at elements B - E in Fig. 6.2b.

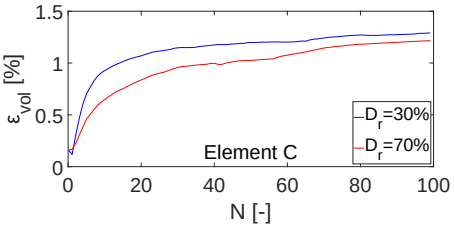

Figure 6.10: Volumetric strain accumulations against the number of cycles at element C.

Overall, Figs. 6.6 - 6.10 give an impression of the valuable information that one can infer from 3D FE simulation results to investigate governing soil-foundation interaction mechanisms. In the following, further evidence of the suitability of the SANISAND-MS model is provided by qualitatively comparing simulated pile tilting to the results of selected small-scale tests.

6.4.2. Response to single-amplitude, one-way cyclic loading

Experimental and numerical results regarding monopile tilt are qualitatively compared in Fig. 6.11 for cyclic loading of varying amplitude ratio ζ_b and nil ζ_c (pure one-way cyclic loading, Eq. (6.1)). $1g$ small-scale experimental results from Richards et al. (2019) (Fig. 6.11a – $D_r = 1\%$, and Fig. 6.11b – $D_r = 60\%$) and LeBlanc et al. (2010) (Fig. 6.11c – $D_r = 4\%$, and Fig. 6.11d – $D_r = 38\%$) were selected for comparison. As noted by Richards et al. (2019), relative densities from very low to low were used in the reference 1g tests 'to better approximate dilation and friction angles at full scale, where the stress level is higher' (Bolton, 1986; Altaee

and Fellenius, 1994) – and therefore to mimic full-scale pile behaviour in loose and dense sand. Out of the simulation programme in Table 6.1, 3D FE results from cases L1–L3 and D1–D3 are illustrated in Fig. 6.11e ($D_r = 30\%$) and 6.11f ($D_r = 70\%$) as being mostcomparable to the experimental data under consideration.

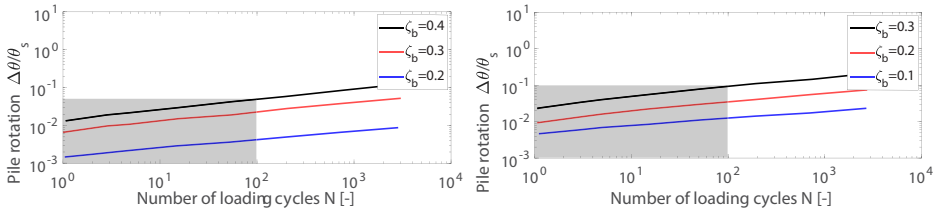

(a) $D_r = 1\%$, experimental data from Richards et al. (2019)

(b) $D_r = 60\%$, experimental data from Richards et al. (2019)

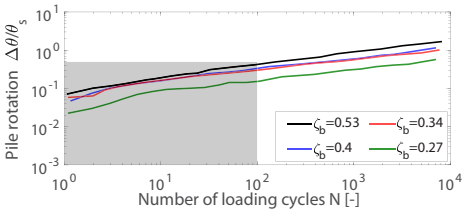

(c) $D_r = 4\%$, experimental data from LeBlanc et al. (2010)

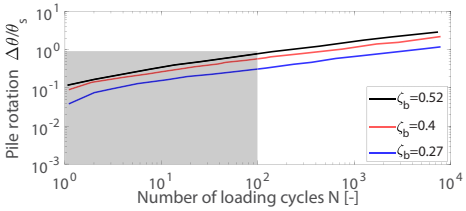

(d) $D_r = 38\%$, experimental data from LeBlanc et al. (2010)

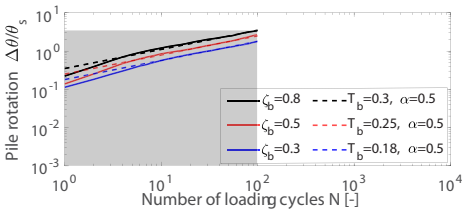

(e) $D_r = 30\%$, SANISAND-MS 3D FE results

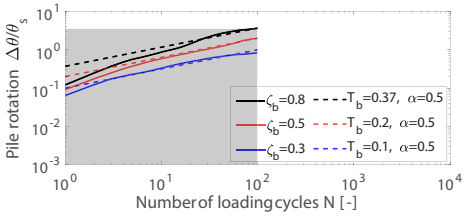

(f) $D_r = 70\%$, SANISAND-MS 3D FE results

Figure 6.11: Influence of cyclic load amplitude ratio (ζ_b) on normalised pile tilt ($\Delta\theta/\theta_s$) against the number of loading cycles (N). Experimental and 3D FE results correspond with pure one-way cyclic loading ($\zeta_c = 0$).

Both experimental and simulation results indicate that, under pure one-way cyclic loading, higher ζ_b values lead to accumulation of larger pile rotation. In particular, all $\Delta\theta/\theta_s - N$ log-log trends seem to approach linearity after about ten cycles. Such occurrence can be observed both in loose and dense sand, and gives confidence that sound conclusions about tilting trends may be inferred from numerical calculations limited to hundreds of cycles – at least in the case of regular, single-amplitude cyclic loading.

From a quantitative standpoint, 3D FE simulations predict $\Delta\theta/\theta_s$ values in the order of 10^0 after 100 cycles. Such values are consistent with experimental data from LeBlanc et al. (2010), where normalised rotation values of about $7 \sim 8 \times 10^{-1}$ are reported. Conversely, Richards et al.'s work shows after 100 cycles $\Delta\theta/\theta_s - N$

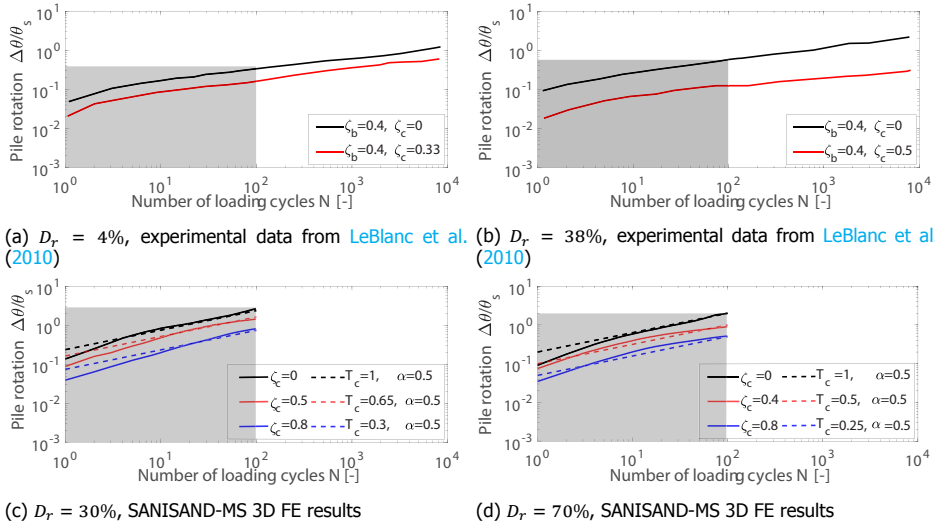

(a) D_r = 4%, experimental data from LeBlanc et al. (2010)

(b) D_r = 38%, experimental data from LeBlanc et al. (2010)

(c) D_r = 30%, SANISAND-MS 3D FE results

(d) D_r = 70%, SANISAND-MS 3D FE results

Figure 6.12: Influence of positive cyclic load asymmetry ratio (ζ_c) on normalised pile tilt ($\Delta\theta/\theta_s$) against the number of loading cycles (N) – ζ_b = 0.5.

6

values in the range of $10^{-3} \sim 10^{-2}$, i.e., about one order of magnitude smaller. Both datasets from LeBlanc et al. (2010) and Richards et al. (2019) suggest that, for given ζ_b, more pile rotation accumulates when sand is denser. This outcome, however, is confirmed by numerical simulations only for high ζ_b values. It is argued that significant quantitative differences may be attributed to, among other factors, difference in sand type and size scaling (Klinkvort et al., 2018). More research in this area is certainly needed to further investigate scaling effects across different modelling approaches, both physical and numerical.

Fig. 6.12 concerns the influence of ζ_c (asymmetry of cyclic load) on monopile tilting under biased one-way loading (i.e., $\zeta_c \geq 0$, no change in the sign of the load). SANISAND-MS 3D FE results (Fig. 6.12c – D_r = 30%, and Fig. 6.12d – and 70%; simulations L2, L4, L5 and D2, D4, D5 in Table 6.1) and experimental results from LeBlanc et al. (2010) (Fig. 6.12a – D_r = 4%, and Fig. 6.12b – D_r = 38%) are compared in the figure. It can be readily noticed that both experiments and numerical simulations support the following general conclusions:

1. nearly linear tilt accumulation trends in bi-logarithmic plots;
2. accumulated rotation after 100 cycles lying in the $10^0 - 10^{-1}$ range;
3. lower accumulated rotation at increasing ζ_c when $\zeta_c \geq 0$.

6.4.3. Response to single-amplitude, two-way cyclic loading

Differences in pile response as cyclic loading shifts from one-way (positive ζ_c) to two-way (negative ζ_c) are examined in this sub-section. Richards et al.'s test results in Fig. 6.13a show that, for ζ_b = 0.2, highest $\Delta\theta/\theta_s$ values emerge at given N as

$\zeta_c = -0.6$. More clearly, evidence of non-monotonic dependence on ζ_c is visible in LeBlanc et al.'s test results (Fig. 6.13b): for the given $\zeta_b = 0.4$, the accumulated rotation associated with $\zeta_c = -0.67$ is larger than in the cases with $\zeta_c = -0.34$ and $\zeta_c = -0.98$. Fig. 6.13c–6.13d illustrate SANISAND-MS 3D FE results associated, for completeness, both with nil and negative ζ_c values and $\zeta_b = 0.5$. Similarly to what suggested by experimental data, the largest rotation is predicted for intermediate negative values of ζ_c, i.e., $\zeta_c = -0.3$ for $D_r = 30\%$ and $\zeta_c = -0.2$ for $D_r = 70\%$.

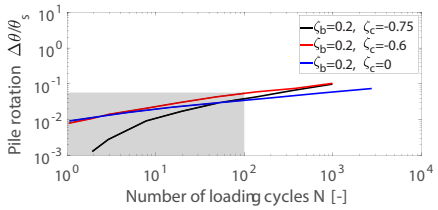

(a) D_r = 60%, experimental data from Richards et al. (2019)

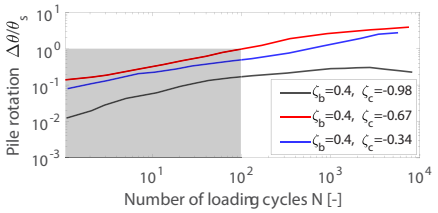

(b) D_r = 4%, experimental data from LeBlanc et al. (2010)

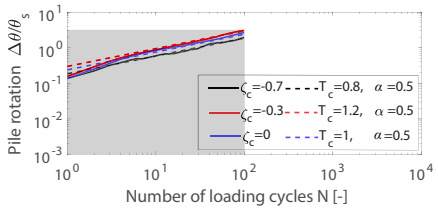

(c) D_r = 30%, SANISAND-MS 3D FE results

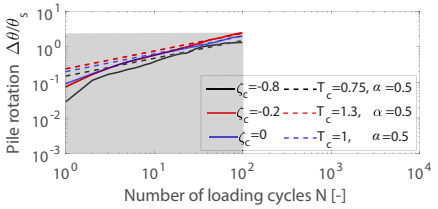

(d) D_r = 70%, SANISAND-MS 3D FE results

Figure 6.13: Influence of negative cyclic load asymmetry ratio (ζ_c) on normalised pile tilt ($\Delta\theta/\theta_s$) against the number of loading cycles (N) – $\zeta_b = 0.5$.

Regarding more quantitative aspects, Fig. 6.13 confirms conclusions similar to those inspired by Fig. 6.11:

1. Richards et al.'s data show accumulated rotations about one order of magnitude smaller than LeBlanc et al.'s data and 3D FE results;
2. for the same sand type, the accumulated rotation after the considered number of loading cycles stays within the same order of magnitude, regardless of the sand relative densities and ζ_c levels;
3. Richards et al.'s data show converging $\Delta\theta/\theta_s - N$ trends in the medium-high N range, i.e., similar values of monopile rotation evolving with practically the same rate (cf. black, blue, and red solid lines in Fig. 6.13a).

6.5. FE-based assessment of empirical laws for tilt prediction

Recent experimental studies have boosted consensus around the use of the following empirical relationship to quantify monopile tilt accumulation under lateral cyclic

loading (LeBlanc et al., 2010):

$$\frac{\Delta\theta}{\theta_s} = T_b\,(\zeta_b)\,T_c\,(\zeta_c)\,N^{\alpha} \tag{6.2}$$

where T_b and T_c are dimensionless functions separately accounting for the influence of ζ_b and ζ_c, respectively. T_c is defined such that $T_c(\zeta_c = 0) = 1$, $T_c(\zeta_c = \pm 1) = 0$. As for the ratcheting exponent α, different conclusions regarding its range have been drawn on the basis of 1g (LeBlanc et al., 2010) and centrifuge (Truong et al., 2019) small-scale test data. 3D FE results are further inspected in this section to gain more insight into the relationship between geotechnical/loading conditions and the validity/calibration of Eq. (6.2).

6.5.1. Assumption 1: unique ratcheting exponent

LeBlanc et al. (2010) suggested T_b to be a monotonically increasing function of ζ_b influenced by D_r, whereas T_c was found to be D_r-insensitive and non-monotonically varying with ζ_c; a unique value of the ratcheting exponent, $\alpha = 0.31$, was proposed, unaffected by $D_r/\zeta_b/\zeta_c$. Curve-fitting of experimental data based on Eq. (6.2) led the authors to identify a linear relationship between T_b and ζ_b, with a higher slope for dense sand than for loose sand.

As shown in Fig. 6.11 (dash lines), Eq. (6.2) with constant α was also used to fit 3D FE results associated with varying ζ_b and $\zeta_c = 0$ ($T_c = 1$). Best-fitting T_b values are reported in the legends of Figs. 6.11e–6.11f, along with the identified ratcheting exponent $\alpha = 0.5$. Empirical extrapolations fit 3D FE tilt trends well, especially after a few initial cycles. $T_b - \zeta_b$ relationships inferred from SANISAND-MS 3D FE simulations are reported in Fig 6.14 both for loose and dense sand. In agreement with LeBlanc et al.'s findings, $T_b - \zeta_b$ trends are practically linear, with a steeper slope for $D_r = 70\%$ than for $D_r = 30\%$.

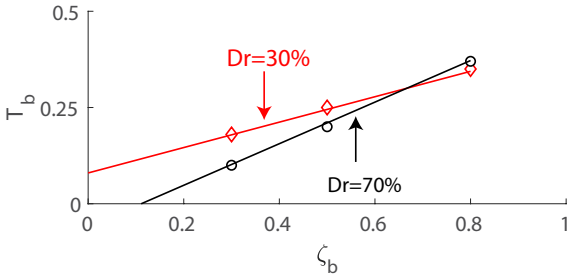

Figure 6.14: $T_b - \zeta_b$ trends for loose and dense sands inferred from SANISAND-MS 3D FE results – pure one one-way cyclic loading ($\zeta_c = 0$).

Numerical $T_c - \zeta_c$ trends were extracted in a similar manner for the 3D FE results plotted in Figs. 6.12–6.13. Using the same exponent $\alpha = 0.5$, identified T_c values are reported in the legends of relevant sub-plots, and re-plotted in Fig. 6.15 against ζ_c for $\zeta_b = 0.5$ and $D_r = 30\%$ ($T_b = 0.25$), 70% ($T_b = 0.2$). Fig. 6.15 also allows comparison to data from previous experimental studies, represented by different

grey markers (LeBlanc et al., 2010; Zhu et al., 2012; Nicolai and Ibsen, 2014; Albiker et al., 2017; Richards et al., 2019).

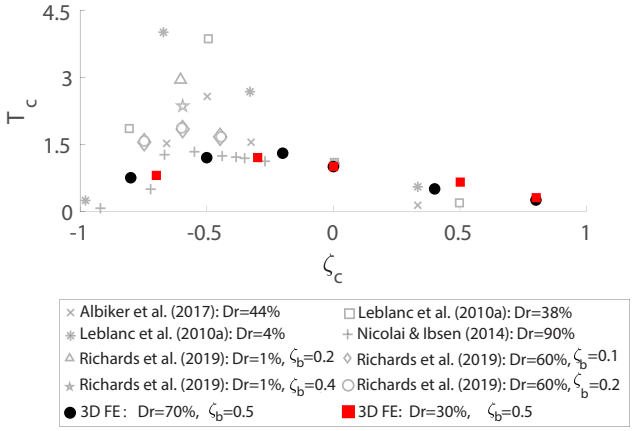

Figure 6.15: $T_c - \zeta_c$ trends for loose/dense sands and $\zeta_b = 0.5$ inferred from SANISAND-MS 3D FE results and compared to experimental data from the literature.

The following conclusions can be drawn based on Fig. 6.15 – integrated with 3D FE results after the initial data survey by Richards et al. (2019):

(1) while LeBlanc et al. (2010) observed D_r-insensitive T_c values, numerical simulations show some (slight) influence of sand relative density, in closer agreement with Richards et al.'s findings;

(2) LeBlanc et al. (2010) indicated a peak T_c value of about 4. This seems to overestimate the outcomes of other test programmes, according to which the maximum T_c would lie in the range from 1 to 2.5. Albiker et al. (2017) attributed this aspect to differences in load eccentricity e_{ecc} among different studies – they argued that larger eccentricity would result in a lower T_c peak. However, this explanation does not justify the differences in peak T_c values obtained, for instance, by LeBlanc et al. (2010) ($e_{ecc}/L = 1.2$) and Richards et al. (2019) ($e_{ecc}/L = 2.5$). Grasping the influence of other factors, such as pile slenderness and flexibility, will require additional research;

(3) LeBlanc et al.'s data show peak T_c corresponding with $\zeta_c \approx -0.6$, i.e., with biased two-way cyclic loading. The set of available 3D FE results indicate somewhat higher ζ_c, around -0.25, which is more in line with Albiker et al.'s results. Other experimental data in Fig. 6.15 show that T_c tends to peak over a certain ζ_c range, namely in between -0.6 and -0.3. It may be concluded that ζ_c values that maximise T_c are likely sensitive to loading conditions, geometry, and soil characteristics.

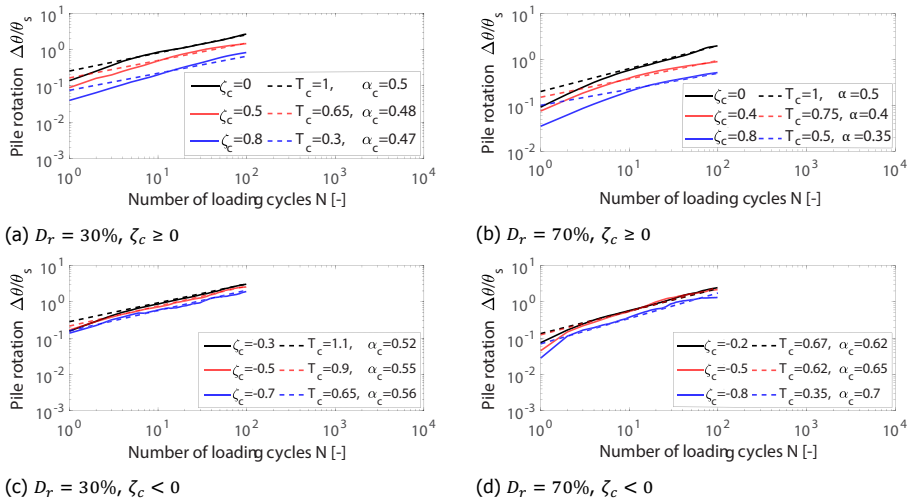

(a) $D_r = 30\%$, $\zeta_c \geq 0$ (b) $D_r = 70\%$, $\zeta_c \geq 0$

(c) $D_r = 30\%$, $\zeta_c < 0$ (d) $D_r = 70\%$, $\zeta_c < 0$

Figure 6.16: Enhanced fitting of SANISAND-MS 3D FE results (solid lines) using Eq. (6.2) with ζ_c/D_r-dependent α (dashed lines). All numerical results relate to lateral cyclic loading with $\zeta_b = 0.5$.

6

6.5.2. Assumption 2: Loading type and relative density dependent ratcheting exponent

Although relatively satisfactory, fitting tilting trends with a constant ratcheting exponent (Figs. 6.12–Fig. 6.13) does not seem to be the most accurate option. Truong et al. (2019) suggested that a better match can be obtained by including the dependence of α (in Eq. (6.2)) on ζ_c and D_r – the symbol α_c is henceforth used to indicate the ζ_c/D_r-dependent ratcheting exponent. The suitability of such an approach was later confirmed by Richards et al. (2019), and is here further assessed in light of SANISAND-MS 3D FE results.

Dashed lines in Fig. 6.16 fit simulated tilting trends with case-specific T_c and α_c values, all reported in relevant legends. As expected, flexibility in the ratcheting exponent results, case by case, in a higher quality-of-fit. Fig. 6.17b overviews the influence of ζ_c and D_r on the α_c/α ratio (with $\alpha = 0.5$) for the 3D FE results taken into consideration. Numerical simulations hint that α_c/α decreases linearly with ζ_c both for loose ($D_r = 30\%$) and dense ($D_r = 70\%$) sand conditions, with a higher decreasing rate in the latter case. The value of α_c/α for pure one-way cyclic loading ($\zeta_c = 0$) is approximately 1 regardless of the relative density.

The conclusions drawn after 3D FE modelling are in excellent agreement with the experiment-based findings of Richards et al. (2019) in Fig. 6.17a – although limited to two-way cyclic loading ($\zeta_c < 0$). Both numerical and experimental results support the use of ζ_c-D_r-dependent α values for the empirical prediction of monopile tilt under lateral cyclic loading.

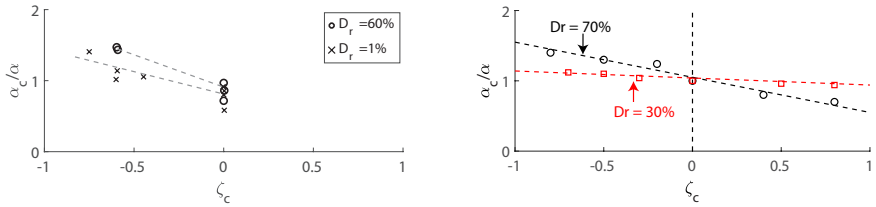

(a) experimental results from Richards et al. (2019) (b) SANISAND-MS 3D FE results

Figure 6.17: Dependence of α_c/α ratio on ζ_c and D_r, as proposed by Truong et al. (2019).

6.5.3. Upscaling of Miner's rule

It has been previously shown that SANISAND-MS can predict the ratcheting of sand samples under multi-amplitude cyclic loading, at the applied loading cycle level (N up to 10^5). In particular, the validity of the empirical Miner's rule (mainly the statement 1) has been numerically confirmed, for the considered cases, at the scale of the laboratory soil samples (Fig. 6.1). Observations from recent experimental studies support the idea of upscaling Miner's rule to describe ratcheting phenomena in monopile-soil systems subjected to cyclic loading (Li et al., 2015; Truong et al., 2019; Abadie et al., 2019). Additional support to such evidence is provided hereafter on the basis of SANISAND-MS 3D FE results. For this purpose, numerical simulations were performed using the same FE model in Fig. 6.2b to study the effect on monopile tilting of different sequences of uni-directional, multi-amplitude cyclic loading – initial $D_r = 30\%$. All simulation cases feature three different load packages of 100 cycles each – see sub-captions in Figs. 6.18 – 6.19.

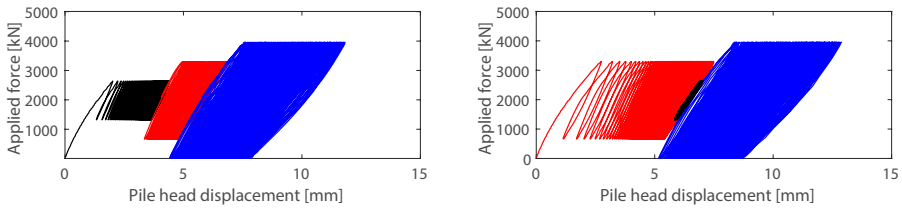

(a) $\zeta_b = 0.3, \zeta_c = 0.5 \rightarrow \zeta_b = 0.375, \zeta_c = 0.2 \rightarrow \zeta_b = 0.45, \zeta_c = 0$ (b) $\zeta_b = 0.375, \zeta_c = 0.2 \rightarrow \zeta_b = 0.3, \zeta_c = 0.5 \rightarrow \zeta_b = 0.45, \zeta_c = 0$

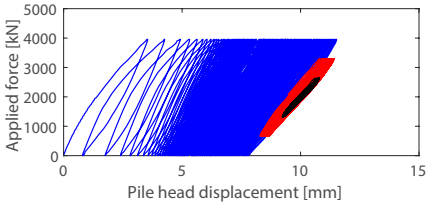

(c) $\zeta_b = 0.45, \zeta_c = 0 \rightarrow \zeta_b = 0.3, \zeta_c = 0.5 \rightarrow \zeta_b = 0.375, \zeta_c = 0.2$

Figure 6.18: Influence of cyclic loading sequence on the monopile tilt – force against pile head displacement ($D_r = 30\%$).

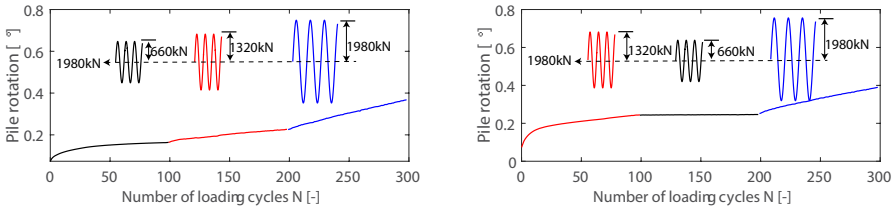

(a) $\zeta_b = 0.3, \zeta_c = 0.5 \rightarrow \zeta_b = 0.375, \zeta_c = 0.2 \rightarrow \zeta_b = 0.45, \zeta_c = 0$ (b) $\zeta_b = 0.375, \zeta_c = 0.2 \rightarrow \zeta_b = 0.3, \zeta_c = 0.5 \rightarrow \zeta_b = 0.45, \zeta_c = 0$

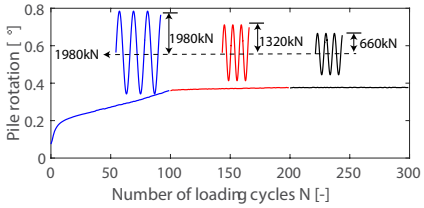

(c) $\zeta_b = 0.45, \zeta_c = 0 \rightarrow \zeta_b = 0.3, \zeta_c = 0.5 \rightarrow \zeta_b = 0.375, \zeta_c = 0.2$

Figure 6.19: Influence of cyclic loading sequence on the evolution of monopile tilt – pile head rotation against loading cycles ($D_r = 30\%$).

6

3D FE results indicate that monopile tilt evolves at a significant rate when the current load amplitude is the highest experienced until that moment. This is clearly visible in Figs. 6.18a – 6.19a, where the increasing cyclic amplitude of subsequent load packages induces progressively higher tilt accumulation rates. Conversely, negligible tilt is observed in Figs. 6.18c – 6.19c for the second and third packages, which are both weaker than the first. The intermediate case in Figs. 6.18b – 6.19b also shows tilting trends in agreement with an upscaled Miner's rule. The validity of such a rule seems to be confirmed by the final rotation of about $0.4°$ predicted after 300 cycles in all three cases. Obviously, a caveat similar to that mentioned with respect to Fig. 6.1 (meso-scale) could be extended here to the upscaled Miner's rule, whose validity will require further research to be ascertained.

3D FE results also give insight into the 'meso-scale' origin of macro-Miner's rule. Indeed, the considered postulate does not only seem to be obeyed by global tilting trends, but also by the local response of the soil around the foundation. Local response consistent with Miner's rule is exemplified in Fig. 6.20 regarding $D_r - N$ trends recorded at element A in Fig. 6.2b. These observations lead to regard macro-Miner's rule as a direct consequence of sand ratcheting behaviour. Using advanced constitutive models in 3D FE simulations allows one to study in detail geotechnical mechanisms that force-resultant macro-models can only incorporate as a *priori* constitutive assumptions (Abadie et al., 2019). Similar considerations apply to the 'meso-scale' SANISAND-MS model, whose formulation and calibration could be supported by parallel micro-mechanical studies (Alonso-Marroquin and Herrmann, 2004; Kawamoto et al., 2018).

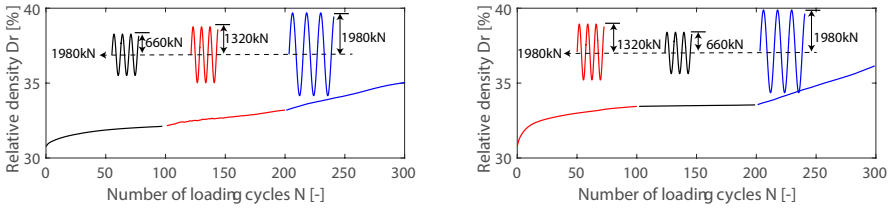

(a) $\zeta_b = 0.3, \zeta_c = 0.5 \rightarrow \zeta_b = 0.375, \zeta_c = 0.2 \rightarrow \zeta_b = 0.45, \zeta_c = 0$ (b) $\zeta_b = 0.375, \zeta_c = 0.2 \rightarrow \zeta_b = 0.3, \zeta_c = 0.5 \rightarrow \zeta_b = 0.45, \zeta_c = 0$

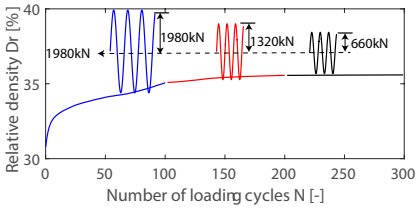

(c) $\zeta_b = 0.45, \zeta_c = 0 \rightarrow \zeta_b = 0.3, \zeta_c = 0.5 \rightarrow \zeta_b = 0.375, \zeta_c = 0.2$

Figure 6.20: Influence of cyclic loading sequence on the evolution of sand relative density at element A in Figure 6.2b ($D_r = 30\%$).

6

6.6. Concluding remarks

In this chapter, implicit 3D FE modelling has been combined with the SANISAND-MS model to numerically analyse monopile tilt in dry sand under lateral cyclic loading. Preliminarily, SANISAND-MS has been confirmed to correctly capture the high-cyclic ratcheting behaviour of dry sand, including the case involving multi-amplitude cyclic loading. Parametric studies have been carried out to numerically investigate the influence of cyclic load settings and sand relative density on cyclic monopile tilt.

Qualitative comparison with experimental evidence has confirmed the suitability of the adopted modelling approach. It has been possible to confirm usual assumptions associated with empirical tilt prediction methods, mostly regarding the relationship between tilting trends and magnitude/asymmetry of (single-amplitude) cyclic loading. The well-known Miner's rule for multi-amplitude loading sequences has also been upscaled from meso-scale (soil stress points) to macro-scale (whole soil-pile system), with numerical results confirming the close link between cyclic soil behaviour and monopile tilting response. It is self-apparent, however, that additional numerical work on the subject will have to clarify the role of relevant geometrical/geotechnical/loading factors, including load multi-directionality and hydro-mechanical effects.

From a more fundamental standpoint, the energy analysis of 3D FE pile simulations will require further consideration. As discussed in Chapter 2, the inclusion of a hyperelastic law in SANISAND-MS seems particularly relevant to properly deal with the arbitrary stress paths that different points in the soil can experience during pile loading. Regarding the compliance with the Second Law of Thermodynamics, assessing the evolution of entropy in the soil-pile system (and particularly the rate

of mechanical dissipation) is still a challenging task for constitutive models not directly derived from thermodynamic principles – for instance, in the framework of hyperplasticity. It may be possible, though, to develop suitable indices for the *a posteriori* analysis of energy dissipation, revealing whether the different stages of a 3D FE implicit simulation have been completed without violating established Laws of Physics.

Overall, the results presented in this chapter encourage further use of 3D FE modelling and SANISAND-MS for cyclically loaded foundations. In the presence of extremely long loading histories, however, it is still not realistic to envisage a direct (implicit) solution through traditional time-domain analysis. While the general increase in computational power will make demanding simulations increasingly feasible, it seems appropriate to regard the tools presented in this dissertation as means to (i) gain insight into the problem in hand, (ii) identify fundamental relationships among governing factors, and (iii) support the conception of 'lighter' methods (e.g., explicit models) for the lifetime analysis of OWT-foundation-soil systems.

7

Conclusion

The offshore wind industry has been steadily growing since the 1990s, with a tendency towards OWTs installed in increasingly deep waters, farther from the shore. This has allowed rapid expansion of the global offshore wind capacity, but has also led to higher costs for the fabrication and installation of support structures. To make offshore wind power competitive in the energy market, serious cost optimisation has been pursued in the past decade, also through – among other aspects – the improvement of geotechnical design. Particularly, the problem of designing OWT foundations to cope with cyclic environmental loading has promoted numerous studies, both experimental and numerical. Several approaches have been considered for the analysis of cyclic soil-foundation interaction, and especially for the prediction of permanent cyclic deformations. Among the available approaches, implicit/step-by-step 3D FE analysis, although computationally demanding, are believed by the Author to possess the highest potential to shed light on governing geotechnical mechanisms, and therefore support design optimisation. It is self-apparent, however, that implicit 3D FE predictions can only be reliable on condition that sound constitutive modelling of cyclic soil behaviour is incorporated in the structure-foundation-soil model.

This work has contributed to the constitutive modelling of sandy soils under (high-)cyclic loading conditions, with emphasis on its use in 3D FE OWT-foundation-soil simulations. The phenomenological modelling of so-called 'fabric effects' (i.e., the impact of microstructural properties on a soil's stiffness and strength), and associated load-induced anisotropy, has been centre stage of all theoretical developments. Such fabric effects and the stress history can severely influence a sand's cyclic behaviour, for instance, in terms of strain accumulation response (ratcheting) and/or cyclic pore pressure build-up. Their numerical simulation at the level of a soil element has been achieved by incorporating a 'memory surface' into the bounding surface plasticity model SANISAND04 by Dafalias and Manzari (2004), and giving rise to the new, 'memory-enhanced', SANISAND-MS model. The proposed model has been validated against a wealth of laboratory test results from the literature, spanning a variety of initial, loading, and drainage conditions. Following thorough validation of the constitutive equations, SANISAND-MS has been then applied to the 3D FE analysis of a cyclically loaded monopile in dry sand, in order to qualitatively assess the 'implicit' performance of the constitutive model in a relevant boundary value problem. Overall, the model appears capable of capturing cyclic soil behaviour and soil-structure interaction at the scale of a soil element and monopile foundation, respectively.

7.1. SANISAND-MS: model features

In Chapter 3, SANISAND-MS has been formulated in the framework of bounding surface plasticity (Dafalias, 1986), in order to reproduce a sand's high-cyclic ratcheting under drained loading conditions. Similar to the SANISAND04 parent model, SANISAND-MS incorporates kinematic hardening and critical state soil mechanics concepts along with the so-called 'state parameter', which is used to define evolution laws for the bounding and dilatancy surfaces. In more detail, the bounding surface sets a limit to admissible/pre-failure stress states, while the dilatancy locus

marks the transition from contractive to dilative soil response (non-associated plastic flow rule). An additional locus, named 'memory surface', has been cast into the SANISAND framework to phenomenologically capture sand fabric effects (Stallebrass and Taylor, 1997; Jafarzadeh et al., 2008; Maleki et al., 2009; Corti et al., 2016). The memory surface and related isotropic-kinematic evolution laws fulfil the following requirements during stages of elasto-plastic straining: (1) the memory surface can only be larger than the yield surface, or at most coincident; (2) the stress state on the yield surface can never lies outside the memory surface; (3) the yield surface always lie inside the memory surface. Expansion of the memory surface size is generated by soil contraction, while dilation is conversely associated with a shrinkage of the memory locus. Together with the bounding surface, the memory locus tunes soil stiffness through the distance between the current stress state (on the yield surface) and its 'memory projection', while the history of load-induced fabric variations is tracked through the size and location of the memory surface. Further, the memory surface is also used to enhance a soil's contractivity (or proneness to pore pressure build-up, in undrained conditions) upon load reversals following stages of dilation.

An upgraded version of the SANISAND-MS model has been presented in Chapter 5, to achieve higher accuracy in the simulation of cyclic pore pressure build-up. For this purpose, some additional ingredients have been cast into the constitutive formulation: (1) a hardening coefficient (h) dependent on the current deviatoric stress ratio; (2) a new fabric history factor in the laws governing memory surface shrinkage and dilatancy; (3) a modified dilatancy coefficient (A_d) to better capture the deviatoric strain accumulation associated with 'cyclic mobility' in medium-dense/dense sand. It should be noted that these additional ingredients do not compromise any of the model features presented in Chapter 3 in relation to drained cyclic loading conditions. Also, the model formulation presented in Chapter 5 can always be reduced to the initial, and 'lighter', version by properly setting relevant constitutive parameters.

7.2. SANISAND-MS: validation against element tests

The SANISAND-MS model as presented in Chapter 3 has been first validated against laboratory test results concerning drained high-cyclic behaviour (see Chapters 3, 4). To this end, literature results of cyclic triaxial, simple shear, and oedometer drained tests have been considered. Specifically:

1. **Drained triaxial cyclic loading**. Simulation results based on the first version of SANISAND-MS formulation exhibit very satisfactory performance. In particular, it was possible to simulate and predict strain accumulation patterns as observed in standard triaxial tests at varying initial confining pressure (p_{in}), initial void ratio (e_{in}), average shear stress level (η^{ave}), and cyclic stress amplitude (q^{ampl}), for a number of loading cycles N up to 10^4. For η^{ave} values close to the critical stress ratio (M), however, the model was found to overestimate the sand ratcheting due to weaker effectiveness of the memory surface mechanism. Under 'non-standard' triaxial loading (i.e., with both axial

and radial stresses cyclically varying during the test as per Wichtmann et al. (2005)), sand specimens experienced, and SANISAND-MS reproduced, faster strain accumulation than at constant radial stress. In Chapter 6, the model was shown to successfully simulate the response of the soil to multi-amplitude cyclic loading histories for $N = 10^5$, confirming on the constitutive modelling side the validity of the 'Miner's rule' (Wichtmann et al., 2010a) about loading sequences including load parcels of different cyclic amplitude.

2. **Drained cyclic simple shear tests**. SANISAND-MS captured well the ultimate accumulated shear strain measured after 2000 loading cycles in both single-direction and multi-directional (CMDSS) cyclic simple shear tests. CMDSS tests were performed in the reference study by varying the direction of horizontal shear by an angle of 90 degrees. Regarding CMDSS test results, the model proved able to predict the acceleration in shear strain accumulation induced by a sudden change in the shear loading direction.

3. **Cyclic oedometer tests**. Under repetitive vertical loading with prevented lateral deformation (oedometer conditions), the void ratio of sand specimens tends towards an asymptotic value, also referred to as the 'terminal density'(i.e., no further volume changes occur thereafter). SANISAND-MS results were compared with experimental results and corresponding empirical interpolations, showing comforting predictive capability.

SANISAND-MS' performance under undrained cyclic loading has been investigated in Chapter 5. Therein, the upgraded version of the model has been validated against undrained triaxial test results spanning cyclic loading at different p_{in}, e_{in}, and q^{ampl}. The enhanced model appears able to accurately predict: (1) liquefaction triggering; (2) cycle-by-cycle pore pressure build-up under symmetric/two-way deviatoric loading; (3) increase in soil liquefaction resistance as a consequence of drained pre-loading cycles. At the same time, the model is well equipped to reproduce the cyclic mobility mechanism, and the associated accumulation of deviatoric strains under either triaxial or simple shear cyclic loading.

7.3. SANISAND-MS: application to the implicit 3D FE analysis of a laterally loaded monopile

The first version of SANISAND-MS (Chapter 3) has been implemented into open-source FE software to perform implicit 3D FE analyses of monopile tilting under lateral cyclic loading – see Chapter 6. 3D FE simulation results have been qualitatively evaluated against small-scale, 1g test data from the literature. The reference simulation cases concerned a tubular monopile subjected to lateral loading in homogeneous sand, either loose or dense. Cyclic loading histories featuring different maximum amplitudes and degrees of asymmetry have been considered in the parametric studies.

3D FE results have confirmed the suitability of SANISAND-MS, particularly regarding the general simulation of monopile tilting trends against the number of

cycles. More quantitatively, the proposed modelling framework seems to comply with, and can potentially add to, established empirical relationships describing the permanent rotation of rigid piles under a variety of (single-amplitude) lateral loading histories – for instance, according to the formulation of LeBlanc et al. (2010). The validity of an 'upscaled' Miner's rule for monopile tilt under multi-amplitude cyclic loading has also been investigated within the set of considered simulation settings.

Additionally, implicit 3D FE analysis has allowed the inspection of governing soil-pile interaction mechanisms, for instance in relation to relative density changes (therefore, stiffness variations) around the pile. Typically observed sand densification patterns have been reproduced, together with their impact on monopile tilting – all in excellent agreement with previous experimental observations (Cuéllar et al., 2009). Overall, the 3D FE modelling thread of this research has boosted confidence about the quality and applicability of the proposed SANISAND-MS formulation, particularly with respect to cyclic loading problems in offshore geotechnics.

This dissertation encourages further use of 3D FE modelling and SANISAND-MS for cyclically loaded foundations. In presence of extremely long loading histories, however, it is still not realistic to envisage direct (implicit) solution through traditional time-domain analysis. It seems appropriate to regard the achievements of this work as means to (i) gain insight into the problem in hand, (ii) identify fundamental relationships among governing factors, and (iii) support the conception of 'lighter' methods (e.g., explicit models) for the lifetime analysis of OWT-foundation-soil systems.

7.4. Recommendations for future research

The SANISAND-MS model has been developed having in mind fundamental problems related to the constitutive modelling of cyclic sand behaviour, including high-cyclic ratcheting, cycle-by-cycle pore water pressure build-up, and different modes of cyclic soil failure (or loss of serviceability). Despite the positive achievements pointed out above, there is certainly room for future improvements of the constitutive formulation:

- The deviatoric component of the incremental plastic strain tensor is defined along the normal to the critical state surface at the image point of the stress state, as inherited from the SANISAND2004 parent model. This assumption does not exactly agree with the flow direction (ratio between plastic volumetric and deviatoric strain increments) observed in laboratory tests. Allowing for more flexibility in the flow rule could in the future remedy this issue.

- The concept of 'memory surface' has been shown to phenomenologically capture fabric effects in sand's cyclic behaviour at a relatively large number of loading cycles. Inevitably, less accuracy has been found when comparing single stress-strain cycles from laboratory tests and numerical simulations. Improvements in this area could be brought about by more detailed (memory surface) modelling of fabric effects at the level of a single cycle.

- Rapid shrinkage of the memory surface size upon soil dilation has been for-

mulated as a way to represent fabric 'weakening'. This feature guarantees the ability to trigger cyclic liquefaction under undrained loading, albeit with some control 'lost' on pore pressure build-up right after the end of dilative deformation. In this respect, fabric evolving mechanisms upon soil dilation require further, in-depth consideration, for instance inspired by micromechanical DEM studies.

- Under undrained conditions, the model appears less accurate in the presence of a significant static pre-shear, i.e., under non-symmetric cyclic loading. The influence of static pre-shear, both on pore pressure build-up and strain accumulation, will receive further attention in future developments of this work.

- A term representing fabric-evolution history has been introduced into the upgraded SANISAND-MS model formulation for better simulation of sand strain development in the cyclic mobility regime. Such a (non-decreasing) term also has an influence on the post-cyclic response. Therefore, the model should be more carefully evaluated for applications involving (very) variable drainage conditions, as well as distinct stages of consolidation. A counter-balancing (erasing) mechanism for the fabric-changing history term could be added to the model. It should also be noted, however, that experimental evidence in support of such a development is hardly available in the literature at the moment.

- SANISAND-MS has been mainly validated with respect to cyclic loading conditions most commonly considered in laboratory tests (triaxial, simple shear, and oedometer loading). Further validation efforts should concern more complex loading programmes and stress paths – such as those produced by hollow cylinder tests. In relation to the same matter, the inclusion of a hyperelastic law seems to be a natural step forward, in order to avoid energy conservation issues under arbitrary small-strain loading cycles (Zytynski et al., 1978; Einav and Puzrin, 2004a).

- The suitability of SANISAND-MS for the implicit 3D FE analysis of cyclically loaded monopiles has been successfully tested. The proposed modelling approach has shown promising potential to accurately reproduce complex soil-structure interaction mechanisms during cyclic loading events. Further work will be carried out to investigate the merits and drawbacks of the upgraded SANISAND-MS formulation in coupled 3D FE problems, i.e., in the presence of varying drainage conditions and pore pressure effects. Regarding the general compliance with thermodynamic principles, it might be possible to develop suitable indices for the *a posteriori* analysis of energy dissipation, revealing whether different stages of a 3D FE implicit simulations have been completed without violating established Laws of Physics (Houlsby and Puzrin, 2006; Yang et al., 2018).

A significant thread of future research will be dedicated to expanding the applicability of SANISAND-MS beyond its original conception in the field of offshore

wind geotechnics. A number of relevant applications in civil engineering demand accurate modelling of cyclic soil behaviour, under a variety of loading/drainage conditions and geometrical configurations. Relevant instances of such applications relate, to the fields of transportation geotechnics and earthquake engineering – e.g., analysis of cyclic settlements under railways and pavements, dynamic performance of earth slopes, and seismic soil-foundation interaction in liquefiable soils.

A

Analytical derivations of memory surface evolution

A

This appendix collects relevant analytical derivations, skipped in Chapter 3 for better readability.

A.1. Memory surface expansion

The expansion law for the memory surface is derived through the consistency condition in Equation (3.14) applied to the stress point A (Figure 3.2). Importantly, the partial derivative $\partial f^M/\partial \boldsymbol{\alpha}^M$ at point A can be expressed as follows:

$$\left.\frac{\partial f^M}{\partial \boldsymbol{\alpha}^M}\right|_A = -p\frac{\boldsymbol{r}_A^M - \boldsymbol{\alpha}^M}{\sqrt{(\boldsymbol{r}_A^M - \boldsymbol{\alpha}^M) : (\boldsymbol{r}_A^M - \boldsymbol{\alpha}^M)}} = p\boldsymbol{n} \tag{A.1}$$

due to the position of A taken diametrically opposed to the projection of the stress point on the memory surface (see Figure 3.2, along $-\boldsymbol{n}$). After computing the derivative $\partial f^M/\partial m^M$ and setting $d\boldsymbol{\sigma}_A^M = 0$, the evolution law (3.15) results from Equation (3.14).

Memory surface contraction

The geometrical factor f_{shr} in Equation 3.16 is evaluated to prevent the memory surface from shrinking smaller than the elastic domain.

It is assumed that the shrinkage of the memory surface occurs at fixed image stress ratio $\boldsymbol{r}^M$, along the direction of the unit tensor $\boldsymbol{n}^M$:

$$\boldsymbol{n}^M = \frac{\boldsymbol{r}^M - \boldsymbol{r}}{\sqrt{(\boldsymbol{r}^M - \boldsymbol{r}) : (\boldsymbol{r}^M - \boldsymbol{r})}} \tag{A.2}$$

The following segments along the $\boldsymbol{n}^M$ directions are defined in agreement with in Figure A.1:

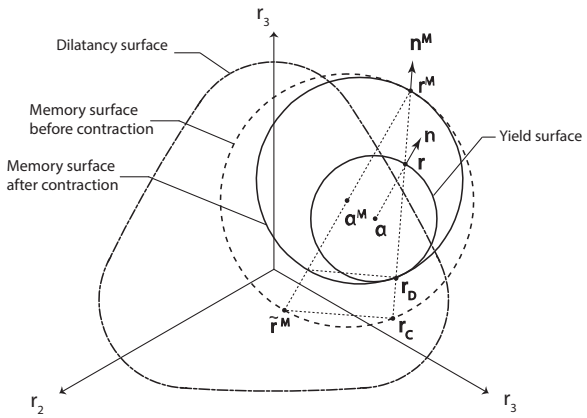

Figure A.1: Geometrical contraction mechanism of the memory surface.

$$\begin{aligned} x_1 &= \boldsymbol{n}^M : (\boldsymbol{r}^M - \boldsymbol{r}) \\ x_2 &= \boldsymbol{n}^M : (\boldsymbol{r} - \boldsymbol{r}_D) \quad &= \boldsymbol{n}^M : (\boldsymbol{r} - \tilde{\boldsymbol{r}}) \\ x_3 &= \boldsymbol{n}^M : (\boldsymbol{r}^M - \boldsymbol{r}_C) \quad &= \boldsymbol{n}^M : (\boldsymbol{r}^M - \tilde{\boldsymbol{r}}^M) \end{aligned} \tag{A.3}$$

where

$$\tilde{\boldsymbol{r}} = \boldsymbol{\alpha} - \sqrt{2/3} m \boldsymbol{n} \qquad \tilde{\boldsymbol{r}}^M = \boldsymbol{\alpha}^M - \sqrt{2/3} m^M \boldsymbol{n} \tag{A.4}$$

It should be recalled that, during virgin loading, $\boldsymbol{r}^M = \boldsymbol{r}$ and $\boldsymbol{n}^M = \boldsymbol{n}$. To avoid undesired intersections, the contraction of the memory surface is gradually decelerated as the yield-memory tangency is approached. For this purpose, the factor f_{shr} in Equation 3.16 is defined as per Corti (2016):

$$f_{shr} = 1 - \frac{x_1 + x_2}{x_3} \tag{A.5}$$

Under general conditions, points C and D do not coincide, so that the segment x_3 is longer than segment $x_1 + x_2$. Therefore, $(x_1 + x_2)/x_3 < 1 \Rightarrow f_{shr} > 0$ and the contraction mechanism is carried on until the segment CD vanishes.

Memory surface translation

As postulated in the relevant section, it assumed that during virgin loading ($\boldsymbol{\sigma} \equiv \boldsymbol{\sigma}^M$) the same magnitude of the incremental plastic strain can be derived by using the yield or memory loci indifferently:

$$\frac{\|d\boldsymbol{\varepsilon}^p\|}{\|\boldsymbol{R}\|} = L = \left(\frac{1}{K_p} \frac{\partial f}{\partial \boldsymbol{\sigma}} : d\boldsymbol{\sigma} \right) = \left(\frac{1}{K_p^M} \frac{\partial f^M}{\partial \boldsymbol{\sigma}^M} : d\boldsymbol{\sigma}^M \right) = L^M \tag{A.6}$$

where $\boldsymbol{R} = \boldsymbol{R}' + D\boldsymbol{I}/3$ (see Equation (3.6)). Under virgin loading conditions, $L^M = L$ and $K_p^M = K_p$ hold rigorously.

By enforcing plastic consistency on the memory surface, it can be found that:

$$\frac{\partial f^M}{\partial \boldsymbol{\sigma}^M} : d\boldsymbol{\sigma}^M = -\left(\frac{\partial f^M}{\partial \boldsymbol{\alpha}^M} : d\boldsymbol{\alpha}^M + \frac{\partial f^M}{\partial m^M} dm^M \right) = L^M K_p^M \tag{A.7}$$

After setting $L = L^M$ and substituting the partial derivatives of the memory function f^M with respect to $\boldsymbol{\alpha}^M$ and m^M, Equation A.7 can be rewritten as:

$$L K_p^M = p\boldsymbol{n} : d\boldsymbol{\alpha}^M + \sqrt{\frac{2}{3}} p dm^M \tag{A.8}$$

Introducing Equation (3.17) into the above equation leads to:

$$K_p^M = \frac{2}{3} p \left[h^M (\boldsymbol{r}_\theta^b - \boldsymbol{r}^M) : \boldsymbol{n} + \sqrt{\frac{3}{2}} \frac{1}{L} dm^M \right] \tag{A.9}$$

A

Imposing virgin loading ($\boldsymbol{r} = \boldsymbol{r}^M$) into Equation (3.8) yields:

$$K_p = \frac{2}{3} p h (\boldsymbol{r}_\theta^b - \boldsymbol{r}) : \boldsymbol{n} = \frac{2}{3} p \tilde{h} (\boldsymbol{r}_\theta^b - \boldsymbol{r}^M) : \boldsymbol{n} \tag{A.10}$$

with

$$\tilde{h} = \frac{b_0}{(\boldsymbol{r}^M - \boldsymbol{r}_{in}) : \boldsymbol{n}} \tag{A.11}$$

Under virgin loading conditions, $K_p^M = K_p$. Combining Equation A.9 with A.10 results in:

$$\tilde{h} (\boldsymbol{r}_\theta^b - \boldsymbol{r}^M) : \boldsymbol{n} = h^M (\boldsymbol{r}_\theta^b - \boldsymbol{r}^M) : \boldsymbol{n} + \sqrt{\frac{3}{2}} \frac{1}{L} dm^M \tag{A.12}$$

The combination of Equations (3.6), (3.16) (A.11) and (A.12) leads to the final Equation (3.18).

B

SANISAND-MS formulation based on the back stress variable

B

SANISAND-MS formulations based on the use of deviatoric stress ratio and back stress ratio are compared in Table B.1. The two sets of equations produce negligible differences in the simulation results presented in this thesis.While using the stress ratio leads to a ”neater” formulation of the memory surface evolution, the adoption of the back stress avoids possible issues associated with artificial softening at low confinement (see discussion in Section 3.3.1).

Table B.1: Constitutive equations based on the use of the stress ratio and back stress ratio.

	Constitutive equations (stress ratio)	**Constitutive equations (back stress ratio)**
Elastic moduli	$G = G_0 p_{atm}[(2.97-e)^2/(1+e)](p/p_{atm})^{1/2}$ $K = 2(1+\nu)G/[3(1-2\nu)]$	[/] (unchanged) [/]
Critical state line	$e_c = e_0 - \lambda_c (p_c/p_{atm})^{\xi}$	[/]
Yield function	$f = \sqrt{(\boldsymbol{s}-p\boldsymbol{\alpha}):(\boldsymbol{s}-p\boldsymbol{\alpha})} - \sqrt{2/3}pm$	[/]
Memory function	$f^M = \sqrt{(\boldsymbol{s}-p\boldsymbol{\alpha}^M):(\boldsymbol{s}-p\boldsymbol{\alpha}^M)} - \sqrt{2/3}pm^M$	[/]
Deviatoric plastic flow	$d\boldsymbol{e}^p = \langle L \rangle \boldsymbol{R}'$ $\boldsymbol{R}' = B\boldsymbol{n} - C\,[\boldsymbol{n}^2 - (1/3)\boldsymbol{I}]$ $\boldsymbol{n} = (\boldsymbol{r}-\boldsymbol{\alpha})/\sqrt{2/3}m$ $B = 1 + 3(1-c)/(2c)g(\theta)\cos 3\theta$ $C = 3\sqrt{3/2}(1-c)g(\theta)/c$ $g(\theta) = 2c/[(1+c)-(1-c)\cos 3\theta]$	[/] [/] [/] [/] [/] [/]
Volumetric plastic flow	$d\varepsilon_{vol}^p = \langle L \rangle D$ $D = \left[A_0 \exp\left(\beta\langle \tilde{b}_d^M \rangle / b_{ref}\right)\right](\boldsymbol{r}_\theta^d - \boldsymbol{r}):\boldsymbol{n}$ $\boldsymbol{r}_\theta^d = \sqrt{2/3}g(\theta)M\exp(n^d\Psi)\boldsymbol{n}$ $\tilde{b}_d^M = (\tilde{\boldsymbol{r}}_\theta^d - \tilde{\boldsymbol{r}}^M):\boldsymbol{n}$ $b_{ref} = (\boldsymbol{r}_\theta^b - \boldsymbol{r}_{\theta+\pi}^b):\boldsymbol{n}$ $\boldsymbol{r}_{\theta+\pi}^b = \sqrt{2/3}g(\theta+\pi)M\exp(n^d\Psi)(-\boldsymbol{n})$	[/] $D = \left[A_0 \exp\left(\beta\langle \tilde{b}_d^M \rangle / b_{ref}\right)\right](\boldsymbol{\alpha}_\theta^d - \boldsymbol{\alpha}):\boldsymbol{n}$ $\boldsymbol{\alpha}_\theta^d = \sqrt{2/3}[g(\theta)M\exp(n^d\Psi) - m]\boldsymbol{n}$ $\tilde{b}_d^M = (\tilde{\boldsymbol{\alpha}}_\theta^d - \tilde{\boldsymbol{r}}_\alpha^M):\boldsymbol{n}$ $b_{ref} = (\boldsymbol{\alpha}_\theta^b - \boldsymbol{\alpha}_{\theta+\pi}^b):\boldsymbol{n}$ $\boldsymbol{\alpha}_{\theta+\pi}^b = \sqrt{2/3}[g(\theta+\pi)M\exp(n^d\Psi) - m](-\boldsymbol{n})$
Yield surface evolution	$d\boldsymbol{\alpha} = (2/3)\langle L \rangle h(\boldsymbol{r}_\theta^b - \boldsymbol{r})$ $\boldsymbol{r}_\theta^b = \sqrt{2/3}g(\theta)M\exp(-n^b\Psi)]\boldsymbol{n}$ $h = \dfrac{b_0}{(\boldsymbol{r}-\boldsymbol{r}_{in}):\boldsymbol{n}}\exp\left[\mu_0\left(\dfrac{p}{p_{atm}}\right)^{0.5}\left(\dfrac{b^M}{b_{ref}}\right)^2\right]$ $b_0 = G_0 h_0(1-c_h e)/\sqrt{(p/p_{atm})}$ $b^M = (\boldsymbol{r}^M - \boldsymbol{r}):\boldsymbol{n}$	$d\boldsymbol{\alpha} = (2/3)\langle L \rangle h(\boldsymbol{\alpha}_\theta^b - \boldsymbol{\alpha})$ $\boldsymbol{\alpha}_\theta^b = \sqrt{2/3}[g(\theta)M\exp(-n^b\Psi) - m]\boldsymbol{n}$ $h = \dfrac{b_0}{(\boldsymbol{\alpha}-\boldsymbol{\alpha}_{in}):\boldsymbol{n}}\exp\left[\mu_0\left(\dfrac{p}{p_{atm}}\right)^{0.5}\left(\dfrac{b^M}{b_{ref}}\right)^2\right]$ [/] $b^M = (\boldsymbol{r}_\alpha^M - \boldsymbol{\alpha}):\boldsymbol{n}$ with $\boldsymbol{r}_\alpha^M = \boldsymbol{\alpha}^M + \sqrt{2/3}(m^M - m)\boldsymbol{n}$
Memory surface evolution	$dm^M = \sqrt{3/2}d\boldsymbol{\alpha}^M:\boldsymbol{n} - (m^M/\zeta)f_{shr}\langle -d\varepsilon_{vol}^p \rangle$ $d\boldsymbol{\alpha}^M = (2/3)\langle L^M \rangle h^M(\boldsymbol{r}_\theta^b - \boldsymbol{r}^M)$ $h^M = \dfrac{1}{2}\left[\dfrac{b_0}{(\boldsymbol{r}^M - \boldsymbol{r}_{in}):\boldsymbol{n}} + \sqrt{\dfrac{3}{2}}\dfrac{m^M f_{shr}\langle -D \rangle}{\zeta(\boldsymbol{r}_\theta^b - \boldsymbol{r}^M):\boldsymbol{n}}\right]$	[/] $d\boldsymbol{\alpha}^M = (2/3)\langle L^M \rangle h^M(\boldsymbol{\alpha}_\theta^b - \boldsymbol{r}_\alpha^M)$ $h^M = \dfrac{1}{2}\left[\dfrac{b_0}{(\boldsymbol{\alpha}_\alpha^M - \boldsymbol{\alpha}_{in}):\boldsymbol{n}} + \sqrt{\dfrac{3}{2}}\dfrac{m^M f_{shr}\langle -D \rangle}{\zeta(\boldsymbol{\alpha}_\theta^b - \boldsymbol{r}_\alpha^M):\boldsymbol{n}}\right]$

References

Abadie, C. N. (2015). *Cyclic lateral loading of monopile foundations in cohesionless soils*. DPhil thesis, University of Oxford.

Abadie, C. N., Byrne, B. W., and Houlsby, G. T. (2019). Rigid pile response to cyclic lateral loading: laboratory tests. *Géotechnique*, 69(10):863–876.

Achmus, M., Kuo, Y.-S., and Abdel-Rahman, K. (2009). Behavior of monopile foundations under cyclic lateral load. *Computers and Geotechnics*, 36(5):725–735.

Albiker, J., Achmus, M., Frick, D., and Flindt, F. (2017). 1g model tests on the displacement accumulation of large-diameter piles under cyclic lateral loading. *Geotechnical Testing Journal*, 40(2):173–184.

Alonso-Marroquín, F. (2004). *Micromechanical investigation of soil deformation: Incremental Response and granular Ratcheting*. PhD thesis, Universität Stuttgart.

Alonso-Marroquin, F. and Herrmann, H. (2004). Ratcheting of granular materials. *Physical Review Letters*, 92(5):054301.

Altaee, A. and Fellenius, B. H. (1994). Physical modeling in sand. *Canadian Geotechnical Journal*, 31(3):420–431.

Amorosi, A., Rollo, F., and Houlsby, G. T. (2020). A nonlinear anisotropic hyperelastic formulation for granular materials: comparison with existing models and validation. *Acta Geotechnica*, 15(1):179–196.

Andersen, K. (2015). Cyclic soil parameters for offshore foundation design. In *Frontiers in Offshore Geotechnics III: Proceedings of the 3rd International Symposium on Frontiers in Offshore Geotechnics (ISFOG 2015)*, volume 1, pages 5–82. Taylor & Francis Books Ltd.

Andersen, K. H. (2009). Bearing capacity under cyclic loading —offshore, along the coast, and on land. The 21st Bjerrum Lecture presented in Oslo, 23 November 2007. *Canadian Geotechnical Journal*, 46(5):513–535.

Andersen, K. H., Kleven, A., and Heien, D. (1988). Cyclic soil data for design of gravity structures. *Journal of Geotechnical Engineering*, 114(5):517–539.

API (2014). Recommended practice 2A-WSD planning, designing and constructing fixed offshore platforms –working stress design, 22nd edn.,. In *Product No. G2AWSD22*. American Petroleum Institute.

Arany, L., Bhattacharya, S., Macdonald, J., and Hogan, S. (2017). Design of monopiles for offshore wind turbines in 10 steps. *Soil Dynamics and Earthquake Engineering*, 92:126–152.

Arany, L., Bhattacharya, S., Macdonald, J. H., Hogan, S. J., et al. (2015). A critical review of serviceability limit state requirements for monopile foundations of offshore wind turbines. In *Offshore Technology Conference*. Offshore Technology Conference.

Arthur, J. and Menzies, B. (1972). Inherent anisotropy in a sand. *Géotechnique*, 22(1):115–128.

Arulmoli, K., Muraleetharan, K., Hossain, M., and Fruth, L. (1992). VELACS: Verification of liquefaction analysis by centrifuge studies. *Laboratory Testing Program, Soil Data Rep. No. 90*, 562.

Barari, A., Bagheri, M., Rouainia, M., and Ibsen, L. B. (2017). Deformation mechanisms for offshore monopile foundations accounting for cyclic mobility effects. *Soil Dynamics and Earthquake Engineering*, 97:439–453.

Bardet, J.-P. (1986). Bounding surface plasticity model for sands. *Journal of Engineering Mechanics*, 112(11):1198–1217.

Barrero, A. R., Taiebat, M., and Dafalias, Y. F. (2020). Modeling cyclic shearing of sands in the semifluidized state. *International Journal for Numerical and Analytical Methods in Geomechanics*, 44(3):371–388.

Been, K. and Jefferies, M. G. (1985). A state parameter for sands. *Géotechnique*, 35(2):99–112.

Bhattacharya, S. (2019). *Design of Foundations for Offshore Wind Turbines*. Wiley.

Bienen, B., Klinkvort, R. T., O'Loughlin, C., Zhu, F., and Byrne, B. W. (2018). Suction caissons in dense sand, part ii: vertical cyclic loading into tension. *Géotechnique*, 68(11):953–967.

Bolton, M. (1986). Strength and dilatancy of sands. *Géotechnique*, 36(1):65–78.

Borja, R. I. (2013). *Plasticity: modeling & computation*. Springer Science & Business Media.

Bouckovalas, G., Whitman, R. V., and Marr, W. A. (1984). Permanent displacement of sand with cyclic loading. *Journal of Geotechnical Engineering*, 110(11):1606–1623.

Boulanger, R. and Ziotopoulou, K. (2013). Formulation of a sand plasticity plane-strain model for earthquake engineering applications. *Soil Dynamics and Earthquake Engineering*, 53:254–267.

Burd, H. J., Taborda, D. M., Zdravković, L., Abadie, C. N., Byrne, B. W., Houlsby, G. T., Gavin, K. G., Igoe, D. J., Jardine, R. J., Martin, C. M., et al. (2020). PISA design model for monopiles for offshore wind turbines: application to a marine sand. *Géotechnique, ahead of print*.

Byrne, B. W., Burd, H. J., Zdravkovic, L., Abadie, C. N., Houlsby, G. T., Jardine, R. J., Martin, C. M., McAdam, R. A., Pacheco Andrade, M., Pedro, A. M., et al. (2019). Pisa design methods for offshore wind turbine monopiles. In *Offshore Technology Conference*. Offshore Technology Conference.

Byrne, B. W., Houlsby, G. T., Burd, H. J., Gavin, K. G., Igoe, D. J., Jardine, R. J., Martin, C. M., McAdam, R. A., Potts, D. M., Taborda, D. M., et al. (2020). PISA design model for monopiles for offshore wind turbines: application to a stiff glacial clay till. *Géotechnique, ahead of print*.

Calvetti, F. and di Prisco, C. G. (2010). Discrete numerical investigation of the ratcheting phenomenon in granular materials. *Comptes Rendus Mécanique*, 338(10-11):604–614.

Casagrande, A. and Carrillo, N. (1944). Discussion on study of failure envelope soils. *Journal of the Soil Mechanics and Foundations Division, ASCE*, 89:243.

Cerfontaine, B., Dieudonné, A.-C., Radu, J.-P., Collin, F., and Charlier, R. (2015). 3D zero-thickness coupled interface finite element: Formulation and application. *Computers and Geotechnics*, 69:124–140.

Chang, C. S. and Whitman, R. V. (1988). Drained permanent deformation of sand due to cyclic loading. *Journal of Geotechnical Engineering*, 114(10):1164–1180.

Chen, X., Pao, W., Thornton, S., and Small, J. (2016). Unsaturated hydro-mechanical–chemical constitutive coupled model based on mixture coupling theory: Hydration swelling and chemical osmosis. *International Journal of Engineering Science*, 104:97–109.

Chiaradonna, A., Tropeano, G., d'Onofrio, A., and Silvestri, F. (2018). Development of a simplified model for pore water pressure build-up induced by cyclic loading. *Bulletin of Earthquake Engineering*, pages 1–26.

Chong, S.-H. (2017). Numerical simulation of offshore foundations subjected to repetitive loads. *Ocean Engineering*, 142:470–477.

Chong, S.-H. and Pasten, C. (2018). Numerical study on long-term monopile foundation response. *Marine Georesources & Geotechnology*, 36(2):190–196.

Chong, S.-H. and Santamarina, J. C. (2016). Sands subjected to repetitive vertical loading under zero lateral strain: accumulation models, terminal densities, and settlement. *Canadian Geotechnical Journal*, 53(12):2039–2046.

Chow, S., O'Loughlin, C., Corti, R., Gaudin, C., and Diambra, A. (2015). Drained cyclic capacity of plate anchors in dense sand: Experimental and theoretical observations. *Géotechnique Letters*, 5(2):80–85.

Cleall, P. J., Seetharam, S. C., and Thomas, H. R. (2007). Inclusion of some aspects of chemical behavior of unsaturated soil in thermo/hydro/chemical/mechanical models. i: Model development. *Journal of Engineering Mechanics*, 133(3):338–347.

Collins, I. (2005). The concept of stored plastic work or frozen elastic energy in soil mechanics. *Géotechnique*, 55(5):373–382.

Collins, I. and Houlsby, G. (1997). Application of thermomechanical principles to the modelling of geotechnical materials. *Proceedings of the Royal Society of London. Series A: Mathematical, Physical and Engineering Sciences*, 453(1964):1975–2001.

Corciulo, S., Zanoli, O., and Pisanò, F. (2017). Transient response of offshore wind turbines on monopiles in sand: role of cyclic hydro–mechanical soil behaviour. *Computers and Geotechnics*, 83:221–238.

Corti, R. (2016). *Hardening memory surface constitutive model for granular soils under cyclic loading*. PhD thesis, University of Bristol.

Corti, R., Diambra, A., Wood, D. M., Escribano, D. E., and Nash, D. F. (2016). Memory surface hardening model for granular soils under repeated loading conditions. *Journal of Engineering Mechanics*, 142(12):04016102.

Corti, R., Gourvenec, S. M., Randolph, M. F., and Diambra, A. (2017). Application of a memory surface model to predict whole-life settlements of a sliding foundation. *Computers and Geotechnics*, 88:152–163.

Cuéllar, P., Baeßler, M., and Rücker, W. (2009). Ratcheting convective cells of sand grains around offshore piles under cyclic lateral loads. *Granular Matter*, 11(6):379.

Cuéllar, P., Mira, P., Pastor, M., Merodo, J. A. F., Baeßler, M., and Rücker, W. (2014). A numerical model for the transient analysis of offshore foundations under cyclic loading. *Computers and Geotechnics*, 59:75–86.

Cundall, P. A. (1971). *The measurement and analysis of accelerations in rock slopes*. PhD thesis, Imperial College London.

Cundall, P. A. and Strack, O. D. (1979). A discrete numerical model for granular assemblies. *Géotechnique*, 29(1):47–65.

Dafalias, Y. and Popov, E. (1975). A model of nonlinearly hardening materials for complex loading. *Acta Mechanica*, 21(3):173–192.

Dafalias, Y. and Taiebat, M. (2016). SANISAND-Z: zero elastic range sand plasticity model. *Géotechnique*, 66(12):999–1013.

Dafalias, Y. F. (1986). Bounding surface plasticity. i: Mathematical foundation and hypoplasticity. *Journal of Engineering Mechanics*, 112(9):966–987.

Dafalias, Y. F. and Manzari, M. T. (2004). Simple plasticity sand model accounting for fabric change effects. *Journal of Engineering Mechanics*, 130(6):622–634.

Day, R. and Potts, D. (1994). Zero thickness interface elements—numerical stability and application. *International Journal for Numerical and Analytical Methods in Geomechanics*, 18(10):689–708.

Di Benedetto, H., Blanc, M., Tiouajni, S., and Ezaoui, A. (2014). Elastoplastic model with loading memory surfaces (lms) for monotonic and cyclic behaviour of geomaterials. *International Journal for Numerical and Analytical Methods in Geomechanics*, 38(14):1477–1502.

di Prisco, C. G. and Mortara, G. (2013). A multi-mechanism constitutive model for plastic adaption under cyclic loading. *International Journal for Numerical and Analytical Methods in Geomechanics*, 37(18):3071–3086.

di Prisco, C. G. and Muir Wood, D. (2012). *Mechanical Behaviour of Soils Under Environmentallly-Induced Cyclic Loads*, volume 534. Springer Science & Business Media.

DNV, G. (2016). DNVGL-ST-0126: Support structures for wind turbines. Technical report, Osol, Norway: DNG GL.

Dobry, R., Pierce, W., Dyvik, R., Thomas, G., and Ladd, R. (1985). Pore pressure model for cyclic straining of sand. *Rensselaer Polytechnic Institute, Troy, New York*.

Dounias, G. T. and Potts, D. M. (1993). Numerical analysis of drained direct and simple shear tests. *Journal of Geotechnical Engineering*, 119(12):1870–1891.

Einav, I. and Puzrin, A. M. (2004a). Continuous hyperplastic critical state (chcs) model: derivation. *International Journal of Solids and Structures*, 41(1):199–226.

Einav, I. and Puzrin, A. M. (2004b). Pressure-dependent elasticity and energy conservation in elastoplastic models for soils. *Journal of Geotechnical and Geoenvironmental Engineering*, 130(1):81–92.

Elgamal, A., Yang, Z., Parra, E., and Ragheb, A. (2003). Modeling of cyclic mobility in saturated cohesionless soils. *International Journal of Plasticity*, 19(6):883–905.

Escribano, D. (2014). *Evolution of stiffness and deformation of Hostun Sand under drained cyclic loading*. PhD thesis, University of Bristol.

Escribano, D., Nash, D., and Diambra, A. (2018). Local and global volumetric strain comparison in sand specimens subjected to drained cyclic and monotonic triaxial compression loading. *Geotechnical Testing Journal*, 42(4):1006–1030.

Europe Wind (2020). Offshore wind in Europe: Key trends and statistics 2019. *WindEurope: Brussels, Belgium*.

Fonseca, J. (2011). *The evolution of morphology and fabric of a sand during shearing*. PhD thesis, Imperial College London.

François, S., Karg, C., Haegeman, W., and Degrande, G. (2010). A numerical model for foundation settlements due to deformation accumulation in granular soils under repeated small amplitude dynamic loading. *International Journal for Numerical and Analytical Methods in Geomechanics*, 34(3):273–296.

Gajo, A. and Bigoni, D. (2008). A model for stress and plastic strain induced nonlinear, hyperelastic anisotropy in soils. *International Journal for Numerical and Analytical Methods in Geomechanics*, 32(7):833–861.

Gajo, A. and Muir Wood, D. (1999a). A kinematic hardening constitutive model for sands: the multiaxial formulation. *International Journal for Numerical and Analytical Methods in Geomechanics*, 23(9):925–965.

Gajo, A. and Muir Wood, D. (1999b). Severn-Trent sand: a kinematic hardening constitutive model for sands: the q-p formulation. *Géotechnique*, 49(5):595–614.

Galavi, V., Beuth, L., Coelho, B. Z., Tehrani, F. S., Hölscher, P., and Van Tol, F. (2017). Numerical simulation of pile installation in saturated sand using material point method. *Procedia Engineering*, 175:72–79.

Gao, Z. and Zhao, J. (2015). Constitutive modeling of anisotropic sand behavior in monotonic and cyclic loading. *Journal of Engineering Mechanics*, 141(8):04015017.

Ghionna, V. N. and Porcino, D. (2006). Liquefaction resistance of undisturbed and reconstituted samples of a natural coarse sand from undrained cyclic triaxial tests. *Journal of Geotechnical and Geoenvironmental Engineering*, 132(2):194–202.

Ghofrani, A. and Arduino, P. (2018). Prediction of leap centrifuge test results using a pressure-dependent bounding surface constitutive model. *Soil Dynamics and Earthquake Engineering*, 113:758–770.

Griffiths, D. (1985). Numerical modelling of interfaces using conventional finite elements. In *5th International Conference on Numerical Methods in Geomechanics, Nagoya, Japan*, pages 837–844. AA Balkema Publishers.

Gudehus, G., Amorosi, A., Gens, A., Herle, I., Kolymbas, D., Mašín, D., Muir Wood, D., Niemunis, A., Nova, R., Pastor, M., et al. (2008). The soilmodels. info project. *International Journal for Numerical and Analytical Methods in Geomechanics*, 32(12):1571–1572.

Hardin, B. O. and Black, W. L. (1966). Sand stiffness under various triaxial stresses. *Journal of Soil Mechanics & Foundations Division*, 92(ASCE# 4712 Proceeding).

Hardin, B. O. and Blandford, G. E. (1989). Elasticity of particulate materials. *Journal of Geotechnical Engineering*, 115(6):788–805.

Houlsby, G., Abadie, C., Beuckelaers, W., and Byrne, B. (2017). A model for non-linear hysteretic and ratcheting behaviour. *International Journal of Solids and Structures*, 120:67–80.

Houlsby, G., Amorosi, A., and Rollo, F. (2019). Non-linear anisotropic hyperelasticity for granular materials. *Computers and Geotechnics*, 115:103167.

Houlsby, G. and Puzrin, A. (2000). A thermomechanical framework for constitutive models for rate-independent dissipative materials. *International Journal of Plasticity*, 16(9):1017–1047.

Houlsby, G. T. (2016). Interactions in offshore foundation design. *Géotechnique*, 66(10):791–825.

Houlsby, G. T., Amorosi, A., and Rojas, E. (2005). Elastic moduli of soils dependent on pressure: a hyperelastic formulation. *Géotechnique*, 55(5):383–392.

Houlsby, G. T. and Puzrin, A. M. (2006). *Principles of hyperplasticity: an approach to plasticity theory based on thermodynamic principles*. Springer Science & Business Media.

Hu, M., O' Sullivan, C., Jardine, R. R., and Jiang, M. (2010). Stress-induced anisotropy in sand under cyclic loading. *Granular Matter*, 12(5):469–476.

Iai, S., Matsunaga, Y., and Kameoka, T. (1992). Strain space plasticity model for cyclic mobility. *Soils and Foundations*, 32(2):1–15.

Ibrahim, A. A. and Kagawa, T. (1991). Microscopic measurement of sand fabric from cyclic tests causing liquefaction. *Geotechnical Testing Journal*, 14(4):371–382.

Idriss, I. and Boulanger, R. (2006). Semi-empirical procedures for evaluating liquefaction potential during earthquakes. *Soil Dynamics and Earthquake Engineering*, 26(2-4):115–130.

IEA (2019). Offshore wind outlook 2019. Technical report, IEA, Paris.

IREND (2019). Future of wind: Deployment, investment, technology, grid integration and socio-economic aspects (a global energy transformation paper). International Renewable Energy Agency, Abu Dhabi.

Ishihara, K. (1993). Liquefaction and flow failure during earthquakes. *Géotechnique*, 43(3):351–451.

Ishihara, K., Tatsuoka, F., and Yasuda, S. (1975). Undrained deformation and liquefaction of sand under cyclic stresses. *Soils and Foundations*, 15(1):29–44.

Ivšić, T. (2006). A model for presentation of seismic pore water pressures. *Soil Dynamics and Earthquake Engineering*, 26(2-4):191–199.

Iwan, W. D. (1967). On a class of models for the yielding behavior of continuous and composite systems. *Journal of Applied Mechanics*, 34(3):612–617.

Jafarzadeh, F., Javaheri, H., Sadek, T., and Muir Wood, D. (2008). Simulation of anisotropic deviatoric response of hostun sand in true triaxial tests. *Computers and Geotechnics*, 35(5):703–718.

Jostad, H., Grimstad, G., Andersen, K., and Sivasithamparam, N. (2015). A FE procedure for calculation of cyclic behaviour of offshore foundations under partly drained conditions. *Frontiers in Offshore Geotechnics III*, pages 153–172.

Kaggwa, W. S., Booker, J. R., and Carter, J. (1991). Residual strains in calcareous sand due to irregular cyclic loading. *Journal of Geotechnical Engineering*, 117(2):201–218.

Kallehave, D., Byrne, B. W., LeBlanc Thilsted, C., and Mikkelsen, K. K. (2015). Optimization of monopiles for offshore wind turbines. *Philosophical Transactions of the Royal Society A: Mathematical, Physical and Engineering Sciences*, 373(2035):20140100.

Kan, M. E., Taiebat, H. A., and Khalili, N. (2013). Simplified mapping rule for bounding surface simulation of complex loading paths in granular materials. *International Journal of Geomechanics*, 14(2):239–253.

Karg, C., François, S., Haegeman, W., and Degrande, G. (2010). Elasto-plastic long-term behavior of granular soils: Modelling and experimental validation. *Soil Dynamics and Earthquake Engineering*, 30(8):635–646.

Kawamoto, R., Andò, E., Viggiani, G., and Andrade, J. E. (2018). All you need is shape: Predicting shear banding in sand with ls-dem. *Journal of the Mechanics and Physics of Solids*, 111:375–392.

Kaynia, A. M. (2019). Seismic considerations in design of offshore wind turbines. *Soil Dynamics and Earthquake Engineering*, 124:399–407.

Kementzetzidis, E., Corciulo, S., Versteijlen, W. G., and Pisanò, F. (2019). Geotechnical aspects of offshore wind turbine dynamics from 3D non-linear soil-structure simulations. *Soil Dynamics and Earthquake Engineering*, 120:181–199.

Kementzetzidis, E., Metrikine, A. V., Versteijlen, W. G., and Pisanò, F. (2020). Geotechnical aspects of offshore wind turbine dynamics from 3D non-linear soil-structure simulations. *Géotechnique, ahead of print*.

Kementzetzidis, E., Versteijlen, W. G., Nernheim, A., and Pisanò, F. (2018). 3D FE dynamic modelling of offshore wind turbines in sand: natural frequency evolution in the pre–to after-storm transition. In *Proceedings of the 9th European Conference on Numerical Methods in Geotechnical Engineering (NUMGE 2018), June 25-27, 2018, Porto, Portugal*, pages 1477–1484. CRC Press.

Khalili, N., Habte, M., and Valliappan, S. (2005). A bounding surface plasticity model for cyclic loading of granular soils. *International Journal for Nnumerical Methods in Engineering*, 63(14):1939–1960.

Khalili, N. and Selvadurai, A. (2004). On the constitutive modelling of thermo-hydro-mechanical coupling in elastic media with double porosity. In *Elsevier Geo-Engineering Book Series*, volume 2, pages 559–564. Elsevier.

Khosravifar, A., Elgamal, A., Lu, J., and Li, J. (2018). A 3D model for earthquake-induced liquefaction triggering and post-liquefaction response. *Soil Dynamics and Earthquake Engineering*, 110:43–52.

Klinkvort, R., Black, J., Bayton, S., Haigh, S., Madabhushi, G., Blanc, M., Thorel, L., Zania, V., Bienen, B., and Gaudin, C. (2018). A review of modelling effects in centrifuge monopile testing in sand. In *9th International Conference on Physical Modelling in Geotechnics*. CRC Press.

Klinkvort, R. T. (2013). *Centrifuge modelling of drained lateral pile-soil response: Application for offshore wind turbine support structures*. Technical University of Denmark.

Klinkvort, R. T. and Hededal, O. (2013). Lateral response of monopile supporting an offshore wind turbine. *Proceedings of the ICE-Geotechnical Engineering*, 166(2):147–158.

Knopf, B., Nahmmacher, P., and Schmid, E. (2015). The European renewable energy target for 2030–An impact assessment of the electricity sector. *Energy policy*, 85:50–60.

Krieg, R. (1975). A practical two surface plasticity theory. *Journal of Applied Mechanics*, 42:641–646.

Kuhn, M. R., Sun, W., and Wang, Q. (2015). Stress-induced anisotropy in granular materials: fabric, stiffness, and permeability. *Acta Geotechnica*, 10(4):399–419.

Kuwano, R. and Jardine, R. (2002). On the applicability of cross-anisotropic elasticity to granular materials at very small strains. *Géotechnique*, 52(10):727–749.

Lackenby, J., Indraratna, B., McDowell, G., and Christie, D. (2007). Effect of confining pressure on ballast degradation and deformation under cyclic triaxial loading. *Géotechnique*, 57(6):527–536.

Ladd, R. S. (1974). Specimen preparation and liquefaction of sands. *Journal of Geotechnical and Geoenvironmental Engineering*, 100(Proc. Paper 10857 Proceeding).

LeBlanc, C., Houlsby, G. T., and Byrne, B. W. (2010). Response of stiff piles in sand to long-term cyclic lateral loading. *Géotechnique*, 60(2):79–90.

Lee, K. L. and Seed, H. B. (1967). Cyclic stress conditions causing liquefaction of sand. *Journal of Soil Mechanics & Foundations Division*, 93(1):47–70.

Lekarp, F. and Dawson, A. (1998). Modelling permanent deformation behaviour of unbound granular materials. *Construction and Building Materials*, 12(1):9–18.

Lentz, R. W. and Baladi, G. Y. (1981). Constitutive equation for permanent strain of sand subjected to cyclic loading. *Transportation Research Record*, 810:50–54.

Li, W., Igoe, D., and Gavin, K. (2015). Field tests to investigate the cyclic response of monopiles in sand. *Proceedings of the Institution of Civil Engineers-Geotechnical Engineering*, 168(5):407–421.

Li, X. and Dafalias, Y. F. (2000). Dilatancy for cohesionless soils. *Géotechnique*, 50(4):449–460.

Li, X. S. and Dafalias, Y. F. (2002). Constitutive modeling of inherently anisotropic sand behavior. *Journal of Geotechnical and Geoenvironmental Engineering*, 128(10):868–880.

Li, X. S. and Dafalias, Y. F. (2011). Anisotropic critical state theory: role of fabric. *Journal of Engineering Mechanics*, 138(3):263–275.

Li, X.-S. and Wang, Y. (1998). Linear representation of steady-state line for sand. *Journal of Geotechnical and Geoenvironmental Engineering*, 124(12):1215–1217.

Lin, H., Suleiman, M. T., Brown, D. G., and Kavazanjian Jr, E. (2015). Mechanical behavior of sands treated by microbially induced carbonate precipitation. *Journal of Geotechnical and Geoenvironmental Engineering*, 142(2):04015066.

Lin, S.-S. and Liao, J.-C. (1999). Permanent strains of piles in sand due to cyclic lateral loads. *Journal of Geotechnical and Geoenvironmental Engineering*, 125(9):798–802.

Liu, H., Zou, D., and Liu, J. (2014). Constitutive modeling of dense gravelly soils subjected to cyclic loading. *International Journal for Numerical and Analytical Methods in Geomechanics*, 38(14):1503–1518.

Liu, H. Y., Abell, J. A., Diambra, A., and Pisanò, F. (2019). Modelling the cyclic ratcheting of sands through memory-enhanced bounding surface plasticity. *Géotechnique*, 69(9):783–800.

Liu, H. Y., Diambra, A., Abell, J. A., and Pisanò, F. (2020a). Memory-enhanced plasticity modelling of sand behaviour under undrained cyclic loading. *Journal of Geotechnical and Geoenvironmental Engineering*, 146(11).

Liu, H. Y., Kementzetzidis, E., Abell, J. A., and Pisanò, F. (2020b). From cyclic sand ratcheting to tilt accumulation in offshore monopiles: 3D FE modelling using SANISAND-MS. *Under review*.

Liu, H. Y. and Pisanò, F. (2019). Prediction of oedometer terminal densities through a memory-enhanced cyclic model for sand. *Géotechnique Letters*, 9(2):1–8.

Liu, H. Y., Zygounas, F., Diambra, A., and Pisanò, F. (2018). Enhanced plasticity modelling of high-cyclic ratcheting and pore pressure accumulation in sands. In *Numerical Methods in Geotechnical Engineering IX, Volume 1: Proceedings of the 9th European Conference on Numerical Methods in Geotechnical Engineering (NUMGE 2018), June 25-27, 2018, Porto, Portugal*, page 87. CRC Press.

López-Querol, S. and Coop, M. (2012). Drained cyclic behaviour of loose dogs bay sand. *Géotechnique*, 62(4):281–289.

Loukidis, D. and Salgado, R. (2009). Modeling sand response using two-surface plasticity. *Computers and Geotechnics*, 36(1):166–186.

Luong, M. (1982). Mechanical aspects and thermal effects of cohesionless soils under cylcic and transient loading. In *Deformation and Failure of Granular Materials. International Union of Theoretical and Applied Mechanics, Delft, the Netherlands*, pages 239–246. AA BALKEMA PUBLISHERS.

Maier, G. and Hueckel, T. (1979). Nonassociated and coupled flow rules of elastoplasticity for rock-like materials. *International Journal of Rock Mechanics and Mining Sciences & Geomechanics Abstracts*, 16(2):77–92.

Majmudar, T. S. and Behringer, R. P. (2005). Contact force measurements and stress-induced anisotropy in granular materials. *Nature*, 435(7045):1079–1082.

Maleki, M., Cambou, B., and Dubujet, P. (2009). Development in modeling cyclic loading of sands based on kinematic hardening. *International Journal for Numerical and Analytical Methods in Geomechanics*, 33(14):1641–1658.

Manzari, M. T. and Dafalias, Y. F. (1997). A critical state two-surface plasticity model for sands. *Géotechnique*, 47(2):255–272.

Mao, X. (2000). *The behaviour of three calcareous soils in monotonic and cyclic loading*. PhD thesis, University of Western Australia.

Marr, W. A. and Chrisitian, J. T. (1981). Permanent displacements due to cyclic wave loading. *Journal of the Geotechnical Engineering Division*, 107(8):1129–1149.

Mašín, D., Mašín, and Ditzinger (2019). *Modelling of Soil Behaviour with Hypoplasticity*. Springer.

Mazzoni, S., McKenna, F., Scott, M., and Fenves, G. (2007). *OpenSees Command Language Manual*.

McGann, C. R., Arduino, P., and Mackenzie-Helnwein, P. (2015). A stabilized single-point finite element formulation for three-dimensional dynamic analysis of saturated soils. *Computers and Geotechnics*, 66:126–141.

McKenna, F. (2011). Opensees: a framework for earthquake engineering simulation. *Computing in Science & Engineering*, 13(4):58–66.

McNamara, S., García-Rojo, R., and Herrmann, H. J. (2008). Microscopic origin of granular ratcheting. *Physical Review E*, 77(3):031304.

Miner, M. et al. (1945). Cumulative fatigue damage. *Journal of Applied Mechanics*, 12(3):A159–A164.

Mitchell, J. K. and Carpenter, G. C. (1976). *The influences of sand fabric on liquefaction behavior*, volume 9. US Army Waterways Experiment Station.

Mitchell, J. K., Soga, K., et al. (2005). *Fundamentals of soil behavior*. John Wiley & Sons New York.

Miura, S. and Toki, S. (1982). A sample preparation method and its effect on static and cyclic deformation-strength properties of sand. *Soils and Foundations*, 22(1):61–77.

Mojtaba, E.-K. and Taiebat, H. A. (2014). On implementation of bounding surface plasticity models with no overshooting effect in solving boundary value problems. *Computers and Geotechnics*, 55:103–116.

Mróz, Z. (1967). On the description of anisotropic workhardening. *Journal of the Mechanics and Physics of Solids*, 15(3):163–175.

Muir Wood, D. (2003). *Geotechnical modelling*, volume 1. CRC press.

Muir Wood, D. (2007). The magic of sands—the 20th bjerrum lecture presented in oslo, 25 november 2005. *Canadian Geotechnical Journal*, 44(11):1329–1350.

Muir Wood, D. and Belkheir, K. (1994). Strain softening and state parameter for sand modelling. *Géotechnique*, 44(2):335–339.

Mulilis, J. P., Arulanandan, K., Mitchell, J. K., Chan, C. K., and Seed, H. B. (1977). Effects of sample preparation on sand liquefaction. *Journal of the Geotechnical Engineering Division*, 103(2):91–108.

Narsilio, A. and Santamarina, J. (2008). Terminal densities. *Géotechnique*, 58(8):669.

Nemat-Nasser, S. (2000). A micromechanically-based constitutive model for frictional deformation of granular materials. *Journal of the Mechanics and Physics of Solids*, 48(6):1541–1563.

Nemat-Nasser, S. and Tobita, Y. (1982). Influence of fabric on liquefaction and densification potential of cohesionless sand. *Mechanics of Materials*, 1(1):43–62.

Nicolai, G. and Ibsen, L. B. (2014). Small-scale testing of cyclic laterally loaded monopiles in dense saturated sand. *Journal of Ocean and Wind Energy*, 1(4):240–245.

Nicolai, G., Ibsen, L. B., O'Loughlin, C., and White, D. (2017). Quantifying the increase in lateral capacity of monopiles in sand due to cyclic loading. *Géotechnique Letters*, 7(3):245–252.

Niemunis, A. (2003). *Extended hypoplastic models for soils*. Habilitation thesis, Inst. für Grundbau und Bodenmechanik.

Niemunis, A., Wichtmann, T., and Triantafyllidis, T. (2005). A high-cycle accumulation model for sand. *Computers and Geotechnics*, 32(4):245–263.

Nova, R. et al. (2010). *Soil mechanics*. Wiley Online Library.

NRCan (2017). Comprehensive energy use database query system – natural resources canada. Natural Resources Canada.

Oda, M. (1972). Initial fabrics and their relations to mechanical properties of granular material. *Soils and Foundations*, 12(1):17–36.

Oda, M. (1982). Fabric tensor for discontinuous geological materials. *Soils and Foundations*, 22(4):96–108.

Oda, M., Nemat-Nasser, S., and Konishi, J. (1985). Stress-induced anisotropy in granular masses. *Soils and Foundations*, 25(3):85–97.

O'Sullivan, C. (2011). *Particulate discrete element modelling: a geomechanics perspective*. CRC Press.

O'Sullivan, C. and Cui, L. (2009). Micromechanics of granular material response during load reversals: combined DEM and experimental study. *Powder Technology*, 193(3):289–302.

O'Sullivan, C., Cui, L., and O'Neill, S. C. (2008). Discrete element analysis of the response of granular materials during cyclic loading. *Soils and Foundations*, 48(4):511–530.

Page, A. M., Næss, V., De Vaal, J. B., Eiksund, G. R., and Nygaard, T. A. (2019). Impact of foundation modelling in offshore wind turbines: Comparison between simulations and field data. *Marine Structures*, 64:379–400.

Papadimitriou, A. G. and Bouckovalas, G. D. (2002). Plasticity model for sand under small and large cyclic strains: a multiaxial formulation. *Soil Dynamics and Earthquake Engineering*, 22(3):191–204.

Papadimitriou, A. G., Bouckovalas, G. D., and Dafalias, Y. F. (2001). Plasticity model for sand under small and large cyclic strains. *Journal of Geotechnical and Geoenvironmental Engineering*, 127(11):973–983.

Papadimitriou, A. G., Chaloulos, Y. K., and Dafalias, Y. F. (2019). A fabric-based sand plasticity model with reversal surfaces within anisotropic critical state theory. *Acta Geotechnica*, 14(2):253–277.

Papadimitriou, A. G., Dafalias, Y. F., and Yoshimine, M. (2005). Plasticity modeling of the effect of sample preparation method on sand response. *Soils and foundations*, 45(2):109–123.

Park, J. and Santamarina, J. (2019). Sand response to a large number of loading cycles under zero-lateral-strain conditions: evolution of void ratio and small-strain stiffness. *Géotechnique*, 69(6):501–513.

Park, J. and Santamarina, J. C. (2020). Soil response to repetitive changes in pore-water pressure under deviatoric loading. *Journal of Geotechnical and Geoenvironmental Engineering*, 146(5):04020023.

Pasten, C., Shin, H., and Santamarina, J. C. (2014). Long-term foundation response to repetitive loading. *Journal of Geotechnical and Geoenvironmental Engineering*, 140(4):04013036.

Petalas, A. L., Dafalias, Y. F., and Papadimitriou, A. G. (2019). Sanisand-fn: An evolving fabric-based sand model accounting for stress principal axes rotation. *International Journal for Numerical and Analytical Methods in Geomechanics*, 43(1):97–123.

Petalas, A. L., Dafalias, Y. F., and Papadimitriou, A. G. (2020). Sanisand-f: Sand constitutive model with evolving fabric anisotropy. *International Journal of Solids and Structures*, 188:12–31.

Pisanò, F. and Gavin, K. G. (2017). General report for TC209 - Offshore Geotechnics. In *19th International Conference on Soil Mechanics and Geotechnical Engineering (ICSMGE2017), Seoul, South Korea*. International Society of Soil Mechanics and Geotechnical Engineering (ISSMGE).

Pisanò, F. and Jeremić, B. (2014). Simulating stiffness degradation and damping in soils via a simple visco-elastic–plastic model. *Soil Dynamics and Earthquake Engineering*, 63:98–109.

Pisanò, F., Schipper, R., and Schreppers, G.-J. (2019). Input of fully 3D FE soil-structure modelling to the operational analysis of jack-up structures. *Marine Structures*, 63:269–288.

Porcino, D. D., Cicciu, G., and Ghionna, V. (2004). Laboratory investigation of the undrained cyclic behaviour of a natural coarse sand from undisturbed and reconstituted samples. In *Int. Conference on cyclic behaviour of soils and liquefaction phenomena CBS04,*, pages 187–192. Th. Thriantafyllidis (Ed.).

Presti, D. L., Pallara, O., Lancellotta, R., Armandi, M., and Maniscalco, R. (1993). Monotonic and cyclic loading behavior of two sands at small strains. *Geotechnical Testing Journal*, 16(4):409–424.

Prévost, J. H. (1982). Two-surface versus multi-surface plasticity theories: A critical assessment. *International Journal for Numerical and Analytical Methods in Geomechanics*, 6(3):323–338.

Prévost, J. H. (1985). A simple plasticity theory for frictional cohesionless soils. *International Journal of Soil Dynamics and Earthquake Engineering*, 4(1):9–17.

Puzrin, A. (2012). *Constitutive modelling in geomechanics: introduction*. Springer Science & Business Media.

Puzrin, A. and Houlsby, G. (2001). Fundamentals of kinematic hardening hyperplasticity. *International journal of solids and structures*, 38(21):3771–3794.

Randolph, M. and Gourvenec, S. (2011). *Offshore Geotechnical Engineering*. CRC Press.

Richards, I. A., Byrne, B. W., and Houlsby, G. T. (2019). Monopile rotation under complex cyclic lateral loading in sand. *Géotechnique, ahead of print*.

Roesler, S. K. (1979). Anisotropic shear modulus due to stress anisotropy. *Journal of the Geotechnical Engineering Division*, 105(7):871–880.

Roten, D., Fäh, D., and Bonilla, L. F. (2013). High-frequency ground motion amplification during the 2011 tohoku earthquake explained by soil dilatancy. *Geophysical Journal International*, 193(2):898–904.

Rothenburg, L. and Bathurst, R. (1989). Analytical study of induced anisotropy in idealized granular materials. *Géotechnique*, 39(4):601–614.

Rudolph, C., Bienen, B., and Grabe, J. (2014). Effect of variation of the loading direction on the displacement accumulation of large-diameter piles under cyclic lateral loading in sand. *Canadian Geotechnical Journal*, 51(10):1196–1206.

Santamarina, J. C. and Cho, G. C. (2001). Determination of critical state parameters in sandy soils—simple procedure. *Geotechnical Testing Journal*, 24(2):185–192.

Sawicki, A. and Swidzinski, W. (1989). Mechanics of a sandy subsoil subjected to cyclic loadings. *International Journal for Numerical and Analytical Methods in Geomechanics*, 13(5):511–529.

Scott, M. H. and Fenves, G. L. (2003). A Krylov subspace accelerated newton algorithm. In *2003 ASCE/SEI Structures Congress and Exposition: Engineering Smarter*.

Seed, B. and Lee, K. L. (1966). Liquefaction of saturated sands during cyclic loading. *Journal of Soil Mechanics & Foundations Division*, 92(ASCE# 4972 Proceeding).

Seed, H. B. (1981). *Earthquake-resistant design of earth dams*. PhD thesis, University of Missouri–Rolla.

Silver, M. L. and Seed, H. B. (1971). Deformation characteristics of sands under cyclic loading. *Journal of Soil Mechanics & Foundations Div*, 97:1081–1098.

Sloan, S. W., Abbo, A. J., and Sheng, D. (2001). Refined explicit integration of elastoplastic models with automatic error control. *Engineering Computations*, 18(1/2):121–194.

Smart, G., Smith, A., Warner, E., Sperstad, I. B., Prinsen, B., and Lacal-Arantegui, R. (2016). Iea wind task 26: Offshore wind farm baseline documentation. Technical report, National Renewable Energy Lab.(NREL), Golden, CO (United States).

Stallebrass, S. and Taylor, R. (1997). The development and evaluation of a constitutive model for the prediction of ground movements in overconsolidatcd clay. *Géotechnique*, 47:235–253.

Staubach, P. and Wichtmann, T. (2020). Long-term deformations of monopile foundations for offshore wind turbines studied with a high-cycle accumulation model. *Computers and Geotechnics*, 124:103553.

Suiker, A. S. and de Borst, R. (2003). A numerical model for the cyclic deterioration of railway tracks. *International Journal for Numerical Methods in Engineering*, 57(4):441–470.

Sweere, G. T. (1992). *Unbound granular bases for roads.* PhD thesis, Delft University of Technology.

Sze, H. and Yang, J. (2014). Failure modes of sand in undrained cyclic loading: impact of sample preparation. *Journal of Geotechnical and Geoenvironmental Engineering*, 140(1):152–169.

Taborda, D. M., Zdravković, L., Potts, D. M., Burd, H. J., Byrne, B. W., Gavin, K. G., Houlsby, G. T., Jardine, R. J., Liu, T., Martin, C. M., et al. (2019). Finite-element modelling of laterally loaded piles in a dense marine sand at Dunkirk. *Géotechnique, ahead of print*.

Taiebat, M. and Dafalias, Y. F. (2008). Sanisand: Simple anisotropic sand plasticity model. *International Journal for Numerical and Analytical Methods in Geomechanics*, 32(8):915–948.

Tasiopoulou, P. and Gerolymos, N. (2016). Constitutive modeling of sand: Formulation of a new plasticity approach. *Soil Dynamics and Earthquake Engineering*, 82:205–221.

Tatsuoka, F. and Ishihara, K. (1974). Drained deformation of sand under cyclic stresses reversing direction. *Soils and Foundations*, 14(3):51–65.

Tatsuoka, F., Ochi, K., Fujii, S., and Okamoto, M. (1986). Cyclic undrained triaxial and torsional shear strength of sands for different sample preparation methods. *Soils and Foundations*, 26(3):23–41.

Tillemans, H.-J. and Herrmann, H. J. (1995). Simulating deformations of granular solids under shear. *Physica A: Statistical Mechanics and its Applications*, 217(3-4):261–288.

Tong, Z., Fu, P., Zhou, S., and Dafalias, Y. F. (2014). Experimental investigation of shear strength of sands with inherent fabric anisotropy. *Acta Geotechnica*, 9(2):257–275.

Triantafyllidis, T., Wichtmann, T., Chrisopoulos, S., Zachert, H., et al. (2016). Prediction of long-term deformations of offshore wind power plant foundations using engineer-oriented models based on HCA. In *The 26th International Ocean and Polar Engineering Conference*. International Society of Offshore and Polar Engineers.

Truong, P., Lehane, B. M., Zania, V., and Klinkvort, R. T. (2019). Empirical approach based on centrifuge testing for cyclic deformations of laterally loaded piles in sand. *Géotechnique*, 69(2):133–145.

Tsuha, C. d. H., Foray, P., Jardine, R., Yang, Z. X., Silva, M., and Rimoy, S. (2012). Behaviour of displacement piles in sand under cyclic axial loading. *Soils and foundations*, 52(3):393–410.

Vaid, Y. and Chern, J. (1985). Cyclic and monotonic undrained response of saturated sands. In *Advances in the art of testing soils under cyclic conditions*, pages 120–147. ASCE.

Vaid, Y. P. and Chern, J.-C. (1983). Effect of static shear on resistance to liquefaction. *Soils and Foundations*, 23(1):47–60.

Van Eekelen, H. and Potts, D. (1978). The behaviour of drammen clay under cyclic loading. *Géotechnique*, 28(2):173–196.

Wan, R. and Guo, P. (2001a). Effect of microstructure on undrained behaviour of sands. *Canadian Geotechnical Journal*, 38(1):16–28.

Wan, R. G. and Guo, J. (2001b). Drained cyclic behavior of sand with fabric dependence. *Journal of Engineering Mechanics*, 127(11):1106–1116.

Wang, G. and Wei, J. (2016). Microstructure evolution of granular soils in cyclic mobility and post-liquefaction process. *Granular Matter*, 18(3):51.

Wang, G. and Xie, Y. (2013). Modified bounding surface hypoplasticity model for sands under cyclic loading. *Journal of Engineering Mechanics*, 140(1):91–101.

Wang, R., Fu, P., Zhang, J.-M., and Dafalias, Y. F. (2016). Dem study of fabric features governing undrained post-liquefaction shear deformation of sand. *Acta Geotechnica*, 11(6):1321–1337.

Wang, Y. and Mok, C. (2008). Mechanisms of small-strain shear-modulus anisotropy in soils. *Journal of Geotechnical and Geoenvironmental Engineering*, 134(10):1516–1530.

Wichtmann, T. (2005). *Explicit accumulation model for non-cohesive soils under cyclic loading*. PhD thesis, Ruhr-Universität Bochum.

Wichtmann, T. (2016). *Soil behaviour under cyclic loading - experimental observations, constitutive description and applications*. Habilitation thesis, Bauhaus-Universität Weimar.

Wichtmann, T., Niemunis, A., and Triantafyllidis, T. (2005). Strain accumulation in sand due to cyclic loading: drained triaxial tests. *Soil Dynamics and Earthquake Engineering*, 25(12):967–979.

Wichtmann, T., Niemunis, A., and Triantafyllidis, T. (2007). On the influence of the polarization and the shape of the strain loop on strain accumulation in sand under high-cyclic loading. *Soil Dynamics and Earthquake Engineering*, 27(1):14–28.

Wichtmann, T., Niemunis, A., and Triantafyllidis, T. (2010a). Strain accumulation in sand due to drained cyclic loading: on the effect of monotonic and cyclic preloading (miner's rule). *Soil Dynamics and Earthquake Engineering*, 30(8):736–745.

Wichtmann, T., Niemunis, A., and Triantafyllidis, T. (2010b). Towards the FE prediction of permanent deformations of offshore wind power plant foundations using a high-cycle accumulation model. In *International Symposium: Frontiers in Offshore Geotechnics, Perth, Australia*, pages 635–640.

Wichtmann, T., Steller, K., and Triantafyllidis, T. (2020). On the influence of the sample preparation method on strain accumulation in sand under high-cyclic loading. *Soil Dynamics and Earthquake Engineering*, 131:106028.

Wichtmann, T. and Triantafyllidis, T. (2016). An experimental database for the development, calibration and verification of constitutive models for sand with focus to cyclic loading: part II—tests with strain cycles and combined loading. *Acta Geotechnica*, 11(4):763–774.

Wichtmann, T. and Triantafyllidis, T. (2017). Strain accumulation due to packages of cycles with varying amplitude and/or average stress–on the bundling of cycles and the loss of the cyclic preloading memory. *Soil Dynamics and Earthquake Engineering*, 101:250–263.

Wichtmann, T., Triantafyllidis, T., Chrisopoulos, S., Zachert, H., et al. (2017). Prediction of long-term deformations of offshore wind power plant foundations using HCA-based engineer-oriented models. *International Journal of Offshore and Polar Engineering*, 27(04):346–356.

Wilkins, E. (1956). Cumulative damage in fatigue. In *Colloquium on Fatigue/Colloque de Fatigue/Kolloquium über Ermüdungsfestigkeit*, pages 321–332. Springer.

Wroth, C. and Bassett, R. (1965). A stress–strain relationship for the shearing behaviour of a sand. *Géotechnique*, 15(1):32–56.

Wu, W., Li, X., Charlier, R., and Collin, F. (2004). A thermo-hydro-mechanical constitutive model and its numerical modelling for unsaturated soils. *Computers and Geotechnics*, 31(2):155–167.

Yamashita, S. and Toki, S. (1993). Effects of fabric anisotropy of sand on cyclic undrained triaxial and torsional strengths. *Soils and Foundations*, 33(3):92–104.

Yang, H., Sinha, S. K., Feng, Y., McCallen, D. B., and Jeremić, B. (2018). Energy dissipation analysis of elastic–plastic materials. *Computer Methods in Applied Mechanics and Engineering*, 331:309–326.

Yang, H., Wang, H., Feng, Y., and Jeremić, B. (2020). Plastic-energy dissipation in pressure-dependent materials. *Journal of Engineering Mechanics*, 146(3):04019139.

Yang, H., Wang, H., Feng, Y., Wang, F., and Jeremić, B. (2019). Energy dissipation in solids due to material inelasticity, viscous coupling, and algorithmic damping. *Journal of Engineering Mechanics*, 145(9):04019060.

Yang, J. and Sze, H. (2011). Cyclic behaviour and resistance of saturated sand under non-symmetrical loading conditions. *Géotechnique*, 61(1):59–73.

Yang, Z. and Elgamal, A. (2008). Multi-surface cyclic plasticity sand model with lode angle effect. *Geotechnical and Geological Engineering*, 26(3):335–348.

Yimsiri, S. and Soga, K. (2010). DEM analysis of soil fabric effects on behaviour of sand. *Géotechnique*, 60(6):483.

Yoshimi, Y. and Oh-oka, H. (1975). Influence of degree of shear stress reversal on the liquefaction potential of saturated sand. *Soils and foundations*, 15(3):27–40.

Youd, T. L. and Idriss, I. M. (2001). Liquefaction resistance of soils: summary report from the 1996 NCEER and 1998 NCEER/NSF workshops on evaluation of liquefaction resistance of soils. *Journal of Geotechnical and Geoenvironmental Engineering*, 127(4):297–313.

Yu, H.-S. (2007). *Plasticity and geotechnics*, volume 13. Springer Science & Business Media.

Zdravkovic, L. and Jardine, R. (1997). Some anisotropic stiffness characteristics of a silt under general stress conditions. *Géotechnique*, 47(3):407–437.

Zhang, J.-M. and Wang, G. (2012). Large post-liquefaction deformation of sand, part i: physical mechanism, constitutive description and numerical algorithm. *Acta Geotechnica*, 7(2):69–113.

Zhang, Y., Zhou, X., and Wen, Y. (2020). Constitutive theory for sand based on the concept of critical fabric surface. *Journal of Engineering Mechanics*, 146(4):04020019.

Zhao, J. and Guo, N. (2013). Unique critical state characteristics in granular media considering fabric anisotropy. *Géotechnique*, 63(8):695.

Zhu, B., Byrne, B., and Houlsby, G. (2012). Long-term lateral cyclic response of suction caisson foundations in sand. *Journal of Geotechnical and Geoenvironmental Engineering*, 139(1):73–83.

Ziegler, H. and Wehrli, C. (1987). Free energy and the dissipation function. *Advances in applied mechanics*, page 183.

Zienkiewicz, O. C., Chan, A., Pastor, M., Schrefler, B., and Shiomi, T. (1999). *Computational Geomechanics*, volume 613. Chichester, Wiley.

Ziotopoulou, K. and Boulanger, R. (2013). Calibration and implementation of a sand plasticity plane-strain model for earthquake engineering applications. *Soil Dynamics and Earthquake Engineering*, 53:268–280.

Ziotopoulou, K. and Boulanger, R. (2016). Plasticity modeling of liquefaction effects under sloping ground and irregular cyclic loading conditions. *Soil Dynamics and Earthquake Engineering*, 84:269–283.

Zografou, D., Gourvenec, S., and O'Loughlin, C. D. (2019). Response of normally consolidated kaolin clay under irregular cyclic loading and comparison with predictions from the accumulation procedure. *Géotechnique*, 69(2):106–121.

Zytynski, M., Randolph, M., Nova, R., and Wroth, C. (1978). On modelling the unloading-reloading behaviour of soils. *International Journal for Numerical and Analytical Methods in Geomechanics*, 2(1):87–93.

List of Figures

List of Tables

Curriculum Vitæ

柳溟元 Haoyuan LIU

23-06-1991 Born in Gansu, China.

Education

2015–2020 PhD candidate
Delft University of Technology (the Netherlands)

2012–2013 Postgraduate in Geotechnical Engineering
University of Nottingham (UK)

2009–2013 Undergraduate in Hydraulic and Hydroelectric Engineering
Sichuan University (China)

List of Publications

Journal publications

4. **Liu**, **H. Y.**., Kementzetzidis, E., Abell, J. A. and Pisanò, F. (2020b). From cyclic sand ratcheting to tilt accumulation in offshore monopiles: 3D FE modelling using SANISAND-MS. Under review.

3. **Liu**, **H. Y.**., Diambra, A., Abell, J. A. and Pisanò, F. (2020a). Memory enhanced plasticity modelling of sand behaviour under undrained cyclic loading. *Journal of Geotechnical and Geoenvironmental Engineering*, 146(11), DOI: 10.1061/(ASCE)GT.1943-5606.0002362.

2. **Liu**, **H. Y.**. and Pisanò, F. (2019). Prediction of oedometer terminal densities through a memory-enhanced cyclic model for sand. *Géotechnique Letters*, 9 (2), 81-88, DOI: 10.1680/jgele.18.00187.

1. **Liu**, **H. Y.**., Abell, J. A., Diambra, A. and Pisanò, F. (2019). Modelling the cyclic ratcheting of sands through memory-enhanced bounding surface plasticity. *Géotechnique*, 69 (9), 783-800, DOI: 10.1680/jgeot.17.P.307.

Conference publications

3. A. Diambra, R. Corti, **H. Y.**. **Liu**, F. Pisanò, J.A. Abell (2019). Comparison of new memory surface hardening models for prediction of high cyclic loading, In *Proceedings of 17th European Conference on Soil Mechanics and Geotechnical Engineering (ECSMGE 2019)*, Reykjavik, Iceland.

2. **Liu**, **H. Y.**., Abell, J. A., Diambra, A. and Pisanò, F. (2019). Capturing cyclic mobility and preloading effects in sand using a memory-surface hardening model. *7th International Conference on Earthquake Geotechnical Engineering (7ICEGE)*, Rome, Italy, pages 17-20.

1. **Liu**, **H. Y.**., Zygounas, F., Diambra, A. and Pisanò, F. (2018). Enhanced plasticity modelling of high-cyclic ratcheting and pore pressure accumulation in sands. *9th European Conference on Numerical Methods in Geotechnical Engineering (NUMGE 2018)*, Porto, Portugal, pages 88-95.

Acknowledgements

First and foremost, I would like to express my gratitude to my supervisors, Prof. Michael Hicks and Dr. Federico Pisanò, for their continuous guidance and support throughout the PhD program. The inspiring insights they shared, together with the enlightening discussions allowed this project to be successful. Their enthusiasm and professionalism for research will continue to have a profound effect on my future academic journey.

My research began under Federico' s supervision, for whom I was also his inaugural doctoral student. After five years together, I believe that we are on track with our professional development and appreciate both our working relationship and personal friendship.

I would like to thank my PhD committee: Prof. Guy Houlsby, Prof. Claudio di Prisco, Prof. Cristina Jommi, Prof. Ken Gavin and Dr. Ronald Brinkgreve. They allowed me to improve my thesis by volunteering their valuable time and expertise.

Special thanks to Dr. José Antonio Abell and Dr. Andrea Diambra for all the discussion and assistance in the development of the SANISAND-MS model. I am looking forward to further cooperation! Many thanks to China Scholarship Council for the financial support –without it I could not have started this meaningful journey. Also, thanks to Norwegian Geotechnical Institute; the lovely colleagues and favourable environment make me excited to continue my work there in the future.

I am grateful to Weiyuan, Dyvia and Leon for being very supportive and honest friends. We started our PhD research together in a confused state. Five years later, I am glad to be successfully finishing this journey together. Thanks to Xiangcou, Qinqin and Qiang; the awesome food and joyful card games brought me not only extra weight and happiness, but also bright memories. Thanks to superwoman Hongfen for being a patient friend, you are a role model. Thanks to Dr. Anne-Catherine Dieudonné for being such a caring person. Thanks to my friends and colleagues: Kus, Mirthe, Vagelis, Varun, Fotis, Stefano, Arash, Ali, Elahe, Ivo, for the joyful moment we spent. Thanks to the warm Chinese community: Kaiyue, Peiwen, Na, Xuehui, Aoxi, Zheng, Yu'en, Liang and Yimu –I wish you a bright future.

Chinese usually do not say thanks to their closest family. Thus, I will not express my gratitude for their understanding and support here. I know they will never stop supporting me and I will take that with a quiet conscience. I also know that they will not blame me for this – because they love me, just like I love them.